



HAL
open science

Conception et synthèse de catalyseurs de cuivre bio-inspirés pour l'activation de liaisons C-H

James Alfred Isaac

► **To cite this version:**

James Alfred Isaac. Conception et synthèse de catalyseurs de cuivre bio-inspirés pour l'activation de liaisons C-H. Chimie inorganique. Université Grenoble Alpes, 2018. Français. NNT : 2018GREAV068 . tel-02145226

HAL Id: tel-02145226

<https://theses.hal.science/tel-02145226>

Submitted on 2 Jun 2019

HAL is a multi-disciplinary open access archive for the deposit and dissemination of scientific research documents, whether they are published or not. The documents may come from teaching and research institutions in France or abroad, or from public or private research centers.

L'archive ouverte pluridisciplinaire **HAL**, est destinée au dépôt et à la diffusion de documents scientifiques de niveau recherche, publiés ou non, émanant des établissements d'enseignement et de recherche français ou étrangers, des laboratoires publics ou privés.

THÈSE

Pour obtenir le grade de

DOCTEUR DE LA COMMUNAUTE UNIVERSITE GRENOBLE ALPES

Spécialité : **Chimie inorganique et bio-inorganique**

Arrêté ministériel : 25 mai 2016

Présentée par

James Alfred ISAAC

Thèse dirigée par **Catherine BELLE**, Directrice de Recherche,
CNRS, et

Co-encadrée par **Aurore THIBON-POURRET**, Maître de
Conférences, **UGA**

préparée au sein du **Département de Chimie Moléculaire UMR
CNRS/UGA 5250, Université Grenoble Alpes**
dans l'**École Doctorale Chimie et Science du Vivant**

Conception et synthèse de catalyseurs de cuivre bio-inspirés pour l'activation de liaisons C-H

Thèse soutenue publiquement le **30 novembre 2018**,
devant le jury composé de :

Monsieur Frédéric BANSE

Professeur, Université Paris-Sud 11, Rapporteur.

Madame Elodie ANXOLABEHERE-MALLART

Directrice de Recherche, CNRS, Université Paris Diderot 7, Rapporteur.

Madame Olivia REINAUD

Professeure, Université Paris Descartes 5, Examinatrice.

Monsieur Marius REGLIER

Directeur de Recherche, CNRS, Aix Marseille Université, Examineur.

Monsieur Fabrice THOMAS

Professeur à l'Université Grenoble Alpes, Examineur.

Madame Isabelle GAUTIER-LUNEAU

Professeure à l'Université Grenoble Alpes, Présidente du jury.

Madame Catherine BELLE

Directrice de Recherche, CNRS, Université Grenoble Alpes, Membre.

Madame Aurore THIBON-POURRET

Maître de Conférences, Université Grenoble Alpes, Invitée.



Acknowledgements

First of all I would like to thank my supervisors Catherine and Aurore for their support though the last three years. You really have demonstrated great leadership, how to be rigorous (I will never forget Aurore's ability to spot a single character in a different font!). I have learnt so much from your example. You have been great bosses, but also great friends making these last few years a wonderful experience. And yes I do not regret doing a PhD.

I would also like to thank the rapporteurs of this thesis (Frédéric Banse and Elodie Anxolabéhère-Mallart), and the members of the jury (Isabelle Gautier-Luneau, Olivia Reinaud, Fabrice Thomas and Marius Réglie). Thank you all for your work going through my manuscript and also for your helpful suggestions.

Thank you to all of those involved in the ANR funded project COMEBAC, which has led to very rich collaborations. Thank you particularly to Nicolas Le Poul for many helpful discussions and for all of his patience for my slow experimental work, I needed three days to take the blank for my cyclic voltammetry experiment! I should also give a special mention to Federica, who welcomed me with wonderful Italian food each time I came to Brest, and really made me feel at home. Thank you also to Marius and Jalila, for their helpful suggestions at our meetings. Thank you Hélène for clearly explaining concepts that I did not understand, when I regularly came to you full of confusion.

Thank you also to Mehdi Yemloul for welcoming me in your lab for a week, your enthusiasm is inspirational. Thank you Wesley Browne and to all of the other brownies for welcoming me at the University of Groningen for Raman experiments.

I would also like to give my thanks to all of those that I have met in the lab, particularly in the group CIRE. I would like to give a special thank you to Gisèle for all of your help, it was great having you as a neighbour in the lab. Thank you also to Robin Louvet, who put up with me by sharing a lab bench for three months. I would like to thank both the permanent staff and students in this lab for friendship and also for your help along the way.

I have also appreciated the friendship of many of you outside the lab. I have wonderful memories of climbing trips with Nico, Jules, Selim and also Felix who has dragged me up many cliffs far too difficult for me to climb. I have also had some fantastic evenings in the bars with Phouling and Rolf (I will never forget your sense of humour, and you're your rather strange fascination with column chromatography). Thank you also to Vianney, your laughter is infectious!!!

Thank you also to the other chemists that I have met during lunch breaks. Thank you Vini, Daniella, Suzanne, David, Matt, Laura, Lucy and Elinor as well as many others for their friendship and for much laughter while eating “delicious” French cuisine (CROUS).

Thank you to my family, to my parents, my brothers and to Gizem for all of your love and support. You have always been there for me. I am really blessed to have you all.

List of abbreviations

BDE	bond dissociation enthalpy
BDFE	bond dissociation free energy
BNAH	1-benzyl-1,4-dihydronicotinamide
Bu	butyl
BzImH	1,3- dimethyl-2,3-dihydrobenzimidazole
COSY	correlation spectroscopy
CV	cyclic voltammetry
DCM	dichloromethane
DHA	dihydroanthracene
DIPE	diisopropyl ether
DMSO	dimethylsulfoxide
DOSY	diffusion-ordered spectroscopy
EI	electron impact
EPR	electron paramagnetic resonance spectroscopy
ESI-MS	electrospray ionisation-mass spectrometry
EXAFS	extended X-ray absorption fine structure
Fc	ferrocene
FOC	fiber optic cable
GCMS	gas chromatography-mass spectrometry
HAT	hydrogen atom transfer
HATU	hexafluorophosphate azabenzotriazole tetramethyl uronium
IR	infrared
KIE	kinetic isotope effect
M	mol.dm ⁻³
n-BuLi	n-Butyllithium
NIR	near infrared absorption spectroscopy
NMR	nuclear magnetic resonance
OTf	trifluoromethanesulfonate
PCET	proton coupled electron transfer
ppm	parts per million
RDS	rate determining step
rR	resonance Raman
TBAP	tetrabutylammonium perchlorate
TEMPO	(2,2,6,6-Tetramethylpiperidin-1-yl)oxyl
THF	tetrahydrofuran
UV-vis	ultra-violet and visible absorption spectroscopy
XAS	X-ray absorption spectroscopy

Table of contents

List of abbreviations	3
Part I: Introduction	13
Chapter 1: General introduction.....	15
Chapter 2: Bibliographic review on copper-oxygen systems: enzymes, models and zeolites .	17
.....	17
2.1. Introduction on enzymatic systems and models.....	17
2.2. Mononuclear copper enzymes.....	17
2.2.1. Lytic Polysaccharide mono-oxygenases (LPMOs).....	17
2.2.2. Peptidylglycine α -hydroxylation monooxygenases (PHM), tyramine β -monooxygenases (T β M) and dopamine β -monooxygenases (D β M)	21
2.2.3. Formylglycine generating enzyme (FGE)	22
2.3. Small molecule models of mononuclear copper-oxygen species	23
2.3.1. Cu-superoxo and Cu-peroxo species	23
2.3.2. Cu hydroperoxo and alkylperoxo complexes [Cu ^I OOR] ⁺ and [Cu ^{III} OOR] ²⁺	27
2.3.3. The [Cu ^{III} OH] ²⁺ species	28
2.4. Dinuclear copper enzymes: tyrosinase and catechol oxidase.....	29
2.4.1. The enzymes	29
2.4.2. Active species of tyrosinase	30
2.5. Particulate methane monooxygenase	31
2.5.1. The enzyme	31
2.5.2. Active site of pMMO: under debate.....	32
2.5.3. Active species responsible for CH ₄ oxidation in pMMO.....	34
2.6. Zeolites	37
2.7. Small molecule models of trinuclear copper-oxygen species	38
2.8. Small molecule models of dinuclear copper-oxygen species.....	42
2.8.1. The μ - η^2 : η^2 -peroxo-Cu ^{II} ₂ and bis(μ -O)Cu ^{III} ₂ species.	42
2.8.2. Other Cu ₂ :O ₂ species	51
2.8.3. The (μ -O)Cu ^{II} ₂ core.....	52
2.8.4. Mixed valent Cu ^{II} Cu ^{III} systems	53
2.9. Conclusion	54
Chapter 3: Context and preliminary results of this thesis	55

3.1.	Context	55
3.2.	Synthetic strategy.....	55
3.3.	Preliminary results from the ANR project.....	56
3.3.1.	Complexes supported by ligands with an alkoxido spacer.....	56
3.3.2.	Complexes supported by ligands with a phenoxido spacer	56
3.4.	Objectives	59
Part II Results and Discussion		61
Chapter 1: Synthesis and characterisation of Cu^I₂ complexes and their reactivity with O₂. 63		63
1.1.	Cu ^I ₂ complexes with the ligand Py ₄	63
1.1.1.	Choice of ligand	63
1.1.2.	Reactivity of the complex (μ-NCCH ₃)Cu ^I ₂ Py ₄ with O ₂	64
1.1.3.	Complex Cu ^I ₂ Py ₄ without an acetonitrile bridging group.	64
1.2.	Cu ^I ₂ complexes with bis-oxazoline coordinating groups	67
1.2.1.	Choice of the coordinating groups	67
1.2.2.	Synthesis of the ligands Ox ₄ and Py ₂ Ox ₂ and their respective complexes	68
1.2.3.	Solid state characterisation of the complexes from the ligands Py ₂ Ox ₂ and Ox ₄	70
1.2.4.	Solution characterisation of complexes (μ-NCCH ₃)Cu ^I ₂ Py ₂ Ox ₂ and (μ-NCCH ₃)Cu ^I ₂ Ox ₄ ..	71
1.2.5.	Reactivity of complexes (μ-NCCH ₃)Cu ^I ₂ Ox ₄ and (μ-NCCH ₃)Cu ^I ₂ Py ₂ Ox ₂ with O ₂	74
1.2.6.	Reactivity of the Cu ₂ :O ₂ species with external substrates.	79
1.2.7.	Summary of Cu ^I ₂ complexes based on the ligands Ox ₄ and Py ₂ Ox ₂ and their reactivity with O ₂	81
1.3.	DFT calculations on the Cu ₂ :O ₂ species from complexes (μ-NCCH ₃)Cu ^I ₂ Ox ₄ , (μ-NCCH ₃)Cu ^I ₂ Py ₂ Ox ₂ and (μ-NCCH ₃)Cu ^I ₂ Py ₄	81
1.3.1.	Optimised structures of the Cu ₂ :O ₂ species from complexes (μ-NCCH ₃)Cu ^I ₂ Ox ₄ , (μ-NCCH ₃)Cu ^I ₂ Py ₂ Ox ₂ and (μ-NCCH ₃)Cu ^I ₂ Py ₄	82
1.4.	Discussion	84
1.5.	Conclusions and perspectives	85
Chapter 2: Synthesis and characterisation of dissymmetric complexes with the aim of generating mixed valent Cu^{II}Cu^{III} species.		87
2.1.	Introduction.....	87
2.2.	Previous complexes based on a phenoxido spacer.....	87
2.2.1.	Structures of complexes based on a phenoxido spacer	88
2.2.2.	Solution studies of complexes Cu ^{II} ₄ (MeH) ₂ and Cu ^{II} ₂ Me ₂	91
2.2.3.	DFT studies of the mono-oxidised species from complex Cu ^{II} ₂ (Me ₂).....	93

2.3.	Synthon used for the generation of dissymmetric ligands and complexes with a naphthyridine spacer.....	93
2.3.1.	Choice of the type of ligand for the work presented in this chapter	93
2.3.2.	Choice of synthon.....	94
2.4.	Complexes with an aniline moiety	95
2.4.1.	The ligand $\text{Py}_2\text{AnH}_2\text{PF}_6$	95
2.4.2.	Complexes from the ligand $\text{Py}_2\text{AnH}_2\text{PF}_6$	96
2.4.3.	Conclusions: complexes with the ligand $\text{Py}_2\text{AnH}_2\text{PF}_6$	102
2.5.	Complexes with a benzimidazole arm.....	103
2.5.1.	The ligand $\text{Py}_2\text{BenzimH}_2$	103
2.5.2.	Complex supported by the ligand $\text{Py}_2\text{BenzimH}_2$	104
2.5.3.	Conclusions with the complex $\text{Cu}^{\text{II}}_4(\text{Py}_2\text{Benzim})_2$	108
2.6.	Complexes with an indole arm.....	109
2.6.1.	The ligand Py_2InH_2	109
2.6.2.	Complexation with the ligand Py_2InH_2	110
2.6.3.	Conclusions with the ligand Py_2InH_2	112
2.7.	Complexes with a bipyrazole arm	112
2.7.1.	The ligand $\text{Py}_2\text{Pyr}_2\text{H}$	112
2.7.2.	Complexes using the ligand $\text{Py}_2\text{Pyr}_2\text{H}$	113
2.7.3.	Conclusions on the complex $\text{Cu}^{\text{II}}_2\text{Py}_2\text{Pyr}_2$	117
2.8.	Discussion	117
2.9.	Conclusions.....	120
Chapter 3: Synthesis of Cu^{II}_2 complexes with access to a $\text{Cu}^{\text{II}}\text{Cu}^{\text{III}}$ oxidation state.....		121
3.1.	Choice of ligands.....	121
3.2.	Synthesis of Cu^{II}_2 complexes.....	122
3.3.	Solid state characterisation of the complexes from the ligands Py_4 , Py_2Ox_2 and Ox_4	122
3.3.1.	Crystal structure of the Cu^{II} complex from the ligand Py_4	122
3.3.2.	Crystal structure of the Cu^{II} complex from the ligand Ox_4	124
3.3.3.	Crystal structure of the Cu^{II} complex from the ligand Py_2Ox_2	125
3.4.	Solution characterisation of complexes $\text{Cu}^{\text{II}}_2\text{Py}_4$, $\text{Cu}^{\text{II}}_2\text{Ox}_4$ and $\text{Cu}^{\text{II}}_2\text{Py}_2\text{Ox}_2$	126
3.4.1.	Characterisation of complex $\text{Cu}^{\text{II}}_2\text{Py}_4$ in acetonitrile by NMR	126
3.4.2.	Characterisation of the complexes $\text{Cu}^{\text{II}}_2\text{Py}_4$, $\text{Cu}^{\text{II}}_2\text{Ox}_4$ and $\text{Cu}^{\text{II}}_2\text{Py}_2\text{Ox}_2$ by ESI-MS.....	128
3.5.	Effect of oxidation on the complexes $\text{Cu}^{\text{II}}_2\text{Py}_4$, $\text{Cu}^{\text{II}}_2\text{Ox}_4$ and $\text{Cu}^{\text{II}}_2\text{Py}_2\text{Ox}_2$	130
3.5.1.	CV of the complexes $\text{Cu}^{\text{II}}_2\text{Py}_4$, $\text{Cu}^{\text{II}}_2\text{Ox}_4$ and $\text{Cu}^{\text{II}}_2\text{Py}_2\text{Ox}_2$	130

3.5.2.	Characterisation of the mono-electronic oxidised species	132
3.6.	Discussion	142
3.7.	Conclusions.....	143
Chapter 4: Reactivity of mixed valent Cu^{II}Cu^{III} species		145
4.1.	Brief introduction to electrocatalysis	145
4.1.1.	Typical shapes of CVs for electrocatalysis	146
4.1.2.	Description of the occurrences at the electrode for each shape of CV	147
4.1.3.	Determining rate constants from the CV of an electrocatalytic reaction	148
4.1.4.	Summary.....	151
4.2.	Reactivity of complexes Cu ^{II} ₂ Py ₂ Ox ₂ and Cu ^{II} ₂ Ox ₄	152
4.2.1.	Reactivity with an external substrate.....	152
4.2.2.	Internal reactivity	154
4.2.3.	Conclusions.....	158
4.3.	Reactivity of complex Cu ^{II} ₂ Py ₄	159
4.3.1.	Reactivity of Cu ^{II} ₂ Py ₄ with an external substrate	159
4.3.2.	Electrocatalytic activity of Cu ^{II} ₂ Py ₄	169
4.4.	Conclusions on the reactivity of a Cu ^{II} Cu ^{III} species.	182
Chapter 5: General conclusions and perspectives		185
Part III: Experimental Section		189
Chapter 1: General methods		191
1.1.	X-ray crystallography.....	191
1.2.	EPR spectroscopy	191
1.3.	NMR spectroscopy	191
1.3.1.	NMR of paramagnetic complexes	191
1.3.2.	NMR general.....	191
1.4.	ESI-MS.....	191
Chapter 2: Part II Chapter 1		192
2.1.	Synthesis of Cu ^I ₂ complexes	192
2.1.1.	Synthesis of the complex (μ-NCCH ₃)Cu ^I ₂ Py ₄	192
2.1.2.	Synthesis of complex Cu ^I ₂ Py ₄	192
2.1.3.	Crystallographic data for the complex Cu ^I ₂ Py ₄	193
2.1.4.	Complexes (μ-CH ₃ CN)Cu ^I ₂ Ox ₄ and (μ-CH ₃ CN)Cu ^I ₂ Py ₂ Ox ₂	193
2.2.	Other procedures	196
2.2.1.	Addition of O ₂ to Cu ^I ₂ complexes followed by UV-vis	196

2.2.2.	Raman spectroscopy	196
2.2.3.	ESI-MS of complex $(\mu\text{-CH}_3\text{CN})\text{Cu}^{\text{I}}_2\text{Ox}_4$	197
2.2.4.	$^1\text{H-NMR}$ of $(\mu\text{-CH}_3\text{CN})\text{Cu}^{\text{I}}_2\text{Ox}_4$ and $(\mu\text{-CH}_3\text{CN})\text{Cu}^{\text{I}}_2\text{Py}_2\text{Ox}_2$	197
2.2.5.	Reactivity of the $\text{Cu}_2\text{:O}_2$ species formed from the complexes $(\mu\text{-CH}_3\text{CN})\text{Cu}^{\text{I}}_2\text{Ox}_4$ and $(\mu\text{-CH}_3\text{CN})\text{Cu}^{\text{I}}_2\text{Py}_2\text{Ox}_2$: screening by GCMS.....	197
2.2.6.	DFT calculations.....	198
Chapter 3: Part II Chapter 2		198
3.1.	Complexes with a phenoxido spacer.....	198
3.2.	Syntheses of dissymmetric ligands.....	198
3.2.1.	Synthesis of the synthon I for dissymmetric ligand synthesis.....	198
3.2.2.	Synthesis of dissymmetric ligands.....	200
3.3.	Syntheses of dissymmetric complexes.....	204
3.3.1.	Syntheses of complexes with the ligand Py_2An	204
3.3.2.	Synthesis of the complex $\text{Cu}^{\text{II}}_4(\text{Py}_2\text{Benzim})_2$	204
3.3.3.	Attempted syntheses of complexes with the ligand Py_2InH_2	205
3.3.4.	Synthesis of the complex $\text{Cu}^{\text{II}}_2\text{Py}_2\text{Pyr}_2$	206
3.3.5.	Crystallographic data complexes.....	207
3.4.	Other procedures	207
3.4.1.	Cyclic voltammetry	207
3.4.2.	UV-vis: Titration of the ligand Py_2InH_2 with $\text{Cu}(\text{OTf})_2$	208
Chapter 4: Part II Chapter 3		208
4.1.	Synthesis.....	208
4.1.1.	Synthesis of the ligands Py_4 , Ox_4 and Py_2Ox_2	208
4.1.2.	Syntheses of the complexes $\text{Cu}^{\text{II}}_2\text{Py}_4$, $\text{Cu}^{\text{II}}_2\text{Ox}_4$ and $\text{Cu}^{\text{II}}_2\text{Py}_2\text{Ox}_2$	208
4.1.3.	Crystallographic data for the complexes.....	210
4.2.	Other procedures	211
4.2.1.	Room temperature CV.....	211
4.2.2.	Spectroelectrochemistry	211
4.2.3.	Low temperature electrolysis.....	211
4.2.4.	EPR of the complexes $\text{Cu}^{\text{II}}_2\text{Py}_4$, $\text{Cu}^{\text{II}}_2\text{Ox}_4$ and $\text{Cu}^{\text{II}}_2\text{Py}_2\text{Ox}_2$ and their mono-electronic-oxidised species.....	212
4.2.5.	Theoretical calculations on the complex $\text{Cu}^{\text{II}}_2\text{Py}_4$ and its oxidised species	212
Chapter 5: Part II Chapter 4		213
5.1.	Cyclic Voltammetry	213

5.1.1.	CVs of complexes $\text{Cu}^{\text{II}}\text{Py}_4$, $\text{Cu}^{\text{II}}\text{Ox}_4$ and $\text{Cu}^{\text{II}}\text{Py}_2\text{Ox}_2$ with toluene	213
5.1.2.	CVs of complex $\text{Cu}^{\text{II}}\text{Py}_4$ with greater than one equivalent of pyridine or 2,6-lutidine	213
5.1.3.	CVs of complex $\text{Cu}^{\text{II}}\text{Py}_4$ with 2,6-lutidine: addition of substoichiometric quantities of 2,6-lutidine and addition of water	213
5.1.4.	Simulations	213
5.2.	Determination of oxidation products.....	214
5.2.1.	Determination of the internal reactivity of complexes $\text{Cu}^{\text{II}}\text{Py}_2\text{Ox}_2$ and $\text{Cu}^{\text{II}}\text{Ox}_4$	214
5.2.2.	Determination of the reactivity of complex $\text{Cu}^{\text{II}}\text{Py}_4$ with Toluene	214
5.2.3.	Determination of the products from the electrocatalytic reactivity of complex $\text{Cu}^{\text{II}}\text{Py}_4$ with 2,6-lutidine and toluene.....	215
Bibliography		217

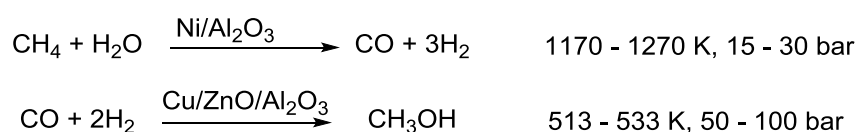
Part I: Introduction

1. General introduction

With growing demands on our energy sources, more efficient use of the earth's resources is required. While we have used coal and oil as combustible fuels, we have largely disregarded natural gas by letting it escape into the atmosphere. In the past, less than 10 percent of the world's methane liberated by mines is used as a fuel.¹ As methane is more potent than CO₂ as a greenhouse gas by a factor of 84,^{2,3} it is not surprising that methane is now the second greatest contributor to human-induced climate change.⁴ The combustion of methane to CO₂ would significantly reduce the potential damage to the atmosphere and at the same time the energy could be harvested. The combustion of methane also produces fewer greenhouse gasses than longer chained hydrocarbons, making it a more environmentally friendly fuel.⁵

One of the issues of using methane as a fuel source is that it is a gas and is therefore difficult to contain, so methane is often flared instead of collected at oil refineries. The use of the energy from methane would be far more accessible if it could easily be converted into methanol, which is arguably one of the best methods for the chemical storage of energy. It is superior to H₂ in terms of energy density and safety, and offers access to the synthesis of other hydrocarbons as it is functionalised.⁶

Current processes for the conversion of methane to methanol are costly in terms of finances and resources as they require high temperatures and pressures. Methane is reacted with water to form syngas in the steam gas reforming reaction, after which the products can be reacted together in a different ratio to form methanol.⁵ Typical conditions are shown in Scheme 1.



Scheme 1 : Formation of methanol *via* a two-step synthesis.⁵

An alternative method for the synthesis of methanol from methane could be direct conversion. The thermodynamics of this reaction are favourable but the kinetics are not: the C-H bond in methane is very strong at 104 kcal.mol⁻¹. As the C-H bonds in methanol (94 kcal.mol⁻¹)⁵ are weaker than in methane, there is always a danger of over-oxidation making selectivity an issue.

Despite the difficulties in the oxidation of methane to methanol, certain enzymes such as particulate or soluble methane mono-oxygenases (pMMO/sMMO) are able to selectively convert methane to methanol at room temperature.⁷ Other copper based enzymes are also capable of the

selective oxidation of other strong C-H bonds such as lytic polysaccharide mono-oxygenase (LPMO), dopamine and tyramine beta mono-oxygenase (D β M, T β M) and tyrosinase (Ty). A better understanding of these enzymes would therefore help with the design of catalysts for methane (and other alkane) oxidation. Copper is also an excellent metal of choice for the design of catalysts as it is cheap, abundant and non-toxic.

While it is heterogeneous catalysts that are the most advanced towards the oxidation of methane to methanol, the techniques for analysis of mechanisms and intermediates involved are very limited in the solid state. Solution studies of model complexes of the active sites of enzymes therefore have a crucial role in understanding C-H activation. It is in this category that this project falls: the synthesis and characterisation of model complexes inspired by copper enzymes with the aim of elucidating nature's secrets on C-H activation. This will contribute to mechanistic information in order to design better catalysts for the direct oxidation of methane to methanol.

This thesis contains the following sections:

- The remainder of Part I contains a literature review on the copper-oxygen systems (chapter 2) including those present in enzymes and model complexes. An introduction to the project and preliminary results will be discussed in Part I Chapter 3.
- Part 2 contains the results obtained in this thesis. Chapter 1 discusses our attempts at activating dioxygen using dinuclear Cu^I complexes. In Chapter 2 our results on attempting to synthesise dissymmetric Cu^{II}₂ complexes with the aim of generating the Cu^{II}Cu^{III} species will be presented. The successful synthesis and characterisation of Cu^{II}Cu^{III} species is given in Chapter 3, with their reactivity towards substrates discussed in Chapter 4.

2. Bibliographic review on copper-oxygen systems: enzymes, models and zeolites

2.1. Introduction on enzymatic systems and models

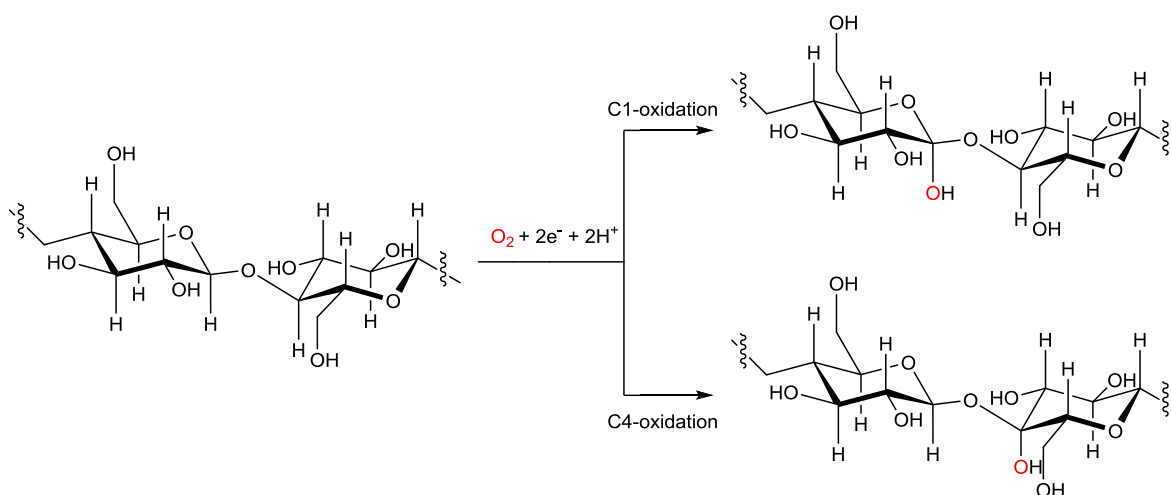
There is a great diversity in the structures of enzymes involved in various biological processes that are able to oxidise strong C-H bonds, and a variety of mechanisms are possible. Despite the structures of some of them having been known for years, the active species responsible for C-H oxidation in many of these active sites is still under debate. Some of these enzymes contain copper at their active sites, making copper a good choice of metal for designing catalysts for the oxidation of alkanes. A whole range of synthetic models have shed some light on the mechanistic aspects of copper enzymes, some of which display very efficient catalytic activity which could have relevance for industrial processes. In this section copper mono-oxygenase enzymes are described and a few selected examples of their model complexes are given.

2.2. Mononuclear copper enzymes

2.2.1. Lytic Polysaccharide mono-oxygenases (LPMOs)

2.2.1.1. The enzymes

LPMO enzymes, present in a wide range of species of bacteria and fungi, are a class of enzyme that is responsible for breaking down polysaccharides into smaller sugars. This process involves the oxidation of an unreactive C-H bond (bond dissociation energy (BDE) of C1 = 101 kcal.mol⁻¹, C4 = 104 kcal.mol⁻¹)⁸, which then allows elimination reaction leading to the cleavage of the 1-4 glycosidic bond through either the oxidation of C1 or C4 (Scheme 2).^{9,10}



Scheme 2 : The oxidation of cellulose by LPMO. Scheme adapted from Eijsink *et al.*⁹

2.2.1.2. Active site of LPMO

The active site of the enzyme is now relatively well understood, and contains some interesting features. A single copper is coordinated by two histidine residues, one of which is terminal (and the N-histidine possibly methylated to prevent deprotonation)¹¹ so that the copper is bound both to the N atom of the side chain and to the NH_2 terminal in what is called a *histidine brace* which is conserved across all species.¹² Electron paramagnetic resonance (EPR) measurements show that these ligands hold the copper in a square planar or a T shaped geometry (depending on the type of LPMO).^{11,13} A tyrosine residue and a glutamine residue are present at around 2.9 Å and 3.8 Å respectively from the copper, which if removed both lead to a significant decrease in the activity of the enzyme¹⁴ and may therefore be responsible for the shuttling of protons. A highly conserved alanine residue is present sterically hindering access to the copper, which is likely to direct the substrate trans to the coordinated NH_2 group of the *histidine brace*.¹¹ These features are summarised in Figure 1.

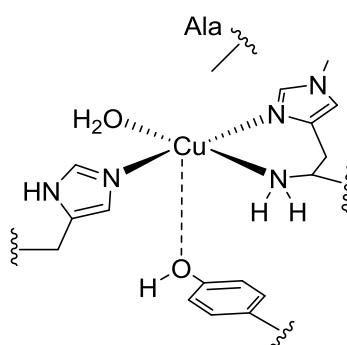
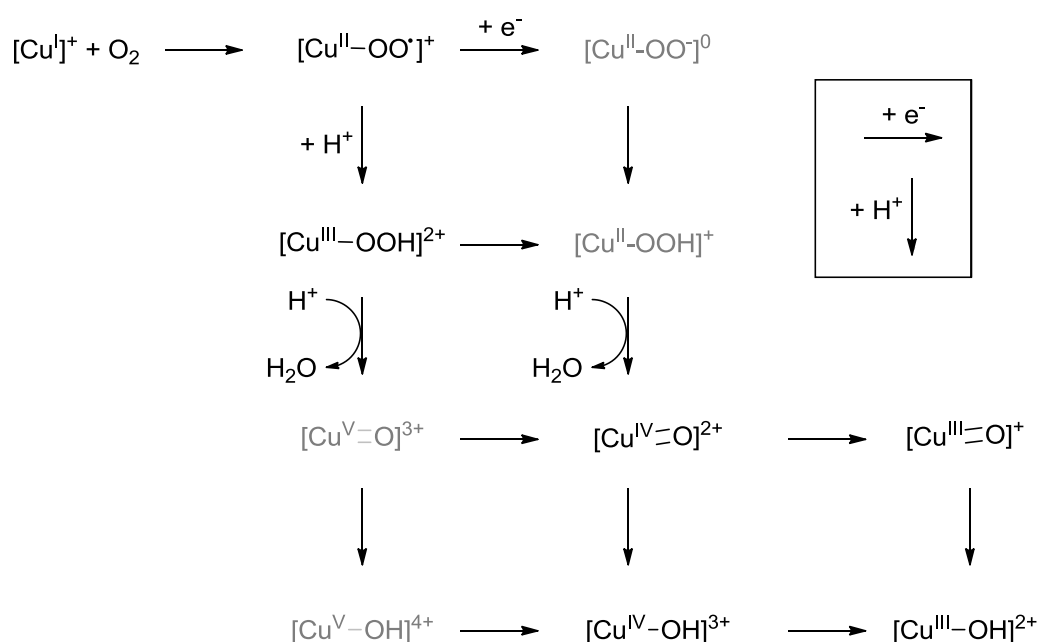


Figure 1 : Diagram of the active site of LPMO. Figure adapted from Walton *et al.*^{11,13}

2.2.1.3. Proposed active species for the enzyme LPMO.

The active species responsible for the reactivity of LPMO is still unclear, and this is further complicated by the fact that it seems as though LPMO can oxidise C-H bonds *via* several different mechanisms. While it is known that the enzyme activates O₂ with a single copper,¹⁵ several Cu:O adducts are possible from this reaction (Scheme 3) of which some are more reactive than others. It is likely that the activation of O₂ by the Cu^I produces a Cu:O species that performs a hydrogen atom abstraction of the C-H bond, followed possibly by a radical rebound mechanism.



Scheme 3: Possible intermediates formed by reaction of Cu^I with O₂ that may be involved in the catalytic cycle of LPMOs. Horizontal arrows and vertical arrows depict electron transfer and proton transfer respectively, and a diagonal (down and right) is therefore a hydrogen atom transfer. Species in grey are unlikely to be involved. Formal oxidation states have been given, but resonance structures are not displayed for simplicity. Scheme adapted from Ryde *et al.*⁸

In a recent paper, Ryde *et al.*⁸ used quantum mechanics/molecular mechanics (QM/MM) to optimise the coordination environment of the crystal structure of LPMO¹⁶ and then used density functional theory (DFT) to calculate the BDEs of the formation of various Cu:O_n-H bonds formed upon hydrogen atom transfer (HAT). While this information ignores the kinetics of the reaction, comparison with the BDE value of the C-H of the substrate gives an idea of the thermodynamic driving force for which species could abstract a hydrogen atom from polysaccharides. The results for BDEs of various copper oxygen species obtained are shown in Table 1. While several of these species

are far out of the ordinary for synthetic chemistry (such as $[\text{Cu}^{\text{IV}}=\text{O}]^{2+}$ or $[\text{Cu}^{\text{IV}}-\text{OH}]^{3+}$ species, *i.e.* formally Cu^{IV} complexes) the values in Table 1 do show a significant trend: BDEs are significantly higher where the O-O bond is broken (over 92 kcal.mol^{-1}) compared to when the O-O bond is still present (below 76 kcal.mol^{-1}). BDEs of some of the species with the broken O-O bond are even higher than that of the substrate cellulose, indicating that the thermodynamics of the reaction of these species with the substrate would be more favourable and even exothermic for the species $[\text{Cu}^{\text{IV}}=\text{O}]^{2+}$ and $[\text{Cu}^{\text{III}}=\text{O}]^+$.⁸ It was also found that the coordination of the tyrosine residue had little influence on the values of the BDEs,⁸ suggesting that the importance of the tyrosine is in the shuttling of protons and not in the stabilisation of intermediates. Interestingly deprotonation of the N terminal amino acid (coordinated in the form of a histidine brace) did not significantly change the BDEs,⁸ presumably because the stabilisation of the higher valent copper (and therefore decreasing the BDE) is coupled with an increase in pK_a of the copper-oxygen species which would increase the BDE.

Table 1 : Calculated BDEs for the formation of the respective OH bonds for possible intermediates responsible for C-H oxidation by LPMOs. Table adapted from Ryde *et al.*⁸

Species	BDE / kcal.mol^{-1}
$[\text{Cu}^{\text{II}}-\text{OO}]^+$	72.0
$[\text{Cu}^{\text{III}}-\text{OOH}]^{2+}$	75.8
$[\text{Cu}^{\text{IV}}=\text{O}]^{2+}$	111.8
$[\text{Cu}^{\text{IV}}-\text{OH}]^{3+}$	96.6
$[\text{Cu}^{\text{III}}=\text{O}]^+$	109.7
$[\text{Cu}^{\text{III}}-\text{OH}]^{2+}$	92.5
Cellulose-C1	101

Beckham *et al.*¹⁷ also used DFT calculations based on a crystal structure of LPMO¹² to compare the energy profiles of the oxidation of the C-H bonds in polysaccharides by $[\text{Cu}^{\text{II}}-\text{OO}]^+$ and $[\text{Cu}^{\text{II}}-\text{O}]^+$, and therefore determining the energy of the transition states. In both cases, the highest energy transition state was hydrogen atom abstraction, with the values of around 40 kcal.mol^{-1} for the $[\text{Cu}^{\text{II}}-\text{OO}]^+$ species and 20 kcal.mol^{-1} for $[\text{Cu}^{\text{II}}-\text{O}]^+$ species.¹⁷ Similarly in a recent DFT study by Rovira *et al.*¹⁸ the reactivity of the mononuclear copper centre of LPMO was computed to determine its reactivity with H_2O_2 instead of O_2 . The O-O bond of H_2O_2 could be cleaved with a minimal energy of $7.7 \text{ kcal.mol}^{-1}$. Interestingly, the $\cdot\text{OH}$ formed could then do a HAT from the $[\text{Cu}^{\text{II}}-\text{OH}]^+$ species, generating the oxyl $[\text{Cu}^{\text{II}}-\text{O}]^+$ species. The $[\text{Cu}^{\text{II}}-\text{O}]^+$ species is then able to cleave the C4-H bond of the substrate with a relatively low transition state energy of $7.8 \text{ kcal.mol}^{-1}$.¹⁸ While these studies are not complete as they do not include several of the realistic copper-oxygen species for C-H oxidation, they do

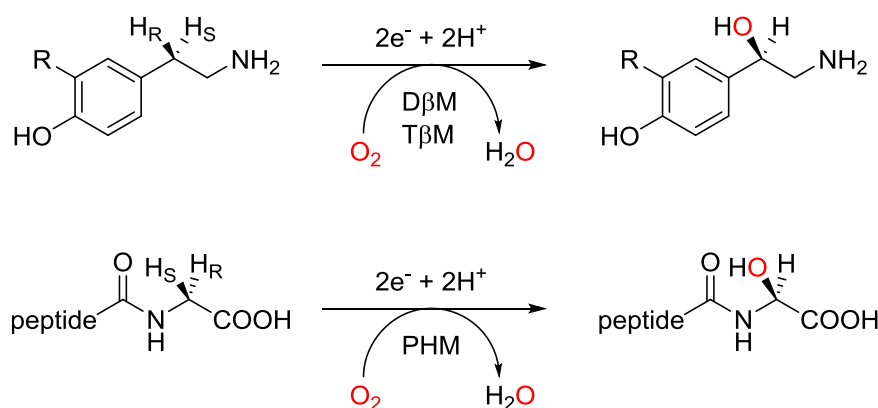
indicate that certain species where the O-O bond is broken could be candidates for the HAT of the C-H bond.

2.2.1.4. Summary

The enzyme LPMO is known to be a mononuclear copper enzyme that activates O_2 and has a rather unique coordination environment: the *histidine brace*. The key step for the mechanism for the cleavage of the 1,4-glycosidic bond is the oxidation of either C1 or C4 to form the alcohol, which is likely to occur by HAT followed by a radical rebound. While it is still unclear which copper-oxygen species is responsible for HAT, it is likely that the O-O bond is fully cleaved before HAT can occur.

2.2.2. Peptidylglycine α -hydroxylation monooxygenases (PHM), tyramine β -monooxygenases (T β M) and dopamine β -monooxygenases (D β M)

D β M and T β M are enzymes found in eukaryotes that catalyse the hydroxylation of the benzylic position of dopamine (BDE of 85 kcal.mol^{-1})¹⁹ (or tyramine), and PHM catalyses the hydroxylation of the C α of a C terminal glycine (BDE = 87 kcal.mol^{-1})¹⁹ (Scheme 4). All of them are important for the regulation of neurotransmitters. The active sites of these enzymes are very similar (Figure 2).



Scheme 4: Reactions catalysed by PHM (bottom) and D β M/ T β M (top). R = H (catalysed by T β M) or OH (D β M). Scheme adapted from Yoshizawa *et al.* and Estrin *et al.*^{20,21}

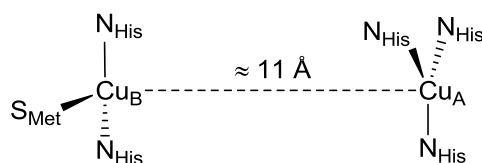
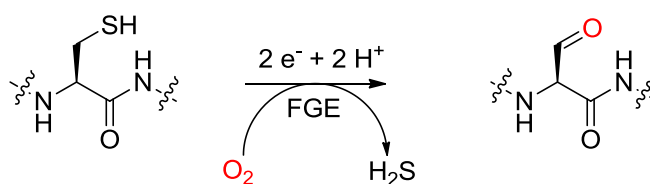


Figure 2: Diagram of the active site of PHM, DβM/ TβM all containing the same features.

DβM and TβM possess two copper atoms at the active site²² but which are chemically distinct and non-coupled so are much greater than 4 Å apart,²³ although a recent structure of human DβM showed that the enzyme could have two different conformations, with the copper atoms 4-5 Å apart (*i.e.* could be coupled) or 14 Å apart.²⁴ It is thought that the activity (O₂ and substrate binding) of the enzyme occurs at one of the copper atoms whereas the other Cu is used to control electron transfer.²³ The active site of PHM is similar in that it contains two (non-coupled) copper atoms 11 Å apart, Cu_A which modulates electron transfer and Cu_B which is responsible for the activation of O₂ and reactivity on the substrate.^{25,26} The crystal structure of PHM showed that Cu_B is coordinated by two histidine residues, a methionine and a solvent molecule in a near tetrahedral geometry.²⁵ When the oxygenated form of the enzyme was crystallised, an end-on [Cu^{II}-OO^{*}]⁺ species was observed,²⁶ indicating conclusively that the enzyme activates oxygen and that copper oxygen intermediates are responsible for the reactivity with substrates. For the purpose of comparing the active species present in these enzymes and designing model complexes, all three of these enzymes can be thought of as mononuclear. The active species are therefore likely to go through one of the intermediates shown in Scheme 3, so synthetic models of DβM and TβM will target Cu:O_n species.

2.2.3. Formylglycine generating enzyme (FGE)

A recent addition to the class of copper mono-oxygenase enzymes is the formylglycine generating enzyme (FGE), responsible for the C-H oxidation allowing conversion of thiols to aldehydes (Scheme 5).²⁷

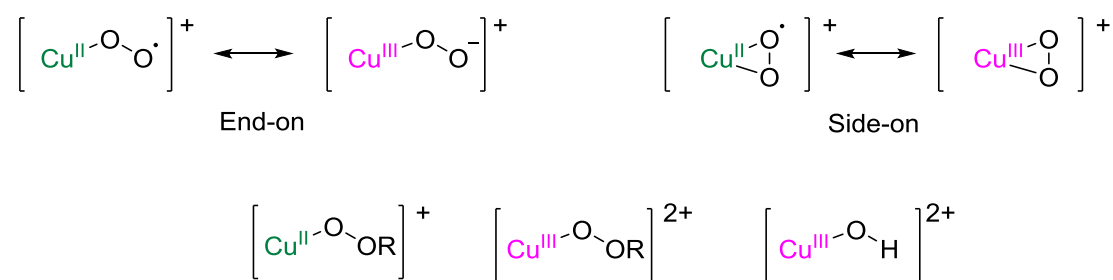


Scheme 5: Reaction catalysed by the enzyme FGE. Scheme adapted from Seebeck *et al.*²⁷

The coordination environment of the active site was determined by crystallisation with Ag^+ or Cd^{2+} in the active site to determine the coordination geometries of the different oxidation states of the native copper (Cu^{I} and Cu^{II}). An unexpected feature is present at the active site: the Ag^+ ion is coordinated by only two sulphur atoms from cysteine residues.²⁷ While this would be expected for an enzyme responsible for electron transfer, it is very unusual for an enzyme that performs C-H oxidation as one would expect oxidation of the coordinating sulphur ligands. When the enzyme is crystallised with Cd^{2+} the geometry is tetrahedral, with the metal coordinated to the two cysteine residues, an acetate and a water molecule. The binding of the acetate group suggests that the deprotonated thiol substrate could bind in the same place, which would allow oxidation of the substrate.

2.3. Small molecule models of mononuclear copper-oxygen species

There is a wealth of synthetic models of the mononuclear copper-oxygen species shown in Scheme 3, some of which have even been crystallised. While most of these species are generated by the same reaction of Cu^{I} with O_2 , their structural diversity is differentiated by the properties of the ligand. In this section a few synthetic examples will be given for different types of mononuclear copper-oxygen species (Scheme 6) and their reactivity discussed.



Scheme 6: Types of mononuclear copper-oxygen species to be discussed in this Chapter. R represents an alkyl group.

2.3.1. Cu-superoxo and Cu-peroxo species

2.3.1.1. Structural characterisation of Cu-superoxo and Cu-peroxo species

One of the first species that is formed upon oxygenation of a single Cu^{I} is the $[\text{Cu}-\text{OO}]^+$ species, accompanied by the weakening of the O-O bond. Either one or two electrons can be transferred, leading to either a formally $[\text{Cu}^{\text{II}}\text{OO}\cdot]^+$ (superoxo) or a $[\text{Cu}^{\text{III}}\text{OO}]^+$ (peroxo) species, or intermediates

between the two. The degree of electron transfer is usually measured by resonance Raman spectroscopy (rR), which determines the vibrational energy (and therefore bond strength) of the O-O bond. The coordination of oxygen to the copper can have two different binding modes: side-on (η^2) or end-on (η^1) (Scheme 6). Synthetic models of both end-on and side-on $[\text{CuO}_2]^+$ species have now been crystallised.

Diagrams of the crystal structures of two side-on $[\text{CuOO}]^+$ species are shown in Figure 3: the first side-on to be crystallised by Kitajama *et al.*²⁸ (complex **1**) and another structure by Tolman *et al.*²⁹ (complex **2**). The X-ray crystal structures allow a detailed analysis of the O-O bond lengths and of the N-Cu bonds. In the case of the complex **1**, the O-O bond distance is of 1.22 Å which is very short, indicating a strong O-O bond. The Cu-N bonds are 2.0 to 2.3 Å, which is typical of a Cu^{II} . These results indicate therefore that only one electron has been passed to the O-O and can therefore best be described as a $[\text{Cu}^{\text{II}}-\text{OO}^*]^+$ species.²⁸ This is in contrast to Tolman's complex **2**, which has a far longer O-O bond at 1.39 Å, indicating a decrease in the O-O bond order. The Cu-N bonds are shorter at around 1.9 Å, indicating the oxidation state of the copper is closer to Cu^{III} , meaning that the complex is best described as a $[\text{Cu}^{\text{III}}-\text{OO}]^+$ species,²⁹ probably due to the more electron donating ability of the ligand. These two complexes indicate therefore that the whole range between one and two electrons can be donated from the copper into the O-O antibond.

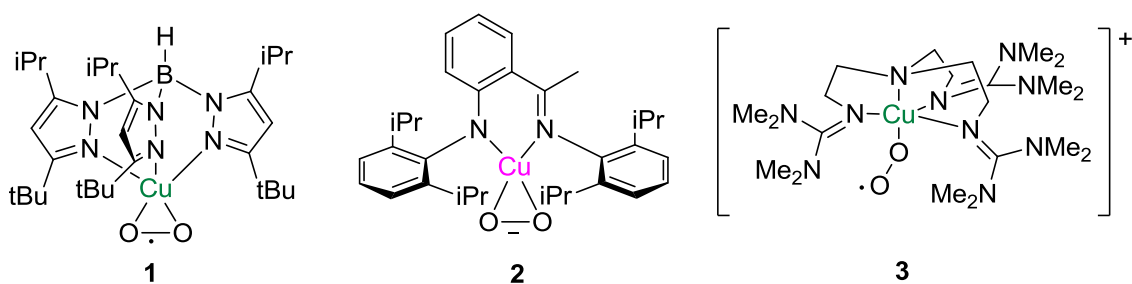
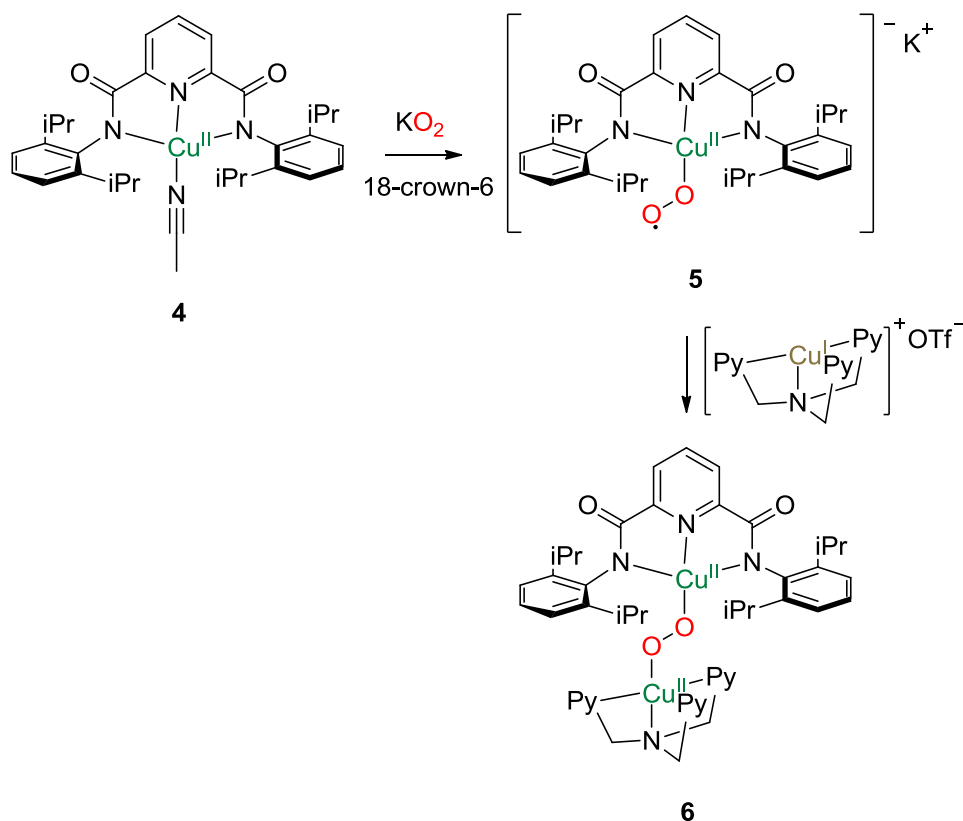


Figure 3 : Diagrammatic representations of crystal structures of complexes **1** (left),²⁸ **2** (centre)²⁹ and **3** (right).³⁰ Figure adapted from Tolman *et al.*³¹

The first crystal structure of an end-on $[\text{Cu-OO}]^+$ complex was characterised by Schindler *et al.*³⁰ and a diagram of the crystal structure is shown in Figure 3 (complex **3**). The O-O bond is of 1.28 Å which is consistent with a superoxo species. Indeed the $[\text{Cu}^{\text{II}}-\text{OO}^*]^+$ intermediate has particular relevance to the enzyme PHM which the crystal structure was observed with O_2 bound in a similar fashion.²⁶



Scheme 7: The formation of a $[\text{Cu}^{\text{II}}\text{-OO}^*]^+$ species followed by addition of $[(\text{tropa})\text{Cu}(\text{CH}_3\text{CN})]\text{OTf}$ to form the (*trans*-1,2-peroxo) complex. Scheme adapted from Tolman *et al.*³²

Steric hindrance is an important factor in the formation of $[\text{Cu}\text{-OO}]^+$ species to inhibit bonding of dioxygen between two mono-copper species. Tolman *et al.* demonstrated the formation of the $[\text{Cu}^{\text{II}}\text{-OO}^*]^+$ complex **5** (Scheme 7) using the bulky ligand based on a pyridine dicarboxamide. However upon the addition of the unhindered complex $[(\text{tropa})\text{Cu}(\text{CH}_3\text{CN})]\text{OTf}$ to complex **5** (where *tropa* = tris(2-pyridylmethyl)amine) yielded the (*trans*-1,2-peroxo) complex **6**,³² (Scheme 7) demonstrating that the steric bulk is essential to avoid the formation of $\text{Cu}_2\text{:O}_2$ species.

2.3.1.2. Reactivity studies of Cu-superoxo and Cu-peroxo species

In order to probe the reactivity of superoxo complexes, Itoh *et al.*³³ used a ligand that mimics the tridentate coordination environment of D β M and PHM. Upon addition of O_2 to the Cu^{I} complex, an end-on $[\text{Cu}^{\text{II}}\text{-OO}^*]^+$ species was assigned based on rR and UV-vis data. Analysis of the solution after decomposition of the superoxo species indicated that the ligand had been hydroxylated in the benzylic position, with molecular oxygen being the source of the O atom (Scheme 8). DFT studies

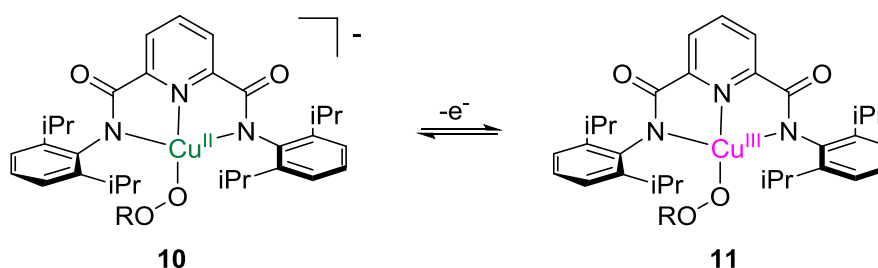
surrounding the copper. This therefore shows that the $[\text{Cu}^{\text{II}}-\text{OO}^*]^+$ species can act either as an electrophile or a nucleophile depending on the coordination environment of the ligand.

In contrast to the wealth literature on the reactivity of end-on $[\text{Cu}^{\text{II}}-\text{OO}^*]^+$ species, the side-on $[\text{Cu}^{\text{III}}-\text{OO}]^+$ seems to be far less reactive.³⁹ This is likely to be due to the strongly electron donating character of the ligands that usually support these complexes (complex **2**, Figure 3) which makes it more difficult to reduce the metal centre upon reaction with a C-H bond thus rendering the reaction less thermodynamically favourable.³¹

2.3.2. Cu hydroperoxo and alkylperoxo complexes $[\text{Cu}^{\text{II}}\text{OOR}]^+$ and $[\text{Cu}^{\text{III}}\text{OOR}]^{2+}$

Hydroperoxo species are invoked as potential intermediates of mononuclear monooxygenases. Their formation in synthetic chemistry is usually achieved through a proton coupled electron transfer (PCET) by the $[\text{Cu}^{\text{II}}-\text{OO}^*]^+$ species, and it is possible that the same occurs in monooxygenases. Other methods have also been used such as the reaction of a Cu^{II} complex with H_2O_2 (or an alkyl peroxo) and a base. The $[\text{Cu}^{\text{II}}-\text{OOH}]^+$ species therefore usually has a fairly limited reactivity towards C-H activation.

In an attempt to increase the oxidising power of a $[\text{Cu}^{\text{II}}-\text{OOR}]^+$ complex, Tolman *et al.*⁴⁰ oxidised the $[\text{Cu}^{\text{II}}-\text{OOR}]^+$ species to a formally $[\text{Cu}^{\text{III}}-\text{OOR}]^{2+}$ species (see Scheme 9). This also acts as a masked $[\text{Cu}^{\text{III}}-\text{OOH}]^{2+}$ species which has been suggested to form upon protonation of the $[\text{Cu}^{\text{III}}-\text{OO}]^+$ unit, and could be responsible for the reactivity of the enzyme PHM.⁴¹ However complex **11** showed minimal reactivity towards the C-H bonds of DHA, and no reaction towards O-H bonds in various derivatives of phenol. Only a reaction with the weak O-H bond in (2,2,6,6-tetramethylpiperidin-1-yl)oxyl (TEMPO-H) was observed.

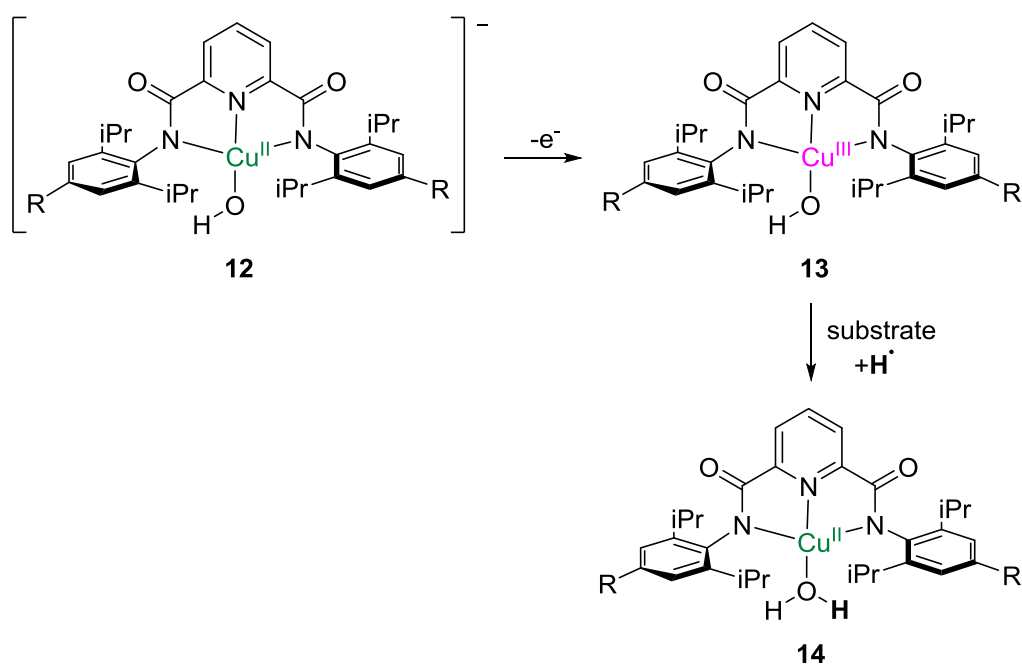


Scheme 9: Generation of a $[\text{Cu}^{\text{III}}-\text{OOR}]^{2+}$ unit. R = tBu or cumyl ($\text{Ph}(\text{CH}_3)_2$). Scheme adapted from Tolman *et al.*⁴⁰

2.3.3. The $[\text{Cu}^{\text{III}}\text{OH}]^{2+}$ species

The $[\text{Cu}^{\text{II}}\text{O}]^+$ core has been suggested to be responsible for the reactivity of several mononuclear enzymes, yet synthetic versions of this species have not been obtained to date. However recently there has been an interest in synthetic versions of the protonated form of the $[\text{Cu}^{\text{III}}\text{O}]^+$ species: the $[\text{Cu}^{\text{III}}\text{-OH}]^{2+}$ core.

The first synthetic example of a $[\text{Cu}^{\text{III}}\text{-OH}]^{2+}$ species was characterised relatively recently by Tolman *et al.*⁴² in 2011. The $[\text{Cu}^{\text{III}}\text{-OH}]^{2+}$ species (complex **13**, Scheme 10) was prepared by chemical or electrochemical oxidation of the $[\text{Cu}^{\text{II}}\text{-OH}]^+$ entity. **13** was capable of the fast O-H activation of phenols or C-H activation of DHA, with a second order rate constant for the C-H activation of $k = 1.1 \text{ M}^{-1}\cdot\text{s}^{-1}$ at -80°C .⁴³ The reaction mechanism with C-H bonds was later determined to be a HAT, with the bond strength of the O-H bond being formed given as $90 \text{ kcal}\cdot\text{mol}^{-1}$ (complex **14**, R = H, Scheme 10), among the highest obtained for synthetic complexes,⁴⁴ indicating that the thermodynamic driving force for C-H activation is very high. A BDE value is a function of the pK_a and the oxidation potential of the species involved (*i.e.* one can equate a hydrogen atom transfer to the transfer of an electron and then a proton, both of which can be experimentally measured). The oxidation potential of the complex **12** (R = H) is low at $-0,08 \text{ V vs. Fc}^+/\text{Fc}$, indicating that the high value of the pK_a is the main component in the high value of the BDE obtained.



Scheme 10: Generation of a $\text{Cu}^{\text{III}}\text{OH}$ species. Scheme adapted from Tolman *et al.*^{42,44}

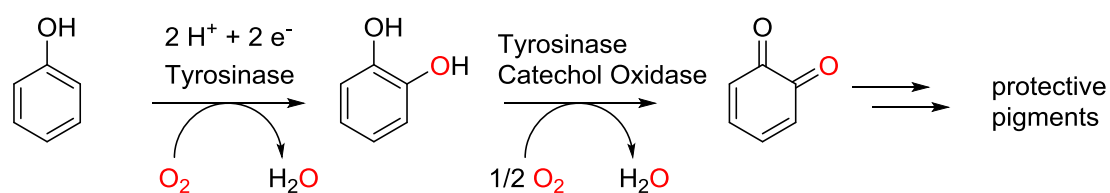
To determine if the oxidation potential or pK_a had more influence on the values of the BDE of the $[\text{Cu}^{\text{II}}\text{-HO-H}]^{2+}$ species formed, Tolman *et al.*⁴⁵ did a further study by making slight alterations to the ligand of complex **12** to make it more or less electron donating. The **R** groups (H) were replaced by NO_2 making the coordination sphere of the copper more electron withdrawing and therefore increasing the oxidation potential to 0.12 V vs. Fc^+/Fc (and as a consequence decreasing the pK_a). A separate complex was synthesised with $\text{R} = \text{H}$ but swapping the pyridine ring for a piperidine ring, increasing the electron donating capacity of the ligand, decreasing the oxidation potential to -0.26 V vs. Fc^+/Fc and increasing the pK_a . An increase in oxidation potential of the complexes was only partially compensated by an decrease in the pK_a , indicating that the value of BDE for the complex with $\text{R} = \text{NO}_2$ (highest oxidation potential) was the greatest, and is also reflected in a higher rate of reaction with DHA.

While the $\text{Cu}^{\text{III}}\text{OH}$ core (postulated for LPMO) seems to be of great interest because of its high reactivity, little is known about how this species would form in the enzyme. At some stage the O-O bond of the oxygen activated by Cu^{I} would have to be cleaved, but no studies have yet demonstrated how mononuclear copper model complexes could do this.

2.4. Dinuclear copper enzymes: tyrosinase and catechol oxidase

2.4.1. The enzymes

Tyrosinase (Ty) is an enzyme found in all organisms, responsible for a key step in melanin synthesis. Ty catalyses the ortho-hydroxylation of phenol to diphenols then the subsequent oxidation to form the quinone. Catechol oxidase is only capable of doing the second step of this reaction (Scheme 11).⁴⁶ Similarities have been drawn between the active site of hemocyanin (Hc), an enzyme responsible for O_2 transport in some arthropods and molluscs, and *in vitro* studies have shown that modifications to Hc can then cause Ty activity.⁴⁷



Scheme 11: Reactions catalysed by Tyrosinase and Catechol Oxidase.

The active sites of Ty and catechol oxidase are composed of six histidine residues coordinating two Cu^I ions in the deoxy form. The side chains of three histidine residues are coordinated to each copper (Figure 5). The coordination environment has been shown to be highly flexible, with several different crystal structures from three different oxidation states (*deoxy*, *met* and *oxy*) showing variation in the Cu-Cu distance. The reasons for the difference in reactivity of Ty and catechol oxidase are still under debate.⁴⁸

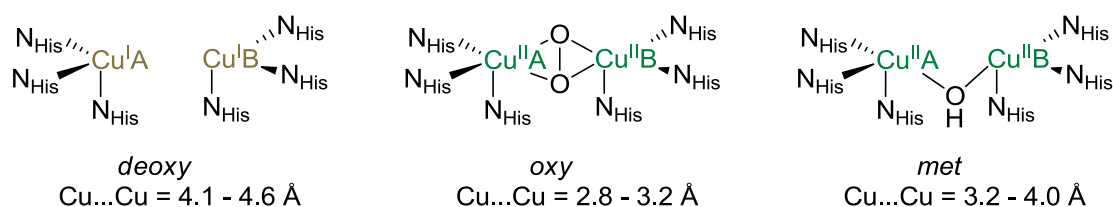
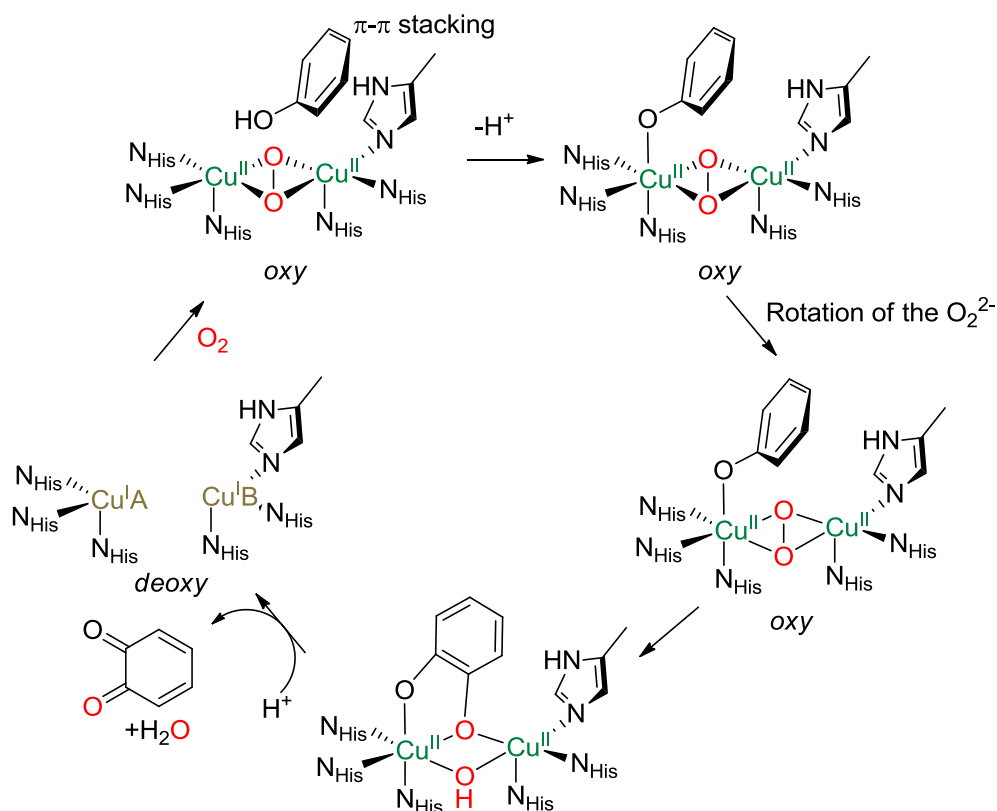


Figure 5: Different forms of Ty and Catechol Oxidase that have been crystallised. Figure adapted from Rompel *et al.*⁴⁸

2.4.2. Active species of tyrosinase

It is well known the active site of the enzyme forms a $\mu\text{-}\eta^2\text{:}\eta^2\text{-peroxo-Cu}^{\text{II}}_2$ adduct, the only $\text{Cu}_2\text{:O}_2$ species observed in the enzyme.⁴⁹ However the mechanism for substrate oxidation by the enzyme is still debated. Tuczek *et al.*⁴⁶ proposed the following mechanism: the phenol coordinates to the less hindered CuA (guided by π/π stacking) followed by a rotation of the O_2^{2-} species. This puts the C_2 of the phenol right next to the peroxo species, enabling electrophilic attack of the peroxo species onto the aromatic ring, cleaving the O-O bond. The diphenolic intermediate is then released to give the quinone and the binuclear Cu^I site, that once again can be activated by O_2 (Scheme 12).⁴⁶ Diedrich *et al.*⁵⁰ confirmed the coordination of the phenol to CuA using molecular dynamics, however they also suggested that instead of a rotation of the O-O unit, the peroxo species was actually in a distorted butterfly shape, giving the proximity of the peroxo species to the phenol allowing the electrophilic attack. Yoshizawa *et al.*⁵¹ proposed a very different mechanism, by which a hydrogen radical is cleaved off the hydroxo group of the phenol by the peroxo species to form a hydroperoxo species, cleavage of the hydroperoxo O-O bond followed by C-O bond formation at the ortho position of the phenol, with O-O bond fission being the rate determining step.



Scheme 12: Proposed mechanism for the oxidation of monophenols to quinones by Ty. Scheme adapted from Tuzcek *et al.*⁴⁶

While much is known about the enzyme Ty and there is agreement that it is a dicopper enzyme that activates oxygen to form a $\mu\text{-}\eta^2\text{:}\eta^2\text{-peroxo-Cu}^{\text{II}}_2$ species (*oxy*), the active species and mechanism for C-H activation is still unknown. Model complexes therefore have a part to play for elucidating the C-H functionalisation of phenols.

2.5. Particulate methane monooxygenase

2.5.1. The enzyme

The copper enzyme particulate methane mono-oxygenase (pMMO) and its iron analogue soluble methane mono-oxygenase (sMMO) are enzymes found in methanotrophic bacteria that use methane as their primary source of energy, metabolising methane to methanol (and then other products) using O₂ at ambient temperature.³ This is no easy task as the C-H bonds in methane are very strong (see Chapter 1).⁵ sMMO has been well characterised and its active site was found to be a di-iron centre, with a still unknown high valent Fe_n:O_n responsible for the activation of C-H bonds in methane.⁵² In contrast pMMO is a membrane bound enzyme which until recently has hampered

purification and the knowledge of pMMO is therefore far behind that of sMMO. While there is general agreement that the enzyme requires copper to function,^{53,54} the number of copper atoms needed is still debated and some groups even suggest an iron active site.⁵⁵

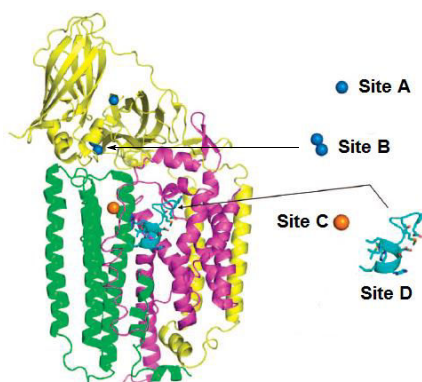


Figure 6: Crystal structure of pMMO.⁵⁶ Pink: PmoA, yellow: PmoB, green: PmoC. Figure adapted from Chan *et al.*⁵⁷

The first crystal structure of pMMO (from *Methylococcus capsulatus*) has only recently been obtained in 2005 by Rosenzweig *et al.*⁵⁶ (Figure 6) and showed the presence of several centres that could be the active site for the enzyme. The enzyme contains a soluble section and a transmembrane section. The soluble section of the enzyme pMMO contains two metal centres which were initially modelled as a dinuclear copper site (site B) and a mononuclear copper site (site A). The transmembrane section of the enzyme was also found to contain a zinc site (site C), which in a later crystal structure (*Methylosinus trichosporium*) was found to be occupied by a copper atom.⁵⁸ The same structure also did not contain the site that was previously modelled as a mononuclear copper site (site A), indication that it is not essential for the enzyme's function. Recombinant soluble fragments of pMMO showed reactivity towards methane, indicating that the active site is present in the soluble domain (PmoB).⁵³ Site specific mutations⁵³ confirmed that it is site B that is responsible for the oxidation of methane and other substrates (n-alkanes between one and 5 carbon atoms).⁷

2.5.2. Active site of pMMO: under debate

The coordination environment of the site B (modelled as a dinuclear site) is shown in Figure 7. There are 3 histidine residues that are present at this site, one of which is the terminal amino acid and therefore forms the unusual *histidine brace* which is also present in LPMO (Section 2.2.1.2). However there are differences with the coordination environment of LPMO as site B in pMMO contains an extra histidine side chain as a ligand. Extended X-ray absorption fine structure (EXAFS)

indicated that there is a Cu-Cu interaction with a very short distance of 2.5-2.7 Å,^{56,58-60} however this interaction was not observed in the latest crystal structure of pMMO from *Methylomicrobium alcaliphilum*, meaning that previous Cu-Cu interactions observed could have been due to an impurity.⁶¹ The assignment of the oxidation states (assuming a binuclear copper centre) was initially given as a mixed valent localised but scrambled Cu^ICu^{II} (*i.e.* there is no electron transfer between the copper ions, but the Cu^{II} can be in either environment) based on the observance of two distinct Cu^{II} EPR signals,⁶² however an alternative interpretation of this data could be that there are two Cu^{II} ions in different environments, one at site B and one in an adventitious binding site. The latest results from Rosenzweig's research group indicate this could well be the case, with quantum refinement calculations of the crystal structure indicating that site B could be modelled just as well with a mononuclear site as a binuclear site.⁶³

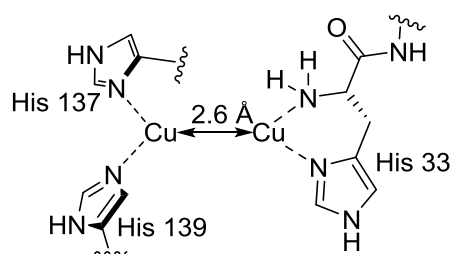


Figure 7: The coordination of site B in PmoB, the active site proposed by Rosenzweig *et al.*⁶² modelled as a dinuclear copper centre.

Further doubt has been cast over which metal centre is responsible for the activity of pMMO by Chan *et al.* who suggested that a trinuclear copper cluster was present based on the EPR signal obtained from the enzyme and comparison with simulations (ferromagnetically coupled Cu^{II}₃).⁶⁴ The spectroscopic features of the trinuclear centre could be separated out from the features of other metal centres in the enzyme by potentiometric titration.⁶⁵ A hydrophilic cavity has been observed in the crystal structures of the enzymes (site D) and has been proposed to house three copper ions and thus balancing out the charge of this cavity that would otherwise be unstable in the enzyme.⁵⁷ Chan *et al.* reasoned the lack of observation of the copper ions in the hydrophilic cavity shown in the crystal structure based on the fact that the crystallised enzymes were inactive, and therefore copper ions must have been lost in the purification process.⁵⁷ However a very recent publication by Rosenzweig *et al.* indicated that when the purified inactive enzymes were placed back into a bicelle membrane, the activity was regained without the addition of copper ions, excluding the possibility that the activity of the enzyme comes from an unobserved metal centre.⁶¹

2.5.3. Active species responsible for CH₄ oxidation in pMMO.

There is still very little experimental detail about the catalytic cycle and the intermediates involved in the oxidation of methane. Rosenzweig *et al.*⁶⁶ demonstrated that the reaction of a recombinant of PmoB with O₂ resulted in the appearance of a band at 345 nm, which is comparable to the band observed in dicopper enzymes that activate O₂ such as Ty and Hc, alluding to the possible formation of a $\mu\text{-}\eta^2\text{:}\eta^2\text{-peroxo-Cu}^{\text{II}}_2$ species. The band disappeared when methane was added, indicating that the copper-oxygen species formed is involved in the catalytic cycle for the oxidation of methane. While this strongly indicated that pMMO is an enzyme that activates O₂ for the oxidation of methane, it is difficult to assign a reactive intermediate solely due to a band observed in the UV-vis spectrum.

Due to disagreement about the active site nuclearity of pMMO, it is no surprise that there have been several different suggested mechanisms for the oxidation of methane by the enzyme. There have been arguments for both dinuclear and trinuclear copper clusters, but since it is only recently that evidence for pMMO possibly being a monocopper enzyme,^{61,63} there have been very few theoretical calculations based on monocopper species.

Chan *et al.*^{67,68} observed experimentally that the oxidation of deuterium and tritium substituted ethane or butane occurred with the retention of configuration indicating that no rotation of the C-C bond during the transition state occurred and therefore demonstrating a concerted mechanism. This led them to suggest the “oxene insertion mechanism”,^{68,69} where a singlet oxene is inserted into the C-H bond (as opposed to a HAT followed by a radical rebound). The oxygen would have to be in the singlet form as the electrons in the C-H bond are in antiparallel (Figure 8).

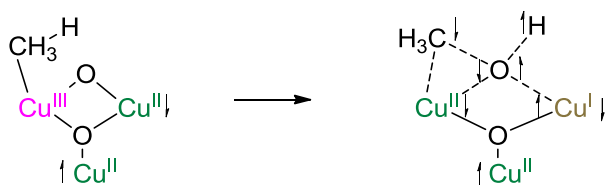


Figure 8: Insertion of a singlet oxene into the C-H bond of methane. Figure adapted from Chan *et al.*⁶⁸

A comparison of various intermediates possibly responsible for the oxidation of methane was also completed by Chan *et al.*⁷⁰ The trinuclear cluster bis($\mu\text{-O}$)Cu^{II}Cu^{II}Cu^{III}, the dinuclear mixed valent species bis($\mu\text{-O}$)Cu^{II}Cu^{III} and the bis($\mu\text{-O}$)Cu^{III}Cu^{III} species (Figure 9) were compared in terms of transition state energy, rate of reaction with CH₄, CD₄ and therefore kinetic isotope effect (KIE). The values are summarised in Table 2. It was found that the bis($\mu\text{-O}$)Cu^{II}Cu^{II}Cu^{III} species had a significantly

lower transition state energy for C-H oxidation of $15.0 \text{ kcal.mol}^{-1}$ (compared to $20.1 \text{ kcal.mol}^{-1}$ for the $\text{bis}(\mu\text{-O})\text{Cu}^{\text{III}}\text{Cu}^{\text{III}}$ and $24.5 \text{ kcal.mol}^{-1}$ for the mixed valent $\text{bis}(\mu\text{-O})\text{Cu}^{\text{II}}\text{Cu}^{\text{III}}$ species). The values of the KIE were around 3 to 8 for the $\text{bis}(\mu\text{-O})\text{Cu}^{\text{II}}\text{Cu}^{\text{II}}\text{Cu}^{\text{III}}$ species (depending on temperature), 3 to 6 for the $\text{bis}(\mu\text{-O})\text{Cu}^{\text{III}}\text{Cu}^{\text{III}}$ species but were far higher for the $\text{bis}(\mu\text{-O})\text{Cu}^{\text{II}}\text{Cu}^{\text{III}}$ at around 11-48, reflecting the fact that the $\text{bis}(\mu\text{-O})\text{Cu}^{\text{II}}\text{Cu}^{\text{III}}$ species reacts *via* a HAT followed by a radical rebound, and therefore not a concerted mechanism.⁷⁰ The latter is consistent with the value of KIE = 17 obtained by Yoshizawa *et al.* for the $\text{bis}(\mu\text{-O})\text{Cu}^{\text{II}}\text{Cu}^{\text{III}}$ species.⁷¹ The smaller values of KIE are most consistent with experimental values determined for the enzyme, which were determined to be around 5.3-5.7 for the oxidation of ethane and butane by pMMO.^{67,68}

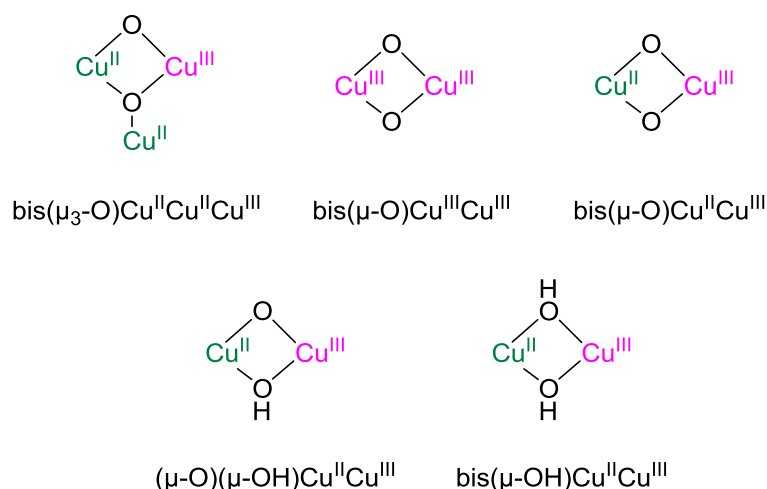


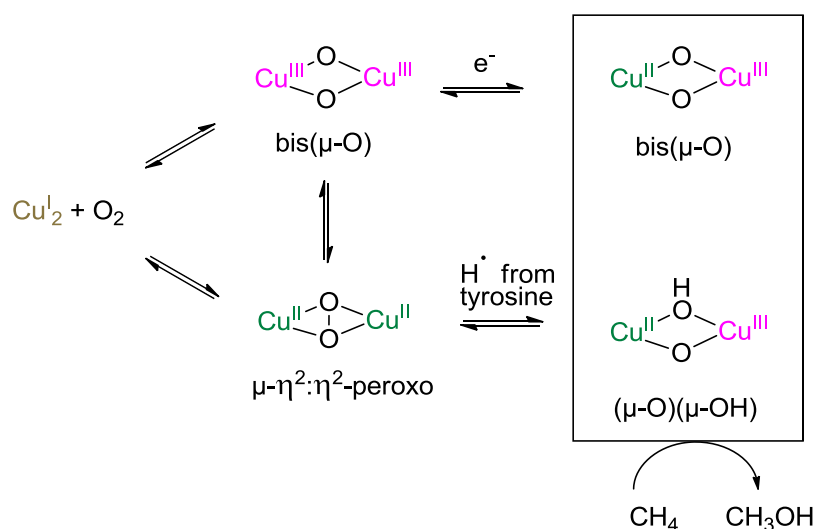
Figure 9: Species that have been suggested for the high oxidising capabilities of pMMO.

Table 2: Transition state energy and KIE upon the reaction of several copper-oxygen intermediates with methane as calculated by Chan *et al.*⁷⁰

Species	Transition state energy / Kcal.mol^{-1}	KIE
$\text{bis}(\mu_3\text{-O})\text{Cu}^{\text{II}}\text{Cu}^{\text{II}}\text{Cu}^{\text{III}}$	15.0	3 to 8
$\text{bis}(\mu\text{-O})\text{Cu}^{\text{III}}\text{Cu}^{\text{III}}$	20.1	3 to 6
$\text{bis}(\mu\text{-O})\text{Cu}^{\text{II}}\text{Cu}^{\text{III}}$	24.5	11 to 48

Yoshizawa *et al.* completed a series of DFT calculations on the oxidising ability of high valent copper species. DFT studies comparing the $\text{bis}(\mu\text{-O})\text{Cu}^{\text{III}}\text{Cu}^{\text{III}}$ with the mixed valent $\text{bis}(\mu\text{-O})\text{Cu}^{\text{II}}\text{Cu}^{\text{III}}$ indicated that the latter oxidised methane with lower energy transition states (16 kcal.mol^{-1} compared to 44 kcal.mol^{-1}) due to the presence of a singularly occupied molecular orbital located on the bridging oxo group in the mixed valent species.^{71,72} A mixed valent $\text{Cu}^{\text{II}}\text{Cu}^{\text{III}}$ species could either be formed by the activation of O_2 by a Cu_2^{I} species to give the $\text{bis}(\mu\text{-O})\text{Cu}^{\text{III}}\text{Cu}^{\text{III}}$ species followed by one

electron reduction, but could also be generated by the formation of a $\mu\text{-}\eta^2\text{:}\eta^2\text{-peroxo-Cu}^{\text{II}}_2$ species which has been shown could be present in the enzyme⁷³ followed by a HAT to form the $(\mu\text{-O})(\mu\text{-OH})\text{Cu}^{\text{II}}\text{Cu}^{\text{III}}$ species (Scheme 13). In fact it has been proposed that a nearby tyrosine residue supplies the hydrogen atom to the peroxo species, and that the $(\mu\text{-O})(\mu\text{-OH})\text{Cu}^{\text{II}}\text{Cu}^{\text{III}}$ species formed is much more reactive towards methane than the non-protonated $\text{bis}(\mu\text{-O})\text{Cu}^{\text{II}}\text{Cu}^{\text{III}}$.⁷⁴ The reactivity of the $(\mu\text{-O})(\mu\text{-OH})\text{Cu}^{\text{II}}\text{Cu}^{\text{III}}$ species is proposed to go *via* a HAT followed by a radical rebound.



Scheme 13: Formation of the mixed valent $\text{Cu}^{\text{II}}\text{Cu}^{\text{III}}$ species that could be responsible for the oxidation of methane by the enzyme pMMO as proposed by Yoshizawa *et al.*^{71–74}

Rocha *et al.* also proposed a radical rebound mechanism, but argued that a $\text{bis}(\mu\text{-O})\text{Cu}^{\text{II}}\text{Cu}^{\text{III}}$ could also perform HAT on methane if in the triplet state.⁷⁵ A radical mechanism would seemingly contradict with the work of Chan *et al.* who propose a concerted mechanism based upon the fact that there is no racemisation during the oxidation of methane.⁷⁰ However Yoshizawa *et al.* explain the lack of racemisation by arguing that the O^{2-} bridge oxidises the $\text{CH}_3\text{-H}$ to CH_3^- and HO^- and therefore forms a methyl intermediate which is coordinated to the copper. A free CH_3^\cdot radical is therefore never formed and thus no racemisation.⁷⁴

While initial claims that a dinuclear or trinuclear copper centre is responsible for the reactivity of pMMO may prove to be false, the DFT studies of dinuclear $\text{Cu}:\text{O}$ species have provided interesting insight towards C-H activation. All the possible trinuclear or dinuclear intermediates proposed (see Figure 9) contain high valent copper, so it is therefore of great interest to attempt the synthesis of model complexes to generate such species.

2.6. Zeolites

The porous frameworks of zeolites are ideal for catalysis because of their high surface area to volume ratio. The downside is that the intermediates formed during the catalysis are much harder to characterise compared to homogeneous catalysis due to them being in the solid state. The characterisation of the zeolites is therefore limited to rR, DFT and extended X-ray absorption fine structure (EXAFS). Several zeolites have been shown to be effective at oxidising methane selectively to methanol at relatively mild conditions,⁷⁶ so a brief section on zeolites has been included in this chapter.

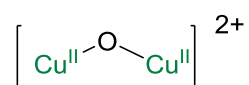
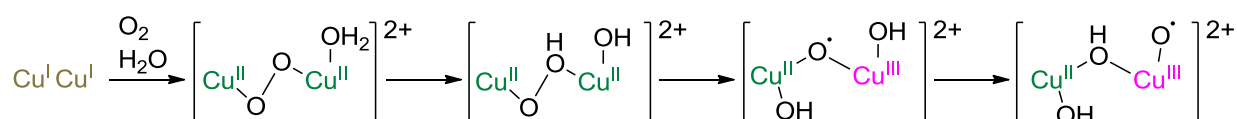


Figure 10: Possible active species responsible for the oxidation of methane to methanol by the zeolite Cu-ZSM-5 proposed by Solomon *et al.*⁷⁷

Solomon *et al.*⁷⁷ were the first to characterise the $[\text{Cu}^{\text{II}}_2\text{O}]^{2+}$ core (Figure 10) in the zeolite Cu-ZSM-5 based on rR data and DFT. It was calculated that HAT was the rate determining step for the oxidation of methane, consistent with experimental results. Interestingly the calculated value of KIE was around 3 (depending on temperature) which is similar to the KIE observed in the enzyme pMMO.⁶⁷ A more recent DFT study by Yoshizawa *et al.*⁷⁶ compared copper zeolites with different pore sizes which significantly affect the Cu-O-Cu angle, where a smaller Cu-O-Cu angle decreases the energy of the transition state for HAT, explaining the increase of the rate of methane oxidation by zeolites with a smaller pore size. Kobayashi *et al.*⁷⁸ also suggested from DFT calculations that the addition of water to the $[\text{Cu}^{\text{II}}_2\text{O}]^{2+}$ centre to form either a $[\text{HO}-\text{Cu}^{\text{II}}-\text{O}^\bullet-\text{Cu}^{\text{III}}-\text{OH}]^{2+}$ or a $[\text{HO}-\text{Cu}^{\text{II}}-\text{OH}-\text{Cu}^{\text{III}}\text{O}^\bullet]^{2+}$ core (Scheme 14) increased the reactivity of the copper zeolite Cu-ZSM-5 towards methane, due to a greater electron density on the oxygen atom (bridged or terminal) giving it oxyl radical characteristics. These results therefore indicate that variations on the $[\text{Cu}^{\text{II}}_2\text{O}]^{2+}$ species should also be targeted for the synthesis of model complexes as they are potentially responsible for the oxidation of methane in zeolites.

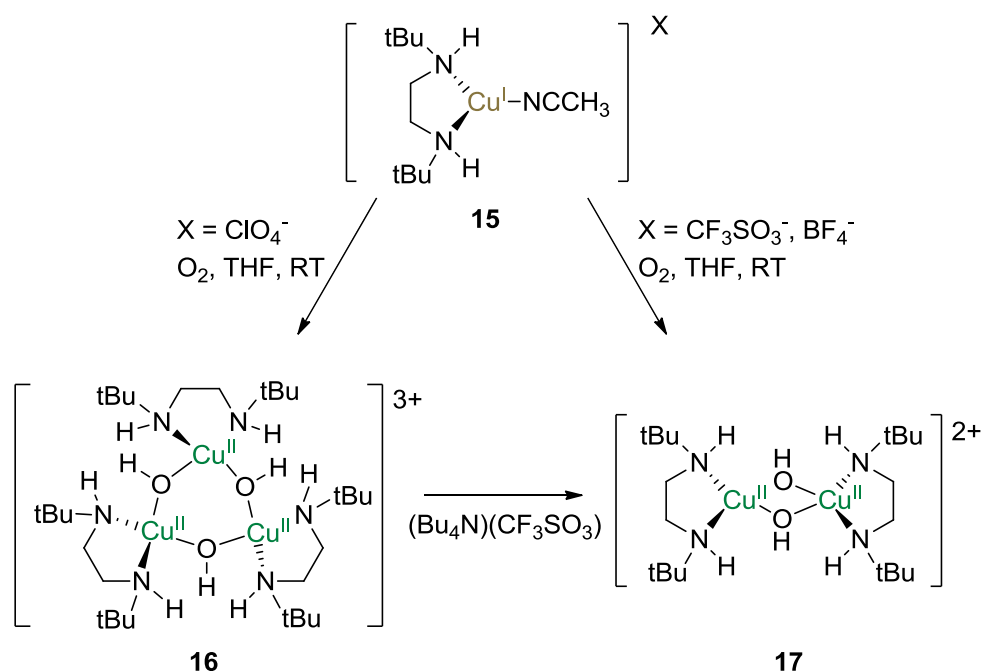


Scheme 14: possible copper-oxygen species present in zeolites starting from the activation of O_2 by a Cu^{I}_2 species. Scheme adapted from Kobayashi *et al.*⁷⁸

Lercher *et al.*⁷⁹ characterised the copper zeolite mordenite, a zeolite with a uniform active site, by X-ray absorption spectroscopy (XAS). The results showed that the zeolite contains Cu_3O_2 clusters that are hydrolysed when water is added (to remove the methanol) but reform when O_2 is added. This indicates that model complexes of trinuclear clusters are also worth investigating.

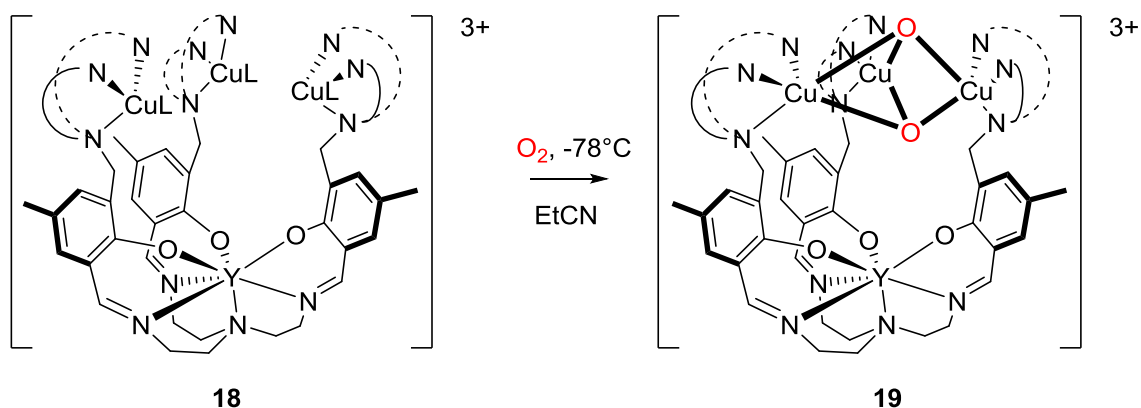
2.7. Small molecule models of trinuclear copper-oxygen species

One of the methods that has been used for the generation of trinuclear copper complexes is to use sterically bulky dinucleating ligands coordinated to Cu^{I} ions, and then react them with O_2 as exemplified by Stack *et al.*⁸⁰ Interestingly the formation of the $\text{tris}(\mu\text{-OH})\text{Cu}_3^{\text{II}}$ complex could be controlled by completing the reaction at room temperature, whether as the $\mu\text{-}\eta^2\text{:}\eta^2\text{-peroxo-Cu}_2^{\text{II}}$ species was formed if the reaction was done at -80°C . The trinuclear cluster could re-arrange to form a binuclear $\text{bis}(\mu\text{-OH})\text{Cu}_2^{\text{II}}$ complex upon changing the counter-ion from a perchlorate to a triflate group, indicating that the coordination of the anion is essential for structural determination (Scheme 15). Unfortunately there is no discussion of the reactivity of such trinuclear species.



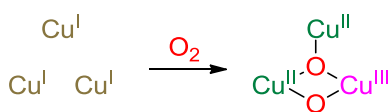
Scheme 15: Formation of trinuclear and dinuclear Cu^{II} complexes upon reaction of a mononuclear Cu^{I} complex with O_2 . Scheme adapted from Stack *et al.*⁸⁰

Agapie *et al.*⁸¹ also synthesised trinuclear copper complexes, but this time with a templated ligand. A yttrium ion that was shown to be essential was used to pre-organise the three Cu^I centres for O₂ activation to form the (μ₃-O)Cu^{II}Cu^{II}Cu^{III} species (complex **19**, Scheme 16) which was characterised by EPR, UV-vis and electrospray ionisation-mass spectrometry (ESI-MS). The copper-oxygen species formed had a modest reactivity, performing HAT on TEMPO-H and oxygen atom transfer (PPh₃ to OPPh₃), but no reaction was observed with 2,4-di-*tert*-butyl phenol.



Scheme 16: O₂ activation by a pre-organised Cu₃^I complex to form the (μ₃-O)Cu^{II}Cu^{II}Cu^{III} species. Scheme adapted from Agapie *et al.*⁸¹

A series of trinuclear Cu^I complexes have been synthesised by Chan *et al.*^{82–87} for which the oxygenated complexes have turned out to be very reactive towards alkanes. Examples of the ligands used are shown in Figure 11. The trinuclear Cu^I complexes were reacted with dioxygen to form a bis(μ₃-O)Cu^{II}Cu^{II}Cu^{III} species (see Scheme 17).



Scheme 17: The activation of O₂ by a trinuclear Cu^I complex. Scheme adapted from Chan *et al.*⁸²

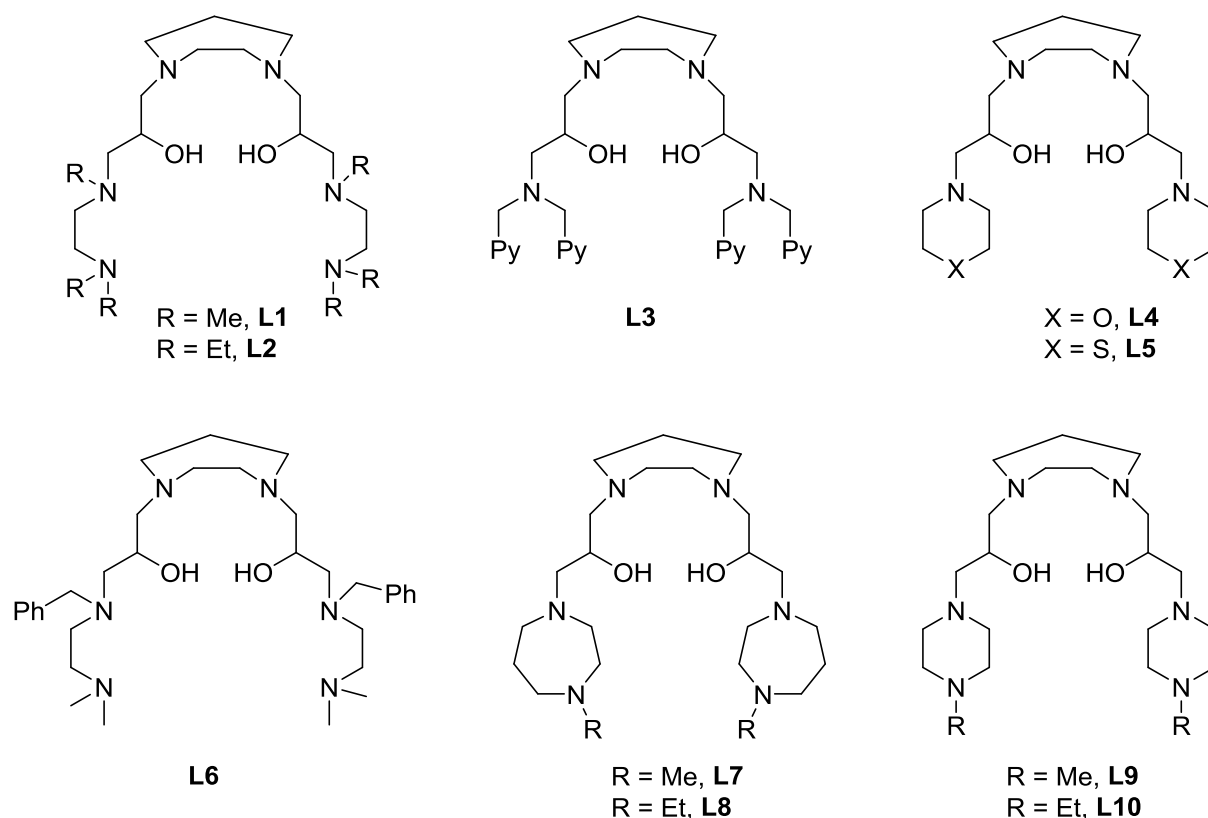
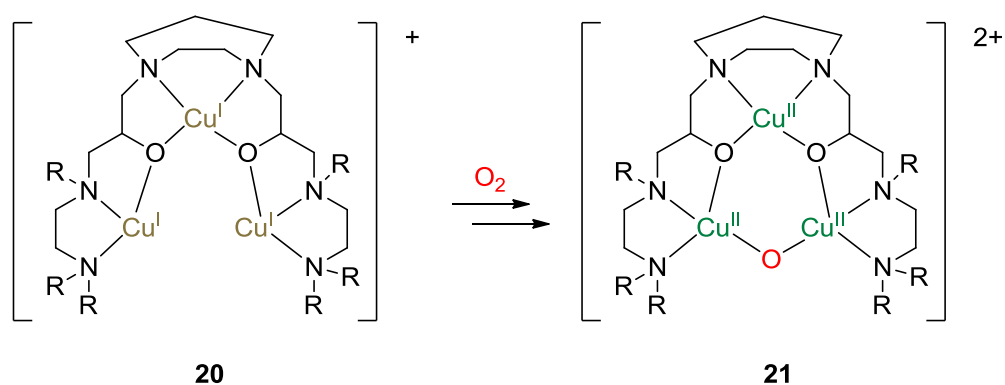


Figure 11: Ligands forming trinuclear Cu^{I} complexes that react with O_2 to form bis($\mu_3\text{-O}$) $\text{Cu}^{\text{II}}\text{Cu}^{\text{II}}\text{Cu}^{\text{III}}$ species. Figure adapted from Chan *et al.*⁸⁶ R = CH_3 or CH_2CH_3 , X = S or O.

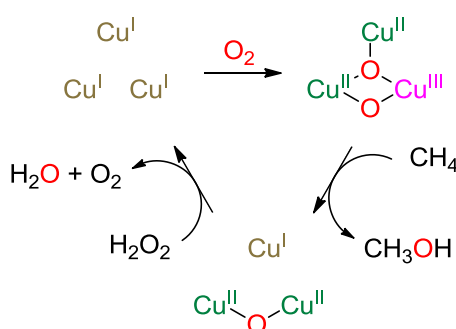


Scheme 18: Oxidation of the trinuclear Cu^{I} complex to form a trinuclear Cu^{II} complex that was crystallised.⁸²

Initially complex **20** was reacted with O_2 in acetonitrile, and the resulting complex **21** was crystallised⁸² (Scheme 18) and it was found that only one oxo bridging group was present. Mass spectrometry results however indicated the presence of complex **21** and a molecule of glyconitrile (CH_2OHCN) indicating that the trinuclear copper complex performed the insertion of an oxygen atom

into the C-H bond of acetonitrile. The presence of glyconitrile was also confirmed by infrared (IR) spectroscopy. The bis(μ_3 -O)Cu^{II}Cu^{II}Cu^{III} species formed upon oxygenation of complex **20** was also shown to insert an oxygen atom into the C-C bond of benzoin.⁸²

The process for the oxidation of alkanes by the bis(μ_3 -O)Cu^{II}Cu^{II}Cu^{III} species could be made catalytic by using H₂O₂ as an oxidant and a reductant instead of using O₂,⁸⁴ or using O₂ as the oxidant and H₂O₂ as the reductant. Scheme 19 demonstrates the suggested catalytic cycle for the latter conditions.



Scheme 19: Regeneration of the Cu^I catalysts as proposed by Chan *et al.*⁸⁵

Chan *et al.* furthered the scope of oxidation mediated by the bis(μ_3 -O)Cu^{II}Cu^{II}Cu^{III} species to include various alkenes such as benzene, cyclohexene and styrene (using complexes from the ligands **L1-L5**)⁸³ and then later even included the oxidation of methane using the complex from the ligand **L10**.⁸⁵ It is interesting that the oxidation of substrates such as methane and cyclohexene can be observed while using CH₃CN as a solvent since the oxidation of acetonitrile has already been observed by the bis(μ_3 -O)Cu^{II}Cu^{II}Cu^{III} species.⁸² This is particularly confusing as a recent paper by Du *et al.* showed using DFT that the first step of the reaction of the bis(μ_3 -O)Cu^{II}Cu^{II}Cu^{III} with methane would be a HAT⁸⁸ (which would therefore be much faster with CH₃CN (C-H BDE = 93 kcal.mol⁻¹)⁸⁹ than with CH₄ (C-H BDE = 104 kcal.mol⁻¹)⁵), not the concerted mechanism proposed by Chan *et al.*^{70,82} Furthermore acetonitrile is the solvent and is therefore in large excess compared to the sparingly soluble methane, so presumably significant quantities of acetonitrile are oxidised to CH₂OHCN during the catalytic reaction.

With this catalytic system, the selectivity of the products formed depends on the substrate chosen. When cyclohexane or longer chained alkanes (butane, pentane and hexane) were used, the reaction was not selective with both the alcohol and the ketone being formed. For the oxidation of a double bond (*e.g.* cyclohexene), the epoxide, the alcohol and the ketone were observed. However with shorter chained alkanes (methane, ethane and propane) oxidation was selective to form only the alcohol.⁹⁰

To overcome problems with solubility of methane in the solvent, Chan *et al.* immobilised the trinuclear complex from ligand **L10** on nanoparticles.⁸⁷ The increased solubility of methane in the mesoporous silica nanoparticles allows for a higher concentration of methane in solution, and thus drastically increasing the rate of the catalytic reaction. The yields of the catalytic reaction were also particularly high reported at 98%,⁸⁷ indicating that these trinuclear copper clusters are clearly of interest for potential industrial application.

2.8. Small molecule models of dinuclear copper-oxygen species

A whole range of copper-oxygen species have been synthesised, investigating Cu^I reactivity with oxygen and then subsequent reactivity of the species formed. The species formed solely from the reaction of Cu^I₂ with O₂ are versatile, and examples are shown in Figure 12 (top). Many of them target the species observed/suggested in the enzymes Ty, catechol oxidase and pMMO however several new species have been discovered that have not been observed in these enzymes. Examples will also be given of similar copper-oxygen species that are not solely generated through activation of O₂ (Figure 12, bottom). Due to the wealth of literature in this area, only a few key examples will be given.

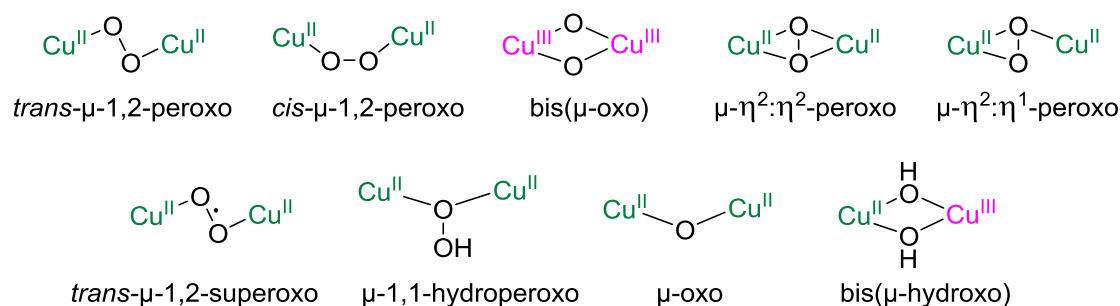


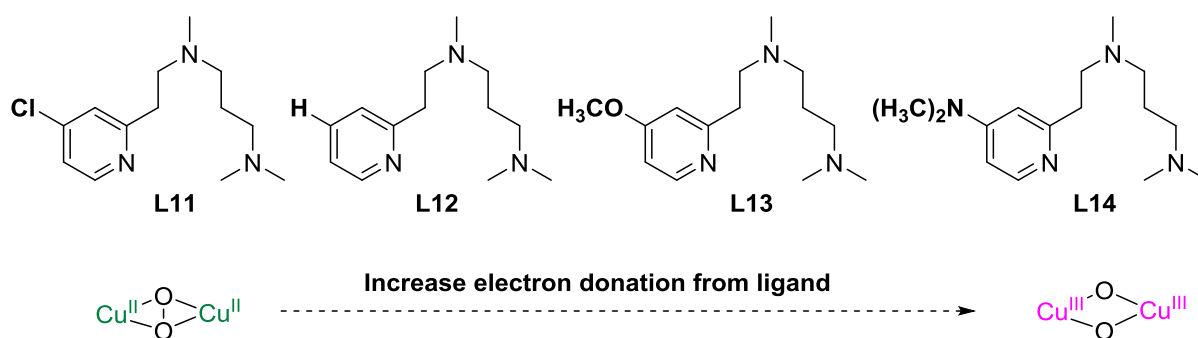
Figure 12: Copper oxygen species discussed in this section. Top: Copper-oxygen species formed upon reaction of Cu^I₂ with O₂. Bottom: copper-oxygen species formed not solely through the activation of O₂ by Cu^I₂. Figure adapted from Tolman *et al.*³⁹

2.8.1. The μ - $\eta^2:\eta^2$ -peroxo-Cu^{II}₂ and bis(μ -O)Cu^{III}₂ species.

2.8.1.1. Equilibrium between the μ - $\eta^2:\eta^2$ -peroxo-Cu^{II}₂ and bis(μ -O)Cu^{III}₂ species.

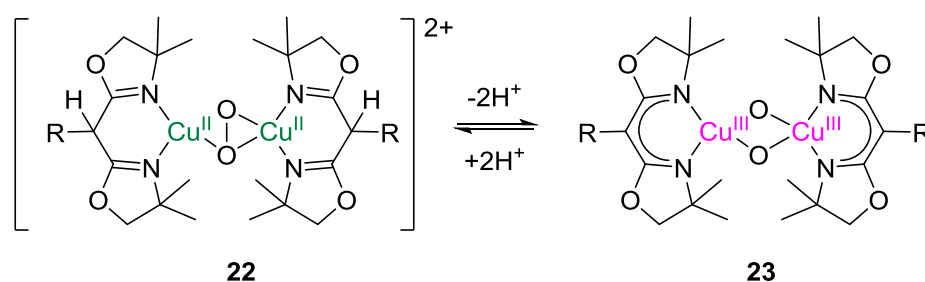
The μ - $\eta^2:\eta^2$ -peroxo-Cu^{II}₂ and bis(μ -O)Cu^{III}₂ species are known to interconvert,⁹¹ depending on the degree of electron transfer from the Cu into the O-O antibonding orbital. This is well exemplified

by Karlin *et al.*⁹² who synthesised a series of tridentate ligands with varying degrees of electron donating capability (see Scheme 20). Resonance Raman of the O-O bond indicated that predominantly the $\mu\text{-}\eta^2\text{:}\eta^2\text{-peroxo-Cu}^{\text{II}}_2$ existed with the more electron withdrawing ligand (**L11**), and the O-O bond was weakened with more electron donating ligands. With the strongest donating ligands **L13** and **L14**, rR could not be observed because the O-O bond had been fully broken. The more electron donating ligands increased the proportion of the $\text{bis}(\mu\text{-O})\text{Cu}^{\text{III}}_2$ species in solution as there was more electron density donated from the ligands to the copper that can then be donated to the π^* orbital of the O-O bond.



Scheme 20: Shift from a $\mu\text{-}\eta^2\text{:}\eta^2\text{-peroxo-Cu}^{\text{II}}_2$ species to a $\text{bis}(\mu\text{-O})\text{Cu}^{\text{III}}_2$ species with increasing electron donating capabilities of the ligand. Scheme adapted from Karlin *et al.*⁹²

Meyer *et al.*⁹³ also demonstrated the interconversion of the $\mu\text{-}\eta^2\text{:}\eta^2\text{-peroxo-Cu}^{\text{II}}_2$ and $\text{bis}(\mu\text{-O})\text{Cu}^{\text{III}}_2$ species using ligands that could be deprotonated. The ligand bis-oxazoline (BOX, see Scheme 21) formed a Cu^{I} complex which, when activated with O_2 , gave a $\mu\text{-}\eta^2\text{:}\eta^2\text{-peroxo-Cu}^{\text{II}}_2$ species. Addition of the base 1,8-diazabicyclo[4.5.0.]undec-7-ene (DBU) to the peroxo species led to deprotonation of the ligand and therefore to the stabilisation of the $\text{bis}(\mu\text{-O})\text{Cu}^{\text{III}}_2$ species.



Scheme 21: Interconversion of the $\mu\text{-}\eta^2\text{:}\eta^2\text{-peroxo-Cu}^{\text{II}}_2$ and $\text{bis}(\mu\text{-O})\text{Cu}^{\text{III}}_2$ species depending on protonation state of the ligand. Scheme adapted from Meyer *et al.*⁹³

Steric bulk also plays an important role in shifting the equilibrium between the $\mu\text{-}\eta^2\text{:}\eta^2\text{-peroxo-Cu}^{\text{II}}_2$ and $\text{bis}(\mu\text{-O})\text{Cu}^{\text{III}}_2$ species. Itoh *et al.*^{94,95} published two Cu_2O_2 complexes generated at -80°C by oxygenation of the Cu^{I} complexes in which the ligands varied only by one methyl group (Figure 13). Without the methyl group present, the 5 membered chelate ring causes significant electron donation from the ligand to the copper, causing the O-O bond to fully break in the Cu_2O_2 species formed. However when a methyl group is added, the increased steric bulk increases the Cu-L separation thus decreasing the electron donating capabilities of the ligand allowing the $\mu\text{-}\eta^2\text{:}\eta^2\text{-peroxo-Cu}^{\text{II}}_2$ species to be formed.

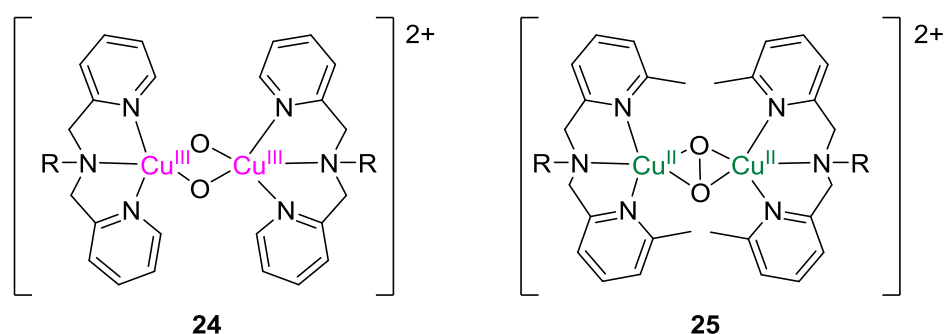
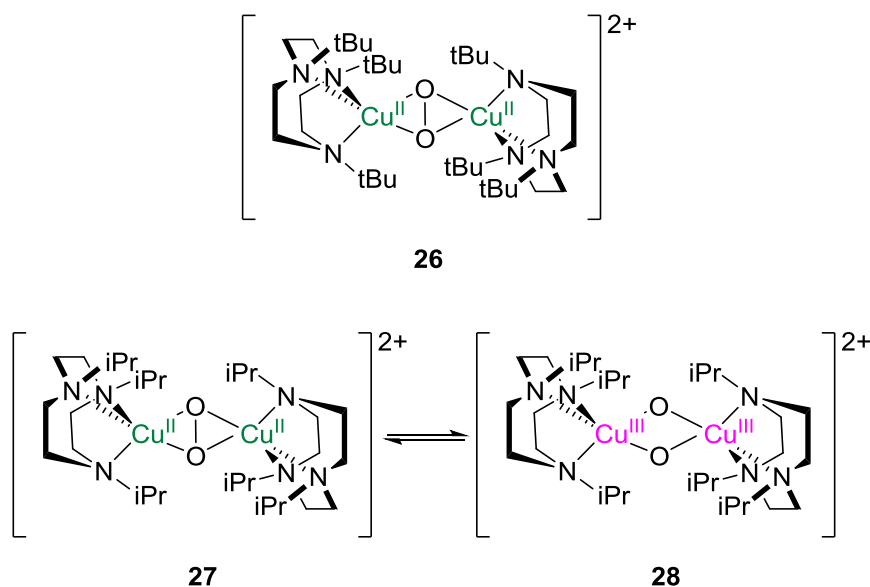


Figure 13: Cu_2O_2 Complexes synthesised by Itoh *et al.*^{94,95} with the ligands differing by methyl groups.

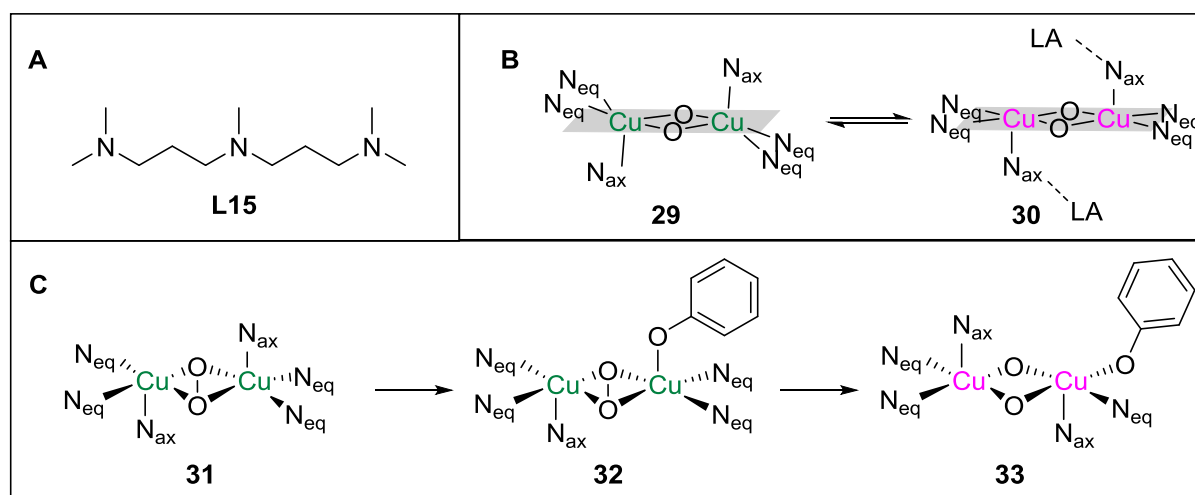


Scheme 22: Complexes synthesised by Scarborough *et al.*⁹⁶ (top) and Tolman *et al.*⁹⁷ (bottom) with similar ligands.

The same concept is also well demonstrated by two similar complexes by Scarborough *et al.*⁹⁶ and Tolman *et al.*⁹⁷ who used ligands differing by a methyl group. The additional steric effects caused by the *tBu* groups in Scarborough's complex **26** instead of the *iPr* groups of Tolman's complexes **27**

and **28** cause a dramatic increase in the Cu-Cu separation which is coupled to a decrease in the O-O separation making the O-O bond in Scarborough's complex one of the strongest for $\text{Cu}_2\text{:O}_2$ species. In Tolman's complex both the $\mu\text{-}\eta^2\text{:}\eta^2\text{-peroxo-Cu}^{\text{II}}_2$ and $\text{bis}(\mu\text{-O})\text{Cu}^{\text{III}}_2$ species are observed in equilibrium (Scheme 22).

Coordination of other molecules also has an effect on the equilibrium of $\text{Cu}_2\text{:O}_2$ species. Coordinating solvents such as tetrahydrofuran (THF) tend to favour the formation of the $\text{bis}(\mu\text{-O})\text{Cu}^{\text{III}}_2$ whether as non-coordinating solvents such as dichloromethane (DCM) favour the formation of the $\mu\text{-}\eta^2\text{:}\eta^2\text{-peroxo-Cu}^{\text{II}}_2$ species,⁹¹ but do not over-rule the ligand effects as shown by the fact that the Cu_2O_2 complex from **L14** (Scheme 20) displays only the $\text{bis}(\mu\text{-O})\text{Cu}^{\text{III}}_2$ form in both THF and DCM.⁹² Stack *et al.*⁹⁸ compared the effect of counterions on the $\mu\text{-}\eta^2\text{:}\eta^2\text{-peroxo-Cu}^{\text{II}}_2$ / $\text{bis}(\mu\text{-O})\text{Cu}^{\text{III}}_2$ equilibrium and found that counterintuitively a coordinating anion in the axial position favours the $\mu\text{-}\eta^2\text{:}\eta^2\text{-peroxo-Cu}^{\text{II}}_2$ species. One would expect the coordinating of a negative charge to favour the higher oxidation state of the copper, however Stack *et al.* also comment that the coordination of a deprotonated phenol (*i.e.* the substrate of Ty) which is far more basic than the counterions used would probably rearrange the coordination sphere to coordinate in an equatorial position, and this could favour the $\text{bis}(\mu\text{-O})\text{Cu}^{\text{III}}_2$ species.⁹⁸



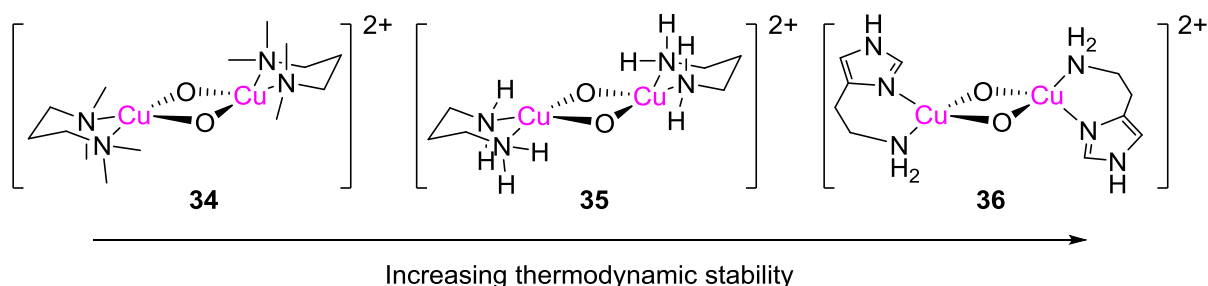
Scheme 23: (A): The ligand used by Karlin *et al.*^{99,100} The effect of coordination of a Lewis acid (LA) (B) and substrate (C) to the $\mu\text{-}\eta^2\text{:}\eta^2\text{-peroxo-Cu}^{\text{II}}_2$ species causing a reorganisation of the coordination sphere leading to the formation of a $\text{bis}(\mu\text{-O})\text{Cu}^{\text{III}}_2$ species. Scheme adapted from Karlin *et al.*⁹⁹

Karlin *et al.*⁹⁹ also showed that the coordination of a phenolate to the $\mu\text{-}\eta^2\text{:}\eta^2\text{-peroxo-Cu}^{\text{II}}_2$ species supported by **L15** (Scheme 23) led to the dissociation of the O-O bond, forming a $\text{bis}(\mu\text{-O})\text{Cu}^{\text{III}}_2$ species that was observed by stop-flow experiments. They proposed from DFT calculations

that the phenolate coordinates in the axial position followed by an isomerisation to the equatorial position which is observed spectroscopically and leads to O-O fission (Scheme 23C, complexes **32** and **33**). The coordination of a Lewis acid also causes the O-O bond to break, but this time due to the Lewis acid coordinating to N_{axial} ligand, allowing the two other N ligands to move into the plane of the O_2 forming a more square planar geometry around the copper (Scheme 23B) and thus leading to better electron donation from the N_{eq} to the Cu, and better electron donation into the O-O antibond.⁹⁹ Despite the coordination of a phenol and the coordination of a Lewis acid both forming bis(μ -O)Cu^{III}₂ with ligand **L15**, complexes **30** and **33** display very different reactivity towards external substrates (see sections 2.8.1.3).

2.8.1.2. Relevance of the bis(μ -O)Cu^{III}₂ to biology

The bis(μ -O)Cu^{III}₂ core has never been observed in a biological system and it was therefore thought that the μ - η^2 : η^2 -peroxo-Cu^{II}₂ species was responsible for the activity of Ty.¹⁰¹ Stack *et al.* have shown through a series of publications that both primary amines¹⁰² and histidines^{103,104} can stabilise the bis(μ -O)Cu^{III}₂ species, indicating that the active sites of several of the enzymes mentioned above could conceivably stabilise Cu^{III} species with either the *histidine brace* (LPMP or pMMO) or histidine residues (Ty).



Scheme 24: Complexes bearing the bis(μ -O)Cu^{III}₂ core. Complexes **35** and **36** are synthesised by using the “core capture” of the Cu₂O₂ centre from complex **34**. Scheme adapted from Stack *et al.*¹⁰³

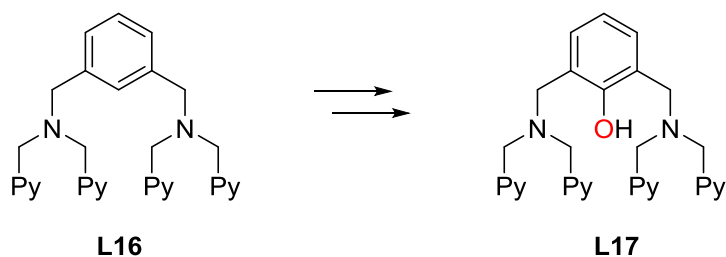
Complexes **35** and **36** (Scheme 24) were synthesised using a “core capture” method (ligand substitution), where the bis(μ -O)Cu^{III}₂ core is generated at very low temperatures (-125°C) using tetramethyl propylenediamine as a ligand (complex **34**), followed by the addition of two equivalents of the ligand in question to replace the tetramethyl propylenediamine. Both complexes **35** and **36** displayed the bis(μ -O)Cu^{III}₂ core, demonstrating the ability of primary amines and histidines to

stabilise this species. The stabilisation of the Cu^{III} core through hydrogen bonding due to the involvement of the original ligand (tetramethyl propylenediamine) cannot be ruled out, but hydrogen bonding could also occur in the context of an enzyme to help to stabilise the high valent $\text{bis}(\mu\text{-O})\text{Cu}^{\text{III}}_2$ intermediate. Interestingly the complex **35** with primary amines was more thermodynamically stable than complexes with tertiary amines, explained by the fact that the steric demand of primary amines is lower and therefore the Cu-N bond can be shorter.¹⁰² The $\text{bis}(\mu\text{-O})\text{Cu}^{\text{III}}_2$ complex **36** with histidine ligands was even more stable than the complex **35** with primary amine ligands.¹⁰³ These complexes demonstrate that the Cu^{III} oxidation state is accessible using biologically relevant ligands.

2.8.1.3. Reactivity of the $\mu\text{-}\eta^2\text{:}\eta^2\text{-peroxo-Cu}^{\text{II}}_2$ and $\text{bis}(\mu\text{-O})\text{Cu}^{\text{III}}_2$ species.

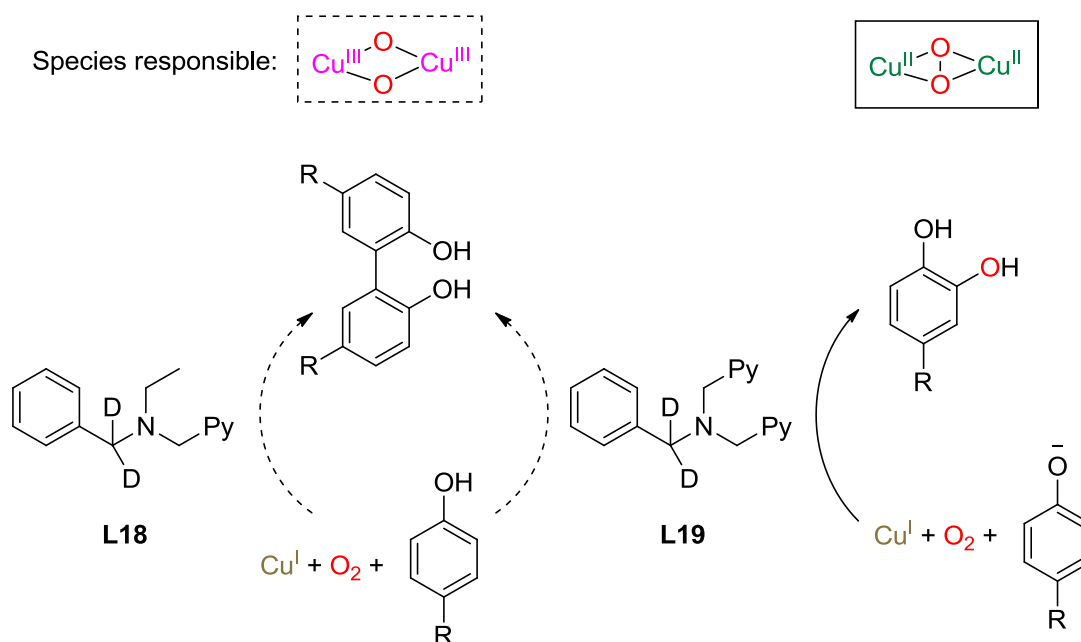
Due to possible interconversion of the $\mu\text{-}\eta^2\text{:}\eta^2\text{-peroxo-Cu}^{\text{II}}_2$ and $\text{bis}(\mu\text{-O})\text{Cu}^{\text{III}}_2$ species, discriminating the reactivity of each of these species can be difficult as there is always the possibility that the unobserved isomer is responsible for the activity in question. That having been said, in general the $\mu\text{-}\eta^2\text{:}\eta^2\text{-peroxo-Cu}^{\text{II}}_2$ core performs Ty-like reactivity and the $\text{bis}(\mu\text{-O})\text{Cu}^{\text{III}}_2$ species usually performs HAT from C-H bond.^{101,105,106} Exceptions and other reactions do occur, and these will also be discussed.

The first example of a model complex doing tyrosinase-like activity was characterised by Karlin *et al.*¹⁰⁷ It was demonstrated that oxygenation of the dinuclear Cu^{I} complex supported by the ligand **L16** led to hydroxylation of the ligand (Scheme 25). Examples of hydroxylation of phenols to catechols or quinones quickly followed, with one of the first examples of catalytic catecholase/tyrosinase activity demonstrated by Réglier *et al.*¹⁰⁸ in 1990 with a turn-over number (TON) of 16. Since then different groups have been able to reproduce catalytic tyrosinase activity using either mononucleating or dinucleating ligands,¹⁰⁹ but there has been little progress in the TON of these systems with the highest TON of 31 reported by Tuczek *et al.*¹¹⁰



Scheme 25: Ligand hydroxylation observed by Karlin *et al.*¹⁰⁷ upon oxygenation of the Cu^{I}_2 complex.

One of the essential features for substrate hydroxylation to occur is substrate coordination. Itoh *et al.* have shown that addition of the phenolate salts to the $\mu\text{-}\eta^2\text{:}\eta^2\text{-peroxo-Cu}^{\text{II}}_2$ complex formed from ligand **L19** (Scheme 26) led to catechol activity¹¹¹ (formation of the 1,2 diphenol), whether as addition of neutral phenols led to C-C coupling.¹¹² This is probably because the neutral phenol is not nucleophilic enough to coordinate to the copper and allow the electrophilic aromatic substitution reaction to occur,¹¹³ and the reaction therefore proceeds *via* outer-sphere proton coupled electron transfer (PCET).¹¹² The species responsible for C-C coupling is unclear. An analogue Cu_2O_2 complex supported by ligand **L18** for which the $\text{bis}(\mu\text{-O})\text{Cu}^{\text{III}}_2$ species is exclusively observed reacts with neutral phenols to form the C-C coupling product a factor of 100 times faster than the complex formed with **L19** (predominantly a $\mu\text{-}\eta^2\text{:}\eta^2\text{-peroxo-Cu}^{\text{II}}_2$ complex). It is therefore possible that the species responsible for the C-C coupling of phenols observed from the complex of **L19** is due to the small amount of (unobserved) $\text{bis}(\mu\text{-O})\text{Cu}^{\text{III}}_2$ species in solution, thus suggesting that with ligands **L18** and **L19** the $\text{bis}(\mu\text{-O})\text{Cu}^{\text{III}}_2$ species reacts *via* PCET and the $\mu\text{-}\eta^2\text{:}\eta^2\text{-peroxo-Cu}^{\text{II}}_2$ reacts *via* electrophilic aromatic substitution if coordination of the phenol to the copper is possible.

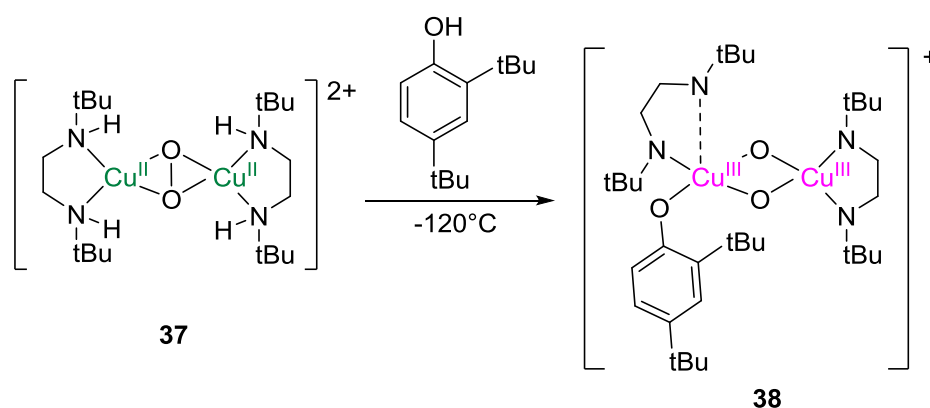


Scheme 26: Ligands used by Itoh *et al.*^{111,112,114} to generate copper-oxygen species for which with the reactivity differs depending on whether phenols or phenolates are used as substrates.

Complex **26** (Scheme 22) synthesised by Scarborough *et al.*⁹⁶ (also identified as a $\mu\text{-}\eta^2\text{:}\eta^2\text{-peroxo-Cu}^{\text{II}}_2$ complex) was shown to have little reactivity towards most phenols and phenolates. However the electron rich 2,4-di-*tert*-butylphenol reacts with complex **26** to give primarily the C-C coupling product over ortho-hydroxylation, presumably due to the steric bulk of the complex (and of the substrate) preventing coordination of the phenol, resulting in an outer-sphere electron transfer.

Another possibility is that an unobserved bis(μ -O)Cu^{III}₂ species is responsible for this reactivity. The complex is however capable of the oxidation of 3,5-di-*tert*-butylcatechol to 3,5-di-*tert*-butyl-*o*-benzoquinone and the oxidation of alcohols (such as benzylalcohol) to the relevant aldehydes, indicating that the steric bulk of this complex has less of an effect on these reactions.⁹⁶

Low temperature spectroscopy has provided further information on which species could be responsible for the ortho-hydroxylation of phenols. Stack *et al.*¹¹⁵ characterised a μ - η^2 : η^2 -peroxo-Cu^{II}₂ complex that reacted with 2,4-di-*tert*-butylphenol to form the catechol with no intermediates observed at -80°C, however when the temperature was decreased to -120°C a bis(μ -O)Cu^{III}₂ species was observed by UV-vis and XAS only upon addition of the phenol. The phenol coordinated to the copper presumably in the equatorial position (Scheme 27) to favour the bis(μ -O)Cu^{III}₂ species. DFT calculations showed that once the phenol is coordinated in the equatorial position, the aromatic ring is in the perfect position for π donation into the σ^* of the Cu₂O₂ system leading to the formation of the catechol, showing that the bis(μ -O)Cu^{III}₂ could potentially be the species responsible for Ty type activity.



Scheme 27: Coordination of the phenol leads to the formation of the bis(μ -O)Cu^{III}₂ species. Scheme adapted from Stack *et al.*¹¹⁵

As the bis(μ -O)Cu^{III}₂ species in complex **38** is only formed after substrate binding,¹¹⁵ the normal radical-type chemistry that is usually observed with this type of species could have been suppressed. Costas *et al.*¹¹⁶ synthesised a bis(μ -O)Cu^{III}₂ complex **39** (Figure 14) which allowed coordination of the phenolate (observed by rR and UV-vis) and subsequent oxidation to form the catechol and the quinone with no products of C-C coupling observed. This therefore indicates that the Ty type reactivity of the bis(μ -O)Cu^{III}₂ does not exclusively occur when the substrate can bind first to the peroxo species causing O-O fission. The reactivity of the bis(μ -O)Cu^{III}₂ species therefore varies from radical chemistry to arene hydroxylation.

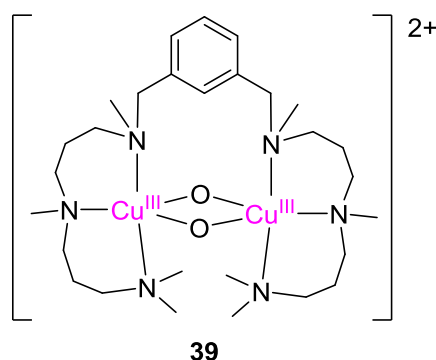


Figure 14: The bis(μ -O)Cu^{III}₂ complex used by Costas *et al.*¹¹⁶ for the oxidation of phenols to catechol and quinones *via* inner sphere electron transfer.

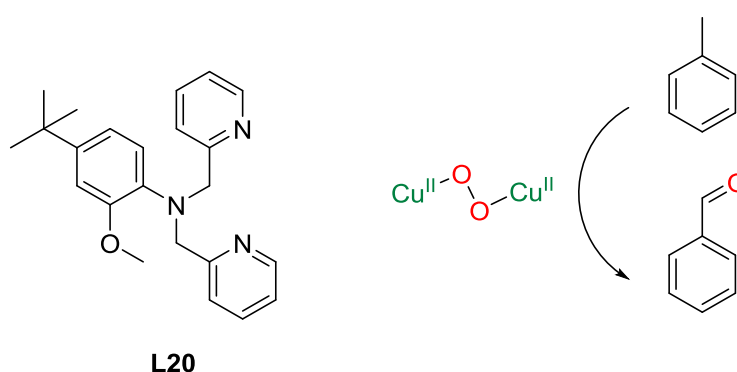
Karlin *et al.* could discriminate between the reactivity of the μ - η^2 : η^2 -peroxo-Cu^{II}₂ complex **31** and the bis(μ -O)Cu^{III}₂ complexes **30** and **33** (Scheme 23) due to the controlled formation of the latter species with either a Lewis acid or the coordination of a phenolate.⁹⁹ Interestingly complex **31** showed no reactivity towards 2,4-di-*tert*-butylphenol (Ty type or C-C coupling) even though the O-O bond is particularly long as displayed by rR and the crystal structure (1.54 Å). One would expect that a longer O-O bond would increase the reactivity of such a species. However when the O-O bond is broken, the reactivity completely changes. Complex **30** (after coordination of the Lewis acid) is able to do HAT from substrates with weak C-H bonds such as BNAH or with the O-H bonds of phenols (electron transfer followed by proton transfer) forming the C-C radical coupling product, both reactions which are not possible without the coordination of the Lewis acid. The role of the Lewis acid in this proposed to be an increase in the reduction potential of the bis(μ -O)Cu^{III}₂ complex, making it a better oxidant. When phenolates are added (as opposed to phenols) complex **33** is formed with coordination of the phenol and leads to the ortho-hydroxylation of the phenol *via* electrophilic aromatic substitution.⁹⁹

In conclusion the reactivity of the bis(μ -O)Cu^{III}₂ and μ - η^2 : η^2 -peroxo-Cu^{II}₂ complexes are versatile. The bis(μ -O)Cu^{III}₂ core can react with C-H bonds *via* HAT or with OH bonds of phenols *via* PCET to give C-C coupling products. The μ - η^2 : η^2 -peroxo-Cu^{II}₂ species can perform ortho-hydroxylation of phenolates if coordination of the phenolate is possible, however a probable mechanism is that the coordination causes the O-O bond of the peroxo species to break forming the bis(μ -O)Cu^{III}₂ species which then performs electrophilic aromatic substitution of the arene ring. This is therefore a possible mechanism in the enzyme Ty, despite a Cu^{III} ion never having been observed in biology.¹⁰¹

2.8.2. Other Cu₂O₂ species

2.8.2.1. *Cis* and *Trans*-μ-1,2-peroxo species

While less common than the side-on peroxo species, the *trans*-μ-1,2-peroxo species may still be implied in enzymatic reactions because of results obtained from model complexes. Karlin *et al.* characterised a *trans*-μ-1,2-peroxo species based on the ligand **L20**. Interestingly the Cu₂O₂ species oxidised toluene to benzaldehyde (Scheme 28). However there is doubt that is it the *trans*-μ-1,2-peroxo species responsible for the reactivity due to the possibility of an unobserved bis(μ-O)Cu^{III}₂ species, which is usually responsible for such types of reaction.



Scheme 28: Oxidation of toluene possibly by the *trans*-μ-1,2-peroxo species supported by the ligand **L20**.¹¹⁷

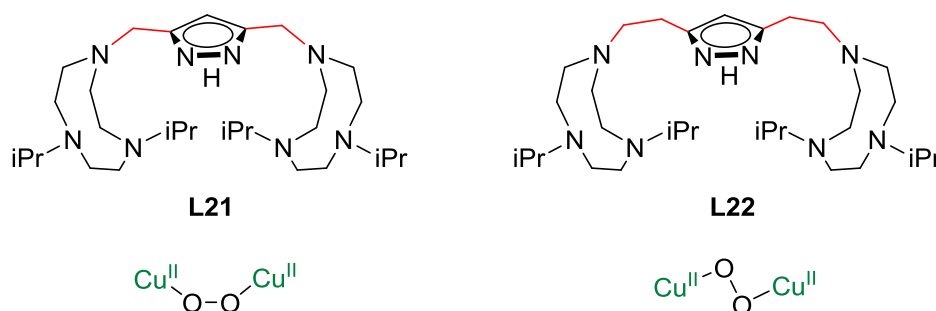


Figure 15: Ligands used by Meyer *et al.* to synthesise *cis* (left) and *trans* (right) peroxo species-1,2-peroxo-Cu^{II}₂.

The *cis*-μ-1,2-peroxo-Cu^{II}₂ species is defined as when the Cu-OO-Cu torsion angle is of less than 90°, as opposed to the *trans*-peroxo when the Cu-OO-Cu is greater than 90°. It is therefore not surprising that slight alterations in the ligand can change the nature of the peroxo species. Meyer *et al.* crystallised the first *cis*-μ-1,2-peroxo-Cu^{II}₂ in 2014 with a Cu-OO-Cu angle of 65.2° using the ligand **L21** (Figure 15).¹¹⁸ However when the methyl linker was replaced by an ethyl linker, the Cu₂O₂ complex formed (also crystallised) displayed a decrease in the Cu-Cu distance occurred which resulted in a larger Cu-OO-Cu angle of 104.5°,¹¹⁹ therefore making the species a *trans*-μ-1,2-peroxo-

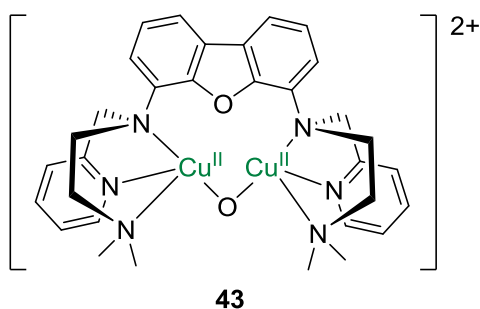


Figure 16: $(\mu\text{-O})\text{Cu}^{\text{II}}_2$ complex generated by reaction of a dinuclear Cu^{I} complex with PhIO.¹²⁴

2.8.4. Mixed valent $\text{Cu}^{\text{II}}\text{Cu}^{\text{III}}$ systems

While mixed valent species have been proposed for a while to be capable of the oxidation of strong C-H bonds,⁷¹ synthetic examples have only recently been achieved. The first example was given by Tolman *et al.*¹²⁶ who used the tetra-amide ligand with a macrocyclic frame to stabilise the $(\mu\text{-OH})\text{Cu}^{\text{II}}\text{Cu}^{\text{III}}$ species. The $\text{Cu}^{\text{II}}\text{Cu}^{\text{II}}$ complex was synthesised and crystallised, displaying a very short Cu-Cu distance of 2.67 Å. CV experiments displayed two reversible oxidation waves at 0.18 and 0.47 V vs. Fc^+/Fc . The use of one equivalent of the chemical oxidant $(\text{AcFc})(\text{SbF}_6)$ or 2 equivalents of $(\text{NH}_4)_2\text{Ce}(\text{NO}_3)_6$ allowed accumulation of the complex in the first and second oxidation state respectively. The first oxidation state was found to be a localised $(\mu\text{-OH})\text{Cu}^{\text{II}}\text{Cu}^{\text{III}}$ species (complex **44**, Figure 17) on the basis of DFT and EPR. The UV-vis-NIR spectrum displayed new bands at 528 nm ($\epsilon = 2150 \text{ M}^{-1}\cdot\text{s}^{-1}$) as well as a band at 1100 nm. The two-electron oxidised product was found to be the $\text{Cu}^{\text{III}}\text{Cu}^{\text{III}}$ species. DFT studies indicated that in both the one and two electron oxidation, the O-H bridging group remained intact. The $\text{Cu}^{\text{II}}\text{Cu}^{\text{III}}$ species was shown to react with DHA to form anthracene, but no mechanism is discussed. This is still to date the only example of the reactivity of such mixed valent species.

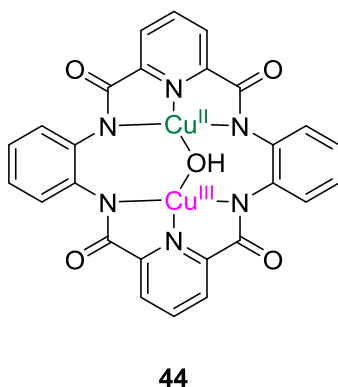


Figure 17: The first mixed valent $\text{Cu}^{\text{II}}\text{Cu}^{\text{III}}$ species described by Tolman *et al.* obtained after oxidation of a Cu^{II}_2 complex.¹²⁶

2.9. Conclusion

Nature has provided several copper mono-oxygenase enzymes with differing active sites, but not all of these active sites have been elucidated. Certain active species and catalytic cycles are still under debate. A whole variety of model complexes have been synthesised with nuclearities varying from mononuclear to trinuclear. Some systems such as the $\mu\text{-}\eta^2\text{:}\eta^2\text{-peroxo-Cu}^{\text{II}}_2$ and $\text{bis}(\mu\text{-O})\text{Cu}^{\text{III}}_2$ species are particularly well characterised with a wealth of literature documenting their structures and reactivity. On the other hand some species which have been proposed by calculations to be responsible for C-H oxidation have very few synthetic examples. The mixed valent $\text{Cu}^{\text{II}}\text{Cu}^{\text{III}}$ species is one of such systems, with only one example of the characterisation and reactivity with substrates before the start of this project. It is therefore the aim of this thesis to explore synthetic $\text{Cu}^{\text{II}}\text{Cu}^{\text{III}}$ systems.

3. Context and preliminary results of this thesis

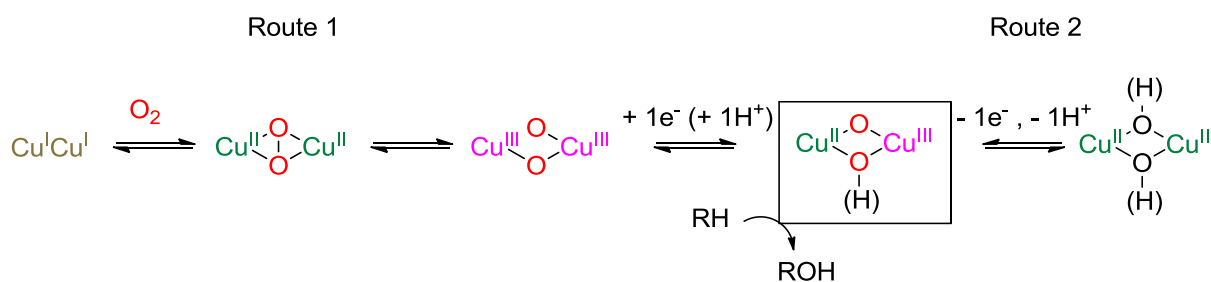
3.1. Context

This thesis was completed within the ANR-funded project COMEBAC (**CO**mplexes à valence **MixtE Bis**(μ -O(H))Cu^{II}Cu^{III} pour l'**ACT**ivation de Liaisons C-H), and therefore with the aim of generating mixed valent Cu^{II}Cu^{III} species for alkane oxidation. Three laboratories participated in this project: the group of M. Réglie and J. Simaan (Université d' Aix Marseille), the group of Y. Le Mest and N. Le Poul (Université de Bretagne Occidentale) and our group led by C. Belle (Université Grenoble Alpes). We have therefore received the support of H. Jamet (Université Grenoble Alpes) for theoretical calculations and N. Le Poul for time resolved spectroelectrochemical and part of the low temperature UV-vis studies, simulations as well as others for the helpful discussions. During my thesis I spent a total of three weeks in Brest doing electrochemical studies and time resolved UV-vis (under the guidance of N. Le Poul), one week in Marseille for NMR measurements (M. Yemloul) and one week in Groningen for rR measurements (W. Browne).

3.2. Synthetic strategy

Two synthetic routes are possible to the formation of a mixed valent bis(μ -oxo)Cu^{II}Cu^{III} species (see Scheme 30):

1. Reacting a Cu₂^I complex with dioxygen to form the μ - η^2 : η^2 -peroxo-Cu₂^{II} or bis(μ -O)Cu₂^{III} species followed by a 1 electron reduction. Our investigations using this synthetic route will be discussed in Part II Chapter 1.
2. Oxidation of a Cu₂^{II} complex (and deprotonation). Our research on this route will be discussed in Part II Chapters 2 to 4.



Scheme 30: Two different synthetic routes to forming a bis(μ -oxo)Cu^{II}Cu^{III} species.

It is worth noting that the both (μ - η^2 : η^2 -peroxo)dicopper and the isoelectronic bis (μ -oxo) dicopper species are of interest in themselves because of their relevance to the enzyme Tyrosinase (and possibly pMMO) (see Section 2.8.1).

3.3. Preliminary results from the ANR project

With the aim of synthesising $\text{Cu}^{\text{II}}\text{Cu}^{\text{III}}$ systems, different types of ligands have been used. Preliminary results with ligands based on alkoxido and phenoxido spacers are discussed below.

3.3.1. Complexes supported by ligands with an alkoxido spacer

Simaan *et al.*¹²⁷ used a tetra-amide ligand with an alkoxide spacer to generate the $\text{Cu}^{\text{II}}\text{Cu}^{\text{III}}$ complex **45** (Figure 18), characterised by UV-vis, EPR and DFT. Despite the presence of four amide groups in the ligand, only two are deprotonated with the N coordinated to the copper. The other two protonated amide groups are coordinated *via* the oxygen atoms. This has a dramatic effect on the oxidation potential of the complex, giving a potential of 0.63 V vs. Fc^+/Fc (compared to 0.18 V vs. Fc^+/Fc for Tolman's tetra anionic ligand).¹²⁶ An exchange of the acetate bridging group upon addition of sodium methoxide led to the formation of **46** (Figure 18), with a lower oxidation potential of 0.40 V vs. Fc^+/Fc ¹²⁸ forming a $\text{Cu}^{\text{II}}\text{Cu}^{\text{III}}$ species characterised by DFT, thus demonstrating how small changes in the coordination environment have significant effects on the oxidation potential of the complex.¹²⁸

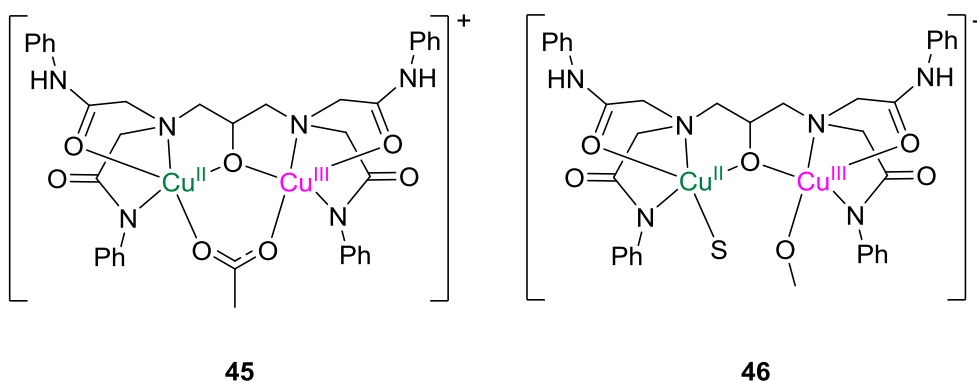
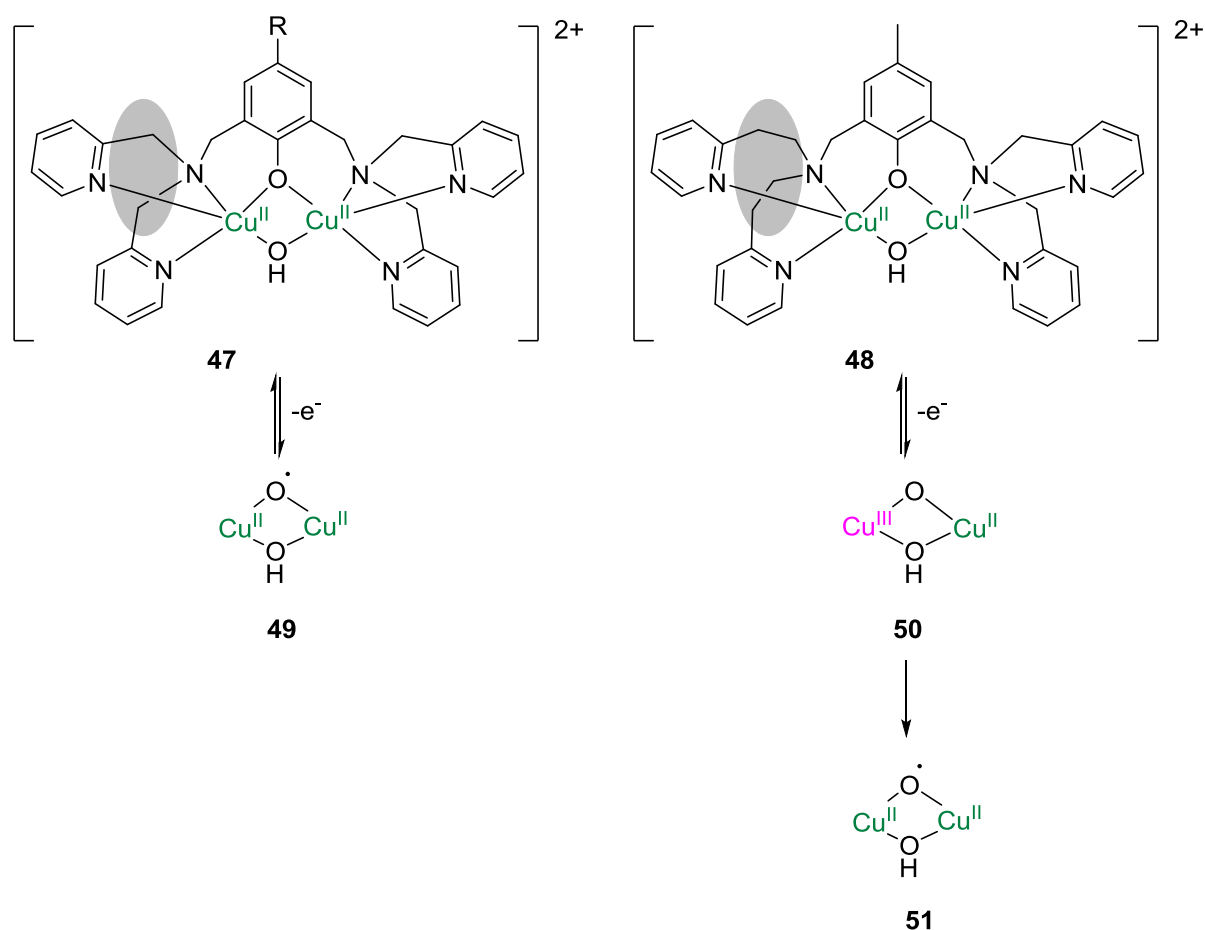


Figure 18: Proposed mixed valent complexes synthesised by Simaan *et al.*^{127,128} S = DMF (the solvent).

3.3.2. Complexes supported by ligands with a phenoxido spacer

As well as the coordination of charged ligands, the effect of other features in the ligand design was investigated by Jamet *et Le Poul*.¹²⁹ A whole series of phenoxido and hydroxide bridged Cu^{II}_2

complexes already synthesised by our group, with R substituents varying from electron withdrawing CF_3 to electron donating OCH_3 (Scheme 31), were used to investigate the effects of mono-electronic oxidation by spectroelectrochemistry and DFT calculations. While the oxidation potentials of the Cu^{II}_2 complexes with methyl spacers varied greatly between 0.45 and 1.22 V vs. Fc^+/Fc , no mixed valent $\text{Cu}^{\text{II}}\text{Cu}^{\text{III}}$ species was observed (Scheme 31, left). However, when the methyl spacer was replaced with an ethyl spacer on one side forming a dissymmetric ligand, a transitory species was observed by time resolved cryo-spectroelectrochemistry upon mono-oxidation: a band at 518 nm appeared and disappeared with a half-life of 14 s to form a new species with a band at 393 nm (Figure 19). TD-DFT calculations attributed the transient band to a $\text{Cu}^{\text{II}}\text{Cu}^{\text{III}}$ species (**50**), decaying into a $\text{Cu}^{\text{II}}\text{Cu}^{\text{II}}\text{PhO}^\bullet$ radical species¹²⁹ (**51**, Scheme 31). This type of species has already been characterised by Thomas *et al.*¹³⁰ This highlights the main difficulty in generating mixed valent $\text{Cu}^{\text{II}}\text{Cu}^{\text{III}}$ species: oxidation often occurs on the ligand instead of on the copper.



Scheme 31: The oxidation of several phenoxido-bridged complexes leading to ligand or copper oxidation. R = OMe, H or CF_3 . Scheme adapted from Jamet *et Le Poul*.¹²⁹

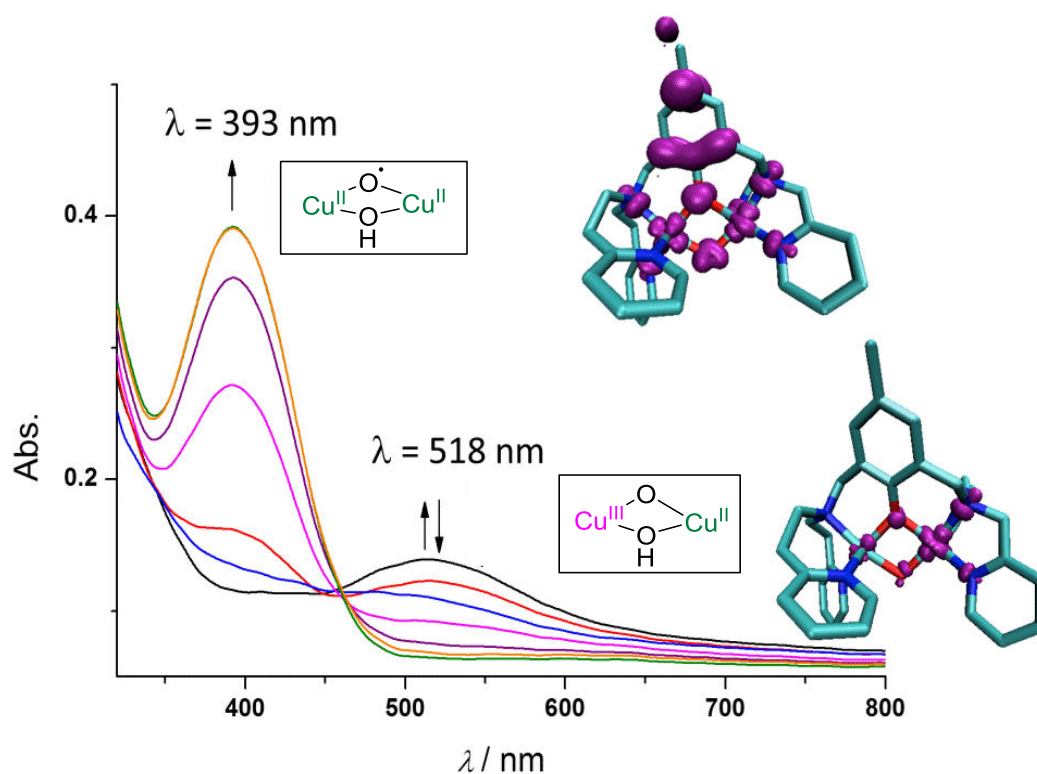


Figure 19: UV-vis of the transient $\text{Cu}^{\text{II}}\text{Cu}^{\text{III}}$ species that decays into a $\text{Cu}^{\text{II}}\text{Cu}^{\text{II}}\text{PhO}^{\bullet}$ radical. Images of the spin density generated by DFT of the two oxidised forms are displayed on the right. Figure adapted from Jamet *et al.* ¹²⁹

As a first approach we have demonstrated the difficulties of generating mixed valent $\text{Cu}^{\text{II}}\text{Cu}^{\text{III}}$ species upon mono-oxidation of Cu^{II}_2 complexes bearing a bridging phenoxido group. The diagrams of three complexes are shown (Figure 20) for which all three display ligand centred oxidations upon mono-oxidation of the Cu^{II}_2 complexes as demonstrated by CV and DFT, despite being coordinated by negatively charged ligands which should stabilise the Cu^{III} oxidation state. This demonstrated the importance of having a redox inactive ligand for the generation of high valent copper.

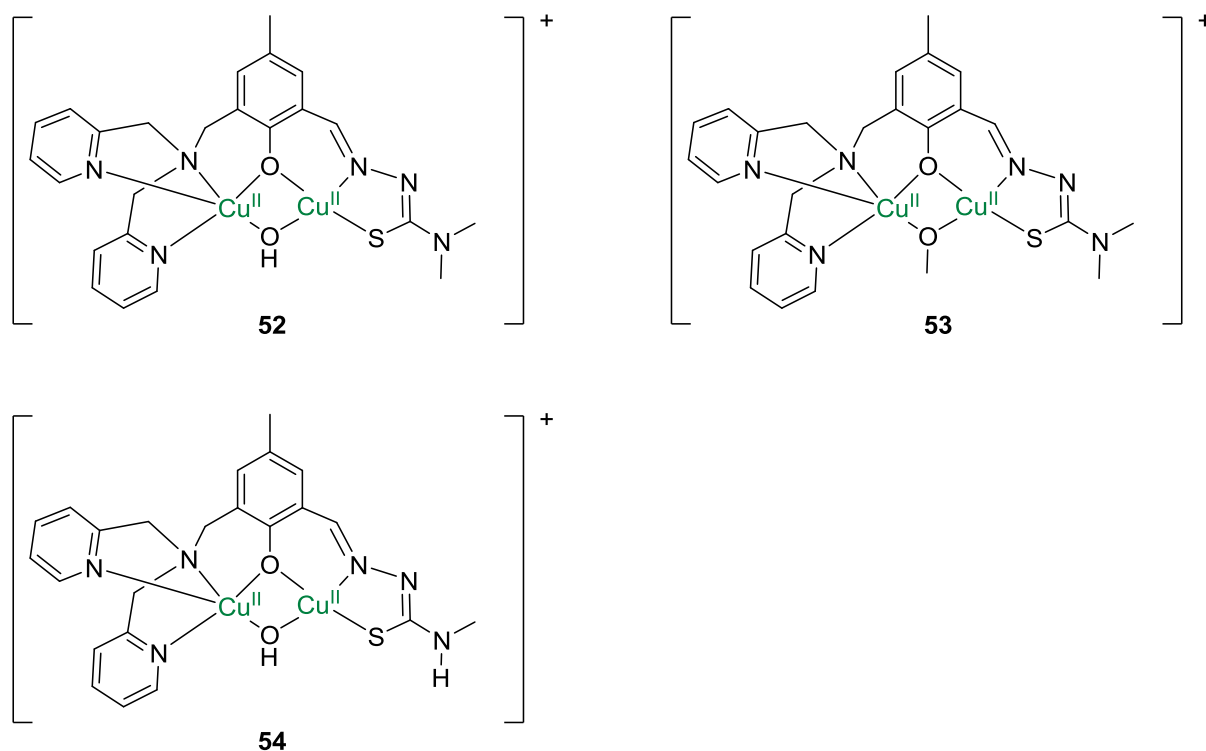


Figure 20: Complexes for which mono-oxidation occurs on the ligand.^{128,131}

3.4. Objectives

This thesis is focussed on the synthesis, characterisation and reactivity of Cu^ICu^{III} systems due to the lack of literature in this area. The ligand design has been based on first principles (*i.e.* use of charge and/or geometry) for the stabilisation of different oxidation states of copper as there is little precedent in this area. Our trials of both synthetic routes introduced in Section 3.2 will be described, and our efforts at probing the reactivity of Cu^ICu^{III} species will be discussed.

Part II Results and Discussion

1. Synthesis and characterisation of Cu^{I}_2 complexes and their reactivity with O_2

In this section, our attempts to generate $\text{Cu}_2:\text{O}_2$ species from the activation of O_2 by Cu^{I}_2 complexes supported by ligands Py_4 , Ox_4 and Py_2Ox_2 (Figure 21) are discussed. The overall aim is to be able to generate mixed valent $\text{Cu}^{\text{I}}\text{Cu}^{\text{III}}$ species by mono-reduction of these $\text{Cu}_2:\text{O}_2$ species. However $\text{Cu}_2:\text{O}_2$ species generated solely by activation of O_2 by Cu^{I}_2 centres are also of interest because of their relevance to certain enzymes such as Ty.¹³² The synthesis of the Cu^{I}_2 complexes have been attempted and their reactivities with O_2 to generate $\text{Cu}_2:\text{O}_2$ intermediates have been probed.

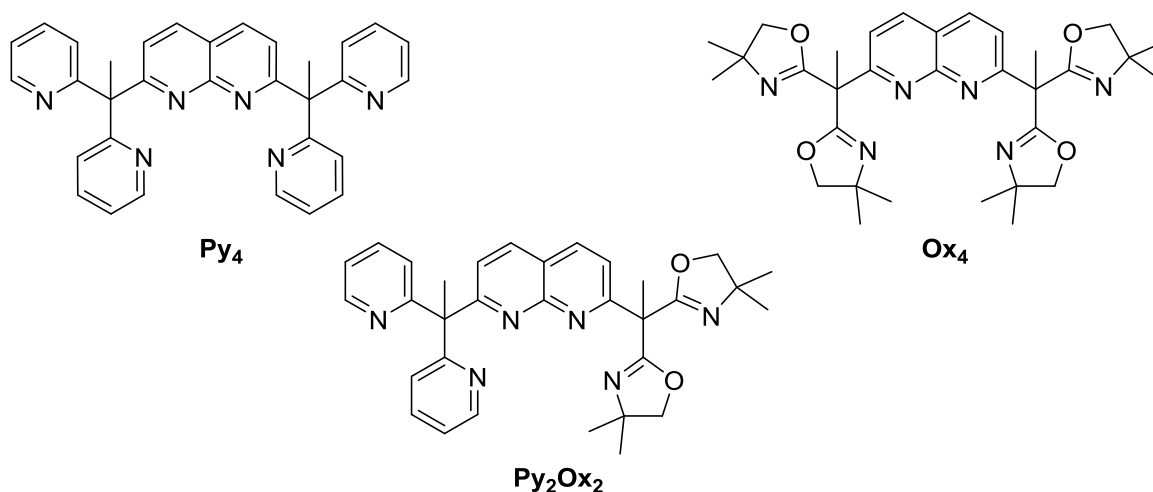


Figure 21: Ligands used in this chapter in order to generate $\text{Cu}_2:\text{O}_2$ complexes.

1.1. Cu^{I}_2 complexes with the ligand Py_4 .

1.1.1. Choice of ligand

Ligands based on a 1,8-naphthyridine spacer have been chosen because the spacer is redox inert, enabling redox chemistry to be controlled on the metal centres instead of on the ligand. The ligand 2,7-bis(1,1-dipyridyl-ethyl)-1,8-naphthyridine (denoted Py_4 , Figure 21) was initially synthesised by Tilley *et al.* to generate Cu^{I}_2 complexes.¹³³ Each copper atom is coordinated by a nitrogen of the naphthyridine spacer and the two pyridine groups, and a bridging acetonitrile group giving each copper a distorted tetrahedral geometry (Figure 22). Dinuclear cobalt complexes supported by the ligand Py_4 has recently been shown to activate oxygen^{134,135} and similar ligands with the methyl group substituted by a fluorine have been used to synthesise a whole series of first row transition metal

complexes¹³⁶ including a mixed valence $\text{Cu}^{\text{I}}\text{Cu}^{\text{II}}$ complex¹³⁷ thus displaying the versatility of this ligand system. An interesting feature of the complex $(\mu\text{-NCCH}_3)\text{Cu}_2^{\text{I}}\text{Py}_4$ is the close proximity in which the ligand holds the two copper ions, with a distance of 2.45 Å.¹³³ The enzyme pMMO displays an EXAFS signal that can be attributed to two copper ions in very close proximity to one another (2.6 Å),⁶⁰ which could be an important feature to replicate in model complexes if the enzyme is in fact dinuclear. The bridging group of $(\mu\text{-NCCH}_3)\text{Cu}_2^{\text{I}}\text{Py}_4$ can be displaced by other ligands (CO, isonitriles)¹³³ and is therefore a good candidate for attempting the activation of dioxygen.

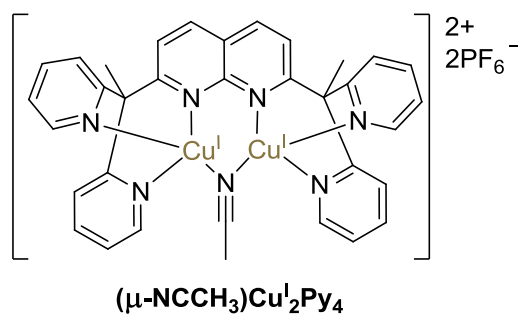


Figure 22: Complex synthesised by Tilley *et al.* based on the ligand Py_4 possessing naphthyridine spacer.¹³³

1.1.2. Reactivity of the complex $(\mu\text{-NCCH}_3)\text{Cu}_2^{\text{I}}\text{Py}_4$ with O_2

Having synthesised the complex $(\mu\text{-NCCH}_3)\text{Cu}_2^{\text{I}}\text{Py}_4$ using the same method as Tilley *et al.*¹³³ the reactivity of the Cu_2^{I} complex with dioxygen was investigated. The solution of the complex (0.35 mM in acetone) was prepared in the glove box, before removing it and placing under a pressure of N_2 . The sample was then cooled to 193 K, and O_2 bubbled through the solution, while monitored by UV-vis spectroscopy. The disappearance of bands was observed on the UV-vis spectrum upon O_2 addition, with no new bands appearing which indicates that no intermediate species accumulates. It is possible that the oxidation of copper either proceeds *via* an outer-sphere electron transfer, or that the reaction is inner-sphere but the $\text{Cu}_2\text{:O}_2$ species formed is very reactive and therefore does not accumulate.

1.1.3. Complex $\text{Cu}_2^{\text{I}}\text{Py}_4$ without an acetonitrile bridging group.

The bridging acetonitrile group in complex $(\mu\text{-NCCH}_3)\text{Cu}_2^{\text{I}}\text{Py}_4$ is relatively tightly bound demonstrated by Cu-NCCH_3 distances of 2.004 and 1.979 Å.¹³³ It is therefore possible that the bridging acetonitrile group is preventing the coordination of O_2 with the Cu_2^{I} complex. The synthesis of a new complex avoiding the CH_3CN bridging group was therefore attempted.

1.1.3.1. Synthesis of complex $\text{Cu}^{\text{I}}_2\text{Py}_4$

Complex $\text{Cu}^{\text{I}}_2\text{Py}_4$ was synthesised by addition of 2.05 equivalents of $\text{Cu}^{\text{I}}(\text{CF}_3\text{SO}_3)\cdot\text{toluene}$ to 1 equivalent of the ligand Py_4 in a mixture of THF and toluene at room temperature in a glove box, resulting in a grey solid (in a quantitative yield). The grey solid turned yellow when dissolved in acetone or DMF. Slow diffusion of DIPE into a solution of DMF left standing for 4 months resulted in a few brown crystals ($\sim 5\%$). The low yield indicates that the structure in Figure 23 may not be representative of the remainder of the complex (grey powder) which was used for all future analysis.

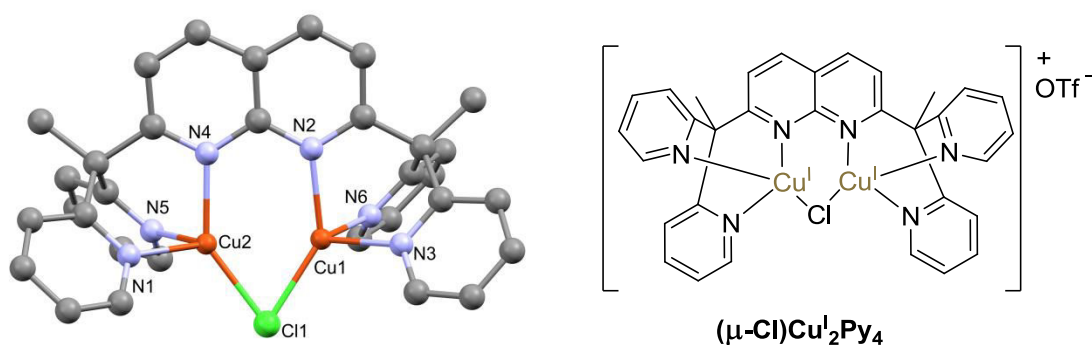


Figure 23: Left: crystal structure of the cation $[(\mu\text{-Cl})\text{Cu}^{\text{I}}_2\text{Py}_4]^+$. Right: diagrammatic representation of $(\mu\text{-Cl})\text{Cu}^{\text{I}}_2\text{Py}_4$.

Table 3: Left: selected bond distances; right: selected bond angles for the complex $(\mu\text{-Cl})\text{Cu}^{\text{I}}_2\text{Py}_4$.

Atom 1	Atom 2	Length / Å	Bond angle	Angle / °
Cu2	N4	2.019(3)	N4-Cu2-Cl1	140.73(9)
Cu2	N5	2.046(3)	N1-Cu2-Cl1	112.0(1)
Cu2	N1	2.052(4)	N1-Cu2-N5	88.0(1)
Cu2	Cl1	2.223(1)	N5-Cu2-N4	89.6(1)
Cu1	N2	2.037(3)	N5-Cu2-Cl1	120.1(1)
Cu1	N6	2.038(4)	N4-Cu2-N1	92.7(1)
Cu1	N3	2.057(3)	N2-Cu1-Cl1	138.84(9)
Cu1	Cl1	2.230(1)	N3-Cu1-Cl1	112.0(1)
Cu1	Cu2	2.5375(8)	N3-Cu1-N6	88.4(1)
			N6-Cu1-N2	87.8(1)
			N6-Cu1-Cl1	123.4(1)
			N3-Cu1-N2	93.2(1)

The X-ray crystal structure reveals that the complex is dinuclear with each copper in a strongly distorted tetrahedral environment. Bond distances and angles around Cu1 and Cu2 are very similar. Bond angles between N1/N5-Cu2-N4 are close to 90° whereas bond angles involving Cu2 and Cl1 are much larger with N4-Cu2-Cl1 at 141° and N1-Cu2-Cl1 at 112°. Cu-N distances are between 2.02 and 2.06 Å and Cu-Cl distances are slightly longer at 2.22-2.23 Å.

The surprising presence of the chloride could be due to the presence of small amounts of DCM present in the ligand that remain after the ligand synthesis, as no chlorine-containing substance was used in the synthesis of the complex. The presence of the bridging chloride also seems to indicate that the complex Cu_2Py_4 requires a bridging group to crystallise.

1.1.1.1. Solution characterisation of the complex Cu_2Py_4

To determine if the solution of the complex Cu_2Py_4 was coherent with the crystal structure of the complex, the $^1\text{H-NMR}$ spectrum was recorded in deuterated acetone. The spectrum is shown in Figure 24.

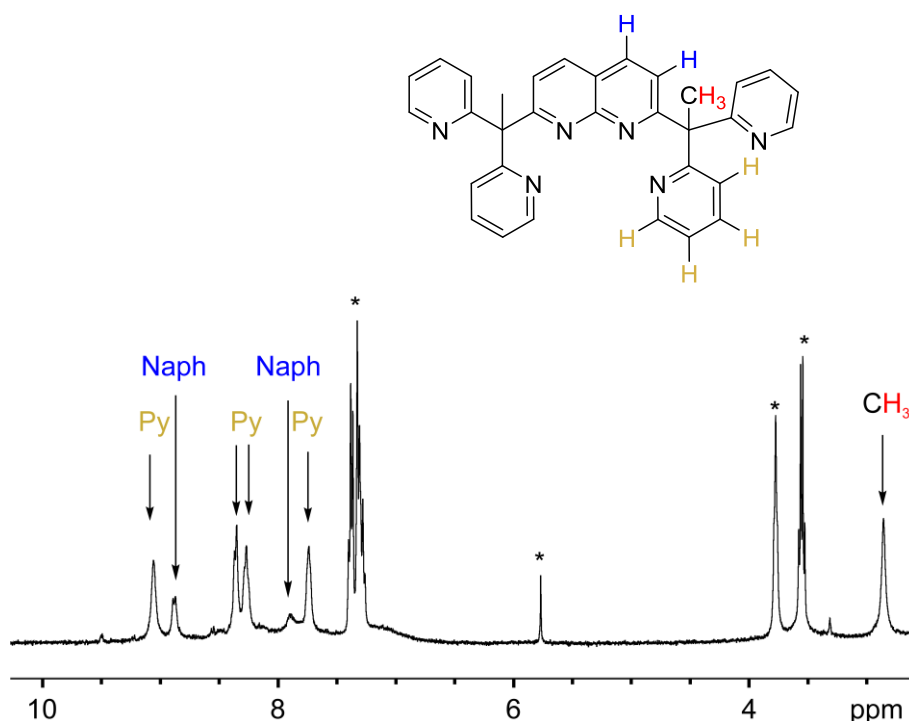


Figure 24: $^1\text{H-NMR}$ spectrum of the complex Cu_2Py_4 in acetone- d_6 . Starred peaks from left to right: toluene, DCM, THF, diethyl ether.

The $^1\text{H-NMR}$ spectrum displays 7 peaks that can be assigned to the protons on the complex: four to the protons of the pyridines, two to the naphthyridine and one to the methyl group. The peaks are all relatively large indicating either the presence of a paramagnetic impurity or a fast exchange. There is no peak that can be clearly attributed to a bridging group, indicating that either there is no bridging group in solution, or that a chloride ion (or other inorganic ion, not visible by $^1\text{H-NMR}$) is present the same as in the crystal structure. The ESI-MS (electrospray ionisation mass spectrometry) gave no further information on the structure in solution of the complex.

In conclusion the structural characterisation of the complex $\text{Cu}_2^{\text{I}}\text{Py}_4$ is rather vague. It is unlikely that the solution of the complex is the same as the crystal structure as it was only a fraction of the complex that formed crystals. $^1\text{H-NMR}$ and ESI-MS failed to give any further information of the structure of this complex in solution. Nevertheless attempts were made to study the reactivity of the complex $\text{Cu}_2^{\text{I}}\text{Py}_4$ with O_2 .

1.1.1.2. Reactivity of complex $\text{Cu}_2^{\text{I}}\text{Py}_4$ with O_2

The reactivity of the complex $\text{Cu}_2^{\text{I}}\text{Py}_4$ with dioxygen was investigated in acetone at 193 K. The solution of the complex (0.33 mM in acetone) was prepared in the glove box, before removing it and placing under a pressure of argon while cooling down. O_2 was then bubbled through the solution, and the reaction monitored by UV-vis. Only the loss of a band centred at 380 nm, and no new bands appeared indicating that no new species are formed (or accumulated). Due to the lack of detection of any $\text{Cu}_2:\text{O}_2$ species, attempts at reacting Cu^{I} complexes supported by the ligand Py_4 with O_2 were not taken any further.

1.2. Cu_2^{I} complexes with bis-oxazoline coordinating groups

Cu_2^{I} complexes based on the ligand Py_4 did not display any intermediates when reacted with O_2 at low temperatures. New ligands based on the 1,8-naphthyridine unit have therefore been designed to determine if $\text{Cu}_2:\text{O}_2$ species can be generated with this unit which is of particular interest because of its ability to generate Cu_2 complexes with low Cu-Cu distances.

1.2.1. Choice of the coordinating groups

Oxazoline ligands have been around for over 30 years, often used to coordinate transition metals, and their tuneable structures and electronics have shown that they are good for catalysis.¹³⁸

Due to the presence of a chiral centre in several examples, they have often been used for asymmetric synthesis.¹³⁹

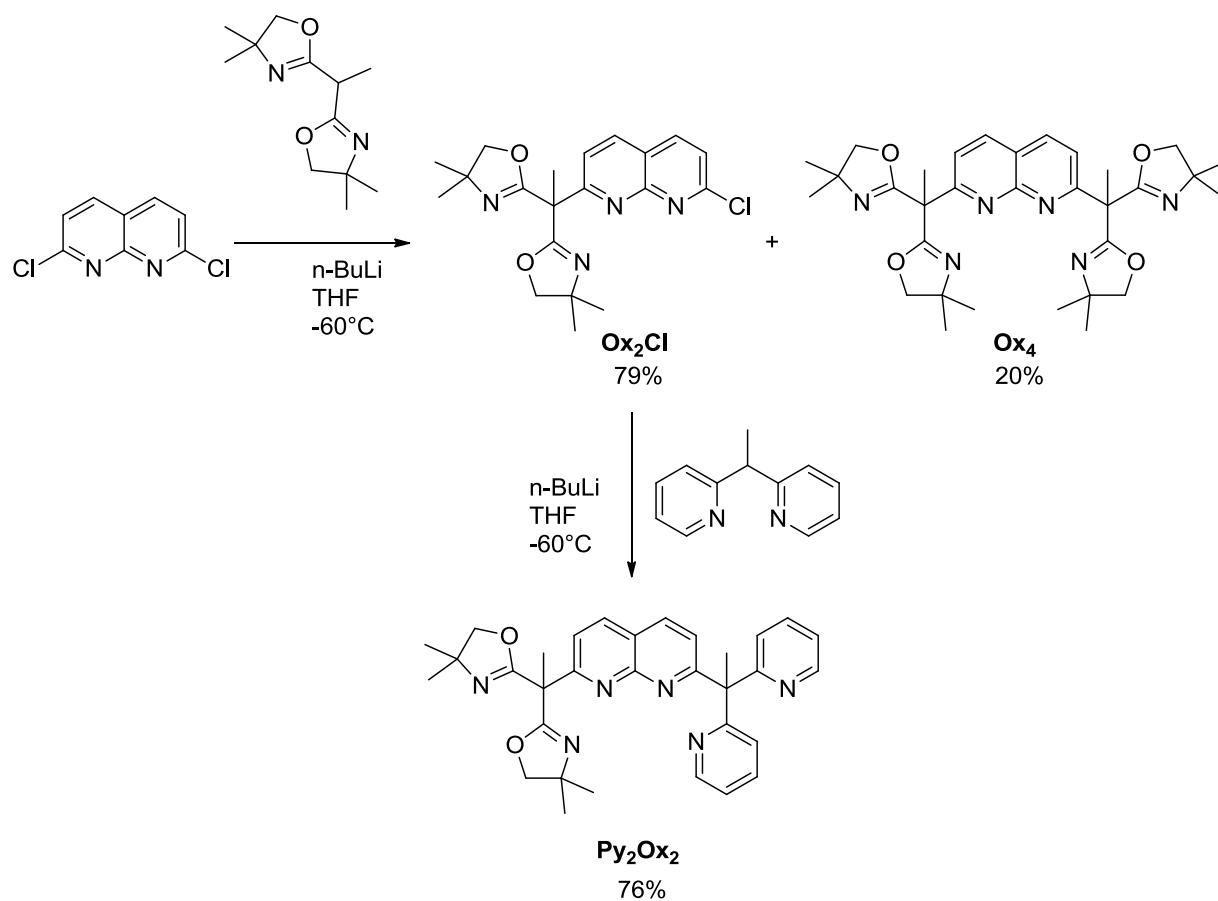
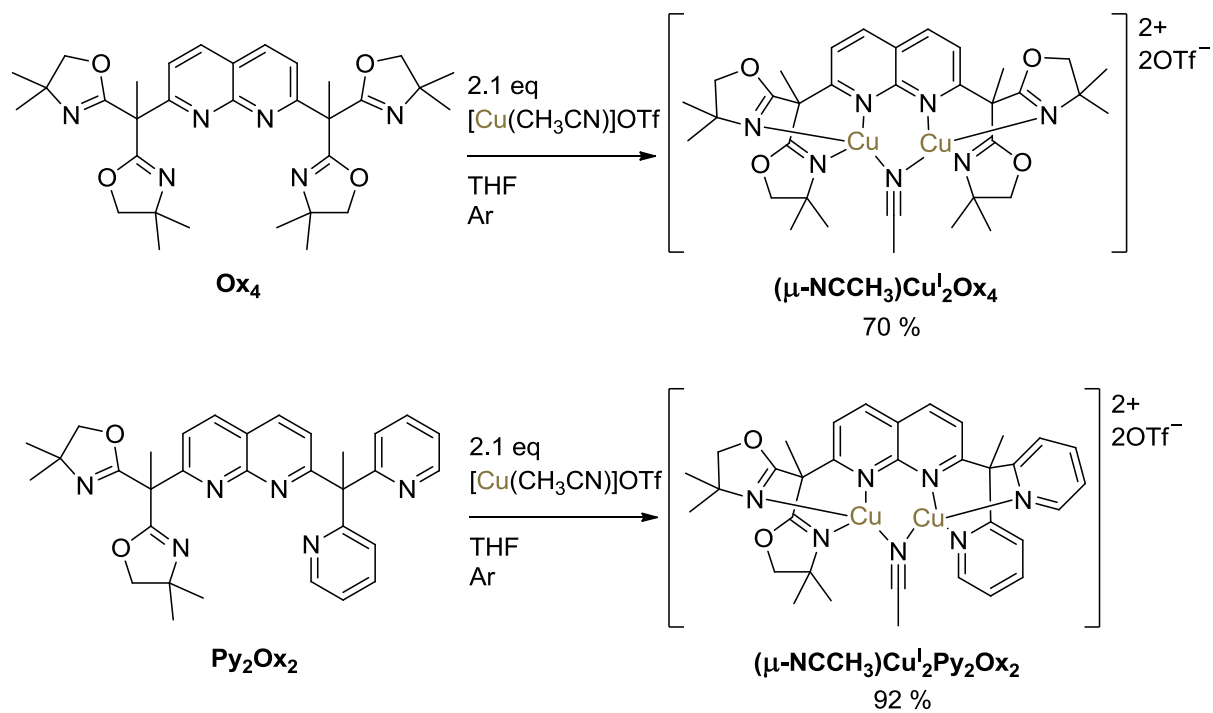
The ligands Ox₄ and Py₂Ox₂ (Scheme 32) were designed based on a 1,8-naphthyridine as the spacer and bis-oxazoline (BOX) or pyridine moieties as the binding pockets. The steric bulk of the oxazoline entity could providing steric hindrance around the metal centre, stabilising any intermediates that could be formed. This concept was inspired by Scarborough *et al.*⁹⁶ who synthesised a $\mu\text{-}\eta^2\text{:}\eta^2\text{-peroxo-Cu}^{\text{II}}_2$ complex that was relatively stable at room temperature. Studies with this entity by Meyer *et al.*¹⁴⁰ have also shown that the BOX entity is able to stabilise Cu₂:O₂ intermediates.

During the synthesis of the ligand Ox₄, a non-negligible amount of the mono-substituted intermediate Ox₂Cl was recovered (Scheme 32). Taking advantage of this compound, we prepared the synthesis of the ligand Py₂Ox₂. There have been very few examples of Cu₂:O₂ species formed using dissymmetric ligands,^{141–144} and a dissymmetric ligand could favour the formation of a mixed valent bis($\mu\text{-O}$)Cu^{II}Cu^{III} species upon reduction of a Cu₂:O₂ adduct as the reduction potentials of the two copper ions would not be the same.

1.2.2. Synthesis of the ligands Ox₄ and Py₂Ox₂ and their respective complexes

The bis-oxazoline entity was synthesised according to the literature procedure.^{145,a} 2,7-dichloro-1,8-naphthyridine (synthesised in three steps according to the literature procedure)^{146–148} was added to a mixture of two equivalents of the bis-oxazoline entity with two equivalents of n-BuLi in THF at -60°C resulting in the formation of the ligand Ox₄ and Ox₂Cl with yields of 20 % and 79 % respectively.^a The mono-substituted products could be reacted with a mixture of 1 equivalent of 1,1-di-(2-pyridyl)-ethane (synthesised in one step)¹⁴⁹ and 1 equivalent of n-BuLi to form the ligand Py₂Ox₂ with a yield of 76%.

^a Synthesis of the ligand Ox₄ and the synthon Ox₂Cl was completed by Dr. A. Thibon-Pourret and G. Gellon.

Scheme 32: Synthetic pathway for the ligands Ox₂ and Py₂Ox₂.Scheme 33: Synthesis of the complexes $(\mu\text{-NCCH}_3)\text{Cu}_2\text{Ox}_4$ and $(\mu\text{-NCCH}_3)\text{Cu}_2\text{Py}_2\text{Ox}_2$.

The two respective complexes were generated under argon by reaction of 1 equivalent of either ligand Ox₄ or Py₂Ox₂ with 2.1 equivalents of [Cu^I(CH₃CN)₄]OTf in THF to give an orange precipitate that were filtered. The yields of the complexes were of 70 % from the ligand Ox₄ and 92 % from ligand Py₂Ox₂ (Scheme 33).

1.2.3. Solid state characterisation of the complexes from the ligands Py₂Ox₂ and Ox₄

Unfortunately the crystal structures of the complexes with the ligands Py₂Ox₂ and Ox₄ could not be obtained. The use of Raman spectroscopy in the solid state was therefore used to characterise the presence of certain groups such as the CH₃CN bridge.^b Samples were prepared in the glove box and only opened to air at the time of measuring. No colour change was observed on the samples over the time scale of the analysis by Raman spectroscopy, indicating no oxidation of the complexes.

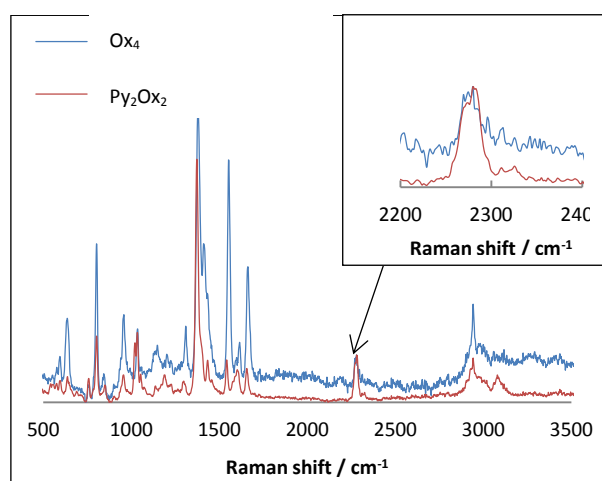


Figure 25: Raman spectra for the Cu^I complexes from the ligands Py₂Ox₂ and Ox₄ obtained in the solid state upon laser excitation of 532 nm. The peaks in the inset correspond to C-N stretches.

The Raman spectra for the Cu₂^I complexes with the ligands Ox₄ and Py₂Ox₂ display peaks at 2278 cm⁻¹ and 2280 cm⁻¹ respectively. These values are very similar to the value of 2280 cm⁻¹ (from IR) obtained by Tilley *et al.*¹³³ attributed to the C-N stretch for the complex (μ-NCCH₃)Cu₂^IPy₄. While terminal NCCH₃ ligands cannot be ruled out from these data, the proximity of the values obtained to those obtained by Tilley *et al.* strongly suggest a bridging acetonitrile group. Complexes from the ligands Py₂Ox₂ and Ox₄ are therefore named (μ-NCCH₃)Cu₂^IPy₂Ox₂ and (μ-NCCH₃)Cu₂^IOx₄ respectively (Scheme 33). The C-N stretching frequency of free acetonitrile is of 2249 cm⁻¹,¹⁵⁰ therefore the CN bond is strengthened upon complexation.¹⁵¹

^b In collaboration with Prof. W. R. Browne.

1.2.4. Solution characterisation of complexes $(\mu\text{-NCCH}_3)\text{Cu}^{\text{I}}_2\text{Py}_2\text{Ox}_2$ and $(\mu\text{-NCCH}_3)\text{Cu}^{\text{I}}_2\text{Ox}_4$.

1.2.4.1. $^1\text{H-NMR}$ of complexes $(\mu\text{-NCCH}_3)\text{Cu}^{\text{I}}_2\text{Ox}_4$ and $(\mu\text{-NCCH}_3)\text{Cu}^{\text{I}}_2\text{Py}_2\text{Ox}_2$

To determine the structures of the complexes in solution, the $^1\text{H-NMR}$ spectra in CD_3CN were recorded at room temperature. CD_3CN solutions of the complexes (2 mM) were prepared in the glove box and removed in a sealed NMR tube. The $^1\text{H-NMR}$ spectra are shown in Figure 26.

The $^1\text{H-NMR}$ of the complex $(\mu\text{-NCCH}_3)\text{Cu}^{\text{I}}_2\text{Ox}_4$ displays two well resolved doublets in the aromatic region corresponding to the four *C-H* on the naphthyridine and a singlet at 2.09 ppm assigned to the two CH_3 groups in the benzylic positions of the naphthyridine. Peaks centred around 4.0 ppm and 1.4 ppm can be assigned to the CH_2 and CH_3 groups of the oxazoline moiety. Interestingly there are two peaks around 4 ppm which does not occur on the $^1\text{H-NMR}$ spectrum of the ligand on its own. This indicates that the copper is coordinated to the ligand, as the two diastereotopic protons (in the ligand) are no longer in the same environment. Two singlets at around 1.4 ppm corresponding to the CH_3 groups of the oxazoline entity support this result. The splitting cannot be caused by a de-coordination of the bridging CH_3CN from one of the Cu ions, otherwise the same splitting effect would be observed in the peaks from the protons of the naphthyridine unit (although it cannot be ruled out that de-coordination of the bridging CH_3CN to form a terminal CH_3CN group may occur faster than the NMR timescale).

Analysis of the $^1\text{H-NMR}$ spectrum of $(\mu\text{-NCCH}_3)\text{Cu}^{\text{I}}_2\text{Py}_2\text{Ox}_2$ is similar, with the same splitting observed in the peaks attributed to the CH_2 and CH_3 of the bis-oxazoline group (centred at 4.0 and 1.4 respectively). Four peaks in the aromatic region of the spectrum of $(\mu\text{-NCCH}_3)\text{Cu}^{\text{I}}_2\text{Py}_2\text{Ox}_2$ can be attributed to protons for the pyridine groups; these peaks are much broader than the rest of the peaks of the two $^1\text{H-NMR}$ spectra shown in Figure 26 indicating a possible fast exchange of conformation around the pyridine groups. Two signals at 2.43 and 2.09 ppm can be assigned to the methyl groups on the benzylic positions of the naphthyridine the side of the pyridine groups and the oxazoline entity respectively.

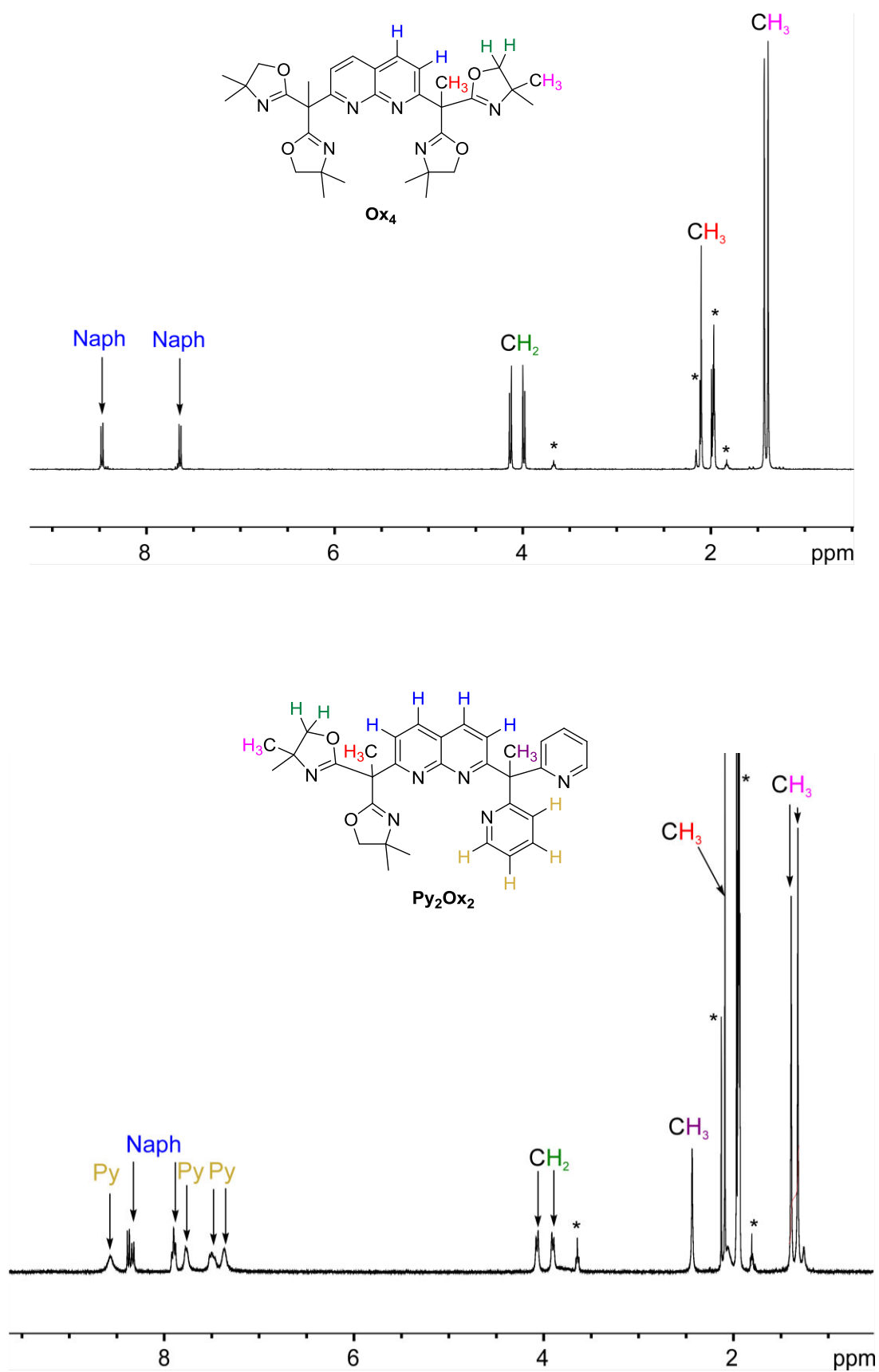


Figure 26: ¹H-NMR spectra of $(\mu\text{-NCCH}_3)\text{Cu}_2\text{Ox}_4$ (top) and $(\mu\text{-NCCH}_3)\text{Cu}_2\text{Py}_2\text{Ox}_2$ (bottom) in CD_3CN , with diagrammatic representations of the relevant ligands. Starred peaks from left to right: THF, water, acetonitrile and THF.

In terms of the bridging acetonitrile group, Karlin *et al.* observed a signal at 2.01 ppm (significantly shifted from the CH₃CN solvent residue at 1.94 ppm) which was assigned to a terminal CH₃CN group. However no signals of this type could confirm the presence of the bridging group in solution for either complex.¹⁵²

1.2.4.2. Mass spectrometry of the complex $(\mu\text{-NCCH}_3)\text{Cu}^{\text{I}}_2\text{Ox}_4$

A solution of the complex $(\mu\text{-NCCH}_3)\text{Cu}^{\text{I}}_2\text{Ox}_4$ in acetone was generated in the glove box then injected into the mass spectrometer that had already been purged with acetone containing no O₂. The ESI-MS spectrum is shown in Figure 27.

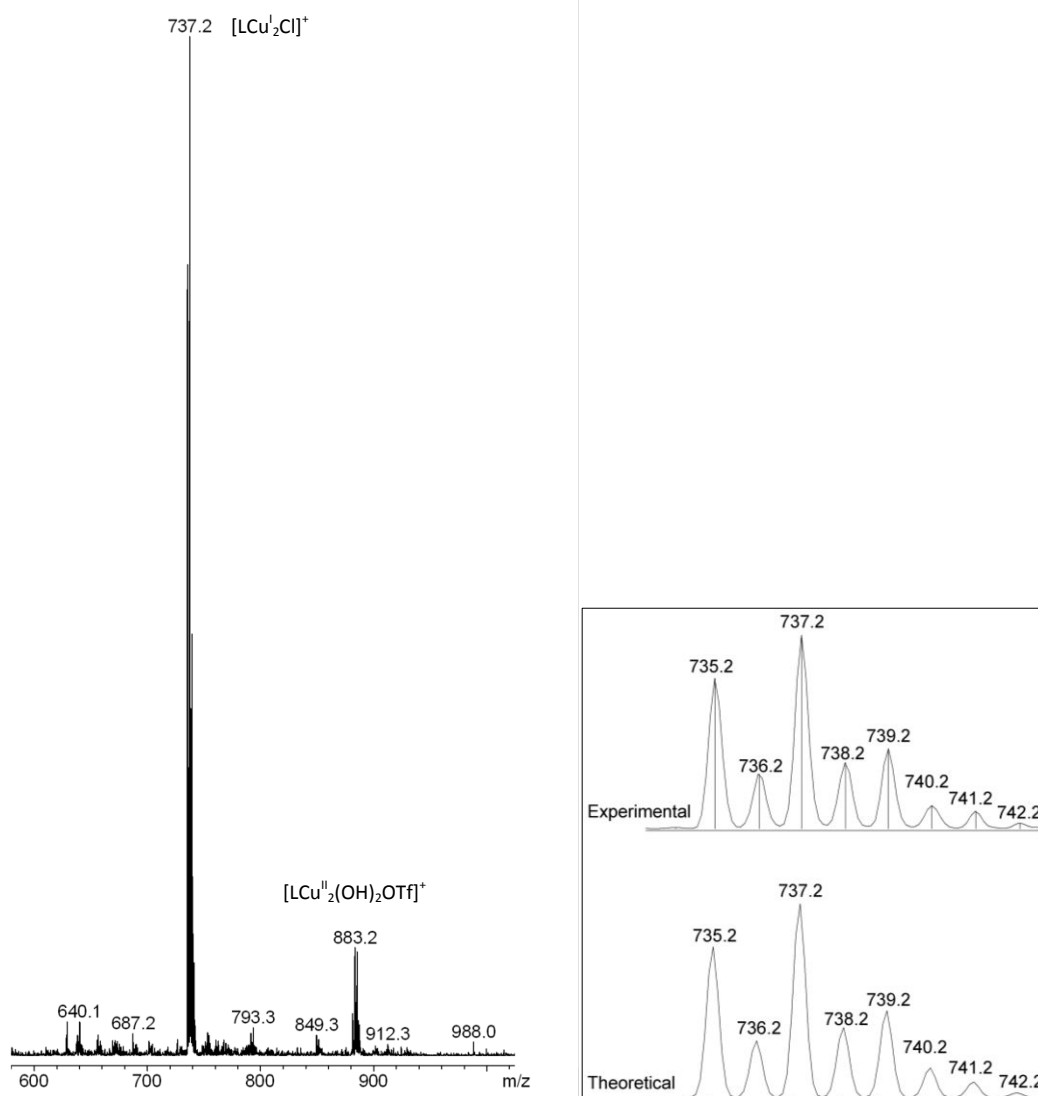


Figure 27: Left: ESI-MS spectrum of the complex $(\mu\text{-NCCH}_3)\text{Cu}^{\text{I}}_2\text{Ox}_4$ in acetone. Right: Experimental (top) and theoretical (bottom) isotopic profile for $[\text{LCu}_2\text{Cl}]^+$.

The ESI-MS spectrum displays two groups of signals, one with the highest peak at $m/z = 737$ attributed to $[\text{LCu}^{\text{I}}_2\text{Cl}]^+$ (where L = ligand Ox_4) due to the isotopic profile (Figure 27, right) and a peak at $m/z = 883$ was assigned to $[\text{LCu}^{\text{II}}_2(\text{OH})_2\text{OTf}]^+$, a dead end product from the reaction of the Cu^{I}_2 complex with dioxygen. The presence of the chloride in $[\text{LCu}^{\text{I}}_2\text{Cl}]^+$ could be due to a reaction in the spectrometer, and therefore the actual bridging group of the complex in solution remains unclear. Mass spectrometry is therefore not particularly revealing in terms of the structure of the Cu^{I} complex other than confirming that the ligand supports two coppers, and this analysis was therefore not attempted on the complex $(\mu\text{-NCCH}_3)\text{Cu}^{\text{I}}_2\text{Py}_2\text{Ox}_2$.

1.2.5. Reactivity of complexes $(\mu\text{-NCCH}_3)\text{Cu}^{\text{I}}_2\text{Ox}_4$ and $(\mu\text{-NCCH}_3)\text{Cu}^{\text{I}}_2\text{Py}_2\text{Ox}_2$ with O_2

1.2.5.1. Addition of O_2 to the complexes $(\mu\text{-NCCH}_3)\text{Cu}^{\text{I}}_2\text{Ox}_4$ and $(\mu\text{-NCCH}_3)\text{Cu}^{\text{I}}_2\text{Py}_2\text{Ox}_2$

To determine if the complexes $(\mu\text{-NCCH}_3)\text{Cu}^{\text{I}}_2\text{Ox}_4$ and $(\mu\text{-NCCH}_3)\text{Cu}^{\text{I}}_2\text{Py}_2\text{Ox}_2$ would react with O_2 to form $\text{Cu}_2:\text{O}_2$ adducts, a solution of each of the complexes was generated in the glove box before removing, cooling to 193 K while under pressure of either N_2 or Ar, then O_2 was bubbled through the solution and the changes were monitored by UV-vis.^c Acetone was chosen as a solvent it has a low freezing point enabling the stabilisation of intermediates because the complexes are soluble even at low temperatures.

1. Spectroscopic data for typical $\text{Cu}_2:\text{O}_2$ species

The optical characteristics of the three most common $\text{Cu}_2:\text{O}_2$ species in the literature are presented in Table 4 and Figure 28.

Table 4: Typical UV-vis data for $\text{Cu}_2:\text{O}_2$ species. Table adapted from Stack *et al.*¹⁰⁶

Species	UV-vis: λ / nm ($\epsilon / \text{mM}^{-1}\cdot\text{cm}^{-1}$)
<i>trans</i> -1,2-peroxo- Cu^{II}_2	500 (10), 600 (7)
$\mu\text{-}\eta^2\text{:}\eta^2\text{-peroxo-}\text{Cu}^{\text{II}}_2$	360 (24), 520 (1)
bis($\mu\text{-O}$) Cu^{III}_2	300 (20), 400 (24)

^c In collaboration with Dr. N. Le Poul.

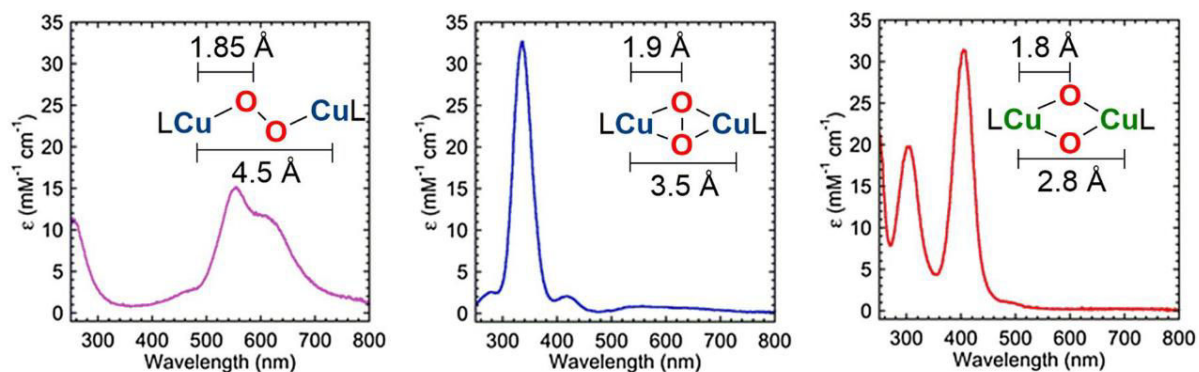


Figure 28: Typical UV-vis spectra for different types of $\text{Cu}_2:\text{O}_2$ species. Figure from Stack *et al.*¹⁰¹

2. UV-vis spectra of the addition of O_2 to complex $(\mu\text{-NCCH}_3)\text{Cu}^{\text{I}}_2\text{Ox}_4$

The UV-vis spectra of the addition of O_2 to complex $(\mu\text{-NCCH}_3)\text{Cu}^{\text{I}}_2\text{Ox}_4$ are shown in Figure 29 (left). The baseline was taken on the Cu^{I} complex so that any new bands that appear are due to new species being formed. Upon addition of O_2 , four new bands are formed with wavelengths and molar absorption coefficients (ϵ) of 338 nm ($\epsilon = 10\,000\ \text{M}^{-1}\cdot\text{cm}^{-1}$), 409 (1800), 539 (610) and 643 (540). This is the typical spectrum for a $\mu\text{-}\eta^2:\eta^2\text{-peroxo-Cu}^{\text{II}}_2$ species (Table 4 and Figure 28), with the first two being ligand-to-metal charge transfer bands from the oxygen to the copper and the latter two being d-d transitions. However these bands exhibit slightly lower molar absorption coefficient (normally the band at around 340 nm has a value of around $\epsilon = 24\,000 - 30\,000\ \text{M}^{-1}\cdot\text{cm}^{-1}$).^{101,106} This could be due to incomplete conversion of the Cu^{I}_2 species to the $\text{Cu}_2:\text{O}_2$ species. The absorption at a wavelength of 338 nm against time after addition of O_2 is shown in Figure 29 (right) and demonstrates that the $\text{Cu}_2:\text{O}_2$ species is formed after 25 seconds.

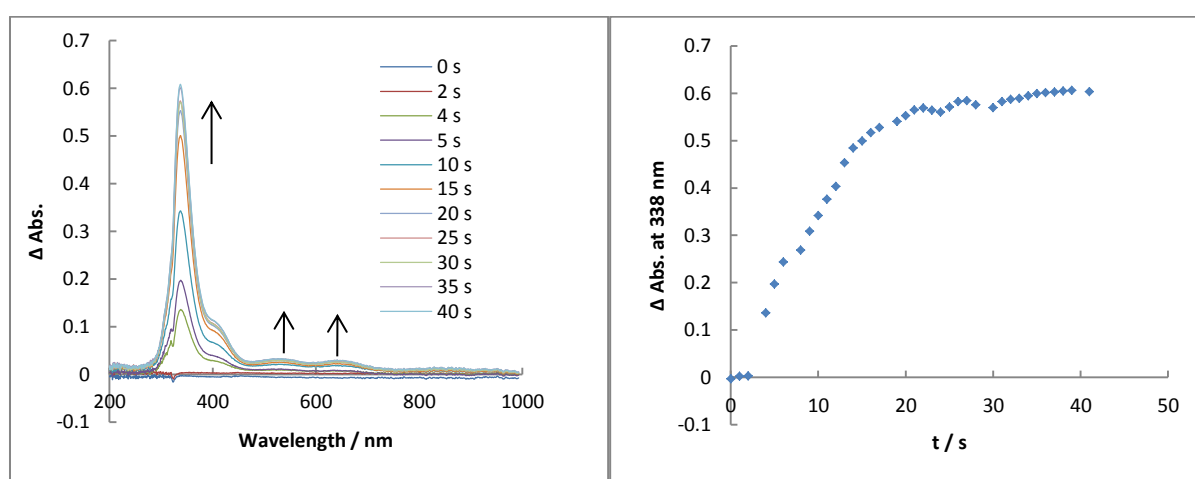


Figure 29: Left: UV-vis spectrum of addition of O_2 to the complex $(\mu\text{-NCCH}_3)\text{Cu}^{\text{I}}_2\text{Ox}_4$. Right: Absorption at 338 nm compared to time after addition of O_2 . Parameters: $l = 1\ \text{cm}$; solvent: acetone, concentration $0.094\ \text{mM}$, $T = 193\ \text{K}$. Baseline taken on the Cu^{I} complex before O_2 addition.

3. UV-vis spectra of the addition of O₂ to complex (μ-NCCH₃)Cu^I₂Py₂Ox₂

The UV-vis spectrum of the complex (μ-NCCH₃)Cu^I₂Py₂Ox₂ is shown in Figure 30 (left). The baseline was taken on acetone before the addition of the Cu^I complex. There are significant differences that are observed upon addition of O₂: there is new band that forms at 368 nm ($\epsilon = 2\,400\text{ M}^{-1}\cdot\text{cm}^{-1}$) and the loss of a band at 446 nm allowed the assignment of a $\mu\text{-}\eta^2\text{:}\eta^2\text{-peroxo-Cu}^{\text{II}}_2$ species upon addition of O₂.¹⁰¹ The Cu₂:O₂ species for complex (μ-NCCH₃)Cu^I₂Py₂Ox₂ forms slightly slower than that of complex (μ-NCCH₃)Cu^I₂Ox₄ with 95 % formed in 50 seconds (Figure 30, right).

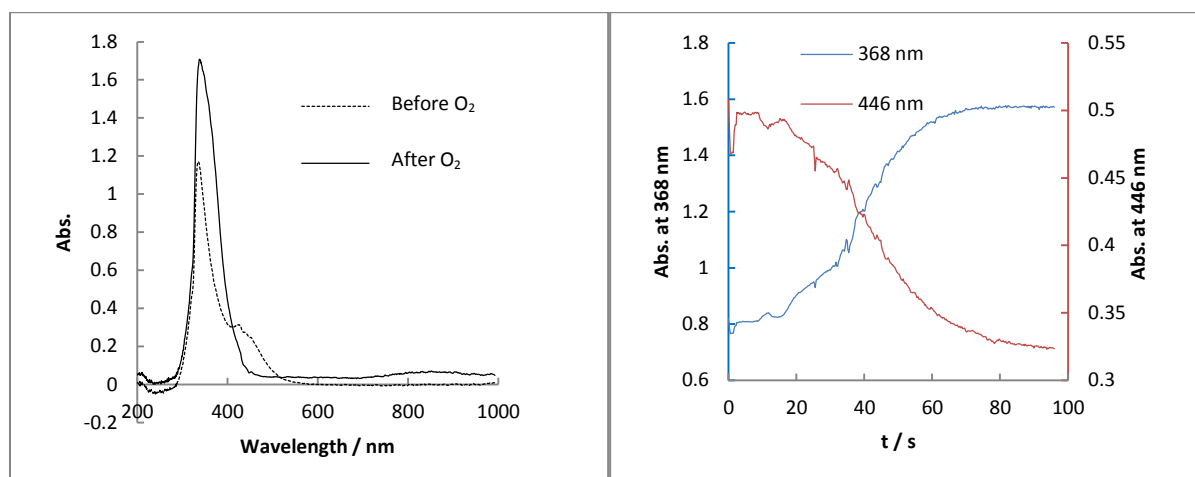


Figure 30: Left: UV-vis spectrum of addition of O₂ to the complex (μ-NCCH₃)Cu^I₂Py₂Ox₂. Right: Absorption at 368 and 446 nm compared to time. Parameters: $l = 1\text{ cm}$; solvent acetone; concentration 0.33 mM, $T = 193\text{ K}$, The baseline taken on acetone before the addition of the Cu^I₂ complex.

1.2.5.2. Stability of the Cu₂:O₂ species formed from the complexes (μ-NCCH₃)Cu^I₂Ox₄ and (μ-NCCH₃)Cu^I₂Py₂Ox₂.

Both of the Cu₂:O₂ species from the complexes (μ-NCCH₃)Cu^I₂Ox₄ and (μ-NCCH₃)Cu^I₂Py₂Ox₂ showed no sign of change to their UV-vis spectra over a 20 minute time frame at 193 K indicating that they are both relatively stable at this temperature. The temperature was therefore increased to 223 K to determine their stability and the changes were monitored by UV-vis. A plot of the absorbance at a wavelength of 338 and 368 nm vs. time are shown for the Cu₂:O₂ species from the complexes (μ-NCCH₃)Cu^I₂Ox₄ and (μ-NCCH₃)Cu^I₂Py₂Ox₂ respectively (Figure 31). The degradation of the Cu₂:O₂ species follow first order kinetics and plots to determine the first order rate constants are also shown.

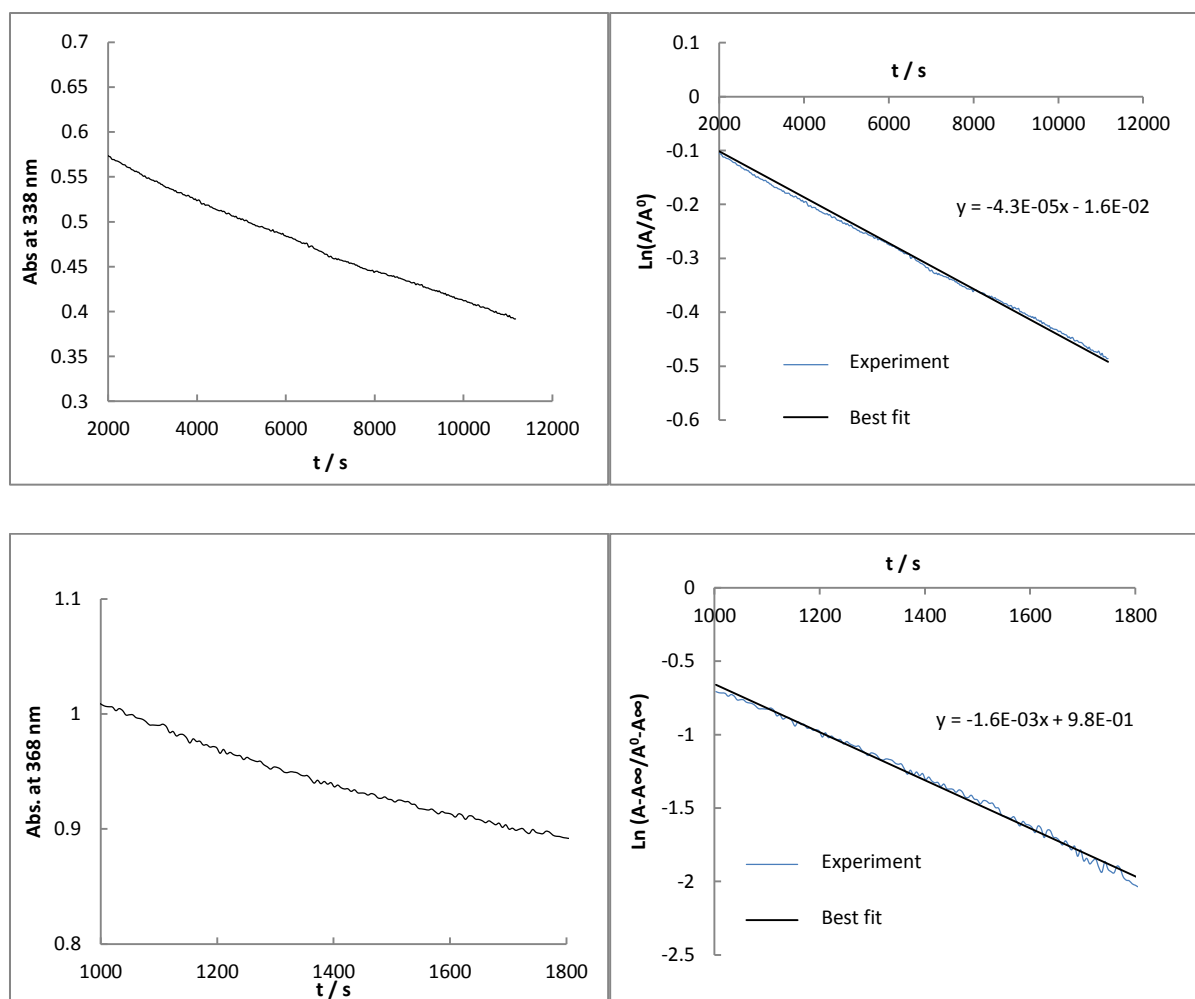


Figure 31: Top: The $\text{Cu}_2:\text{O}_2$ complex from $(\mu\text{-NCCH}_3)\text{Cu}^1_2\text{Ox}_4$. Top left: Absorbance at 338 against time. Top right: First order rate plot. Bottom: The $\text{Cu}_2:\text{O}_2$ complex from $(\mu\text{-NCCH}_3)\text{Cu}^1_2\text{Py}_2\text{Ox}_2$. Bottom left: Absorbance at 368 nm against time. Bottom right: first order rate plot. For the first order rate plots: A = absorbance of complex. $A^\infty = 0.85$ (absorbance at $t = \infty$). A^0 = initial absorbance. Parameters: $l = 1$ cm; $T = 223$ K; solvent: acetone; under an atmosphere of O_2 .

It took a certain amount of time for the temperature to stabilise at 223 K after increasing the temperature from 193 K, so the first section of the graph has been cut as it does not follow first order kinetics. For the $\text{Cu}_2:\text{O}_2$ species from the complex $(\mu\text{-NCCH}_3)\text{Cu}^1_2\text{Ox}_4$, the band at 338 nm decreases to zero at $t = \infty$, whereas the band at 368 nm for $\text{Cu}_2:\text{O}_2$ species $(\mu\text{-NCCH}_3)\text{Cu}^1_2\text{Py}_2\text{Ox}_2$ decreases to $A = 0.85$.

The first order rate plots (Figure 31, right) of the $\text{Cu}_2:\text{O}_2$ species exhibit gradients of $-4.3 \times 10^{-5} \text{ s}^{-1}$ and $-1.6 \times 10^{-3} \text{ s}^{-1}$ giving values of the first order rate constants of $4.3 \times 10^{-5} \text{ s}^{-1}$ and $1.6 \times 10^{-3} \text{ s}^{-1}$ for the $\text{Cu}_2:\text{O}_2$ species from complexes $(\mu\text{-NCCH}_3)\text{Cu}^1_2\text{Ox}_4$ and $(\mu\text{-NCCH}_3)\text{Cu}^1_2\text{Py}_2\text{Ox}_2$ respectively. From these values, the half-lives ($t_{1/2}$) of the $\text{Cu}_2:\text{O}_2$ species formed are $t_{1/2} = 16000 \text{ s}$ (4.5 hours) from $(\mu\text{-NCCH}_3)\text{Cu}^1_2\text{Ox}_4$ and are $t_{1/2} = 420 \text{ s}$ (7 minutes) from $(\mu\text{-NCCH}_3)\text{Cu}^1_2\text{Py}_2\text{Ox}_2$ indicating that the former

is factor of 40 times more stable at 223 K than the latter. This could be because the steric bulk of the ligand Ox_4 is far greater and therefore protects the $Cu_2:O_2$ core.

1.2.5.3. Resonance Raman spectroscopy of the $Cu_2:O_2$ species formed from the complexes $(\mu\text{-NCCH}_3)Cu^I_2Ox_4$ and $(\mu\text{-NCCH}_3)Cu^I_2Py_2Ox_2$

Resonance Raman spectroscopy is often the method of choice for assigning the type of $Cu_2:O_2$ species formed because the vibrational wavenumber obtained is directly related to the strength of the O-O bond. The degree of electron donation into the O-O π^* can therefore be determined. While bands on a Raman spectrum are usually relatively small, isotope labelling using the reaction of Cu^I with $^{18}O_2$ can be used, leading to a shift enabling the assignment of a band as an O-O vibration.

The resonance Raman (rR) spectroscopy of the frozen solution of the complexes $(\mu\text{-NCCH}_3)Cu^I_2Ox_4$ and $(\mu\text{-NCCH}_3)Cu^I_2Py_2Ox_2$ was therefore undertaken in order to further characterise the $Cu_2:O_2$ species formed from the complexes.^d A solutions of 5 mM in acetone of each complex was prepared using schlenk technique then cooled to 213 K before addition of O_2 then freezing in liquid nitrogen. The rR spectra were recorded using a laser of 355 nm.

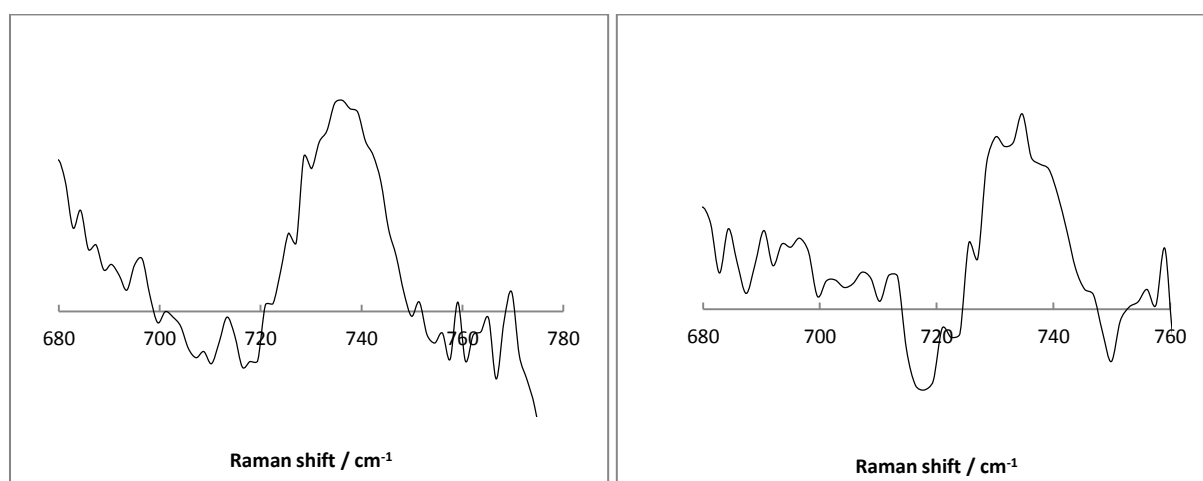


Figure 32: rR spectra of the frozen solution of the $Cu_2:O_2$ species generated by reaction of complexes $(\mu\text{-NCCH}_3)Cu^I_2Ox_4$ (left) and $(\mu\text{-NCCH}_3)Cu^I_2Py_2Ox_2$ (right) with O_2 at 213 K. Parameters: $T = 77$ K; laser wavelength = 355 nm; solvent: acetone; the spectrum of the frozen solution of acetone was subtracted from the spectra of $Cu_2:O_2$ species in frozen acetone.

The rR spectra of the $Cu_2:O_2$ species generated by reaction of complexes $(\mu\text{-NCCH}_3)Cu^I_2Ox_4$ and $(\mu\text{-NCCH}_3)Cu^I_2Py_2Ox_2$ with O_2 both display peaks at 735 cm^{-1} (Figure 32). These are typical values for $\mu\text{-}\eta^2:\eta^2\text{-peroxo-Cu}^{II}_2$ species for both complexes (see Table 5), which is in agreement with the UV-vis data. The very similar wavenumbers obtained from complexes $(\mu\text{-NCCH}_3)Cu^I_2Ox_4$ and $(\mu\text{-$

^d In collaboration with Prof. W. R. Browne.

NCCH₃)Cu^I₂Py₂Ox₂ indicate that the O-O bond strengths for the two $\mu\text{-}\eta^2\text{:}\eta^2\text{-peroxo-Cu}^{\text{II}}_2$ species are very similar.

Table 5: Typical Raman shifts for Cu₂:O₂ species. Values obtained from Stack *et al.*¹⁰⁶

Species	rR / cm ⁻¹
<i>trans</i> -1,2-peroxo- Cu ^{II} ₂	830
$\mu\text{-}\eta^2\text{:}\eta^2\text{-peroxo-Cu}^{\text{II}}_2$	740
bis($\mu\text{-O}$) Cu ^{III} ₂	600

1.2.6. Reactivity of the Cu₂:O₂ species with external substrates.

1.2.6.1. Screening for oxidation products: analysis by GCMS

The reactivity of the two $\mu\text{-}\eta^2\text{:}\eta^2\text{-peroxo-Cu}^{\text{II}}_2$ described in section 1.2.5 was tested with various substrates. The substrates PPh₃, benzaldehyde and 2,4-di-*tert*-butylphenol (and sodium 2,4-di-*tert*-butylphenolate) were selected: PPh₃ to determine if oxygen insertion occurs, benzaldehyde to determine if over-oxidation of an aldehyde occurs, and 2,4-di-*tert*-butylphenol(ate) to test for tyrosinase (or catechol oxidase) type arene hydroxylation and C-C coupling.

The complexes ($\mu\text{-NCCH}_3$)Cu^I₂Ox₄ and ($\mu\text{-NCCH}_3$)Cu^I₂Py₂Ox₂ were dissolved in acetone in the glove box to form a 0.3 mM solution, and were removed from the glove box in a schlenk. When under a pressure of Ar, the solutions were cooled to 193 K < T < 203 K. O₂ was bubbled through the solutions for 60 s, 5 - 10 equivalents of the substrate added and the solution was degassed by 5 cycles of vacuum/argon. The solutions were stirred at 193 K < T < 203 K for 30 min then allowed to rise to room temperature, filtered over silica to remove the copper complexes then analysed by GCMS.

In the case of the substrates PPh₃ and benzaldehyde, no oxidation products (OPPh₃, benzoic acid) were observed by GCMS in the case of either complex.

In the case of the substrates 2,4-di-*tert*-butylphenol and sodium-2,4-di-*tert*-butylphenolate, both Cu₂:O₂ complexes gave rise to the C-C coupling product 3,3',5,5'-tetra-*tert*-butyl-2,2'-biphenol (Scheme 34), detected by GCMS (the results from complex ($\mu\text{-NCCH}_3$)Cu^I₂Ox₄ are displayed in Figure 33). Neither catechol nor quinone products (from *ortho*-hydroxylation of the arene and further oxidation) were observed. In order to determine if the C-C coupling product was generated by the Cu₂:O₂, the starting Cu^I₂ complex or an analogue Cu^{II}₂ complex (see Part II Chapter 3 Section 3.2 for the synthesis), a series of control experiments were performed. For testing the Cu^I₂ complexes, a 0.3 mM solution of each of ($\mu\text{-NCCH}_3$)Cu^I₂Ox₄ and ($\mu\text{-NCCH}_3$)Cu^I₂Py₂Ox₂ were generated in acetone in the

glove box. 5-10 equivalents of 2,4-di-*tert*-butylphenol was added, and the solution was stirred at room temperature for half an hour, filtered over silica while still in the glove box before being analysed by GCMS. For the control experiments with the Cu^{II}₂ complexes Cu^{II}₂Ox₄ and Cu^{II}₂Py₂Ox₂, the same experiment was performed but outside the glove box. In the case of the Cu^{II}₂ complexes, no C-C coupling product was observed. However in the control experiments with the Cu^I₂ complexes, the C-C coupling product was observed, which could be due to small quantities of oxygen in the glove box.

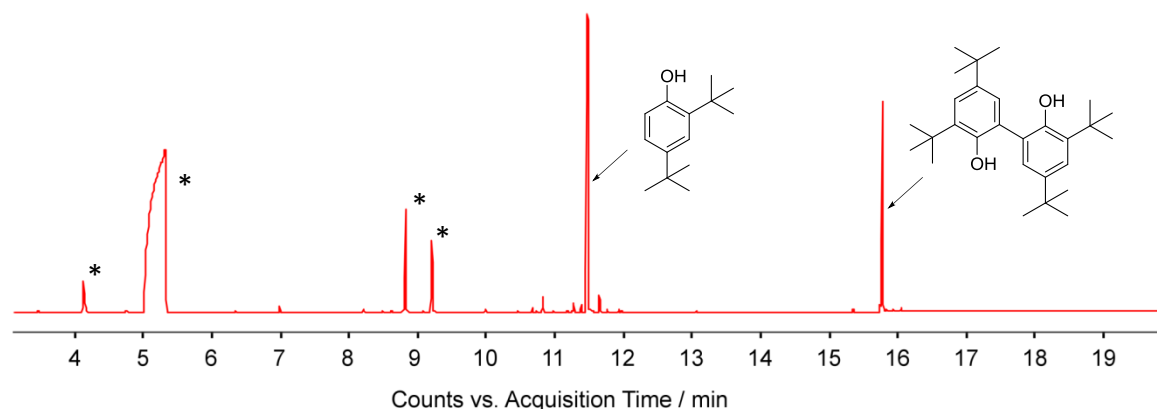
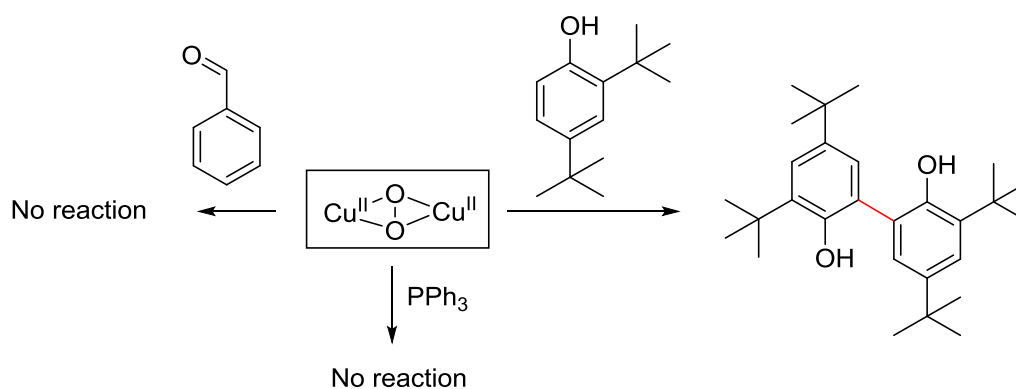


Figure 33: GCMS of the resulting solution after reaction of the $\mu\text{-}\eta^2\text{:}\eta^2\text{-peroxo-Cu}^{\text{II}}_2$ species from complex $(\mu\text{-NCCH}_3)\text{Cu}^{\text{I}}_2\text{Ox}_4$ with 2,4-di-*tert*-butylphenol at $193\text{ K} < T < 203\text{ K}$. Starred peaks are present in the acetone (the solvent used). Results from the complex $(\mu\text{-NCCH}_3)\text{Cu}^{\text{I}}_2\text{Py}_2\text{Ox}_2$ are very similar.



Scheme 34: Summary of the observed reactivity of the $\mu\text{-}\eta^2\text{:}\eta^2\text{-peroxo-Cu}^{\text{II}}_2$ species from complexes $(\mu\text{-NCCH}_3)\text{Cu}^{\text{I}}_2\text{Py}_2\text{Ox}_2$ and $(\mu\text{-NCCH}_3)\text{Cu}^{\text{I}}_2\text{Ox}_4$.

1.2.6.2. UV-vis of the $\mu\text{-}\eta^2\text{:}\eta^2\text{-peroxo-Cu}^{\text{II}}_2$ species upon addition of 2,4-di-*tert*-butylphenolate

In order to determine the kinetics of the reaction of the $\mu\text{-}\eta^2\text{:}\eta^2\text{-peroxo-Cu}^{\text{II}}_2$ species from the complexes $(\mu\text{-NCCH}_3)\text{Cu}^{\text{I}}_2\text{Py}_2\text{Ox}_2$ and $(\mu\text{-NCCH}_3)\text{Cu}^{\text{I}}_2\text{Ox}_4$ with 2,4-di-*tert*-butylphenolate, the reaction

was monitored by UV-vis at 193 K in acetone. A 22 mL, 0.13-0.14 mM solution of each of the complexes was prepared in the glove box then removed, placed under a pressure of Ar and cooled to 193 K before O₂ was bubbled for 60 s. The UV-vis spectra of the $\mu\text{-}\eta^2\text{:}\eta^2\text{-peroxo-Cu}^{\text{II}}_2$ species were taken before addition of the substrate. 3.4 equivalents of sodium-2,4-di-*tert*-butylphenolate was dissolved in 0,2 mL of acetone then added to the $\mu\text{-}\eta^2\text{:}\eta^2\text{-peroxo-Cu}^{\text{II}}_2$. The reaction was monitored by UV-vis using a fibre optic cable (FOC) inserted into the cell. The absorbance saturates with this cable below 350 nm in acetone, so the main peaks corresponding to the peroxo species are difficult to observe. This compounded by the fact that the band of the excess 2,4-di-*tert*-butylphenolate superimposes upon the bands characteristic for the Cu₂O₂ species renders the UV-vis results inconclusive.

1.2.7. Summary of Cu₂ complexes based on the ligands Ox₄ and Py₂Ox₂ and their reactivity with O₂

Two new Cu₂^I complexes based on the ligands Ox₄ and Py₂Ox₂ have been synthesised and characterised by ¹H-NMR (CD₃CN) and Raman spectroscopy in the solid state. The Raman spectra revealed the presence of bridging CH₃CN groups in the solid state, and in solution the ¹H-NMR spectra supported the presence of a dinuclear complex however the presence of the bridging group could not be confirmed. Interestingly, oxygenation of the Cu₂^I complexes in acetone at 193 K revealed the formation of a $\mu\text{-}\eta^2\text{:}\eta^2\text{-peroxo-Cu}^{\text{II}}_2$ species supported by UV-vis and rR in frozen solution in both cases, with very similar O-O bond strengths.

For both $\mu\text{-}\eta^2\text{:}\eta^2\text{-peroxo-Cu}^{\text{II}}_2$, there was no reactivity towards PPh₃ or benzaldehyde. Reaction of the $\mu\text{-}\eta^2\text{:}\eta^2\text{-peroxo-Cu}^{\text{II}}_2$ species from both complexes with 2,4-di-*tert*-butylphenol (or 2,4-di-*tert*-butylphenolate) resulted in the formation of the C-C coupling product detected by GCMS, however no insertion of oxygen to form the catechol or the quinone product occurred.

1.3. DFT calculations on the Cu₂:O₂ species from complexes ($\mu\text{-NCCH}_3$)Cu₂Ox₄, ($\mu\text{-NCCH}_3$)Cu₂Py₂Ox₂ and ($\mu\text{-NCCH}_3$)Cu₂Py₄

DFT calculations were performed to attempt to elucidate the differences in the reactivity between the Cu₂^I complexes and O₂: the complexes ($\mu\text{-NCCH}_3$)Cu₂Ox₄ and ($\mu\text{-NCCH}_3$)Cu₂Py₂Ox₂ both form $\mu\text{-}\eta^2\text{:}\eta^2\text{-peroxo-Cu}^{\text{II}}_2$ species whether as with the complex ($\mu\text{-NCCH}_3$)Cu₂Py₄ no peroxo species has been observed.

1.3.1. Theoretical optimised structures of the $\text{Cu}_2\text{:O}_2$ species from complexes $(\mu\text{-NCCH}_3)\text{Cu}^{\text{I}}_2\text{Ox}_4$, $(\mu\text{-NCCH}_3)\text{Cu}^{\text{I}}_2\text{Py}_2\text{Ox}_2$ and $(\mu\text{-NCCH}_3)\text{Cu}^{\text{I}}_2\text{Py}_4$

In order to determine if the lack of observation of a $\mu\text{-}\eta^2\text{:}\eta^2\text{-peroxo-Cu}^{\text{II}}_2$ from complex $(\mu\text{-NCCH}_3)\text{Cu}^{\text{I}}_2\text{Py}_4$ was due to thermodynamic reasons, the $\mu\text{-}\eta^2\text{:}\eta^2\text{-peroxo-Cu}^{\text{II}}_2$ species using the ligand from complex Py_4 was optimised by DFT. The same was repeated with the $\mu\text{-}\eta^2\text{:}\eta^2\text{-peroxo-Cu}^{\text{II}}_2$ species from ligands Ox_4 and Py_2Ox_2 to confirm the structure determined by experimental evidence. The functional BLYP was used, and the structures were optimised in the gas phase. The structures are shown in Figure 34, with a list of distances shown in Table 6.

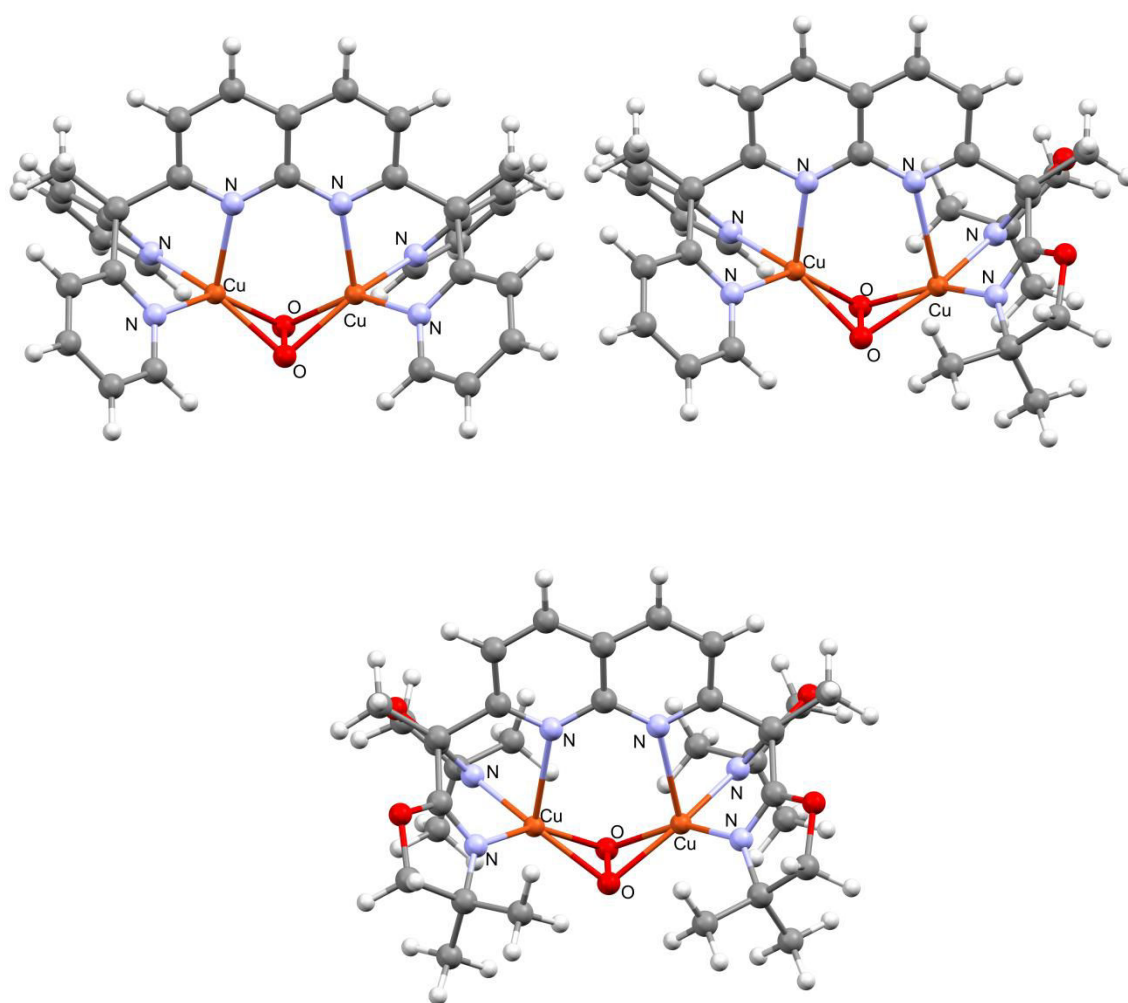


Figure 34: DFT structures of the optimised $\text{Cu}_2\text{:O}_2$ complexes bearing the ligands Py_4 (top left), Ox_2Py_2 (top right) and Ox_4 (bottom). Structures optimised in the gas phase using the functional BLYP.

Table 6: List of bond distances for the optimised DFT structures of $\mu\text{-}\eta^2\text{:}\eta^2\text{-peroxo-Cu}^{\text{II}}_2$ species from the ligands Py_4 (top left), Py_2Ox_2 (top right) and Ox_4 (bottom). Naph: naphthyridine, Py: pyridine and Ox: oxazoline.

Atom1	Atom2	Distance / Å
O	O	1.433
Cu	Cu	3.076
Cu	O	2.062
Cu	O	2.067
Cu	O	2.067
Cu	O	2.061
Cu	N _{naph}	2.259
Cu	N _{naph}	2.259
Cu	N _{py}	2.016
Cu	N _{py}	2.015
Cu	N _{py}	2.015
Cu	N _{py}	2.015

Atom1	Atom2	Distance / Å
O	O	1.431
Cu	Cu	3.170
Cu	O	2.079
Cu	O	2.052
Cu	O	2.083
Cu	O	2.050
Cu	N _{naph}	2.673
Cu	N _{naph}	2.225
Cu	N _{Ox}	2.030
Cu	N _{Ox}	2.027
Cu	N _{py}	2.003
Cu	N _{py}	2.004

Atom1	Atom2	Distance / Å
O	O	1.427
Cu	Cu	3.240
Cu	O	2.064
Cu	O	2.072
Cu	O	2.069
Cu	O	2.070
Cu	N _{naph}	2.593
Cu	N _{naph}	2.545
Cu	N _{Ox}	2.016
Cu	N _{Ox}	2.016
Cu	N _{Ox}	2.018
Cu	N _{Ox}	2.019

As can be seen in Figure 34, the $\text{Cu}_2\text{:O}_2$ structures for all three complexes could be optimised in the form of a non-planar $\mu\text{-}\eta^2\text{:}\eta^2\text{-peroxo-Cu}^{\text{II}}_2$ species, with none of the complexes showing a rupture of the O-O bond. Interestingly, the O-O bond distances are very similar in the three structures at 1.427 Å for the $\text{Cu}_2\text{:O}_2$ species from ligand Ox_4 , 1.431 Å from Py_2Ox_2 and 1.433 Å from ligand Py_4 (Table 6). The similar values for the calculated O-O bond distances for the $\mu\text{-}\eta^2\text{:}\eta^2\text{-peroxo-Cu}^{\text{II}}_2$ species from ligands Ox_4 and Py_2Ox_2 are consistent with experimental evidence: the rR shifts (a measure of O-O bond strength) are very similar for the two $\mu\text{-}\eta^2\text{:}\eta^2\text{-peroxo-Cu}^{\text{II}}_2$ species at 736 and 735 cm^{-1} respectively.

It is interesting that the O-O bonds in the structures of all three $\text{Cu}_2\text{:O}_2$ complexes are very similar (around 1.43 Å) despite relatively large differences in the bond distances between the Cu and

coordinating atoms. With Ox₄ as a ligand, the Cu-N_{naph} (where naph is the naphthyridine) distances are of 2.54 and 2.59 Å, whereas for the complex from the ligand Py₄ displays Cu-N_{naph} distances that are much shorter of 2.26 Å. The complex from the ligand Py₂Ox₂ displays two Cu-N_{naph} distances that are very different from one another: 2.26 Å for the Cu-N_{naph} the side of the pyridine groups and 2.67 for the Cu-N_{naph} on the side of the oxazoline groups. Most importantly the Cu-Cu distance in all three structures is different: 3.24 Å for the complex from ligand Ox₄, 3.17 Å from ligand Py₂Ox₂ and 3.08 Å from ligand Py₄. The significant changes to the distances of the structures but consistency in the O-O distance suggests that the electron donation from the ligand into the O-O π* orbital hardly changes in the differing structures.

1.4. Discussion

The complex (μ-NCCH₃)Cu^I₂Py₄ with a particular feature of having a short Cu-Cu distance was synthesised to attempt to generate a Cu₂:O₂ species by reaction with O₂ at low temperature. Upon reactivity with O₂ the UV-vis bands of the Cu^I₂ complex disappeared, indicating a change has occurred but no new bands appeared indicating that no Cu₂:O₂ species was stabilised. It is possible that this was due to the bridging CH₃CN group that prevents the binding of O₂ forcing the reaction to go *via* an outer-sphere electron transfer.

The synthesis of a complex without the CH₃CN bridge was therefore attempted and was crystallised with a bridging chloride but it is unclear whether the bridge remains intact in solution. Reactivity of this complex with O₂ in solution at low temperature also just led to the loss of UV-vis bands and no new intermediates observed.

It is therefore confusing that with two very similar ligands (Py₂Ox₂ and Ox₄) can both support μ-η²:η²-peroxo-Cu^{II}₂ species as demonstrated by UV-vis and rR spectroscopy, since they are structurally not so different from the ligand Py₄. All three ligands are based on the 1,8-naphthyridine unit and have branched arms of around the same length with coordinating N-atoms. Indeed DFT calculations showed that the μ-η²:η²-peroxo-Cu^{II}₂ from all three of these ligands can be optimised to a minimum, indicating no steric or electronic factors should prevent their formation. The factors preventing the observation of the Cu₂:O₂ species for the ligand Py₄ could be kinetic. It is possible that a Cu₂:O₂ species is formed, but that its rate of a further reaction (due to a lack of steric bulk protecting the core) is greater than its rate of formation, so no accumulation occurs.

It is unlikely that the bridging CH_3CN group prevents the formation of the $\text{Cu}_2:\text{O}_2$ species from the ligand Py_4 , because both other Cu^{I}_2 complexes from the ligands Py_2Ox_2 and Ox_4 have the bridging CH_3CN groups but are capable of forming $\mu\text{-}\eta^2\text{:}\eta^2\text{-peroxo-Cu}^{\text{II}}_2$ species. Furthermore the complex $\text{Cu}^{\text{I}}_2\text{Py}_4$ was synthesised without a CH_3CN bridge (and possible with a bridging chloride) did not form a $\text{Cu}_2:\text{O}_2$ species.

1.5. Conclusions and perspectives

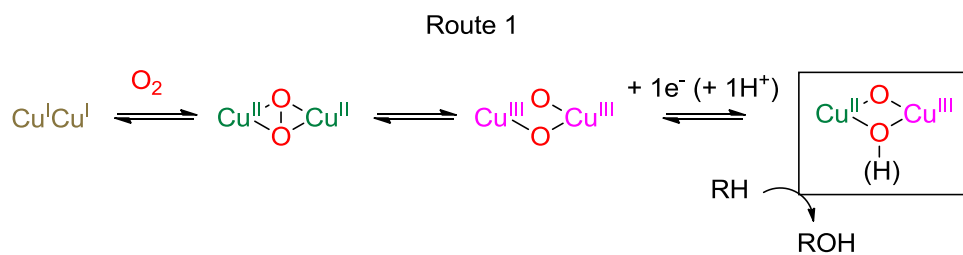
The Cu^{I}_2 complex $(\mu\text{-NCCH}_3)\text{Cu}^{\text{I}}_2\text{Py}_4$ initially chosen to generate a $\text{Cu}_2:\text{O}_2$ by low temperature reaction with O_2 did not lead to the accumulation of any $\text{Cu}_2:\text{O}_2$ intermediates. A new complex based on the same ligand but without the bridging acetonitrile group was therefore synthesised and its reactivity with O_2 tested. This complex also did not demonstrate the accumulation of a $\text{Cu}_2:\text{O}_2$ species.

Two new ligands based on the same 1,8-naphthyridine bridging group were therefore synthesised but this time with different moieties: one symmetric ligand with two bis-oxazoline entities and one dissymmetric ligand with a bis-oxazoline on one side and a bi-pyridine on the other. Oxazoline groups were chosen as it was hoped that their steric bulk would stabilise the $\text{Cu}_2:\text{O}_2$ species, and the dissymmetric ligand was chosen due to the possibility of forming a mixed valent $\text{bis}(\mu\text{-O})\text{Cu}^{\text{II}}\text{Cu}^{\text{III}}$ upon mono-reduction of a $\text{Cu}_2:\text{O}_2$ species as a dissymmetric ligand would differentiate the reduction potentials of the two copper ions. Both ligands were shown to support a $\mu\text{-}\eta^2\text{:}\eta^2\text{-peroxo-Cu}^{\text{II}}_2$ species, characterised by *rR* and UV-vis. *rR* spectroscopy of the $\mu\text{-}\eta^2\text{:}\eta^2\text{-peroxo-Cu}^{\text{II}}_2$ species using $^{18}\text{O}_2$ should be completed to confirm this result. Interestingly the half-life of the $\mu\text{-}\eta^2\text{:}\eta^2\text{-peroxo-Cu}^{\text{II}}_2$ supported by ligand Ox_4 is 40 times longer than that of the $\mu\text{-}\eta^2\text{:}\eta^2\text{-peroxo-Cu}^{\text{II}}_2$ supported by the ligand Py_2Ox_2 at 223 K, suggesting that the increased steric bulk of the ligand Ox_4 could help to stabilise the $\mu\text{-}\eta^2\text{:}\eta^2\text{-peroxo-Cu}^{\text{II}}_2$ species. Spectroelectrochemistry of both of these $\mu\text{-}\eta^2\text{:}\eta^2\text{-peroxo-Cu}^{\text{II}}_2$ species should be attempted to see if any related $\text{Cu}_2:\text{O}_2$ species could be generated, particularly the $\text{bis}(\mu\text{-O})\text{Cu}^{\text{II}}\text{Cu}^{\text{III}}$ species which could be formed upon mono-reduction.

The reactivity of the $\mu\text{-}\eta^2\text{:}\eta^2\text{-peroxo-Cu}^{\text{II}}_2$ species from ligands Ox_4 and Py_2Ox_2 was limited. No reactivity was observed with PPh_3 or with benzaldehyde. However both $\mu\text{-}\eta^2\text{:}\eta^2\text{-peroxo-Cu}^{\text{II}}_2$ reacted with 2,4-di-*tert*-butylphenol (and sodium-2,4-di-*tert*-butylphenolate) to form the C-C coupling product, but no insertion of oxygen was observed.

This work has demonstrates that the 1,8-naphthyridine spacer can support $\mu\text{-}\eta^2\text{:}\eta^2\text{-peroxo-Cu}^{\text{II}}_2$ species at low temperature. While the $\mu\text{-}\eta^2\text{:}\eta^2\text{-peroxo-Cu}^{\text{II}}_2$ species is well documented, the $\mu\text{-}\eta^2\text{:}\eta^2\text{-peroxo-Cu}^{\text{II}}_2$ complexes reported in this work provide a stepping stone for the generation of other

$\text{Cu}_2\text{:O}_2$ species, either by changing the redox states or by observing the effect of protonation (e.g. Route 1 introduced in Part I Chapter 3, see Scheme 35).

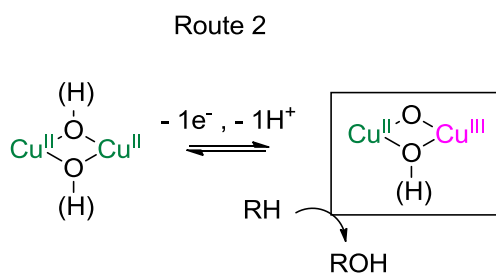


Scheme 35: Synthetic route 1: generation of a mixed valent $\text{Cu}^{\text{II}}\text{Cu}^{\text{III}}$ species *via* the activation of O_2 .

2. Synthesis and characterisation of dissymmetric complexes with the aim of generating mixed valent Cu^{II}Cu^{III} species.

2.1. Introduction

For the generation of localised mixed valent Cu^{II}Cu^{III} systems, the stabilisation of two different oxidation states of the copper is important. In this chapter our efforts have therefore been focussed on the synthesis of dissymmetric ligands with two differentiated binding sites that exhibit markedly distinct affinities: one site suited for the Cu^{II} redox state and the other for stabilising the Cu^{III} redox state. Attempts at generating the mono-oxidised species starting from Cu^{II}₂ complexes (Scheme 36) through synthetic route 2 are also discussed.

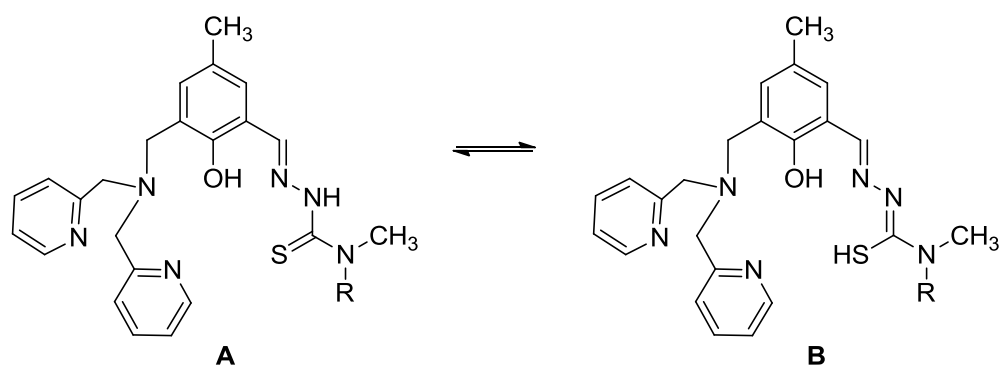


Scheme 36: Generation of a mixed valent Cu^{II}Cu^{III} species *via* synthetic route 2, introduced in Part 1 Chapter 3 Section 3.2.

2.2. Previous complexes based on a phenoxido spacer

Previous attempts in our lab have made use of complexes based on compartmental ligands with a phenoxido spacer bearing two different coordination sites. Cu^{II}₂ complexes based on this ligand system displayed interesting structural properties when the solid and solution structures are compared. The effect of mono-electronic oxidation was also investigated, which gave useful insight into the choice of the spacer used for most of the work presented in this chapter. A brief summary of work based on complexes with a phenoxido spacer is therefore included.

The chosen ligands both contain a bis(2-methylpyridyl)aminomethyl (BPA) arm suited for Cu^{II} and a thiosemicarbazone (TSC) moiety which can exist in two tautomeric forms (Scheme 37), of which the deprotonated form **B** is suited to stabilise the Cu^{III} redox state. Both ligands contain a phenoxido spacer, and differ only by a single methyl group on the TSC moiety.



Scheme 37: Two possible tautomers displayed by the ligands with a phenoxido spacer. R = H or CH₃.

2.2.1. Structures of complexes based on a phenoxido spacer

The structures of two complexes with their respective ligands are shown below in Figure 35 and Figure 36 with bond distances and angles displayed in Table 7 and Table 8.

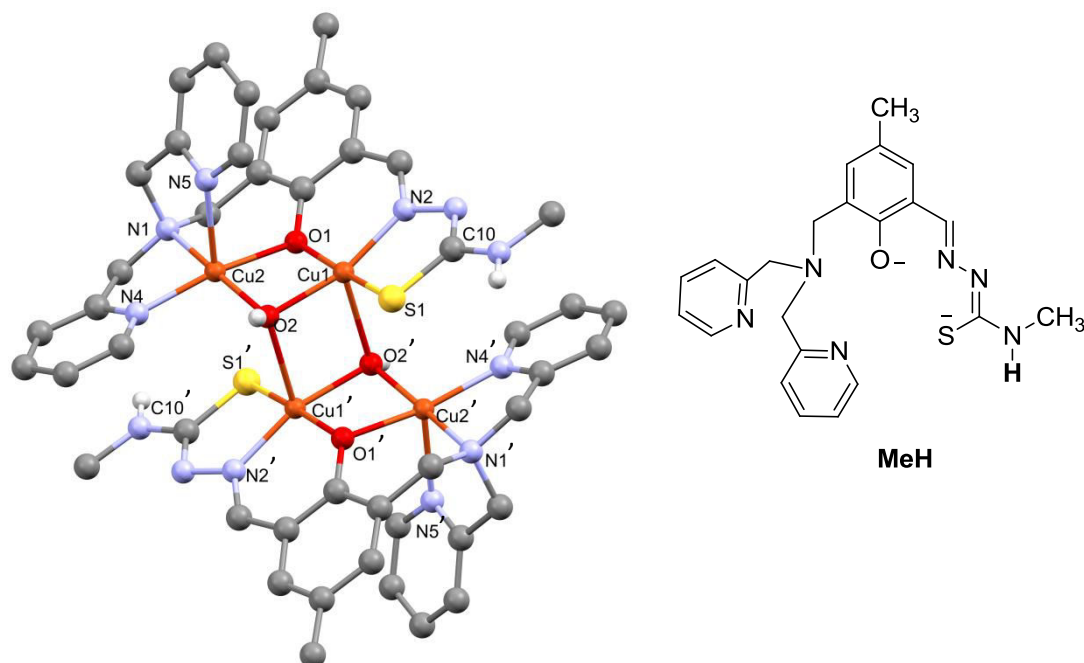


Figure 35: Molecular structure of the dication of $[\text{Cu}^{\text{II}}_4(\text{MeH})_2(\text{OH})_2](\text{OTf})_2$, named as $\text{Cu}^{\text{II}}_4(\text{MeH})_2$. Hydrogen atoms (except for the hydroxido bridge and the secondary amine of the TSC moiety), solvent molecules and triflate ions were removed for clarity. CCDC1520304.

Table 7: Bond distances and angles for the complex $\text{Cu}_4^{\text{II}}(\text{MeH})_2$.

Atom1	Atom2	Length / Å	Bond angle	Angle / °
Cu1	S1	2.241(1)	S1-Cu1-O2	97.65(6)
Cu1	O2	1.962(2)	S1-Cu1-O1	173.11(6)
Cu1	O1	1.959(2)	S1-Cu1-N2	86.53(7)
Cu1	N2	1.939(2)	S1-Cu1-O2	93.97(5)
Cu1	O2	2.409(2)	O2-Cu1-O1	81.11(7)
Cu2	O2	1.934(2)	O2-Cu1-N2	164.13(9)
Cu2	O1	2.007(2)	O2-Cu1-O2'	83.12(7)
Cu2	N1	2.018(2)	O1-Cu1-N2	92.90(8)
Cu2	N4	1.979(2)	O1-Cu1-O2	92.61(7)
Cu2	N5	2.253(2)	N2-Cu1-O2	111.96(8)
S1	C10	1.747(3)	O2-Cu2-O1	80.57(7)
O2'	Cu1	2.409(2)	O2-Cu2-N1	171.91(8)
			O2-Cu2-N4	100.52(9)
			O2-Cu2-N5	104.10(8)
			O1-Cu2-N1	94.27(8)
			O1-Cu2-N4	166.99(9)
			O1-Cu2-N5	85.96(8)
			N1-Cu2-N4	83.12(9)
			N1-Cu2-N5	81.59(9)
			N4-Cu2-N5	106.16(9)

The crystal structure of complex $\text{Cu}_4^{\text{II}}(\text{MeH})_2$ is tetranuclear (Figure 35), containing two symmetry-related dinuclear units linked to form the tetranuclear entity. In each dinuclear unit, the two copper atoms Cu1 and Cu2 are at a distance of 2.96 Å from each other. The copper at the TSC site (Cu1) is pentacoordinated in square based pyramidal geometry (τ parameter equal to 0.15).¹⁵³ In the equatorial plane, Cu1 is coordinated to the phenoxido oxygen O1, the hydroxido bridge O2, the sulphur S1 and the nitrogen N2. The axial position is occupied by the oxygen atom O2' from the hydroxido bridge of the other dinuclear entity. The copper at the BPA site (Cu2) is coordinated in a square-based pyramidal geometry (τ parameter equal to 0.08).¹⁵³ In the axial position the Cu2 is bound to the pyridine nitrogen N5 and the equatorial positions are occupied by the phenoxido oxygen O1, the tertiary amine N1, the pyridine nitrogen N4, and the bridging hydroxido O2. In addition, a weak interaction between the Cu2 and the sulphur S1' from the other dinuclear unit is observed at 3.14 Å along the Jahn-Teller distortion axis. The C10–S1 bond distance (1.75 Å) is comparable to that of the equivalent distance in crystal structure of the ligand (1.77 Å) in the thiol form (**B**, Scheme 37) and significantly longer than the one observed in the thione form **A** (1.63 Å).¹³¹ This is consistent with the increased single bond character expected for the ligand in the thiolate form (generated after deprotonation of the SH function in basic medium).

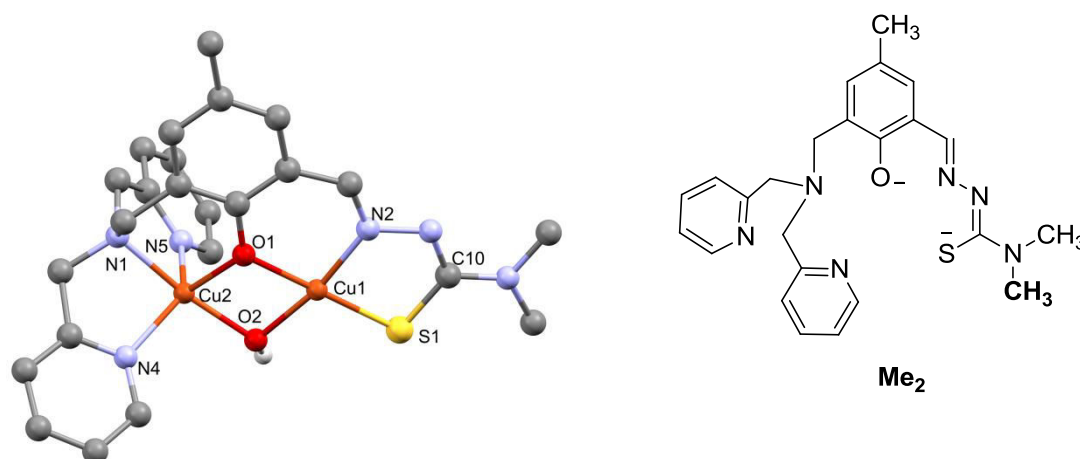


Figure 36: Molecular structure of cation of $[\text{Cu}^{\text{II}}_2(\text{Me}_2)(\text{OH})](\text{OTf})$, named as $\text{Cu}^{\text{II}}_2(\text{Me}_2)$. Hydrogen atoms (except on the hydroxido bridge) and solvent molecules have been removed for clarity. CCDC1520306.

Table 8: Bond distances and angles for the complex $\text{Cu}^{\text{II}}_2(\text{Me}_2)$.

Atom1	Atom2	Length / Å
Cu1	S1	2.211(1)
Cu1	O2	1.930(2)
Cu1	O1	1.936(2)
Cu1	N2	1.926(2)
Cu2	O2	1.905(2)
Cu2	O1	2.058(2)
Cu2	N1	2.020(2)
Cu2	N5	2.041(3)
Cu2	N4	2.013(2)
S1	C10	1.749(3)

Bond angle	Angle / °
S1-Cu1-O2	99.89(6)
S1-Cu1-O1	178.92(6)
S1-Cu1-N2	87.94(7)
O2-Cu1-O1	79.45(8)
O2-Cu1-N2	170.19(9)
O1-Cu1-N2	92.63(9)
O2-Cu2-O1	77.03(8)
O2-Cu2-N1	168.11(9)
O2-Cu2-N5	103.09(9)
O2-Cu2-N4	100.68(9)
O1-Cu2-N1	91.22(9)
O1-Cu2-N5	109.44(9)
O1-Cu2-N4	119.64(9)
N1-Cu2-N5	82.4(1)
N1-Cu2-N4	83.4(1)
N5-Cu2-N4	129.0(1)

The crystal structure of complex $\text{Cu}^{\text{II}}_2\text{Me}_2$ is dinuclear, where the two copper atoms are separated by 2.98 Å, a distance slightly longer than the tetranuclear complex $\text{Cu}^{\text{II}}_4(\text{MeH})_2$ (2.96 Å). The two copper atoms are doubly bridged by the phenoxido and the hydroxido groups. In contrast to the tetranuclear complex $\text{Cu}^{\text{II}}_4(\text{MeH})_2$ where all the copper ions have a similar distorted square based pyramidal geometry, in $\text{Cu}^{\text{II}}_2\text{Me}_2$ the two-ligand compartments provide dissimilar coordination environments and thereby induce different coordination geometries for each copper. Even though the number and type of coordinating atoms are the same (the tertiary amine, the two pyridines,

phenoxido and hydroxido groups) in $\text{Cu}^{\text{II}}_4(\text{MeH})_2$ and $\text{Cu}^{\text{II}}_2(\text{Me}_2)$, the Cu2 in the dinuclear complex has a geometry best described as a distorted trigonal bipyramid (TBP) rather than a square based pyramid (τ parameter equal to 0.65),¹⁵³ with N4, N5, and O1 atoms in the basal plane and N1 and O2 atoms in the axial positions. The Cu1 in $\text{Cu}^{\text{II}}_2\text{Me}_2$ is tetracoordinated by oxygen atoms from phenoxido and hydroxido bridges and N2 and S1 atoms from the TSC arm, forming a distorted square planar geometry around Cu1. Similarly, for complex $\text{Cu}^{\text{II}}_4(\text{MeH})_2$, the S1-C10 bond distance (1.75 Å) is in accordance with a thiolate form.

2.2.2. Solution studies of complexes $\text{Cu}^{\text{II}}_4(\text{MeH})_2$ and $\text{Cu}^{\text{II}}_2\text{Me}_2$

In CH_3CN , the complex $\text{Cu}^{\text{II}}_4(\text{MeH})_2$ displays UV-Vis transitions at 320 ($\epsilon \sim 32\,000\ \text{M}^{-1}\ \text{cm}^{-1}$), 332 ($\epsilon \sim 31\,000\ \text{M}^{-1}\ \text{cm}^{-1}$) and 384 ($\epsilon \sim 30\,000\ \text{M}^{-1}\ \text{cm}^{-1}$) nm. A slight red shift of the absorbance bands is observed for $\text{Cu}^{\text{II}}_2\text{Me}_2$ with transitions at 326 ($\epsilon \sim 16\,000\ \text{M}^{-1}\ \text{cm}^{-1}$), 338 ($\epsilon \sim 16\,000\ \text{M}^{-1}\ \text{cm}^{-1}$) and 390 ($\epsilon \sim 18\,000\ \text{M}^{-1}\ \text{cm}^{-1}$) nm. The transitions around 380–390 nm were assigned to LMCT from sulphur to Cu^{II} as observed in copper complexes derived from TSC sulphur-donor ligands.¹⁵⁴ Double humped bands around 330 nm may correspond to the hydroxido and phenoxido LMCT to Cu^{II} .^{155,156} In addition, d–d transitions are observed at 790 ($\epsilon \sim 350\ \text{M}^{-1}\ \text{cm}^{-1}$) and 760 ($\epsilon \sim 185\ \text{M}^{-1}\ \text{cm}^{-1}$) nm for $\text{Cu}^{\text{II}}_4(\text{MeH})_2$ and $\text{Cu}^{\text{II}}_2\text{Me}_2$ respectively.

Complexes $\text{Cu}^{\text{II}}_4(\text{MeH})_2$ and $\text{Cu}^{\text{II}}_2\text{Me}_2$ in frozen solution (1 mM at 100 K, CH_3CN) are EPR silent which is in agreement with a $S = 0$ spin state between the two Cu^{II} atoms for both complexes.

The ESI-MS of $\text{Cu}^{\text{II}}_4(\text{MeH})_2$ recorded in CH_3CN displays a peak centred at $m/z = 1301$ assigned to $[\text{Cu}^{\text{II}}_4(\text{MeH})_2 - \text{OTf}]^+$ consistent with the presence of the tetranuclear species in solution as well as a peak at $m/z = 575$ assigned to the mono-charged fragment $[(\text{Cu}^{\text{II}}_2\text{MeH}) - \text{OTf}]^+$. While the latter may originate from fragmentation under the ESI-MS conditions, this likely suggests that both the tetranuclear and the corresponding dinuclear species are present in solution. The ESI mass spectrum from $\text{Cu}^{\text{II}}_2\text{Me}_2$ in CH_3CN exhibits only a peak at $m/z = 589$ corresponding to the $[\text{Cu}^{\text{II}}_2\text{Me}_2 - \text{OTf}]^+$ ion. All isotope patterns matched the simulated ones.

2.2.2.1. $^1\text{H-NMR}$ of complexes $\text{Cu}^{\text{II}}_4(\text{MeH})_2$ and $\text{Cu}^{\text{II}}_2\text{Me}_2$

The paramagnetic $^1\text{H-NMR}$ of complexes $\text{Cu}^{\text{II}}_2\text{Me}_2$ and $\text{Cu}^{\text{II}}_4(\text{MeH})_2$ in CD_3CN are displayed in Figure 37. Peaks were assigned based on the integrals and correlation spectroscopy (COSY) cross

signals, and the peaks at -45 and -48 ppm were assigned to the bridging OH groups exchangeable with a drop of D₂O leading to their disappearance.

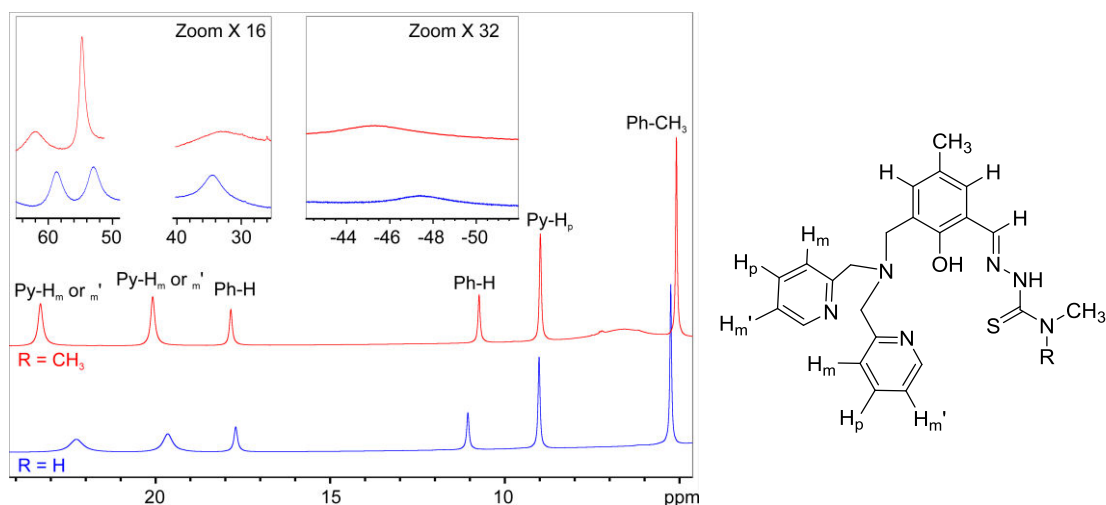


Figure 37: Left: Portions of ¹H NMR spectra of complex Cu^{II}₄(MeH)₂ (R = H, blue) and complex Cu^{II}₂Me₂ (R = CH₃, red) CD₃CN, from +25 to +5 ppm, and with insets from +65 to +25 ppm (top left) and -43 to -45 ppm (top centre). Right: diagrammatic representation of the corresponding ligands.

The ¹H-NMR spectra of the complexes Cu^{II}₂Me₂ and Cu^{II}₄(MeH)₂ are very similar in acetonitrile, the main difference being the broadness of the peaks assigned to Py-H_m or Py-H_{m'} in the complex Cu^{II}₄(MeH)₂ suggesting a possible fast exchange.

The ESI-MS spectra of the complex Cu^{II}₄(MeH)₂ in acetonitrile revealed the presence of tetranuclear and dinuclear entities in solution. In order to determine whether the dissociation occurred in solution, the diffusion ordered spectroscopy (DOSY) of the complex Cu^{II}₄(MeH)₂ was obtained in CD₃CN at 233 K (Figure 38).

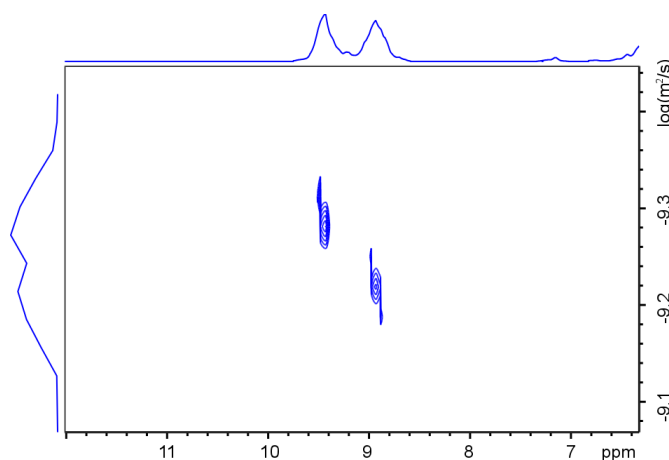


Figure 38: DOSY spectra of the complexes Cu^{II}₄(MeH)₂ in CH₃CN recorded at 233 K.

At 233 K two peaks are observable at around 9 ppm on the DOSY NMR spectrum of $\text{Cu}^{\text{II}}_4(\text{MeH})_2$ (Figure 38), in contrast to a single peak observed on the ^1H -NMR spectrum at room temperature (Figure 37). Diffusion coefficient measurements at 233 K provided two different values ($6.0 \times 10^{-10} \text{ m}^2 \cdot \text{s}^{-1}$ and $4.4 \times 10^{-10} \text{ m}^2 \cdot \text{s}^{-1}$) indicating the unambiguous existence of two species in solution.

2.2.3. DFT studies of the mono-oxidised species from complex $\text{Cu}^{\text{II}}_2(\text{Me}_2)$

DFT calculations were undertaken to determine the nature of the (dinuclear) mono-oxidised species of $\text{Cu}^{\text{II}}_2(\text{Me}_2)$, to see if a $\text{Cu}^{\text{II}}\text{Cu}^{\text{III}}$ species could be generated. Upon mono-electronic oxidation however, the complex displayed oxidation on the ligand instead of the copper, with electron spin density for the oxidised state being delocalised on the phenoxido bridge and the TSC side arm (Figure 39). This indicated the importance of using ligands that are relatively redox inert for attempting to generate $\text{Cu}^{\text{II}}\text{Cu}^{\text{III}}$ species. The results from this part have recently been published.^e

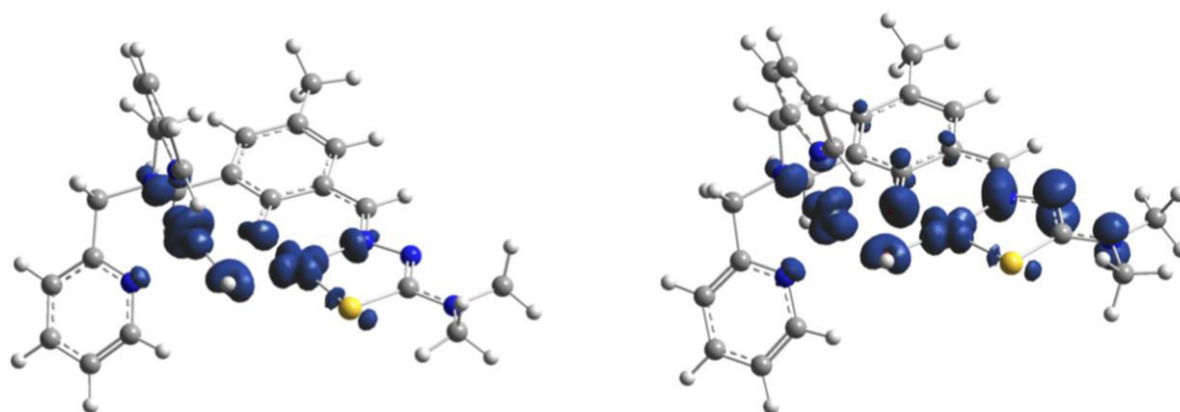


Figure 39 : Spin density plot for the high spin state of complex $\text{Cu}^{\text{II}}_2\text{Me}_2$ (left) and its mono-oxidised species (right).¹³¹

2.3. Synthons used for the generation of dissymmetric ligands and complexes with a naphthyridine spacer

2.3.1. Choice of the type of ligand for the work presented in this chapter

The 1,8-naphthyridine unit, presented in Part 2 Chapter 1, was therefore selected as it is relatively redox inert in oxidation. The bis pyridine arm was used on one side to stabilise the Cu^{II}

^e Isaac, J. A.; Mansour, A.-T.; David, R.; Kochem, A.; Philouze, C.; Demeshko, S.; Meyer, F.; Réglier, M.; Simaan, A. J.; Caldarelli, S.; Yemloul, M.; Jamet, H.; Thibon-Pourret, A.; Belle, C. *Dalton Trans.* **2018**, 47 (29), 9665.

oxidation state, and a negatively charged moiety was used on the other side to stabilise the Cu^{III} oxidation state (Figure 40).

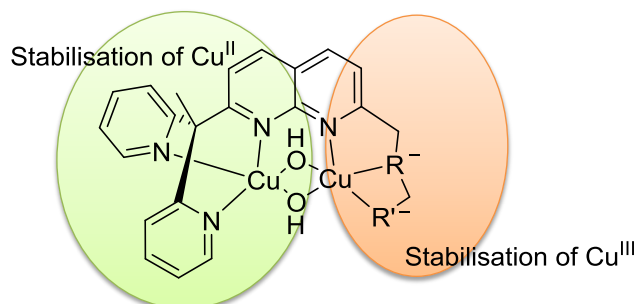
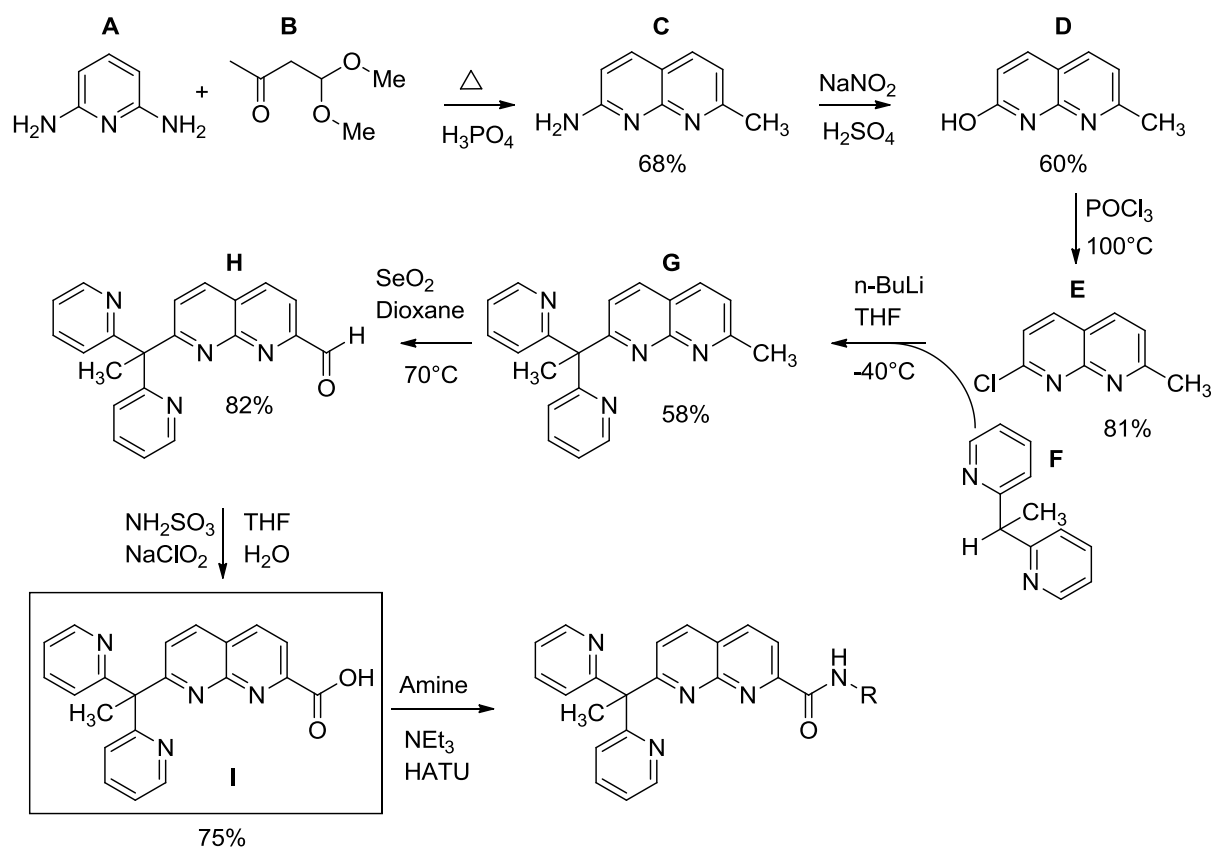


Figure 40: Strategy used in this chapter to stabilise Cu^{II}/Cu^{III} species.

2.3.2. Choice of synthon

The key intermediate **I** has been selected as the synthon from which different ligands will be synthesised (Scheme 38). This synthon allows several different arms to be added with only one new synthetic step. Another advantage is that upon reaction of the synthon **I** with amines, an amide will be formed which can be deprotonated when coordinated to copper and therefore will stabilise a higher oxidation state of the metal.

The synthesis of **I** is completed in six steps (Scheme 38) with the first three synthetic steps (up to **E**) following a published literature procedure.¹⁵⁷ 1.0 eq of 2,6-diaminopyridine (**A**) was mixed with 1.3 eq of 3-ketobutanal dimethylacetal (**B**) in concentrated phosphoric acid at 90 °C, forming the cyclised product **C**. Diazotisation of the product **C** in acidic media with sodium nitrite and then hydrolysis formed the alcohol **D**. **E** was produced by a chlorination reaction of **D** in excess POCl₃ at 100°C. **G** was synthesised using a procedure adapted from Tilley *et al.* involving lithiation of **F** (1.1 eq) at -40°C followed by addition of **E**.¹³³ Oxidation of the methyl group of **G** to the aldehyde was completed using 1.4 eq of selenium dioxide in dioxane at 70°C,¹⁵⁸ followed by further oxidation to the carboxylic acid using sulfamic acid and sodium chlorite in a mixture of THF and water. The ligands in this chapter are then synthesised by adding the coupling agent hexafluorophosphate azabenzotriazole tetramethyl uronium (HATU) to the synthon **I** in the presence of triethylamine (NEt₃) followed by the respective amine. The products of all steps were neutralised and extracted in DCM. Only the products **G** and the ligand required further purification by column chromatography.



Scheme 38: Synthetic pathway for the key intermediate **I** which is used to prepare the dissymmetric ligands of this chapter.

2.4. Complexes with an aniline moiety

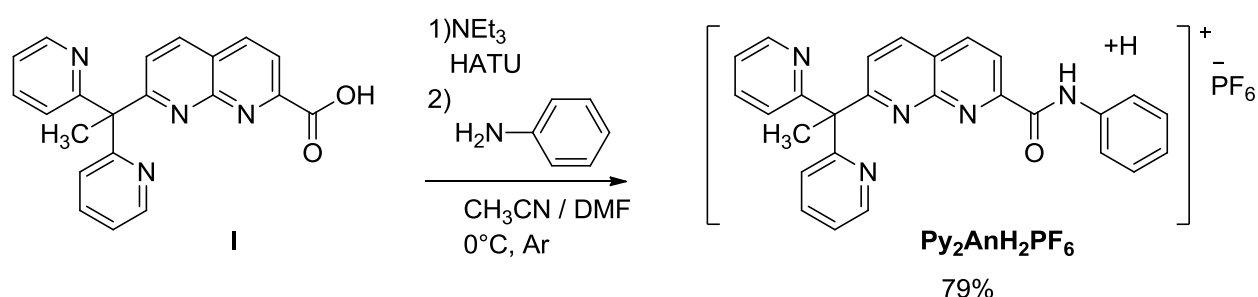
2.4.1. The ligand $\text{Py}_2\text{AnH}_2\text{PF}_6$

2.4.1.1. Choice of the ligand $\text{Py}_2\text{AnH}_2\text{PF}_6$

The chosen ligand $\text{Py}_2\text{AnH}_2\text{PF}_6$ is displayed in its protonated form in Scheme 39. Aniline was chosen as an arm as it is a simple amine that would be a good first test for complexes with this system. It is partly inspired by Tolman *et al.*¹²⁶ who used a cyclic ligand with an amide bonds linked to aromatics on either side to generate the mixed valent $\text{Cu}^{\text{II}}\text{Cu}^{\text{III}}$ species (see Part I Chapter 2, complex **44**), and the motif has also been used to stabilise mononuclear Cu^{III} complexes (e.g. Part I Chapter 2 complex **12**). The down side of aniline is that it is redox active, however the negative charge of the deprotonated amide could stabilise the Cu^{III} state and so that mono oxidation of the Cu^{II}_2 complex would occur on the copper instead of the ligand, generating a $\text{Cu}^{\text{II}}\text{Cu}^{\text{III}}$ species.

2.4.1.2. Synthesis of the ligand $\text{Py}_2\text{AnH}_2\text{PF}_6$

The ligand $\text{Py}_2\text{AnH}_2\text{PF}_6$ was synthesised with a yield of 79 % from the synthon I. 1.3 eq of HATU was added to the synthon I with 9 eq of NEt_3 followed by the addition of 1.3 eq of aniline in a mixture of DMF and CH_3CN under an inert atmosphere at 0°C . The product was extracted in DCM and purified by column chromatography.



Scheme 39: Synthesis of the ligand $\text{Py}_2\text{AnH}_2\text{PF}_6$.

2.4.2. Complexes from the ligand $\text{Py}_2\text{AnH}_2\text{PF}_6$

2.4.2.1. Synthesis and solid state characterisation of complexes from the ligand $\text{Py}_2\text{AnH}_2\text{PF}_6$

$\text{Py}_2\text{AnH}_2\text{PF}_6$ was added to 2.1 eq of $\text{Cu}^{\text{II}}\text{OTf}_2$ and an excess of NEt_3 in THF, forming a green precipitate that was isolated. The green precipitate was crystallised by slow diffusion of di-isopropyl ether (DIPE) into a solution of methanol yielding a few crystals. The structure is displayed in Figure 41. The green powder was also dissolved in CH_3CN and a 10 fold excess of NaClO_4 was added to change the counterion. A green precipitate was obtained that was isolated, and slow diffusion of DIPE into a solution of DMF yielded a few crystals with structure displayed in Figure 42.

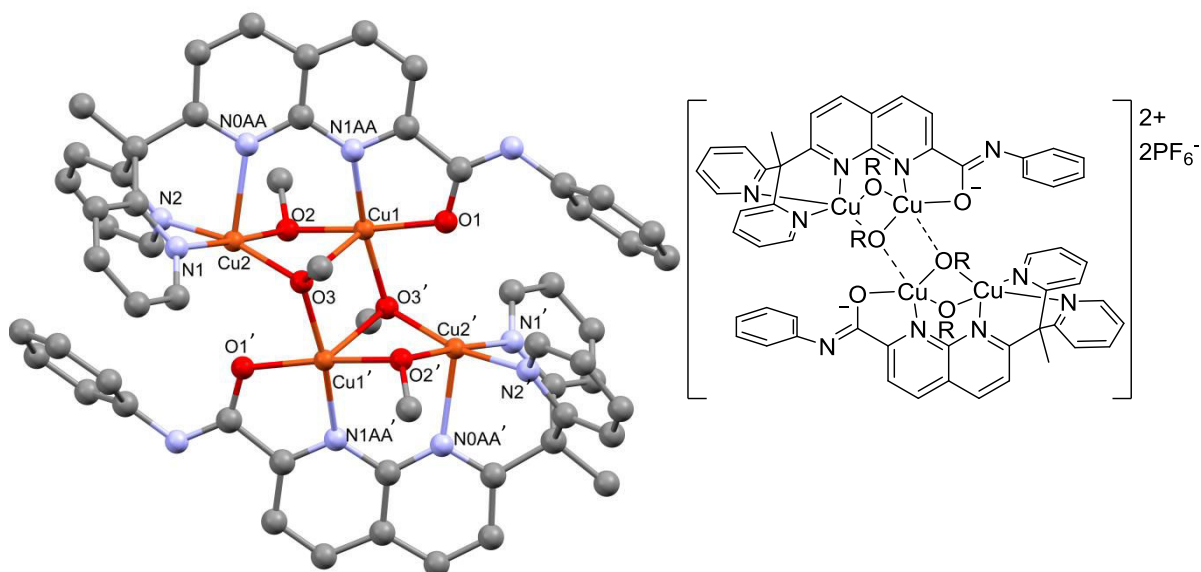


Figure 41: Left: crystal structure of the dication $[\text{Cu}^{\text{II}}_4(\text{Py}_2\text{An})_2(\text{OCH}_3)_4](\text{PF}_6)_2$, obtained from the green powder generated after complexation of the ligand $\text{Py}_2\text{AnH}_2\text{PF}_6$ with $\text{Cu}^{\text{II}}(\text{OTf})_2$ and crystallisation by slow diffusion of DIPE into a methanol solution. The complex is named $\text{Cu}^{\text{II}}_4(\text{Py}_2\text{An})_2$. Hydrogen atoms and solvent molecules and the non-coordinating hexafluorophosphate counterions have been removed for clarity. Right: diagrammatic representation of the crystal structure obtained, with R indicating a methyl group.

Table 9: Selected distances and bond angles for the tetranuclear structure obtained from ligand $\text{Py}_2\text{AnH}_2\text{PF}_6$.

Atom1	Atom2	Length / Å	Bond Angle	Angle / °
Cu1	Cu2	2.959(1)	N1AA-Cu1-O2	98.0(2)
Cu1	O1	1.921(5)	N1AA-Cu1-O3	90.4(2)
Cu1	O2	1.912(5)	N1AA-Cu1-O1	82.2(2)
Cu1	O3	2.360(5)	O2-Cu1-O1	170.7(2)
Cu1	N1AA	2.063(5)	O1-Cu1-O3	111.8(2)
Cu1	O3'	1.961(5)	O3-Cu1-O2	77.5(2)
Cu2	O2	1.952(4)	O3-Cu1-O3	88.5(2)
Cu2	O3	1.965(5)	O3-Cu1-O2	92.0(2)
Cu2	N0AA	2.233(5)	O3-Cu1-O1	88.5(2)
Cu2	N2	1.988(6)	N0AA-Cu2-O2	90.6(2)
Cu2	N1	1.997(5)	N0AA-Cu2-O3	102.4(2)
			N0AA-Cu2-N1	86.9(2)
			N0AA-Cu2-N2	91.2(2)
			O2-Cu2-O3	87.0(2)
			O3-Cu2-N1	95.4(2)
			N1-Cu2-N2	85.7(2)
			N2-Cu2-O2	92.4(2)

When crystallised from methanol, a tetranuclear structure is observed containing two identical entities each with a ligand coordinating two copper ions (Figure 41), thus the structure is named $\text{Cu}^{\text{II}}_4(\text{Py}_2\text{An})_2$. The Cu ions within the entity are bridged by two methoxido groups, one of which is also coordinated to the Cu1 ion of the adjacent entity with a Cu1-O3' distance of 1.96 Å (see Table 9). Cu1 is in a square based pyramid geometry ($\tau = 0.02$),¹⁵³ coordinated to N1AA of the naphthyridine, the bridging groups O3' and O2 and the oxygen of the deprotonated amide O1 in the equatorial positions with the bridging group O3 in the axial position. Distances within the amide function display a C-O bond length of 1.28 Å and a C-N bond of 1.29 Å consistent with a deprotonated amide and delocalisation onto the oxygen. These distances are different to a Cu^{II} complex reported by Thibon-Pourret *et al.*¹⁵⁹ which contains a protonated amide moiety coordinated by the oxygen atom (O-C = 1.24 Å and C-N = 1.33 Å). Cu2 is also in a slightly distorted square based pyramid geometry ($\tau = 0.17$)¹⁵³ coordinated to the two nitrogens of the pyridines N1 and N2, the two methoxido bridges (O2 and O3) and with the N0AA of the naphthyridine in the axial position. Bond distances around the copper atoms are typical for the Cu^{II} oxidation state,³¹ between 1.9 and 2.0 Å except for the axial bonds which are longer. Despite using a triflate salt for the complexation reaction, the counter ions are hexafluorophosphates which probably come from the use of HATU for the synthesis of the ligand (Scheme 39).

When the green powder obtained upon complexation of the ligand $\text{Py}_2\text{AnH}_2\text{PF}_6$ with $\text{Cu}^{\text{II}}(\text{OTf})_2$ (followed by a change of counterion) is crystallised from DMF, a hexanuclear structure is obtained (Figure 42).

The structure consists of two entities containing a ligand coordinating two copper ions (Cu1 and Cu3) with bridging hydroxido groups, and the entities are bridged by two additional copper ions (Cu2) that coordinate to the bridging hydroxido groups of each of the entities. The structure is therefore named $\text{Cu}^{\text{II}}_6(\text{Py}_2\text{An})_2$. Cu1 is in a square based pyramid geometry ($\tau = 0.00$),¹⁵³ coordinated to N6 and N8 of the pyridine groups, the two hydroxido bridges and N12 from the naphthyridine unit in the axial position. Interestingly Cu3 is in a distorted trigonal bipyramid geometry ($\tau = 0.58$),¹⁵³ coordinating the two bridging hydroxido groups and the deprotonated N3 of the aniline (in contrast to the tetranuclear structure that is coordinated by the oxygen of the amide) in equatorial positions and the N5 of the naphthyridine and O0AA bridging the two Cu2 atoms in the axial positions. The two Cu2 ions (symmetrically identical) are in a distorted octahedral geometry, with each Cu2 coordinated to the two bridging hydroxido groups (O0AA and O0AA'), the bridging hydroxido groups between Cu1 and Cu3 (O1, O2') and with the oxygen atoms of two DMF molecules. Bond distances are in agreement with distances between a Cu^{II} and N/O donor groups.³¹ Surprisingly the distance between

Cu3 and the deprotonated amide N3 is shorter at 1.85 Å (Table 10), indicating a strong coordination of the amide compared to the other Cu-N bonds.

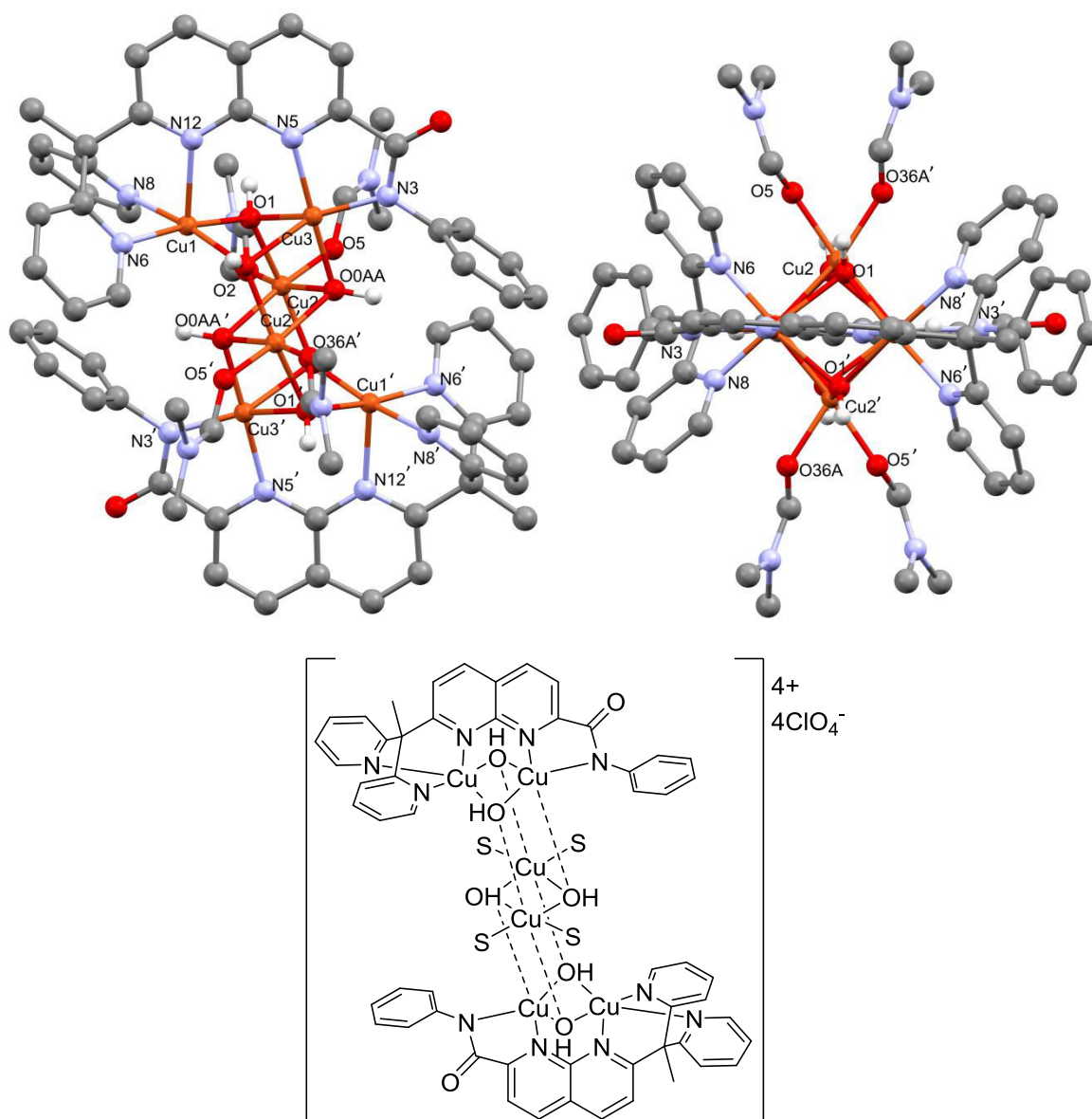


Figure 42: Top: Crystal structure of the tetracation of $[\text{Cu}_6(\text{Py}_2\text{An})_2(\text{OH})_6(\text{S})_4]^{4+}$, crystallised by slow diffusion of DIPE into a solution in DMF. The complex is named $\text{Cu}_6^{\text{II}}(\text{Py}_2\text{An})_2$ Hydrogen atoms (except the hydroxido bridges), non-coordinating solvent molecules and the perchlorate counterions have been removed for clarity. Top left: viewed perpendicular to the plane of the naphthyridine; top right: viewed along the plane of the naphthyridine unit. Bottom: diagrammatic representation of the crystal structure with S indicating a solvent molecule (DMF).

Table 10: List of bond distances and bond angles for the hexanuclear structure for the complex $\text{Cu}^{\text{II}}_6(\text{Py}_2\text{An})_2$.

Atom1	Atom2	Length / Å
Cu1	O1	1.968(2)
Cu1	O2	1.966(3)
Cu1	N6	1.991(3)
Cu1	N8	1.984(4)
Cu1	N12	2.212(3)
Cu2	O2'	1.989(2)
Cu2	O0AA'	2.137(3)
Cu2	O5	1.898(7)
Cu2	O36A	1.88(1)
Cu2	O1	1.982(2)
Cu2	O0AA	2.194(4)
Cu3	O1	2.177(3)
Cu3	O2	2.113(3)
Cu3	N3	1.85(2)
Cu3	O0AA	1.940(3)
Cu3	N5	2.031(3)

Bond Angle	Angle / °
N5-Cu3-N3	84.7(7)
N5-Cu3-O1	98.0(1)
N5-Cu3-O2	99.8(1)
N3-Cu3-O2	138.7(7)
N3-Cu3-O1	143.8(7)
O2-Cu3-O1	76.74(9)
N12-Cu1-N8	88.6(1)
N12-Cu1-N6	88.5(1)
N12-Cu1-O2	99.4(1)
N12-Cu1-O1	99.2(1)
N6-Cu1-N8	86.2(1)
N8-Cu1-O1	93.5(1)
O1-Cu1-O2	85.2(1)
O2-Cu1-N6	93.9(1)
O0AA-Cu3-N3	94.3(7)
O0AA-Cu3-O2	81.8(1)
O0AA-Cu3-O1	82.1(1)
O2-Cu2-O36A	96.4(3)
O2-Cu2-O0AA	80.1(1)
O2-Cu2-O5	91.8(2)
O0AA-Cu2-O36A	107.0(3)
O36A-Cu2-O5	67.2(4)
O5-Cu2-O0AA	101.7(2)
O0AA-Cu2-O0AA	84.4(1)
O1-Cu2-O0AA	88.4(1)
O1-Cu2-O36A	97.3(3)
O1-Cu2-O5	100.7(2)
O1-Cu2-O0AA	80.7(1)

The same green powder obtained after complexation gives rise to two different crystal structures, each with different Cu:ligand ratios (2:1 for the tetranuclear complex and 3:1 for the hexanuclear structure) suggesting that some copper must decoordinate from the ligand when the solvent is changed from methanol to DMF. The complexes were therefore characterised in solution to evaluate if their structures are retained in solution. Crystals of the complex $\text{Cu}^{\text{II}}_4(\text{Py}_2\text{An})_2$ were used for all further analysis because it has the right ratio of Cu:ligand to generate binuclear complexes if dissociated in solution as opposed to $\text{Cu}^{\text{II}}_6(\text{Py}_2\text{An})_2$ that, if dissociated, would give two binuclear complexes and copper salts.

2.4.2.2. Solution state characterisation of complexes from the ligand $\text{Py}_2\text{AnH}_2\text{PF}_6$

A. ^1H -NMR

To determine the behaviour of the tetranuclear complex in solution, the ^1H -NMR spectrum of $\text{Cu}^{\text{II}}_4(\text{Py}_2\text{An})_2$ was recorded in CD_3OD (Figure 43). The spectrum exhibits paramagnetic resonances within the range of 0 to 40 ppm with sharp peaks. The well resolved spectrum in methanol supports antiferromagnetic coupling between the copper ions in accordance with a silent EPR feature (CH_3OH , 100 K) and an $S = 0$ spin state. This indicates that two copper ions remain coordinated to the ligand and that the methoxido bridges are probably retained. Whether the structure remains tetranuclear in methanol is difficult to determine. We have previously shown with similar complexes that a complex that displays a tetranuclear structure in the solid state can display a mix of both tetra and dinuclear species in solution (see Section 2.2 of this Chapter).¹³¹

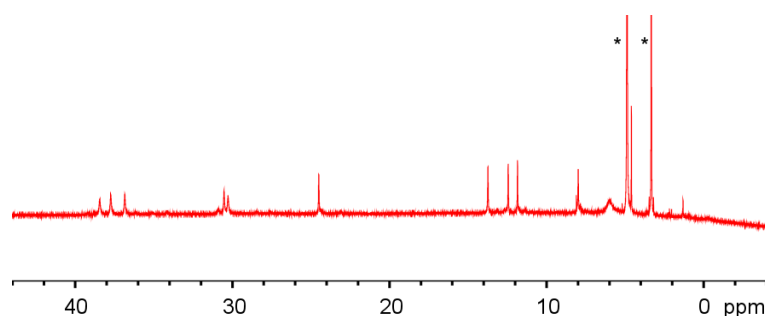


Figure 43: ^1H -NMR of a solution of the crystals from $\text{Cu}^{\text{II}}_4(\text{Py}_2\text{An})_2$ in CD_3OD . Starred peaks from left to right: H_2O and CH_3OH .

B. Cyclic voltammetry

To determine if a $\text{Cu}^{\text{II}}\text{Cu}^{\text{III}}$ species could be generated from the complex $\text{Cu}^{\text{II}}_4(\text{Py}_2\text{An})_2$, CV experiments were completed. Methanol was chosen as a solvent as the complex seems to at least partially retain its structure (a dinuclear entity antiferromagnetically coupled) in solution.

CV experiments were performed in a 0.1 M solution of NBu_4ClO_4 in methanol. Unfortunately the complex $\text{Cu}^{\text{II}}_4(\text{Py}_2\text{An})_2$ was not soluble at a concentration of 0.5 mM, but was soluble enough to be able to determine the oxidation potential. When scanning in oxidation, a small irreversible peak is observed at $E_{\text{Pa}} = 1.17$ V vs. Fc^+/Fc (where E_{Pa} is the anodic peak potential). This is indicative of an EC mechanism (where E stands for electron transfer and C stands for chemical reaction), where the

generated oxidised complex immediately reacts either with itself or with another molecule so that the reverse electron transfer is not possible. The lack of solubility of the complex limits the decrease of temperature to attempt to stabilise the oxidised species.

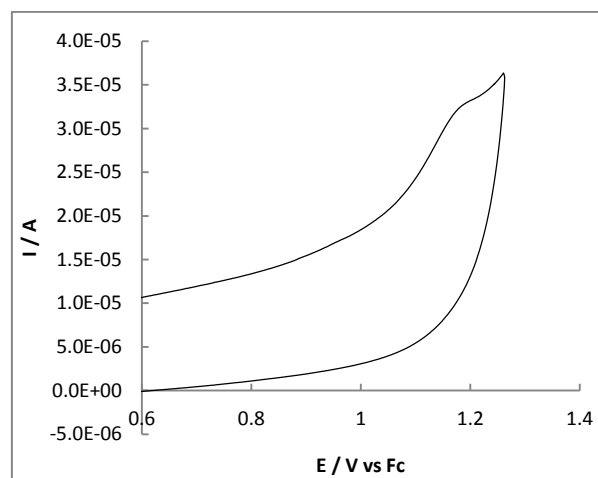


Figure 44: CV of the complex $\text{Cu}^{\text{II}}_4(\text{Py}_2\text{An})_2$ in oxidation. Parameters: NBu_4ClO_4 (0.1 M) in CH_3OH ; working electrode: glassy carbon (GC); atmosphere of air; $\nu = 100 \text{ mV}\cdot\text{s}^{-1}$.

2.4.3. Conclusions: complexes with the ligand $\text{Py}_2\text{AnH}_2\text{PF}_6$

The ligand $\text{Py}_2\text{AnH}_2\text{PF}_6$ was designed to stabilise mixed valent $\text{Cu}^{\text{II}}\text{Cu}^{\text{III}}$ species by being dissymmetric, with the pyridine groups stabilising the Cu^{II} oxidation state and the deprotonated amide of the aniline group for stabilising the Cu^{III} oxidation state. Unfortunately the ligand does not coordinate the copper ions well: two different structures with different Cu:ligand ratios are observed in the solid state which were obtained from the same complexation reaction. A tetranuclear structure was obtained when crystallised from methanol with a 2:1 Cu:ligand ratio and a hexanuclear structure was obtained from DMF with a 3:1 ratio. This demonstrates that the copper must decoordinate from the ligand in the presence of DMF to form the hexanuclear structure with a higher Cu:ligand ratio.

The oxidation potential of the complex is high at 1.17 V vs. Fc^+/Fc , and the irreversibility of the CV indicates that the species generated is either unstable or that it reacts immediately after its generation and is therefore difficult to characterise (because the lack of solubility prevents a decrease in temperature).

The reason for the high oxidation potential and the variety of structures obtained could be down to the coordination geometry of the ligand: in the structure $\text{Cu}^{\text{II}}_4(\text{Py}_2\text{An})_2$, the copper atom the side of the amide group is only coordinated twice to the ligand, with two other bonds to the bridging

methoxido groups. This makes the copper four coordinate within the entity, and forms the fifth bond with the opposite entity (forcing the nuclearity to be greater than 2). The argument is similar with the structure $\text{Cu}^{\text{II}}_6(\text{Py}_2\text{An})_2$, with the copper atom the side of the amide forming four bonds within the entity and therefore completes its coordination sphere by coordination to another (this time bridging OH) entity. If the entities break apart, the copper is no longer in the correct geometry to form a Cu^{III} as a rearrangement would be necessary to form a square planar geometry, making the oxidation potential high and the oxidation irreversible. The location of the oxidation could therefore not be determined.

The formation of a dinuclear complex could be controlled by having an extra coordinating atom on the containing the amide group, as the coordination sphere of the Cu^{II} oxidation state would be complete, and the ligand could pre-organise the Cu to form a square planar geometry (by having a similar geometry such as square base pyramid). New ligands were therefore designed with an extra coordinating atom.

2.5. Complexes with a benzimidazole arm

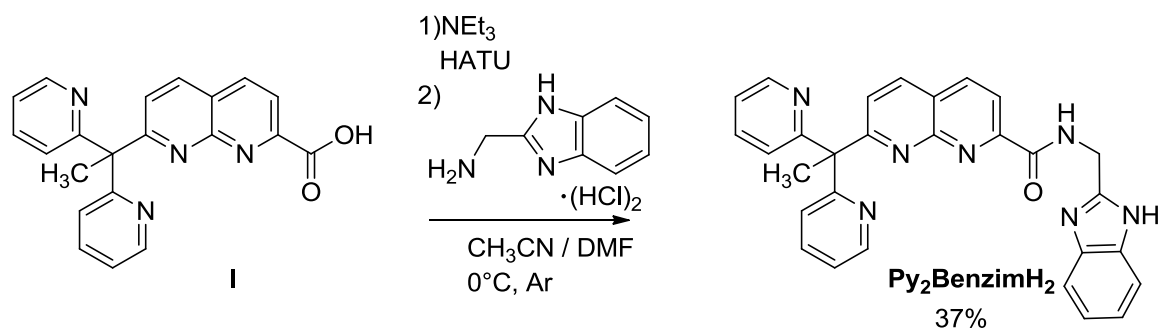
2.5.1. The ligand $\text{Py}_2\text{BenzimH}_2$

2.5.1.1. Choice of the ligand $\text{Py}_2\text{BenzimH}_2$

In Section 2.4 complexes based on the ligand $\text{Py}_2\text{AnH}_2\text{PF}_6$ are discussed, with the difficulties in with controlling the formation of a dinuclear complex demonstrated, as well as problems with decoordination of the copper from the ligand in different solvents. An extra coordinating atom is therefore necessary on the side that is designed to stabilise Cu^{III} . A benzimidazole arm (see Scheme 40) has been chosen to fulfil this requirement, with the added benefit that imidazoles are biologically relevant and has been shown to stabilise the Cu^{III} oxidation state (Part 1 Chapter 2 complex **36**).¹⁰³ The NH of the benzimidazole group could be deprotonated as well as the amide group, making the ligand dianionic, with both negative charges pre-organised for coordinating the same metal ion.

2.5.1.2. Synthesis of the ligand $\text{Py}_2\text{BenzimH}_2$

$\text{Py}_2\text{BenzimH}_2$ was synthesised by addition of 1.3 eq of HATU and 7 eq of NEt_3 to one equivalent of **I** at 0°C under Ar in a mixture of CH_3CN and DMF, followed by the addition of a mixture of NEt_3 (5 eq) and Aminomethyl benzimidazole dihydrochloride (1.6 eq). The ligand was extracted in DCM and purified by column chromatography. The synthesis is summarised in Scheme 40.



Scheme 40: Synthesis of the ligand Py₂BenzimH₂.

2.5.2. Complex supported by the ligand Py₂BenzimH₂

2.5.2.1. Synthesis and solid state characterisation of the complex from the ligand Py₂BenzimH₂

Triethylamine (10 eq) was added to 1 eq of Py₂BenzimH₂ in a solution of THF, followed by the addition of 2.1 eq of Cu^{II}OTf₂. The resulting dark green precipitate was isolated and crystallised by slow diffusion of THF into a methanol solution with a yield of 24 %, giving the structure shown in Figure 45.

A tetranuclear structure is obtained from the copper complex of Py₂BenzimH₂ consisting of two dinuclear copper entities bridged by the benzimidazole group, with one nitrogen of the benzimidazole group coordinating to each of the dicopper centres. The complex is thus named Cu^{II}₄(Py₂Benzim)₂. The two dicopper entities are identical in terms of bond distances and angles. Each dicopper centre is bridged by a single hydroxido group, and the Cu-Cu distance is relatively long at 3.1 Å. Cu1 is in a distorted square based pyramid geometry with the N8 of the naphthyridine unit in the axial position, the N4 and N5 of the pyridine groups, the OH bridge and the N1 of the benzimidazole group in the equatorial positions with bond angles between 85° and 95° except N8-Cu1-N1 which is of 111°. Cu2 is also in a distorted square based pyramid geometry with the O4 of the coordinating triflate group in the axial position and the equatorial positions occupied by the N7AA of the amide, N1BA of the benzimidazole group, the bridging hydroxido group and N1AA of the naphthyridine unit. Bond angles around the Cu2 atom are more variable than with Cu1, varying between 80° and 104°. All bond distances are standard for a Cu^{II} complex (1.9-2.2 Å) except bond between the O4 of the counterion (OTf) and Cu2 which is longer (2.71 Å) indicating a weaker bond.

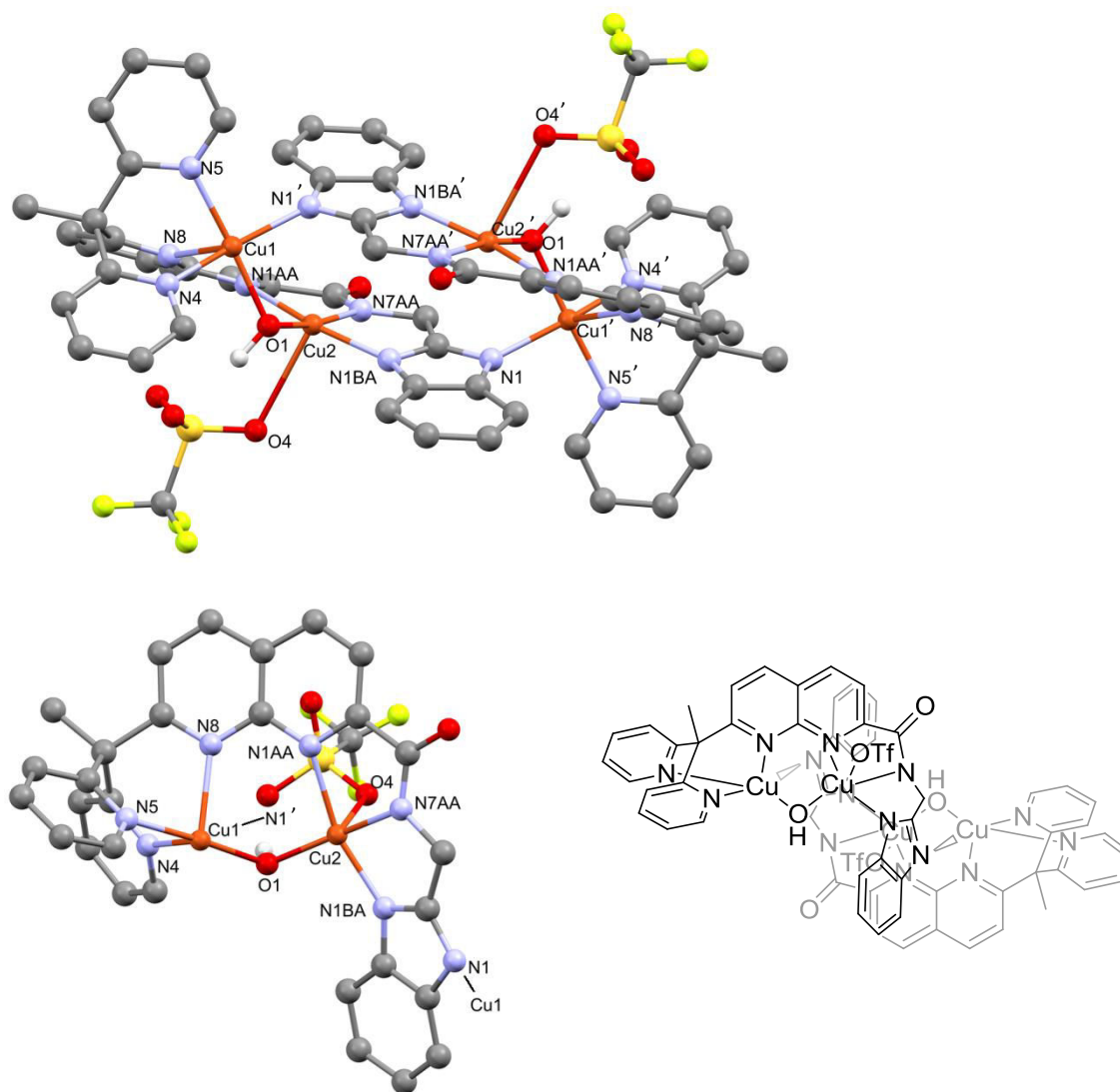


Figure 45: Crystal structure of the complex $[\text{Cu}^{\text{II}}_4(\text{Py}_2\text{Benzim})_2(\text{OH})_2(\text{OTf})_2]$. The complex is named $\text{Cu}^{\text{II}}_4(\text{Py}_2\text{Benzim})_2$. Top: full crystal structure. Bottom left: structure cut along the Cu1-N1 bonds. Hydrogens (except the hydroxido bridges) and solvent molecules have been omitted for clarity. Bottom right: diagrammatic representation of the crystal structure.

Table 11: List of bond distances and angles for copper complex obtained from the ligand Py₂BenzimH₂.

Atom1	Atom2	Length / Å	Bond angle	Angle / °
Cu1	Cu2	3.1082(7)	O1-Cu1-N4	89.7(1)
Cu1	O1	1.937(2)	O1-Cu1-N5	175.1(1)
Cu1	N4	2.011(3)	O1-Cu1-N8	94.5(1)
Cu1	N5	2.001(2)	O1-Cu1-N1'	90.1(1)
Cu1	N8	2.218(3)	N4-Cu1-N5	85.8(1)
Cu1	N1'	2.002(2)	N4-Cu1-N8	87.9(1)
Cu2	O1	1.896(2)	N4-Cu1-N1'	161.6(1)
Cu2	N7AA	1.907(3)	N5-Cu1-N8	87.3(1)
Cu2	N1BA	1.975(2)	N5-Cu1-N1'	93.5(1)
Cu2	N1AA	2.133(2)	N8-Cu1-N1'	110.5(1)
Cu2	O4	2.709(5)	O1-Cu2-N7AA	170.3(1)
			O1-Cu2-N1BA	98.5(1)
			O1-Cu2-N1AA	99.6(1)
			O1-Cu2-O4	86.1(1)
			N7AA-Cu2-N1BA	81.9(1)
			N7AA-Cu2-N1AA	80.0(1)
			N7AA-Cu2-O4	103.5(1)
			N1BA-Cu2-N1AA	161.8(1)
			N1BA-Cu2-O4	97.3(1)
			N1AA-Cu2-O4	85.2(1)
			Cu1-O1-Cu2	108.4(1)

2.5.2.2. Solution characterisation of complex Cu^{II}₄(Py₂Benzim)₂

The characterisation of the complex Cu^{II}₄(Py₂Benzim)₂ was carried out to ensure that it maintained its structure in solution.

A. ESI-MS

The ESI-MS spectrum of the complex Cu^{II}₄(Py₂Benzim)₂ was recorded in methanol (Figure 46). The spectrum displays a peak at $m/z = 1553.0$ corresponding to the tetranuclear entity [Cu^{II}₄(Py₂Benzim)₂ + H]⁺, with the appropriate isotopic profile. A peak at $m/z = 1403$ corresponds to the neutral tetranuclear entity with the loss of a triflate anion [Cu^{II}₄(Py₂Benzim) – OTf]⁺. These results indicate that the tetranuclear structure of the complex remains at least partially intact in a methanol solution. A peak is also observed at $m/z = 778$ which corresponds the protonated form of one of the dinuclear entities [Cu^{II}₂Py₂Benzim + H]⁺. The dissociation could have occurred in the spectrometer or this result could indicate the partial dissociation of the tetranuclear entity to form two dinuclear entities in solution.

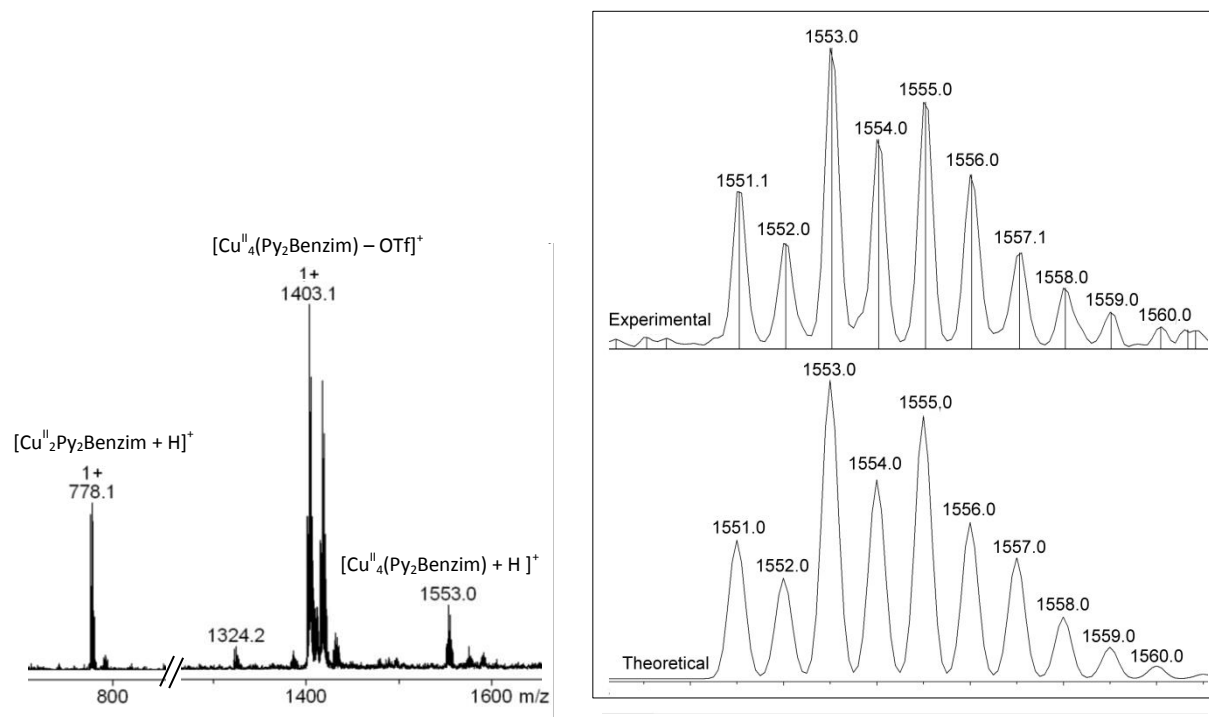


Figure 46: ESI-MS of the complex $\text{Cu}^{\text{II}}(\text{Py}_2\text{Benzim})_2$ recorded in methanol.

B. $^1\text{H-NMR}$

To further probe any differences between the solid and solution state of the complex $\text{Cu}^{\text{II}}(\text{Py}_2\text{Benzim})_2$, the $^1\text{H-NMR}$ spectrum was recorded in a solution of CD_3CN . The paramagnetic spectrum displays eighteen sharp peaks in the range of 110 to 0 ppm in accordance with an antiferromagnetic coupling in between the two copper centres. There is one broad peak at 6.5 ppm which could be the bridging OH group, probably broad due to its proximity to the paramagnetic copper. In total the 19 peaks observed are consistent with the crystal structure with all peaks accounted for, so the complex is therefore not a mix of structures in solution (or at least the equilibrium occurs faster than the NMR timescale). All of these results indicate that the structure is not significantly changed between solid and solution states.

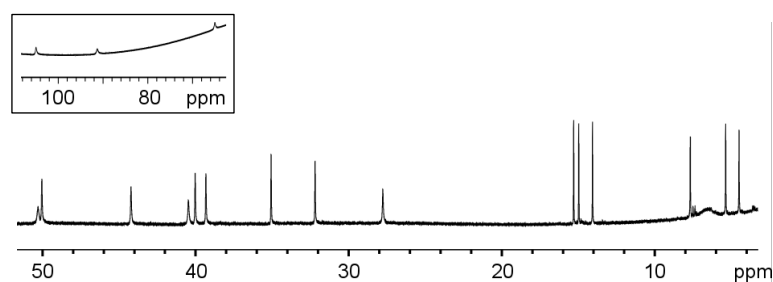


Figure 47: $^1\text{H-NMR}$ spectrum of the complex $\text{Cu}^{\text{II}}(\text{Py}_2\text{Benzim})_2$ in a solution of CD_3CN .

C. EPR (electron paramagnetic resonance spectroscopy)

The X band EPR spectrum of the complex $\text{Cu}^{\text{II}}_4(\text{Py}_2\text{Benzim})_2$ in a frozen solution of either CH_3CN or DMF were shown to be EPR silent at 100 K.

2.5.2.3. The first oxidation state of the complex $\text{Cu}^{\text{II}}_4(\text{Py}_2\text{Benzim})_2$

As the structure seems to be maintained for the complex $\text{Cu}^{\text{II}}_4(\text{Py}_2\text{Benzim})_2$ in solution, CV experiments were performed to access the first oxidation state (Figure 48). A 0.1 M solution of NBu_4ClO_4 in DMF was chosen as the solvent due to the lack of solubility of the complex in a 0.1 mM solution of NBu_4ClO_4 in either acetonitrile or methanol.

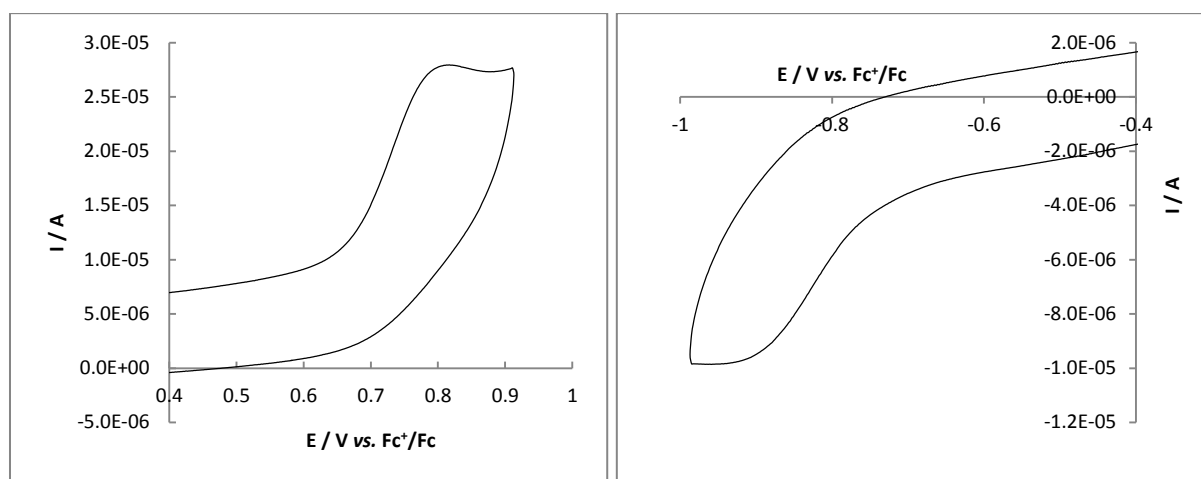


Figure 48: CV of the complex sweeping in oxidation (left) and reduction (right). Parameters: CV; $\nu = 100 \text{ mV}\cdot\text{s}^{-1}$; NBu_4ClO_4 in DMF (0.1 M); concentration of $\text{Cu}^{\text{II}}_4(\text{Py}_2\text{Benzim})_2 = 0.50 \text{ mM}$; glassy carbon as the working electrode; experiment open to air, room temperature.

The CV (Figure 48) display irreversible ($100 < \nu < 1000 \text{ mV}\cdot\text{s}^{-1}$) oxidation and reduction waves at $E_p = 0.81$ and $-0.91 \text{ V vs. Fc}^+/\text{Fc}$ respectively. Both of these CV curves are characteristic of an EC mechanism, where the generated oxidised (or reduced) complex immediately reacts either with itself or with another molecule so that the reverse electron transfer is not possible. It is possible that as soon as the complex $\text{Cu}^{\text{II}}_4(\text{Py}_2\text{Benzim})_2$ is oxidised or reduced, the tetranuclear structure breaks up.

2.5.3. Conclusions with the complex $\text{Cu}^{\text{II}}_4(\text{Py}_2\text{Benzim})_2$

The complex $\text{Cu}^{\text{II}}_4(\text{Py}_2\text{Benzim})_2$ was synthesised with a ligand that has a dianionic moiety, with negative charges on the deprotonated amide group and the deprotonated benzimidazole group. The

tetranuclear complex was characterised by X-ray crystallography and in solution by ESI-MS, $^1\text{H-NMR}$ and EPR which indicates that the complex remains intact in solution. The oxidation potential of the complex $\text{Cu}^{\text{II}}_4(\text{Py}_2\text{Benzim})_2$ is of 0.81 V vs. Fc^+/Fc , which is significantly lower than that of the complex formed with the ligand $\text{Py}_2\text{AnH}_2\text{PF}_6$. It is unclear where the oxidation occurs in either case, but the lower oxidation potential of the complex $\text{Cu}^{\text{II}}_4(\text{Py}_2\text{Benzim})_2$ could be due to the presence of the two negative charges on the ligand $\text{Cu}^{\text{II}}_4(\text{Py}_2\text{Benzim})_2$ making the Cu^{III} oxidation state more accessible. When the complex $\text{Cu}^{\text{II}}_4(\text{Py}_2\text{Benzim})_2$ is oxidised the species formed is unstable, which could be due to the breaking of the tetranuclear structure. Controlling the formation of a dinuclear species could therefore be important for being able to access a more stable $\text{Cu}^{\text{II}}\text{Cu}^{\text{III}}$ state.

The ligand $\text{Py}_2\text{BenzimH}_2$ was designed with to be tridentate for each copper in the hope that if a complex formed with two OH bridges the coordination sphere of the copper would be complete, preventing a structure with greater than two copper atoms. Unfortunately the two nitrogen atoms either side of the benzimidazole group bridge between two dicopper entities, giving a tetranuclear structure. Our efforts were therefore continued by using similar ligands with arms that would not have the ability to bridge between two dicopper centres.

2.6. Complexes with an indole arm

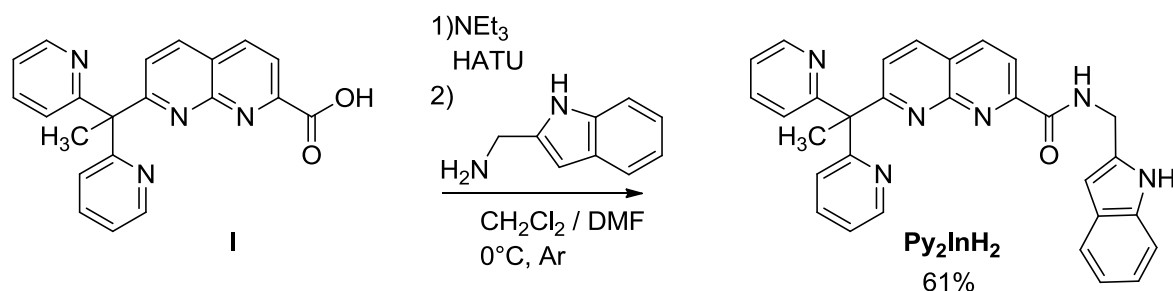
2.6.1. The ligand Py_2InH_2

2.6.1.1. Choice of the ligand Py_2InH_2

The ligand $\text{Py}_2\text{BenzimH}_2$ gives the copper a dianionic environment and the correct geometry (square pyramid) which should help to stabilise the Cu^{III} oxidation state. The ligand Py_2InH_2 with an indole motif was therefore selected as the nitrogen atom of the benzimidazole is replaced by a non-coordinating carbon atom, which should prevent the formation of the tetranuclear structure.

2.6.1.2. Synthesis of the ligand Py_2InH_2

Py_2InH_2 was synthesised by addition of 1.3 eq of HATU and 9 eq of NEt_3 to one equivalent of **1** at 0°C under Ar in a mixture of CH_2Cl_2 and DMF, followed by the addition of (aminomethyl)indole (1.3 eq). The ligand was extracted with DCM and purified by column chromatography. The synthesis is summarised in Scheme 41.



Scheme 41: Synthesis of the ligand Py_2InH_2 .

2.6.2. Complexation with the ligand Py_2InH_2

The first complexation attempt was made using similar conditions to the complexation reactions with the ligands $\text{Py}_2\text{AnH}_2\text{PF}_6$ and $\text{Py}_2\text{BenzimH}_2$. The ligand was dissolved in acetonitrile then water and NEt_3 were added followed by $\text{Cu}^{\text{II}}\text{OTf}_2$. THF was added to form a green precipitate that was isolated but crystallisation attempts were unsuccessful.

2.6.2.1. Titration of the ligand Py_2InH_2 with $\text{Cu}^{\text{II}}\text{OTf}_2$

To determine the nuclearity of the copper complex formed, a titration was completed. A solution of the ligand Py_2InH_2 was dissolved in acetonitrile at two different concentrations (0.037 mM and 1.0 mM) and two equivalents of NEt_3 were added resulting in no changes to the UV-vis spectrum. The solutions were then titrated with 0-2.8 equivalents of $\text{Cu}^{\text{II}}\text{OTf}_2$ in increments of 0.2 equivalents with a UV-vis spectrum recorded after each addition. The results are displayed in Figure 49 (0.037 mM of the ligand concentration as the main figure and 1.0 mM for the inset) with the addition of 0-1.4 eq of $\text{Cu}^{\text{II}}\text{OTf}_2$ shown in black and 1.6-2.8 eq shown in light red.

As can be seen in Figure 49, the addition of 0-1.4 equivalents of $\text{Cu}^{\text{II}}\text{OTf}_2$ results in a decrease in absorption 305-330 nm and an increase between 270 and 305 nm resulting in an isosbestic point at 305 nm indicating the clean conversion of one species to another. Upon addition of 1.6 to 2.8 equivalents, the isosbestic point is lost and there are new bands that are formed at 249 nm, 300 nm and 525 nm indicating the formation of a new species. This gives the ratio of copper: ligand to be 3:2 for the first species formed upon titration and greater or equal to 3:1 for the second, indicating that a dinuclear complex is not formed.

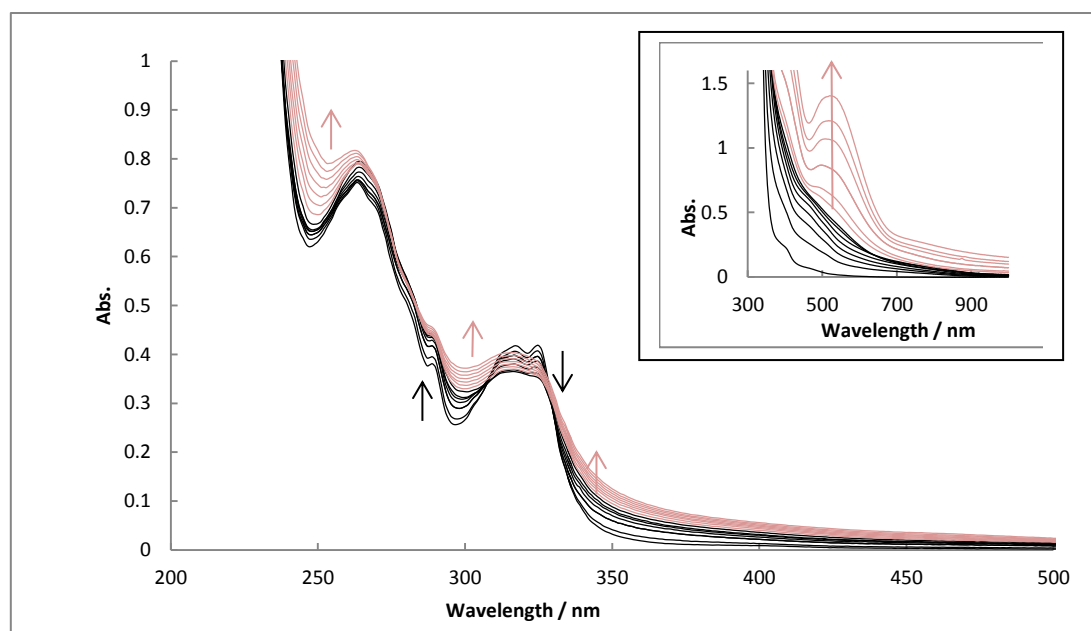


Figure 49: Titration of Py_2InH_2 with $\text{Cu}^{\text{II}}\text{OTf}_2$. Additions of $\text{Cu}^{\text{II}}\text{OTf}_2$ from 0-1.4 eq are shown in black and 1.6-2.8 eq in light red. Parameters: solvent: acetonitrile; concentration of the ligand: 0.037 mM (inset 1.0 mM); 2 eq NEt_3 ; $l = 1$ cm; room temperature.

2.6.2.2. Other complexation reaction attempts

Due to the lack of formation of a dinuclear complex and difficulties with obtaining the structure of the complex using the ligand Py_2InH_2 , several attempts were made and the conditions are summarised in Table 12.

Table 12: Various conditions used for the complexation reactions using the ligand Py_2InH_2 .

Solvent	Eq Py_2InH_2	Eq Cu^{II}	Salt	Base	Eq base	Eq H_2O
CH_3CN	1	2.1	$\text{Cu}^{\text{II}}\text{OTf}_2$	NEt_3	10	5.5
THF	1	2.1	$\text{Cu}^{\text{II}}\text{OTf}_2$	NEt_3	10	5.5
MeOH	1	2.1	$\text{Cu}^{\text{II}}(\text{ClO}_4)_2$	$\text{N}(\text{CH}_3)_4\text{OH}$	4.0	0
THF	1	2.1	$\text{Cu}^{\text{II}}\text{OTf}_2$	n-BuLi	2.2	20.0

The ligand was dissolved in THF then water and NEt_3 were added followed by $\text{Cu}^{\text{II}}\text{OTf}_2$ resulting in a dark green precipitate that was sparingly soluble in acetonitrile and methanol. The dark green powder could not be crystallised.

Supposing that NEt_3 was not a strong enough base to deprotonate the nitrogen of the indole, attempts with stronger bases were completed. The base $\text{N}(\text{CH}_3)_4\text{OH}$ was used as a 25 % solution in methanol, so methanol was also used as the solvent. The base was added to a solution of the ligand

followed by the addition of $\text{Cu}(\text{ClO}_4)_2 \cdot 6\text{H}_2\text{O}$. No additional water was added to generate hydroxido bridges as the base carried OH^- anions and the copper salt contains water of crystallisation. A precipitate formed that was not soluble in acetonitrile, acetone or methanol but was soluble in DMF, DMSO (dimethylsulfoxide) and nitromethane. Unfortunately crystals could not be obtained from this synthesis either.

A final synthesis was attempted by using $n\text{-BuLi}$ as the base. A solution of the ligand in dry THF was cooled to -25°C in under Ar and $n\text{-BuLi}$ (n -butyllithium) was added followed by $\text{Cu}^{\text{II}}\text{OTf}_2$ and then H_2O forming a dark green/brown solution. Pentane was added to form a dark green solid not soluble in acetonitrile, THF, nitromethane or water but soluble in DMF and DMSO. Crystals could not be obtained from this powder either.

2.6.3. Conclusions with the ligand Py_2InH_2

The ligand Py_2InH_2 was chosen as the indol group only has one nitrogen so that, unlike the benzimidazole arm used previously, the indol would not bridge between two dinuclear entities. As crystals could not be obtained, a titration of the ligand with copper was completed to determine the stoichiometry between the copper and the ligand. A species with a copper:ligand ratio of 3:2 was obtained, with addition of more copper resulting in a different species being formed. As a dinuclear complex could not be synthesised, attempts at generating a pure complex from the ligand Py_2InH_2 were not taken any further.

2.7. Complexes with a bipyrazole arm

2.7.1. The ligand $\text{Py}_2\text{Pyr}_2\text{H}$

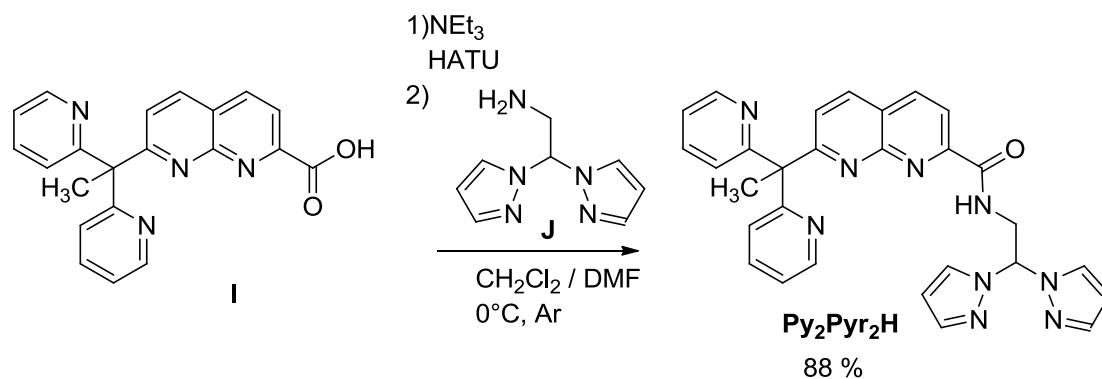
2.7.1.1. Choice of ligand

The ligand $\text{Py}_2\text{Pyr}_2\text{H}$ (Scheme 42) was chosen to see the effects of a “pincer” arm, *i.e.* with the arm that divides into two and therefore the ligand provides a total of three coordinating atoms for the copper in one of the coordination site.^f As with previous ligands, the arm is still attached to the naphthyridine spacer *via* an amide bond which can be deprotonated, providing a negative charge to stabilise Cu^{III} .

^f The synthetic work in this section was completed by R. Louvet, a student from the IUT de Chimie de Grenoble whose work I was overseeing.

2.7.1.2. Synthesis of the ligand $\text{Py}_2\text{Pyr}_2\text{H}$

The bipyrazole arm **J** was synthesised in three steps according to the literature procedure.¹⁶⁰ The ligand $\text{Py}_2\text{Pyr}_2\text{H}$ was synthesised by addition of 1.3 eq of HATU and 9 eq of NEt_3 to one eq of **I** at 0°C under Ar in a mixture of CH_2Cl_2 and DMF, followed by the addition of **J** (1.4 eq). The ligand was extracted in DCM and purified by column chromatography. The synthesis is summarised in Scheme 42.



Scheme 42: Synthesis of the ligand $\text{Py}_2\text{Pyr}_2\text{H}$.

2.7.2. Complexes using the ligand $\text{Py}_2\text{Pyr}_2\text{H}$

2.7.2.1. Synthesis and solid state characterisation of the complex bearing the ligand $\text{Py}_2\text{Pyr}_2\text{H}$

The ligand $\text{Py}_2\text{Pyr}_2\text{H}$ was dissolved in acetonitrile and two eq of NEt_3 and 10 eq of water were added followed by 2.1 eq of $\text{Cu}^{\text{II}}\text{OTf}_2$. The solution was concentrated and the complex was precipitated with the addition of THF at -40°C to give a green precipitate that was crystallised by slow diffusion of THF into a solution of acetonitrile with a yield of 53 %. The crystal structure is shown in Figure 50 with a list of bond distances and angles in Table 13.

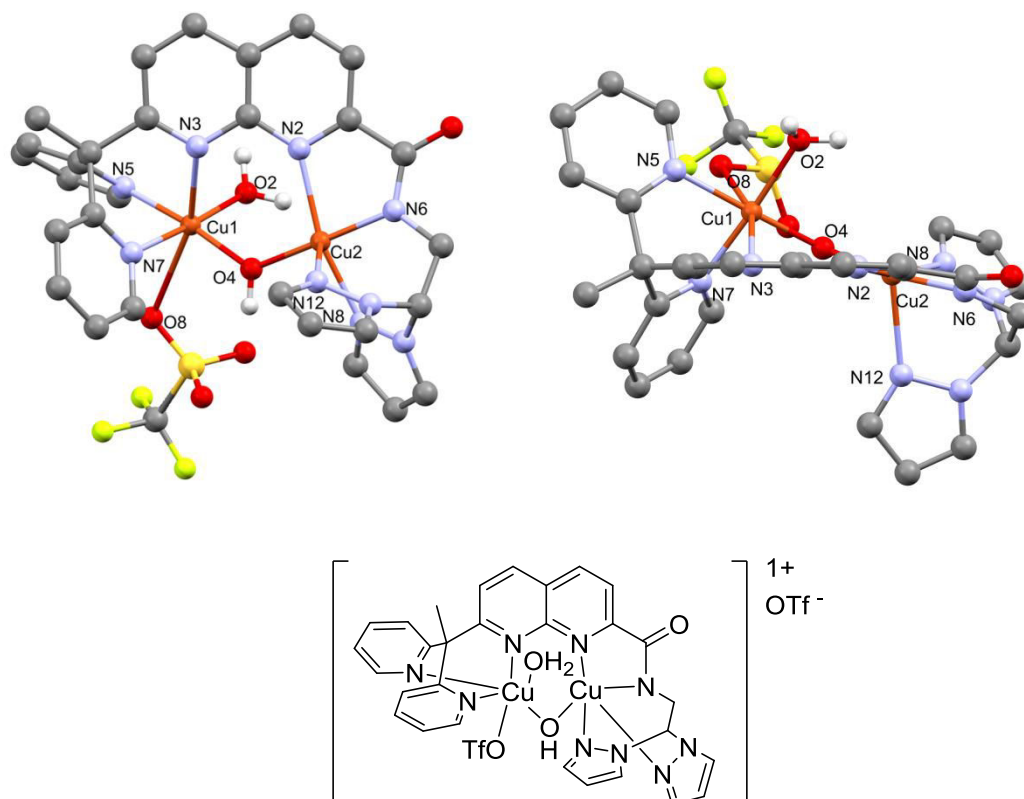


Figure 50: Top: Crystal structure of the monocation of the complex $[\text{Cu}^{\text{II}}_2(\text{Py}_2\text{Pyr}_2)(\text{OH})(\text{H}_2\text{O})(\text{OTf})](\text{OTf})$. The complex is named $\text{Cu}^{\text{II}}_2(\text{Py}_2\text{Pyr}_2)$. Hydrogen atoms (except the hydroxido bridge and coordinated water molecule), solvent molecules and the non-coordinating triflate counterion have been removed for clarity. Top left: viewed perpendicular to the plane of the naphthyridine. Top right: viewed along the plane of the naphthyridine. Bottom: diagrammatic representation of the crystal structure.

The structure obtained is a dinuclear complex, bridged by a single hydroxido group. Cu1 (distorted octahedral geometry) is coordinated to the N3 of the naphthyridine unit, N5 and N7 from the pyridines, the oxygen atom O8 of a triflate group, a terminal water molecule and the bridging hydroxido group. The bond between Cu1 and O8 (from the triflate) is long at 2.67 Å and other bonds are in the range for the Cu^{II} oxidation state (1.9–2.3 Å). Cu2 is coordinated to the deprotonated nitrogen atom of the amide N6, the naphthyridine unit N2, the bridging hydroxido group and the two nitrogen atoms of the bipyrazole unit N8 and N12 in a geometry best described as a slightly distorted square based pyramid ($\tau = 0.15$).¹⁵³ Bond distances to the copper are as expected between 1.9 and 2.3 Å. Cu2 is more or less in the plane of the naphthyridine unit whether as Cu1 is not, making the complex appear strained (Figure 50, right). The Cu–Cu distance is relatively long at 3.4 Å. The dinuclear complex is named $\text{Cu}^{\text{II}}_2\text{Py}_2\text{Pyr}_2$.

Table 13: List of bond lengths and bond angles for the copper complex obtained from the ligand Py₂Pyr₂H.

Atom1	Atom2	Length / Å	Bond angle	Angle / °
Cu1	Cu2	3.402(1)	O2-Cu1-N3	96.2(2)
Cu1	O2	2.021(4)	O2-Cu1-O4	91.7(2)
Cu1	N3	2.288(5)	O2-Cu1-N5	89.4(2)
Cu1	O4	1.894(5)	O2-Cu1-N7	176.3(2)
Cu1	N5	1.994(5)	O2-Cu1-O8	98.1(4)
Cu1	N7	2.008(6)	N3-Cu1-O4	95.5(2)
Cu1	O8	2.67(2)	N3-Cu1-N5	91.0(2)
Cu2	O4	1.882(5)	N3-Cu1-N7	82.7(2)
Cu2	N8	2.100(6)	N3-Cu1-O8	163.4(4)
Cu2	N2	2.164(5)	O4-Cu1-N5	173.2(2)
Cu2	N6	1.913(5)	O4-Cu1-N7	91.9(2)
Cu2	N12	2.308(5)	O4-Cu1-O8	92.5(4)
			N5-Cu1-N7	87.1(2)
			N5-Cu1-O8	80.7(4)
			N7-Cu1-O8	82.5(4)
			O4-Cu2-N8	89.8(2)
			O4-Cu2-N2	98.5(2)
			O4-Cu2-N6	172.3(2)
			O4-Cu2-N12	103.7(2)
			N8-Cu2-N2	163.2(2)
			N8-Cu2-N6	89.5(2)
			N8-Cu2-N12	80.7(2)
			N2-Cu2-N6	80.4(2)
			N2-Cu2-N12	111.1(2)
			N6-Cu2-N12	83.8(2)

2.7.2.2. Electrochemistry of the complex Cu^{II}₂Py₂Pyr₂

CV experiments of the complex Cu^{II}₂Py₂Pyr₂ were performed in a 0.1 M solution of NBu₄ClO₄ in acetonitrile to determine the oxidation potential and the stability of the first oxidation state. The results at a scan rate of 1000 mV.s⁻¹ are displayed in Figure 51. The CV display an irreversible oxidation wave with an E_{pa} = 1.32 V vs. Fc⁺/Fc and a second oxidation irreversible wave with an E_{pa} = 1.50 V vs. Fc⁺/Fc. These both suggest an EC mechanism where the generated oxidised species either reacts with itself or with an external molecule so that the species formed cannot be reduced. The first and second oxidation states are therefore very unstable and would be difficult to characterise.

The instability of the mono-oxidised complex could be linked to the strained nature of the complex observed in the crystal structure, where upon oxidation a rearrangement would occur. The high oxidation potential could be due to the terminal water molecule: if it was deprotonated and bridged between the two copper atoms the oxidation potential could be lowered.

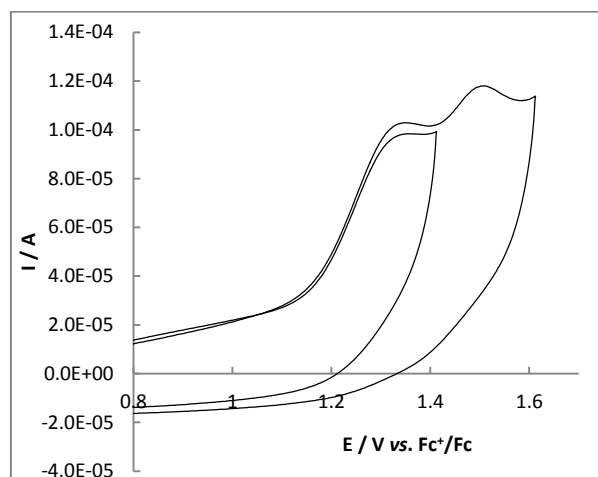


Figure 51: CV in oxidation of the copper complex $\text{Cu}^{\text{II}}\text{Py}_2\text{Pyr}_2$. Parameters: NBu_4ClO_4 in CH_3CN (0.1 M); $\nu = 1000 \text{ mV}\cdot\text{s}^{-1}$; working electrode: glassy carbon; concentration of complex = 1.0 mM.

2.7.2.3. Attempts to deprotonate the terminal water molecule

In the crystal structure of the complex $\text{Cu}^{\text{II}}\text{Py}_2\text{Pyr}_2$, there is one bridging hydroxido group and one terminal H_2O molecule. If the water molecule could be deprotonated so that it bridges across the two copper centre, it will also coordinate to Cu2 (the side with the amide and pyrazole groups designed to stabilise the Cu^{III} oxidation state), making the Cu^{III} oxidation state more accessible. Attempts were therefore made to deprotonate the terminal water molecule.

The synthesis of a binuclear copper complex from the ligand $\text{Py}_2\text{Pyr}_2\text{H}$ was therefore attempted using similar conditions displayed in Section 2.7.2.1, (1 eq of ligand $\text{Py}_2\text{Pyr}_2\text{H}$, 2.1 eq of $\text{Cu}^{\text{II}}\text{OTf}_2$, 10 eq of water in acetonitrile) but this time using 3.5 eq of triethylamine instead of 2 eq. A precipitate was formed upon addition of THF to the acetonitrile solution, which was isolated and crystallised by slow diffusion of THF into a solution of acetonitrile. Unfortunately analysis of the crystals indicated that the structure contained the same unit cell, so there is no significant change from the structure shown in Figure 50 and therefore no deprotonation of the terminal H_2O molecule.

Deprotonation of the terminal water molecule was also attempted by adding 1 eq of triethylamine to crystals of the complex $\text{Cu}^{\text{II}}\text{Py}_2\text{Pyr}_2$ that had been solubilised in acetonitrile. The

resulting solution was crystallised from the acetonitrile solution by slow evaporation to give the same crystal structure observed in Figure 50.

2.7.3. Conclusions on the complex $\text{Cu}^{\text{II}}_2\text{Py}_2\text{Pyr}_2$

A new dissymmetric ligand $\text{Py}_2\text{Pyr}_2\text{H}$ was synthesised bearing a bipyridine moiety on one side and a bipyrazole on the other linked to the naphthyridine spacer by an amide group. The crystal structure of the dinuclear copper complex $\text{Cu}^{\text{II}}_2\text{Py}_2\text{Pyr}_2$ appears strained. A single hydroxido bridge between the coppers is present, and one of the coppers is coordinated by a terminal water molecule. The oxidation potential of the complex is high at 1.32 V vs. Fc^+/Fc and the first oxidation state is unstable. Attempts were therefore made to deprotonate the terminal water molecule so that it would bridge between the two copper centres, but these were unsuccessful.

2.8. Discussion

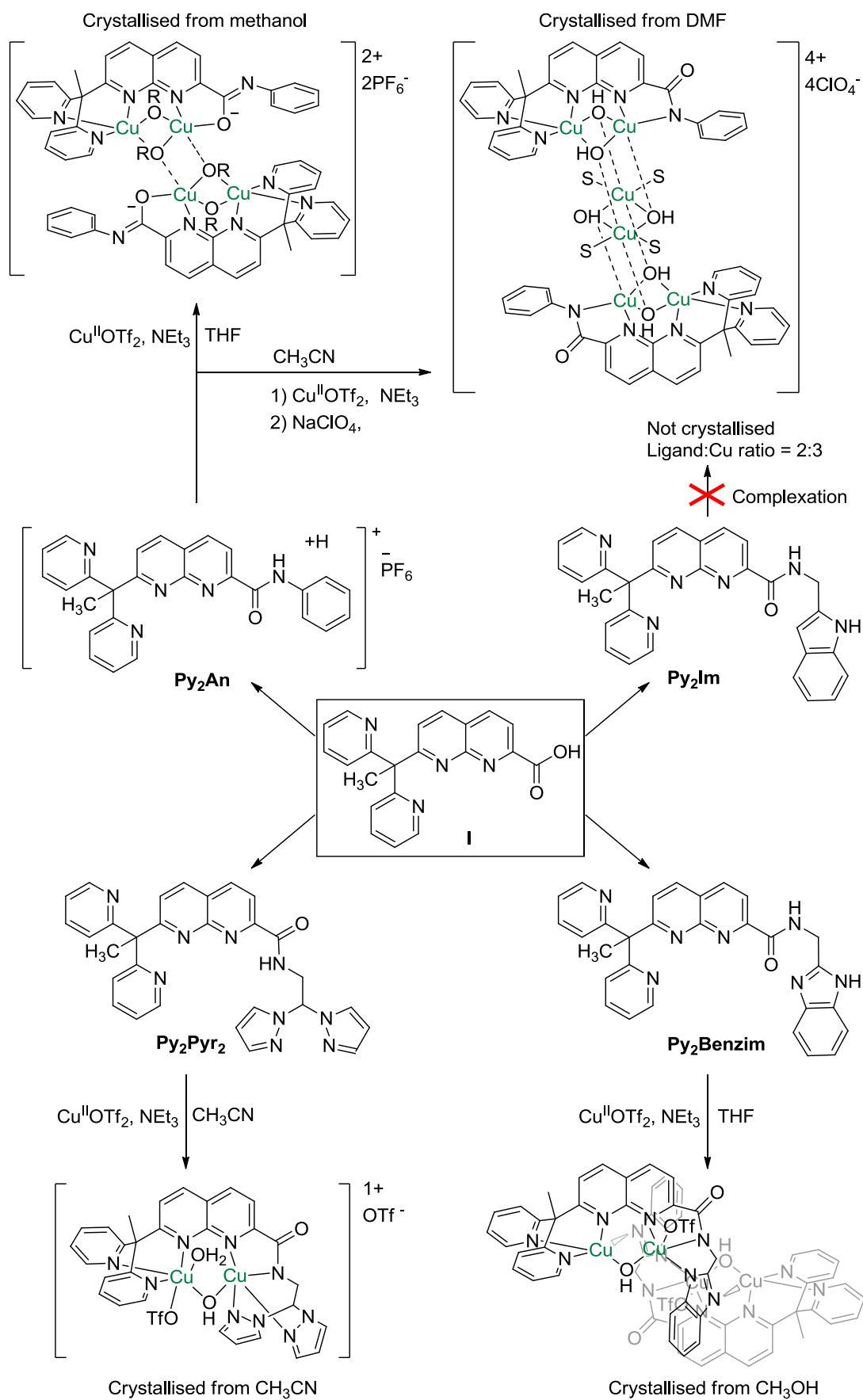
A series of dissymmetric complexes have been synthesised with their ligands all synthesised from the same synthon I (Scheme 43). A variety of structures have been obtained from dinuclear to tetranuclear or hexanuclear, demonstrating the difficulties of controlling the formation of dinuclear species. The reasons for the formation of complexes with greater than two copper atoms vary.

In the case of the complex $\text{Cu}^{\text{II}}_4(\text{Py}_2\text{An})_2$, only four atoms coordinate to the copper (two from the ligand and two from bridging groups) in one of the coordination sites, so the copper also binds to the methoxido bridge of the opposite entity to complete its coordination sphere.

In the case of the complex $\text{Cu}^{\text{II}}_4(\text{Py}_2\text{Benzim})_2$, a tetranuclear structure is obtained because the two dinuclear entities are bridged by the two nitrogens of the benzimidazole group.

Several complexation reactions were completed with the ligand Py_2InH_2 , however none resulted in the formation of crystals so the solid state structure could not be determined. Titration of the ligand with copper in the presence of triethylamine indicated however that the nuclearity of the complex in acetonitrile had a ratio of 3 Cu:2 ligand.

On the other hand complexation of the ligand $\text{Py}_2\text{Pyr}_2\text{H}$ successfully led to the formation of a dinuclear complex in relatively good yields.



Scheme 43: Ligands synthesised from the synthon I, and diagrams of the corresponding complexes. R = CH₃, S = DMF.

The structures that are presented in this chapter exhibit geometries of the copper on the side of the amide group are not suited for both Cu^{II} and Cu^{III} oxidation states. This is supported by the high oxidation potentials and instability of the oxidised species formed. In all of the structures obtained with dissymmetric ligands, the amide stays in the plane of the naphthyridine group. However the bridging groups between the copper atoms tend to be orthogonal to the plane of the naphthyridine group. This means that a square based pyramid/ (pre-organised) square planar geometry cannot be formed around Cu_B with both the amide group, the N of the naphthyridine and the two bridging groups (Figure 52). This is in contrast to the geometry of Cu_A which is generally obtained in the structures with the dissymmetric ligands on the side of the pyridine groups: the nitrogen atoms of the pyridines are orthogonal to plane of the naphthyridine group allowing a square based pyramid geometry to be formed around the copper with the N of the naphthyridine group in the axial position (see Figure 52).

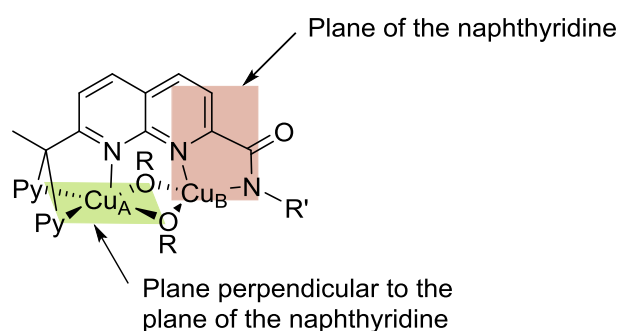


Figure 52: Schematic representation displaying the geometry generally obtained with the dissymmetric ligands presented in this chapter.

In the case of the ligand $\text{Py}_2\text{Pyr}_2\text{H}$, the crystal structure displays only one OH bridge present between two copper atoms, and the copper on the side of the pyridine rings also has a water molecule coordinated. Attempts to deprotonate this terminal water molecule to form a bridging hydroxido group were unsuccessful. The copper atom the side of the pyridine groups is out of the plane of the naphthyridine group, which prevents the water molecule getting into close proximity to bind with the second copper atom (see the crystal structure in Figure 50). The lack of two hydroxido bridges could contribute to difficulties in forming a relatively stable $\text{Cu}^{\text{II}}\text{Cu}^{\text{III}}$ species as the bridging hydroxido groups would stabilise the higher oxidation state of the copper as they are negatively charged. The geometry of the ligand $\text{Py}_2\text{Pyr}_2\text{H}$ is therefore not the correct geometry as it prevents the formation of two hydroxido bridges.

2.9. Conclusions

A series of dissymmetric ligands have been synthesised with the aim of giving the two copper atoms different coordination environments. After putting aside the redox active phenoxido moiety, our efforts were focussed on the use of a naphthyridine spacer. To control the formation of two different binding pockets with this spacer, we have developed the synthesis of the dissymmetric synthon I. This synthon has allowed the synthesis of various dissymmetric ligands bearing two distinct coordination environments, by involving negatively charged deprotonated nitrogen atoms (amides, indole and benzimidazole groups) to stabilise the Cu^{III} oxidation state and pyridine groups to stabilise the Cu^I oxidation state. None of the complexes synthesised in this chapter gave access to a Cu^ICu^{III} state that was stable enough to be characterised.

The lack of formation of a Cu^ICu^{III} can be explained because of the poor geometry of the copper the side of the amide groups for the formation of the Cu^{III} oxidation state. A square planar geometry is preferable for the formation of a Cu^{III}, or a similar geometry such as a square based pyramid which also has four equatorial ligands. The ligands in this chapter give copper complexes with distorted square based pyramid geometries only because of the formation of tetranuclear entities, for which the first oxidation states are unstable (presumably because the tetranuclear structure breaks apart upon oxidation). The ligand Py₂Pyr₂H is an exception but also has limitations to the geometries of the copper complexes formed as the complex does not have two bridging hydroxido groups.

Interestingly the complexes described in this chapter display a better coordination geometry on the copper the side of the pyridine groups to access the Cu^{III} oxidation state: the geometry with this “pincer” motif usually allows the copper to be in a square based pyramid with charged ligands hydroxido/methoxido or triflate groups in the equatorial positions. Future work will therefore aim at synthesising complexes with the geometry obtained on the side of the pyridine groups for the stabilisation of the Cu^{III} oxidation state.

3. Synthesis of Cu^{II}_2 complexes with access to a $\text{Cu}^{\text{II}}\text{Cu}^{\text{III}}$ oxidation state

3.1. Choice of ligands

As discussed in Part II Chapter 2, difficulties occurred in generating $\text{Cu}^{\text{II}}\text{Cu}^{\text{III}}$ species from the relevant Cu^{II}_2 dissymmetric complexes. The formation of tetranuclear complexes and the coordination of copper in a non-ideal geometry (where a large reorganisation would be needed) both prevented access to the $\text{Cu}^{\text{II}}\text{Cu}^{\text{III}}$ state. Interestingly it was observed that the ligands in Part II Chapter 2 could generate a square based pyramid on the side of the pyridine moieties if two bridging exogenous ligands are present, with the pyridine and bridging groups coordinating in the equatorial positions and the nitrogen of the naphthyridine in the axial position (see Figure 53). The ligands in this chapter are therefore designed to give access to this type of geometry for the copper.

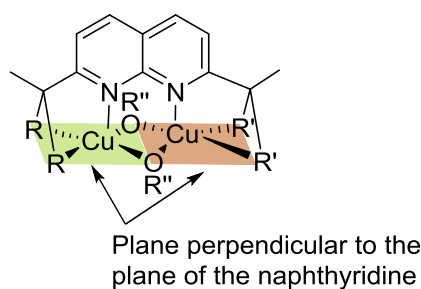


Figure 53: Geometry of the copper aimed for by ligands in this section.

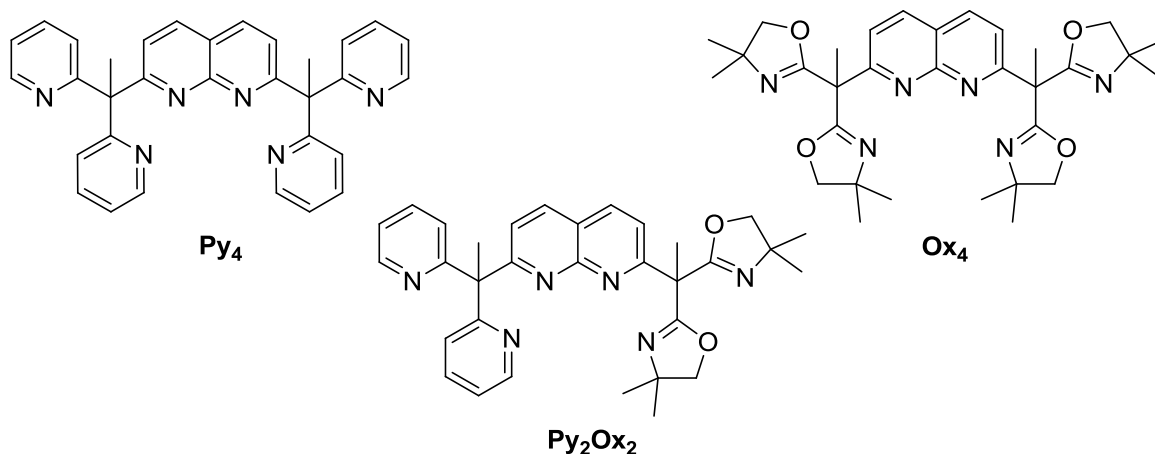


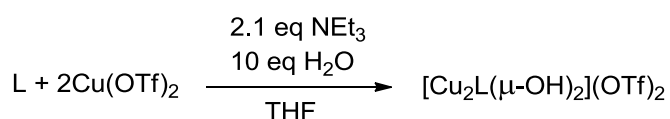
Figure 54: Ligands used in this chapter.

The ligands opted for in this chapter are shown in Figure 54. The syntheses of these ligands have already been described in Part II Chapter 1. The ligand Ox₄ was selected to evaluate the effect

of steric bulk on stabilising the intermediates, and therefore the ligand Py_4 was used for comparison. The ligand Py_2Ox_2 was chosen to determine the effect of a dissymmetric ligand.

3.2. Synthesis of Cu^{II}_2 complexes.

The complexation reactions of the three ligands displayed in Figure 54 were completed in the same fashion: 1 eq of the ligand was dissolved in THF and 2.1 eq of triethylamine and 10 eq of water were added, followed by 2.1 eq of $\text{Cu}(\text{OTf})_2$. The resulting blue/purple precipitates were isolated and crystallised from acetonitrile by slow diffusion of DIPE.⁵ The yields of the complexes were quantitative from the ligand Py_4 , 71 % from the ligand Ox_4 and 75 % from the ligand Py_2Ox_2 .



Scheme 44: Synthetic pathway to the complexes from ligands Py_4 , Py_2Ox_2 and Ox_4 . L = ligand.

3.3. Solid state characterisation of the complexes from the ligands Py_4 , Py_2Ox_2 and Ox_4

3.3.1. Crystal structure of the Cu^{II} complex from the ligand Py_4

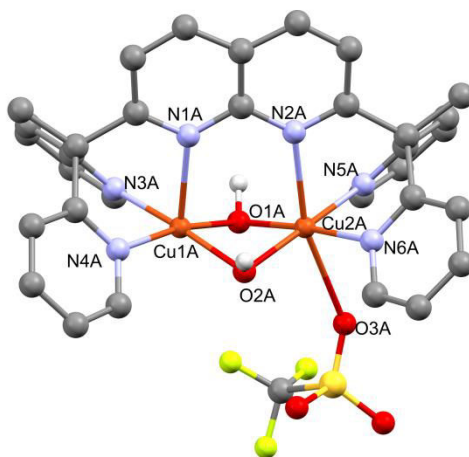


Figure 55: Crystal structure of the mono cationic part of $[\text{Cu}_2^{\text{II}}\text{Py}_4(\mu\text{-OH})_2(\text{OTf})](\text{OTf})$. The complex is named $\text{Cu}_2^{\text{II}}\text{Py}_4$. H atoms (except the hydroxido bridges) have been omitted for clarity. CCDC1449817.

The unit cell contains two independent $[\text{Cu}_2^{\text{II}}(\text{Py}_4)(\mu\text{-OH})_2(\text{OTf})](\text{OTf}) \cdot 1.8\text{CH}_3\text{CN}$ entities A and B which show no significant differences in their bond distances and angles. The cationic unit of A is

⁵ Synthesis of the complex with the ligand Ox_4 was completed by Dr. A. Thibon-Pourret and G. Gellon.

shown in Figure 55, with a list of bond distances and angles in Table 14. Each unit consists of two Cu atoms (the complex is thus named $\text{Cu}^{\text{II}}_2\text{Py}_4$) bridged by hydroxido groups with Cu1-OH-Cu2 angles in the range of 90.11–90.67°. The Cu1-Cu2 distance of 2.75 Å is one of the shortest reported for bis(μ -hydroxido)dicopper(II) complexes bridged by a spacer.^{161–163} The coordination geometry around the Cu1A atom is best described as a slightly distorted square based pyramid ($\tau = 0.08$)¹⁵³ where the axial position is occupied by the N1A of the naphthyridine atom at 2.276 Å. Because of the coordination of a triflate anion to the Cu2A atom, the two Cu atoms are not in identical coordination environments. Cu2A is found in a distorted octahedral geometry with axial positions occupied by the N2A atom at an elongated distance of 2.353 Å compared to 2.276 Å for Cu1–N1A and the O3A atom from the triflate group at 2.615 Å.

Table 14: Bond distances and angles obtained from the crystal structure of $\text{Cu}^{\text{II}}_2\text{Py}_4$.

Atom1	Atom2	Length / Å	Bond angle	Angle / °
Cu1A	Cu2A	2.751(1)	O2A-Cu1A-O1A	83.1(1)
Cu1A	O2A	1.925(3)	O2A-Cu1A-N4A	94.1(1)
Cu1A	O1A	1.936(3)	O2A-Cu1A-N1A	100.7(1)
Cu1A	N4A	1.987(4)	O2A-Cu1A-N3A	173.6(1)
Cu1A	N1A	2.276(3)	O1A-Cu1A-N4A	168.8(1)
Cu1A	N3A	1.989(3)	O1A-Cu1A-N1A	103.1(1)
Cu2A	O2A	1.946(3)	O1A-Cu1A-N3A	93.5(1)
Cu2A	O1A	1.942(2)	N4A-Cu1A-N1A	88.1(1)
Cu2A	N6A	1.978(3)	N4A-Cu1A-N3A	88.2(1)
Cu2A	N5A	1.995(4)	N1A-Cu1A-N3A	85.4(1)
Cu2A	O3A	2.615(4)	O2A-Cu2A-O1A	82.4(1)
Cu2A	N2A	2.353(4)	O2A-Cu2A-N6A	95.0(1)
			O2A-Cu2A-N5A	175.5(1)
			O2A-Cu2A-O3A	94.5(1)
			O2A-Cu2A-N2A	98.3(1)
			O1A-Cu2A-N6A	174.9(1)
			O1A-Cu2A-N5A	93.6(1)
			O1A-Cu2A-O3A	89.2(1)
			O1A-Cu2A-N2A	99.0(1)
			N6A-Cu2A-N5A	88.8(1)
			N6A-Cu2A-O3A	86.6(1)
			N6A-Cu2A-N2A	85.7(1)
			N5A-Cu2A-O3A	83.3(1)
			N5A-Cu2A-N2A	84.4(1)
			O3A-Cu2A-N2A	165.6(1)
			Cu1A-O2A-Cu2A	90.6(1)
			Cu1A-O1A-Cu2A	90.4(1)

3.3.2. Crystal structure of the Cu^{II} complex from the ligand Ox₄

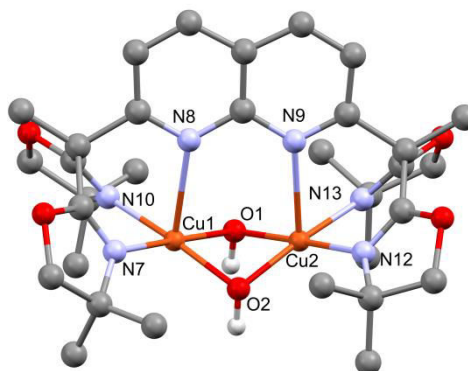


Figure 56: Crystal structure of the dication of complex $[\text{Cu}^{\text{II}}_2\text{Ox}_4(\text{OH})_2](\text{OTf})_2$. The complex is named $\text{Cu}^{\text{II}}_2\text{Ox}_4$. Hydrogens (except the hydroxido bridges) have been omitted for clarity.

Table 15: List of bond distances and angles from the crystal structure of $\text{Cu}^{\text{II}}_2\text{Ox}_4$.

Atom1	Atom2	Length / Å
Cu1	Cu2	2.7537(7)
Cu1	O1	1.940(2)
Cu1	O2	1.946(2)
Cu1	N7	1.997(2)
Cu1	N10	2.011(2)
Cu1	N8	2.460(2)
Cu2	O1	1.941(2)
Cu2	O2	1.934(2)
Cu2	N9	2.427(2)
Cu2	N12	2.016(2)
Cu2	N13	2.010(2)

Bond angle	Angle / °
O1-Cu1-O2	82.13(7)
O1-Cu1-N7	177.93(7)
O1-Cu1-N10	94.97(7)
O1-Cu1-N8	96.80(6)
O2-Cu1-N7	95.82(7)
O2-Cu1-N10	173.82(7)
O2-Cu1-N8	102.75(6)
N7-Cu1-N10	87.10(7)
N7-Cu1-N8	83.33(7)
N10-Cu1-N8	82.98(7)
O1-Cu2-O2	82.42(7)
O1-Cu2-N9	98.71(6)
O1-Cu2-N12	177.22(7)
O1-Cu2-N13	94.33(7)
O2-Cu2-N9	105.09(6)
O2-Cu2-N12	94.88(7)
O2-Cu2-N13	172.42(7)
N9-Cu2-N12	81.34(7)
N9-Cu2-N13	82.12(7)
N12-Cu2-N13	88.44(7)
Cu1-O1-Cu2	90.39(7)
Cu1-O2-Cu2	90.42(7)

The crystal structure of the dication of the complex from the ligand Ox₄ is shown in Figure 56, with a list of bond distances and angles in Table 15. The complex is dinuclear (hence named $\text{Cu}^{\text{II}}_2\text{Ox}_4$),

with the copper atoms bridged by two hydroxido groups with Cu-O-Cu angles of 90.39° and 90.42°. Each copper is also coordinated by the nitrogen atoms of the BOX groups and the nitrogen atoms of the naphthyridine. The geometries of both copper atoms are best described as square based pyramid ($\tau = 0.07$ for Cu1 and 0.08 for Cu2),¹⁵³ with N8 and N9 of the naphthyridine occupying the axial position. Although the two coppers are not crystallographically identical, they are in very similar coordination environments considering the bond distances and angles. The bond distances between the copper and the equatorial positions are of 1.93-2.02 Å and longer at 2.43-2.46 Å for the axial position. Importantly this complex also displays a short Cu-Cu distance of 2.75 Å.

3.3.3. Crystal structure of the Cu^{II} complex from the ligand Py₂Ox₂

The unit cell contains two independent [Cu^{II}₂(Py₂Ox₂)(μ-OH)₂](OTf)₂·1CH₃CN entities A and B (with a dinuclear entity named Cu^{II}₂Py₂Ox₂) which show no significant differences in their bond distances and angles. The crystal structure of entity A is displayed in Figure 57 with a list of bond distances and angles in Table 16. The Cu-Cu distance is short but slightly longer at 2.80 Å compared to complexes Cu^{II}₂Py₄ and Cu^{II}₂Ox₄ with a distance of 2.75 Å. Each copper is in a square based pyramid geometry ($\tau = 0.01$ for Cu1 and 0.02 for Cu2),¹⁵³ with the equatorial positions occupied by the hydroxido groups of the N atoms of either the pyridines or the BOX moieties and the axial position occupied by the nitrogen atoms of the naphthyridine unit. Bond distances between the copper atoms and equatorial positions are of 1.9-2.0 Å, whether as the axial bonds are longer at 2.47 Å for Cu1-N12 (the side of the BOX moiety) and 2.26 Å for Cu2-N9 (the side of the pyridine groups).

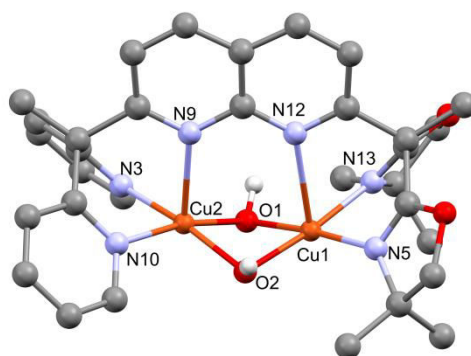


Figure 57: Crystal structure of the dication of complex [Cu^{II}₂Ox₂Py₂(OH)₂](OTf)₂. The complex is named Cu^{II}₂Py₂Ox₂. Hydrogen atoms (except the hydroxido bridges) have been omitted for clarity.

Table 16: List of bond distances and angles for the structure of the complex $\text{Cu}^{\text{II}}_2\text{Py}_2\text{Ox}_2$.

Atom1	Atom2	Length / Å	Bond angle	Angle / °
Cu1	Cu2	2.795(1)	O1-Cu1-O2	80.4(2)
Cu1	O1	1.937(5)	O1-Cu1-N5	174.9(2)
Cu1	O2	1.932(4)	O1-Cu1-N12	97.2(2)
Cu1	N5	1.978(5)	O1-Cu1-N13	94.9(2)
Cu1	N12	2.469(5)	O2-Cu1-N5	97.7(2)
Cu1	N13	2.011(5)	O2-Cu1-N12	94.4(2)
Cu2	O1	1.940(4)	O2-Cu1-N13	174.1(2)
Cu2	O2	1.929(5)	N5-Cu1-N12	87.7(2)
Cu2	N9	2.259(5)	N5-Cu1-N13	87.3(2)
Cu2	N10	1.991(4)	N12-Cu1-N13	82.6(2)
Cu2	N3	1.997(5)	O1-Cu2-O2	80.5(2)
			O1-Cu2-N9	105.2(2)
			O1-Cu2-N10	167.9(2)
			O1-Cu2-N3	93.7(2)
			O2-Cu2-N9	103.5(2)
			O2-Cu2-N10	96.1(2)
			O2-Cu2-N3	169.0(2)
			N9-Cu2-N10	86.9(2)
			N9-Cu2-N3	87.0(2)
			N10-Cu2-N3	87.6(2)
			Cu1-O1-Cu2	92.2(2)
			Cu1-O2-Cu2	92.8(2)

3.4. Solution characterisation of complexes $\text{Cu}^{\text{II}}_2\text{Py}_4$, $\text{Cu}^{\text{II}}_2\text{Ox}_4$ and $\text{Cu}^{\text{II}}_2\text{Py}_2\text{Ox}_2$

3.4.1. Characterisation of complex $\text{Cu}^{\text{II}}_2\text{Py}_4$ in acetonitrile by NMR

The crystal structure of the complex $\text{Cu}^{\text{II}}_2\text{Py}_4$ displays a triflate counterion that is coordinated to one of the copper atoms, making the complex dissymmetric. The NMR spectra of the complex in CD_3CN were therefore recorded to determine if there is any significant change in the solution structure of this complex.

The ^1H -NMR spectrum at 25°C displays a paramagnetic behaviour with seven observable signals in the range of +160 to +6 ppm (Figure 58, top left) consistent with a more symmetrical structure in solution. When the temperature is increased to 75°C, there is a sharpening and a shift of the signals towards the diamagnetic region (Figure 58 top right). The overlapping signals at 7-8 ppm

(25°C) become well resolved at 75°C and integrated to two protons at 8.25 ppm and six protons at 6.97 ppm, allowing identification of the two methyl group.

The ^1H - ^1H COSY spectrum (correlation spectroscopy) was recorded at 25°C and displays a correlation between the peaks at 12.03 and 8.10 ppm (Figure 58, bottom left). Considering their coupling and their integration value, these signals can be assigned to the protons of the naphthyridine spacer. The additional resonances at 17.21, 42.31, 54.17 and 132.6 ppm correspond to the protons of the pyridine rings that are expected to be closer to the Cu^{II} ion, which causes line broadening and precludes the observation of COSY cross signals.

The ^{19}F -NMR spectrum in the range of +460 to -140 ppm (Figure 58, bottom right) displays a single peak at +85 ppm, indicating a single fluorine environment. This result suggests that the triflate group coordinated to the copper in the crystal structure may de-coordinate in solution so that both triflate groups are in the counterion environment, however a fast exchange on the NMR time scale cannot be ruled out.

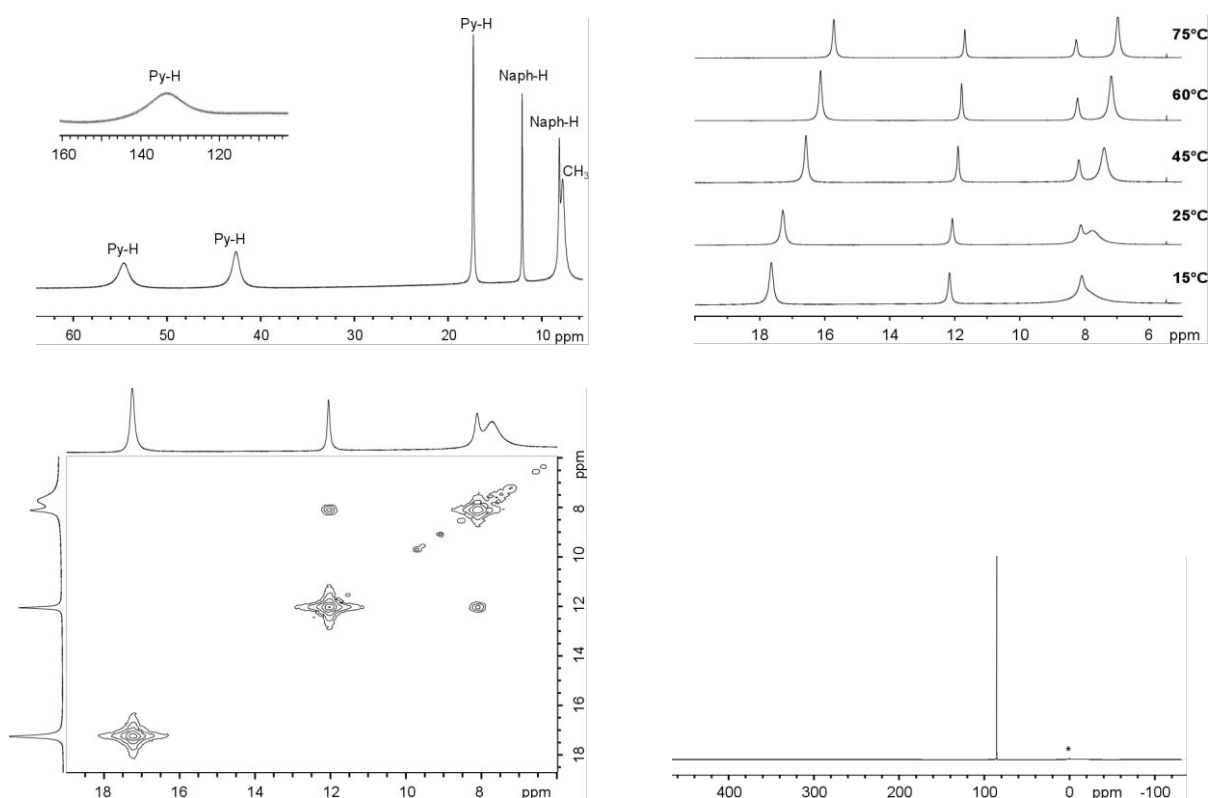


Figure 58: NMR spectra of the complex $\text{Cu}^{\text{II}}_2\text{Py}_4$, all recorded in CD_3CN . Top left: ^1H -NMR spectrum at 25°C. Top right: ^1H -NMR spectrum at variable temperature. Bottom left: COSY spectrum at 25°C. Bottom right: ^{19}F -NMR spectrum at 25°C; the small starred peak is the reference product C_6F_6 .

3.4.2. Characterisation of the complexes $\text{Cu}^{\text{II}}_2\text{Py}_4$, $\text{Cu}^{\text{II}}_2\text{Ox}_4$ and $\text{Cu}^{\text{II}}_2\text{Py}_2\text{Ox}_2$ by ESI-MS

The ESI spectra of the complexes $\text{Cu}^{\text{II}}_2\text{Py}_4$, $\text{Cu}^{\text{II}}_2\text{Ox}_4$ and $\text{Cu}^{\text{II}}_2\text{Py}_2\text{Ox}_2$ were analysed by ESI-MS in acetonitrile. Peaks are observed at $m/z = 803$, 883 and 843 corresponding to $[\text{M-OTf}]^+$ for the complexes $\text{Cu}^{\text{II}}_2\text{Py}_4$, $\text{Cu}^{\text{II}}_2\text{Ox}_4$ and $\text{Cu}^{\text{II}}_2\text{Py}_2\text{Ox}_2$ respectively, with theoretical isotopic profiles that matched those of the experiment (Figure 59, Figure 60 and Figure 61). Thus the complexes all remain dinuclear in solution.

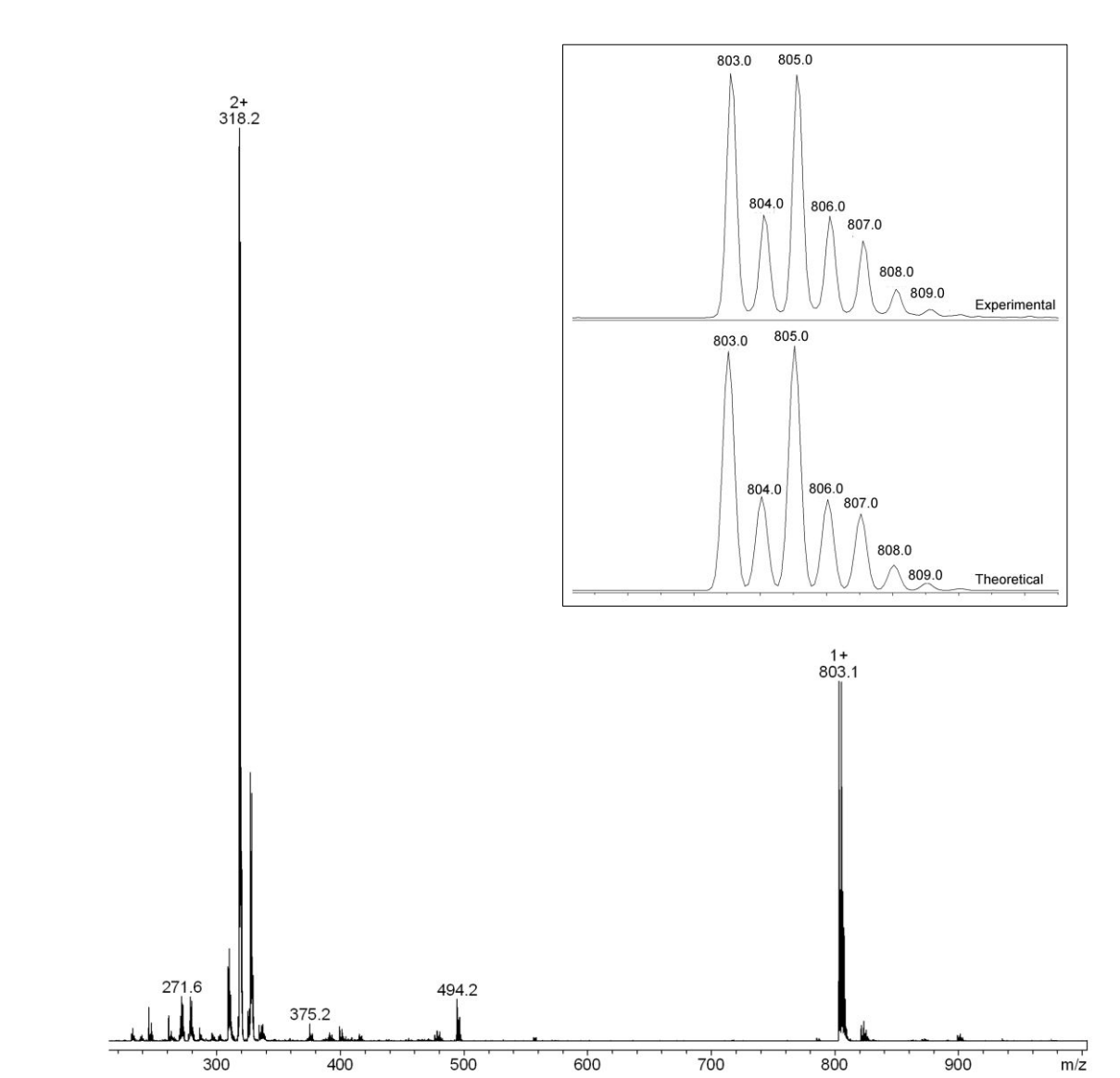


Figure 59: ESI-MS of the complex $\text{Cu}^{\text{II}}_2\text{Py}_4$ in acetonitrile. Inset: Theoretical and experimental isotopic profile of the peak $m/z = 803$.

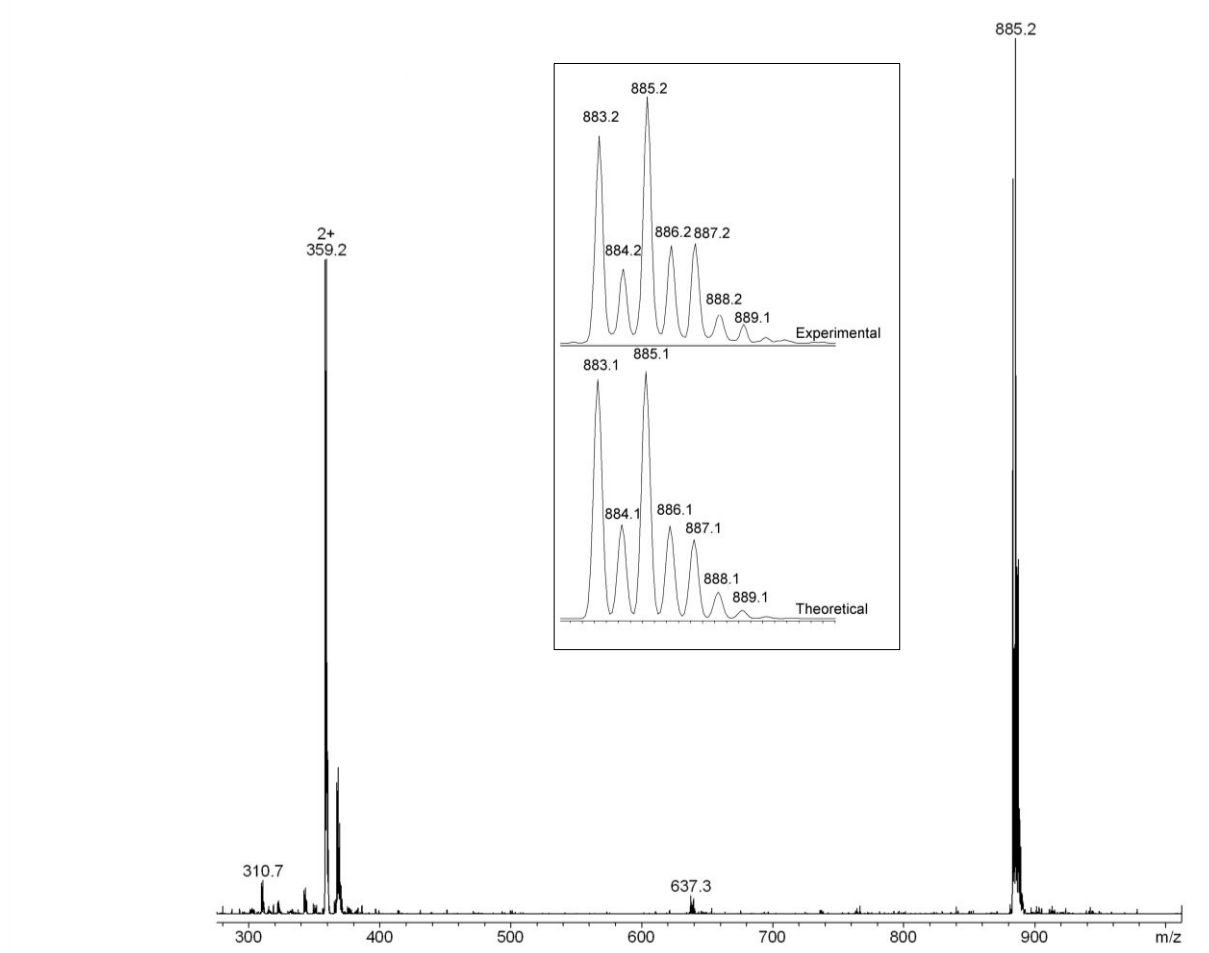


Figure 60: ESI spectrum of the complex $\text{Cu}^{\text{II}}_2\text{Ox}_4$ recorded in acetonitrile. Inset: Theoretical and experimental isotopic profile of the peak at $m/z = 885$.

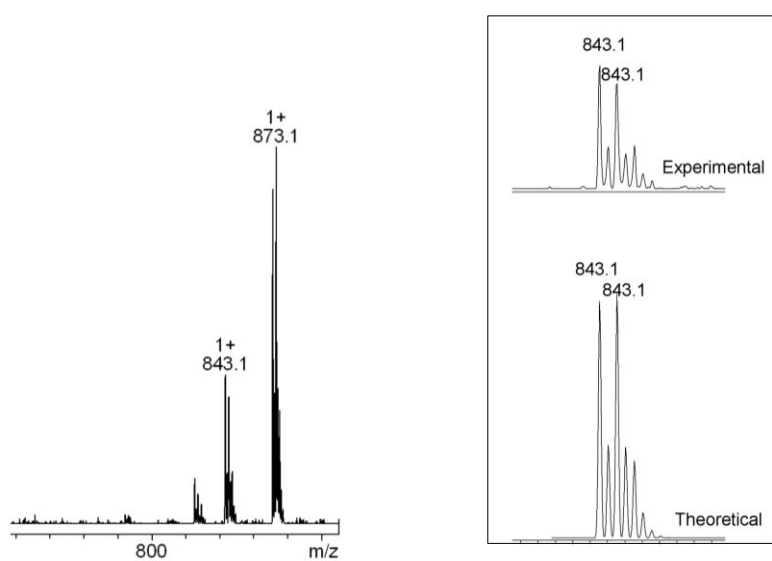


Figure 61: Left: ESI-MS spectrum of the complex $\text{Cu}^{\text{II}}_2\text{Py}_2\text{Ox}_2$ recorded in acetonitrile. Right: Theoretical and experimental isotopic profiles obtained for the peak at $m/z = 843$.

3.5. Effect of oxidation on the complexes $\text{Cu}^{\text{II}}_2\text{Py}_4$, $\text{Cu}^{\text{II}}_2\text{Ox}_4$ and $\text{Cu}^{\text{II}}_2\text{Py}_2\text{Ox}_2$

3.5.1. CV of the complexes $\text{Cu}^{\text{II}}_2\text{Py}_4$, $\text{Cu}^{\text{II}}_2\text{Ox}_4$ and $\text{Cu}^{\text{II}}_2\text{Py}_2\text{Ox}_2$

3.5.1.1. Room temperature CV

The room temperature CV in a 0.1 M solution of NBu_4ClO_4 / acetonitrile of all three complexes display an oxidation wave that is irreversible at low scan rates but becomes reversible at $\nu > 100 \text{ mV}\cdot\text{s}^{-1}$ (Figure 62). The complex $\text{Cu}^{\text{II}}_2\text{Ox}_4$ shows a loss of reversibility at higher scan rates than complexes $\text{Cu}^{\text{II}}_2\text{Py}_4$ and $\text{Cu}^{\text{II}}_2\text{Py}_2\text{Ox}_2$ and is completely irreversible at $\nu = 10 \text{ mV}\cdot\text{s}^{-1}$. The oxidation potentials of the complexes $\text{Cu}^{\text{II}}_2\text{Py}_4$, $\text{Cu}^{\text{II}}_2\text{Ox}_4$ and $\text{Cu}^{\text{II}}_2\text{Py}_2\text{Ox}_2$ are high at $E_{1/2}$ (formal reduction potential) = 1.12 V, 1.27 V and 1.09 V vs. Fc^+/Fc respectively, making them all out of reach of commonly used chemical oxidants.¹⁶⁴

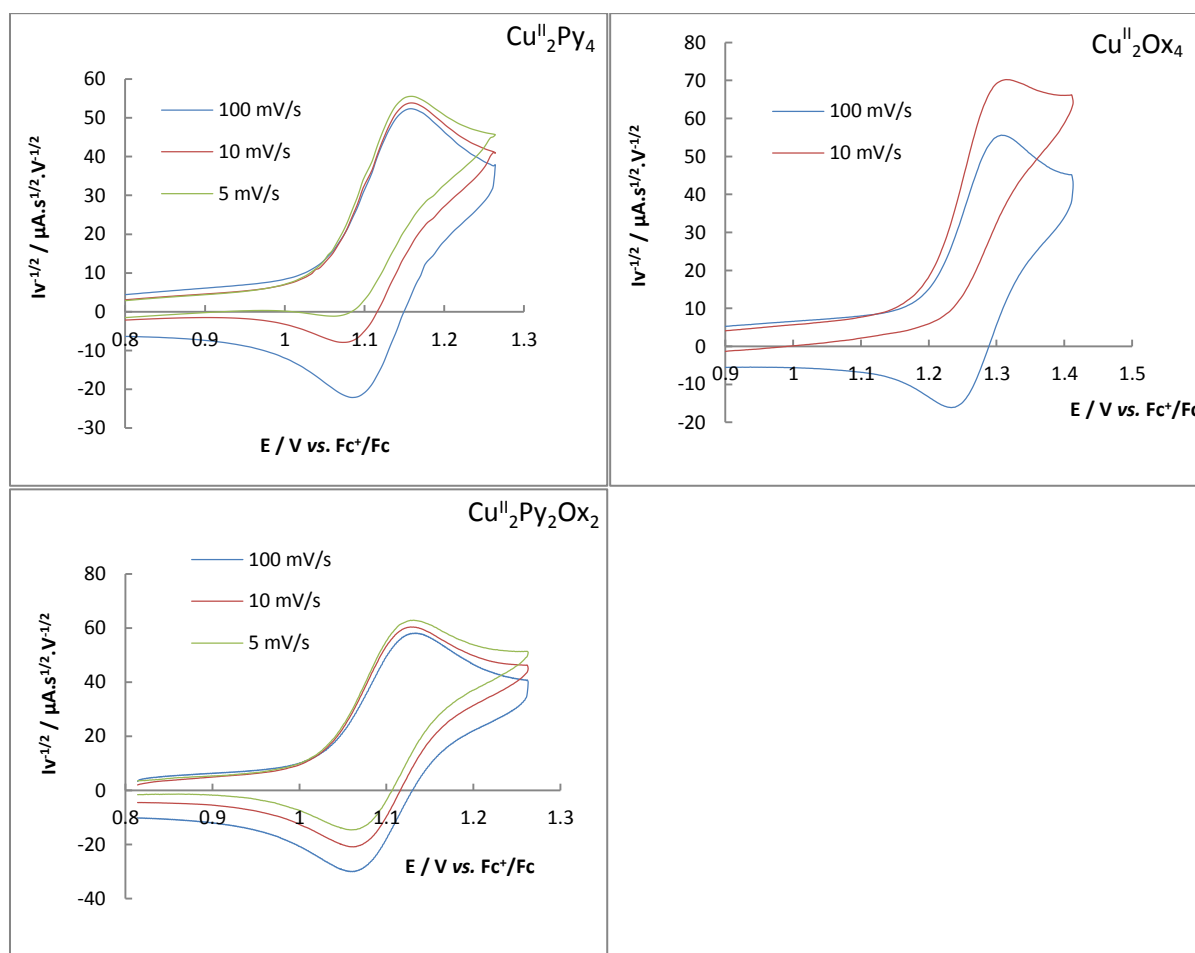


Figure 62: Scan rate normalised CV for the complexes $\text{Cu}^{\text{II}}_2\text{Py}_4$ (top left), $\text{Cu}^{\text{II}}_2\text{Ox}_4$ (top right) and $\text{Cu}^{\text{II}}_2\text{Py}_2\text{Ox}_2$ (bottom). Parameters: 0.1 M NBu_4ClO_4 in acetonitrile; concentration of complexes = 0.1 mM; room temperature; scan rates $100 \text{ mV}\cdot\text{s}^{-1}$ (blue), $10 \text{ mV}\cdot\text{s}^{-1}$ (red) and $5 \text{ mV}\cdot\text{s}^{-1}$ (green).

Plots of the normalised peak current $I_p v^{-1/2}$ (where I_p is the peak current on the CV) against the scan rate v (Figure 63, left) showed an increase in I_p at lower scan rates, indicative of an ECE mechanism where the oxidation of the complex is followed by a chemical reaction on the time scale of the experiment forming a new species, which in turn can be oxidised. The oxidation of the three complexes therefore involves the formation of a transient oxidised species that has a half-life of several seconds at room temperature.

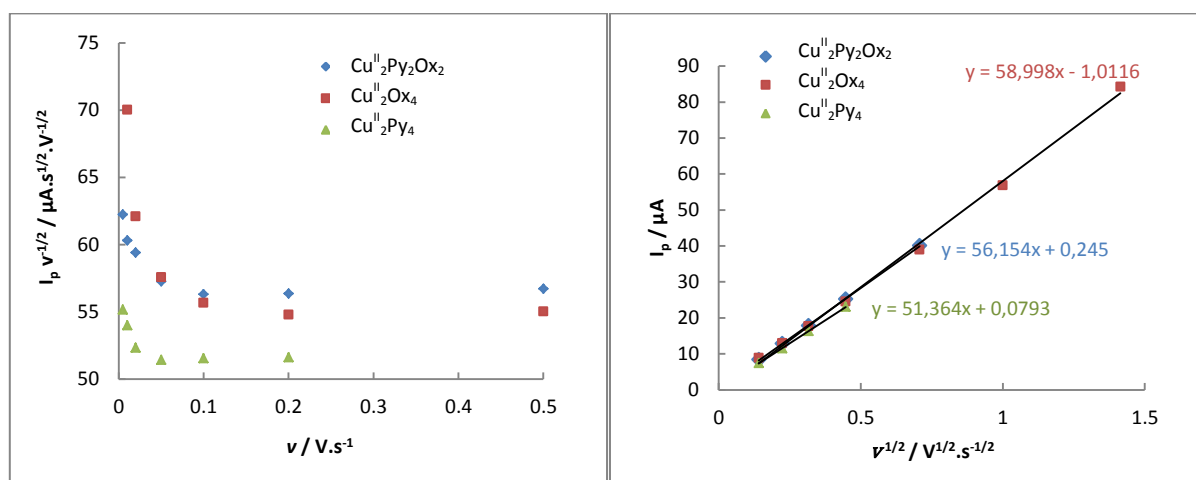


Figure 63: left: plots of current function ($I_p \cdot v^{-1/2}$) against v . Right: plot of I_p against $v^{1/2}$ for scan rates greater than 0.02 $V \cdot s^{-1}$. Parameters: NBu_4ClO_4 in acetonitrile (0.1 M); concentration of complexes $Cu^{II}Py_4$, $Cu^{II}Ox_4$ and $Cu^{II}Py_2Ox_2 = 0.85$ mM, 0.68 mM, 0.70 mM respectively; working electrode: glassy carbon.

3.5.1.2. Determining the number of electrons for the oxidation processes

With the aim of determining the number of electrons involved in the oxidation process, the diffusion coefficients of the complexes needed to be determined by NMR DOSY^h (diffusion ordered spectroscopy) experiments. The value of $1.0 (\pm 0.1) \times 10^5 \text{ cm}^2 \cdot \text{s}^{-1}$ was obtained for the complex $Cu^{II}Py_4$ (0.012 M) in a 0.1 M solution of KPF_6 in CD_3CN at 25°C (Figure 64). Due to the similarities between the complexes $Cu^{II}Py_4$, $Cu^{II}Ox_4$ and $Cu^{II}Py_2Ox_2$ (same charge and similar size), the value of the diffusion coefficient was used for all three complexes.

^h NMR DOSY experiment completed by B. Gennaro.

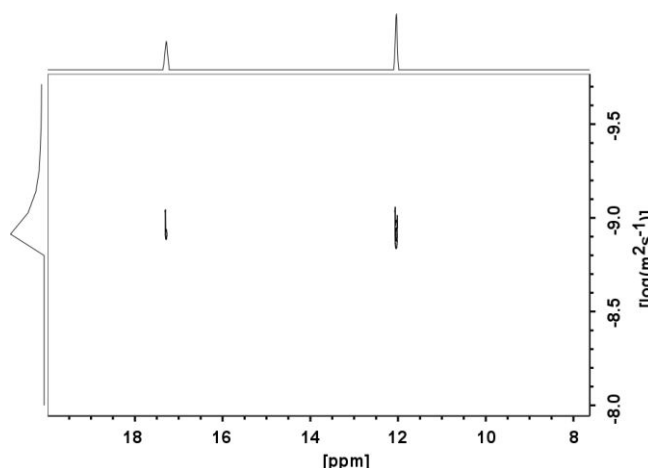


Figure 64: NMR DOSY experiment for the complex $\text{Cu}^{\text{II}}\text{Py}_4$ (0.01 M) in a 0.1 M solution of KPF_6 in CD_3CN at 25°C .

The number of electrons was determined for the oxidation process of each complex by using the Randles-Sevcik Equation 1 (valid for $T = 298\text{ K}$),¹⁶⁵ where I_p is the peak potential (A) at a certain scan rate ν ($\text{V}\cdot\text{s}^{-1}$), n is the number of electrons involved, A is the surface area of the electrode (cm^2), D ($\text{cm}^2\cdot\text{s}^{-1}$) is the diffusion coefficient of the complex and C is the bulk concentration of the complex in solution ($\text{mol}\cdot\text{cm}^{-3}$).

Equation 1:

$$I_p = (2.69 \times 10^5)n^{3/2}AD^{1/2}\nu^{1/2}C$$

I_p was plotted against $\nu^{1/2}$ for all three complexes (Figure 63, right). Values of $A = 0,071\text{ cm}^2$, and concentrations of 0.85, 0.68 and 0.7 mM for the complexes $\text{Cu}^{\text{II}}\text{Py}_4$, $\text{Cu}^{\text{II}}_2\text{Ox}_4$ and $\text{Cu}^{\text{II}}_2\text{Py}_2\text{Ox}_2$ gave values of $n = 1.0$, 1.3 and 1.2 respectively indicating a mono-electronic oxidation for all three complexes.

3.5.2. Characterisation of the mono-electronic oxidised species

3.5.2.1. EPR characterisation of the mono-oxidised species

The one electron oxidised species was generated at -40°C by bulk electrolysis of the complexes (0.7 mM) in a 0.1 M NBU_4ClO_4 / acetonitrile solution to the potentials of 1.26 V vs. Fc^+/Fc for the complexes $\text{Cu}^{\text{II}}_2\text{Py}_4$ and $\text{Cu}^{\text{II}}_2\text{Py}_2\text{Ox}_2$ and 1.41 V vs. Fc^+/Fc for the complex $\text{Cu}^{\text{II}}_2\text{Ox}_4$. Bulk oxidation was accompanied by a colour change from pale blue/colourless to bright yellow for the complexes $\text{Cu}^{\text{II}}_2\text{Py}_4$ and $\text{Cu}^{\text{II}}_2\text{Py}_2\text{Ox}_2$ and colourless to brown for the complex $\text{Cu}^{\text{II}}_2\text{Ox}_4$. Samples were taken out during the course of the electrolysis (every 5 minutes) and immediately frozen in liquid nitrogen, and

their EPR spectra recorded. The oxidised species was also heated to room temperature then frozen in liquid nitrogen to obtain the EPR spectrum of the end product. Before electrolysis, all three complexes are EPR silent (acetonitrile, 100 K). The EPR spectra after electrolysis are displayed in Figure 65, along with the spectrum of the product heated to room temperature. All spectra presented in Figure 65 are recorded at 15 K, but the same features are observed in the range of 15 - 100 K.

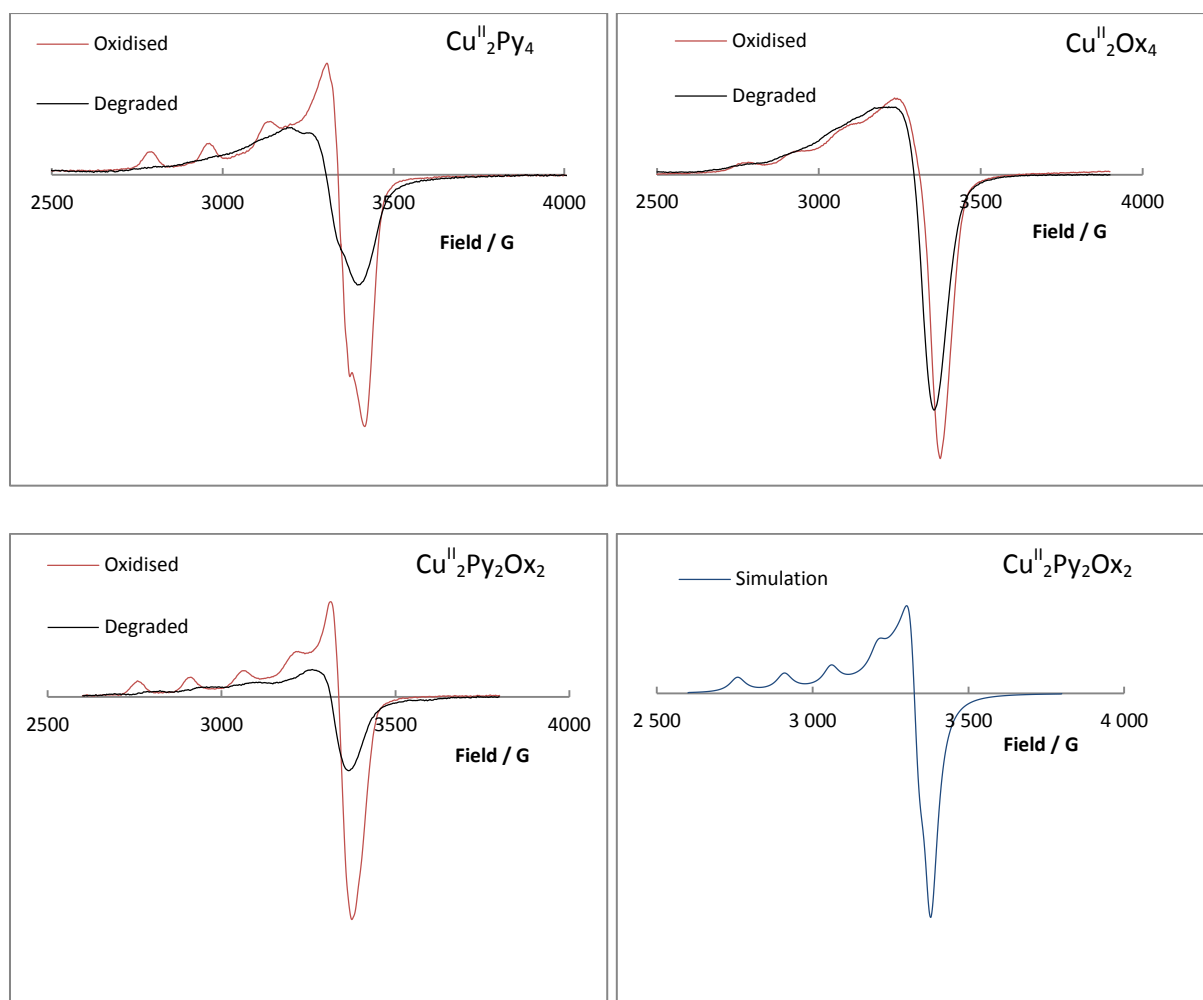


Figure 65: EPR spectra of the complexes $\text{Cu}^{\text{II}}\text{Py}_4$, $\text{Cu}^{\text{II}}\text{Ox}_4$ and $\text{Cu}^{\text{II}}\text{Py}_2\text{Ox}_2$ after bulk electrolysis at -40°C (oxidised), and after heating to room temperature (black). Bottom right: example of the simulation obtained from the oxidised spectrum of $\text{Cu}^{\text{II}}\text{Py}_2\text{Ox}_2$ (using the software EasySpin). Parameters: frozen solution of 0.7 mM of the respective complex in 0.1 M NBu_4ClO_4 in acetonitrile; $T = 15\text{ K}$; frequency = 9.419 GHz.

Upon mono-electronic oxidation the complexes $\text{Cu}^{\text{II}}\text{Py}_4$ and $\text{Cu}^{\text{II}}\text{Py}_2\text{Ox}_2$ display four clear lines (Figure 65) with coupling constants A_{\parallel} of 174 and 173 G respectively, the typical EPR spectrum for a single Cu^{II} complex in an axial geometry (an unpaired electron coupling to the nuclear spin of one

copper with $I = \frac{3}{2}$). This is consistent with a valence localised $\text{Cu}^{\text{II}}\text{Cu}^{\text{III}}$ species (the Cu^{III} being EPR silent), defined as a class I in the Robin Day classification system (where class II and class III represent moderate and significant delocalisation respectively). The spectrum of the oxidised $\text{Cu}^{\text{II}}_2\text{Ox}_4$ complex is less resolved but four lines are still observable ($A_{\parallel} = 177$ G). The lack of resolution of the signal from complex $\text{Cu}^{\text{II}}_2\text{Ox}_4$ could be due to the greater instability of the mono-oxidised species that can also be observed by a lower reversibility of the CV at room temperature compared to the complexes $\text{Cu}^{\text{II}}_2\text{Py}_4$ and $\text{Cu}^{\text{II}}_2\text{Py}_2\text{Ox}_2$ (Figure 62). The EPR parameters of the spectra (with $g_x = g_y = g_{\perp}$ and $g_z = g_{\parallel}$) (Table 17) extracted after simulation indicate a Cu^{II} in an axial geometry in all three cases. It is therefore clear that mono-oxidation of the complexes $\text{Cu}^{\text{II}}_2\text{Py}_4$, $\text{Cu}^{\text{II}}_2\text{Py}_2\text{Ox}_2$ and $\text{Cu}^{\text{II}}_2\text{Py}_4$ lead to the formation of mixed valent $\text{Cu}^{\text{II}}\text{Cu}^{\text{III}}$ species. After the oxidised samples had been heated to room temperature, the recorded spectra of all three complexes display broad signals indicating a mix of several Cu^{II} complexes in solution.

Table 17: Parameters obtained from simulation of the mono-oxidised species of the complexes $\text{Cu}^{\text{II}}_2\text{Py}_4$, $\text{Cu}^{\text{II}}_2\text{Ox}_4$ and $\text{Cu}^{\text{II}}_2\text{Py}_2\text{Ox}_2$. The software Easyspin was used for the simulation of the spectra from $\text{Cu}^{\text{II}}_2\text{Ox}_4$ and $\text{Cu}^{\text{II}}_2\text{Py}_2\text{Ox}_2$ and Simfonia for the spectrum of $\text{Cu}^{\text{II}}_2\text{Py}_4$.

Complex	$\text{Cu}^{\text{II}}_2\text{Py}_4$	$\text{Cu}^{\text{II}}_2\text{Ox}_4$	$\text{Cu}^{\text{II}}_2\text{Py}_2\text{Ox}_2$
g_{\parallel}	2.210	2.291	2.307
g_{\perp}	2.020 (g_x), 2.015 (g_y)	2.070	2.065
A_{\parallel} / G	174	177	173
A_{\perp} / G	40 (A_x), 10 (A_y)	18	0

3.5.2.2. Spectroelectrochemistry of the complexes $\text{Cu}^{\text{II}}_2\text{Py}_4$, $\text{Cu}^{\text{II}}_2\text{Ox}_4$ and $\text{Cu}^{\text{II}}_2\text{Py}_2\text{Ox}_2$.

The complexes $\text{Cu}^{\text{II}}_2\text{Py}_4$, $\text{Cu}^{\text{II}}_2\text{Ox}_4$ and $\text{Cu}^{\text{II}}_2\text{Py}_2\text{Ox}_2$ were characterised by time resolved spectroelectrochemistry in order to further characterise the mono-oxidised species.ⁱ The advantage of using thin layer UV-vis-NIR spectroelectrochemistry is that the spectra of unstable species can be obtained on the time scale of a CV, as opposed to bulk electrolysis which can take tens of minutes to oxidise or reduce a sample. A home-designed cell was used where the electrode reflects the beam from the UV-vis-NIR, hence the optical absorption spectra are recorded right at the surface of the electrode. The optical length is very small (0.2 mm), hence high concentrations of the complex are required.

The complexes $\text{Cu}^{\text{II}}_2\text{Ox}_4$ and $\text{Cu}^{\text{II}}_2\text{Py}_2\text{Ox}_2$ were characterised at room temperature in a 0.1 M dry solution of NBU_4ClO_4 in acetonitrile whether as the complex $\text{Cu}^{\text{II}}_2\text{Py}_4$ was characterised at -40 °C in a

ⁱ In collaboration with Dr. N. Le Poul.

0.1 M dry solution of NBu_4PF_6 in acetonitrile, all experiments completed in a glove box. Concentrations of 10 mM, 6.8 mM and 7.0 mM were used for the complexes $\text{Cu}^{\text{II}}_2\text{Py}_4$, $\text{Cu}^{\text{II}}_2\text{Ox}_4$ and $\text{Cu}^{\text{II}}_2\text{Py}_2\text{Ox}_2$ respectively. The UV-vis/NIR (near infra-red) spectra of the mono-oxidised species of complex $\text{Cu}^{\text{II}}_2\text{Py}_4$ were obtained by applying a potential of 2.1 V vs. Fc^+/Fc then switching the potential to 0.8 V vs. Fc^+/Fc (below the oxidation potential of the complex). The potential vs. time, the corresponding current vs. time plot and the UV-vis/NIR spectra are displayed in Figure 66. The UV-vis/NIR spectra of the oxidised species of complexes $\text{Cu}^{\text{II}}_2\text{Ox}_4$ and $\text{Cu}^{\text{II}}_2\text{Py}_2\text{Ox}_2$ were generated by gradually increasing the voltage above that of the complex then decreasing again (as with a CV). The CV and the corresponding time vs. current, UV-vis and NIR spectra for the complexes $\text{Cu}^{\text{II}}_2\text{Ox}_4$ and $\text{Cu}^{\text{II}}_2\text{Py}_2\text{Ox}_2$ are displayed in Figure 67 and Figure 68 respectively.

1. Spectra of the mono-oxidised species from complex $\text{Cu}^{\text{II}}_2\text{Py}_4$

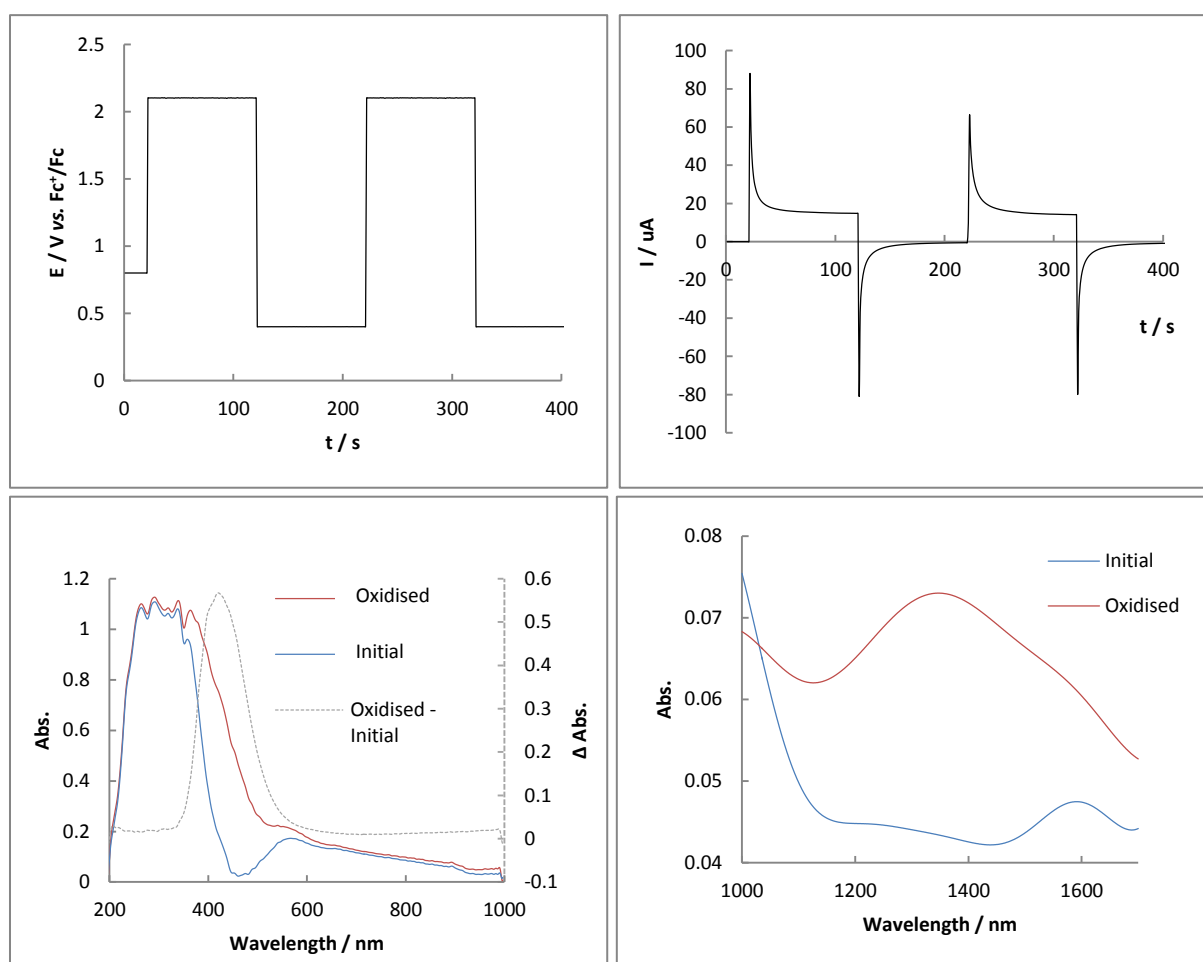


Figure 66: Spectroelectrochemistry of the complex $\text{Cu}^{\text{II}}_2\text{Py}_4$. Top: plot of the potential applied (left) and current (right) against time. Bottom left: UV-vis of the initial and oxidised species, along with the band obtained upon subtraction. Bottom right: NIR of the initial and oxidised species. Parameters: Concentration of complex = 10 mM; solvent: 0.1 M NBu_4PF_6 in acetonitrile; $l = 0.2$ mm; working electrode: Pt; $T = -40^\circ\text{C}$.

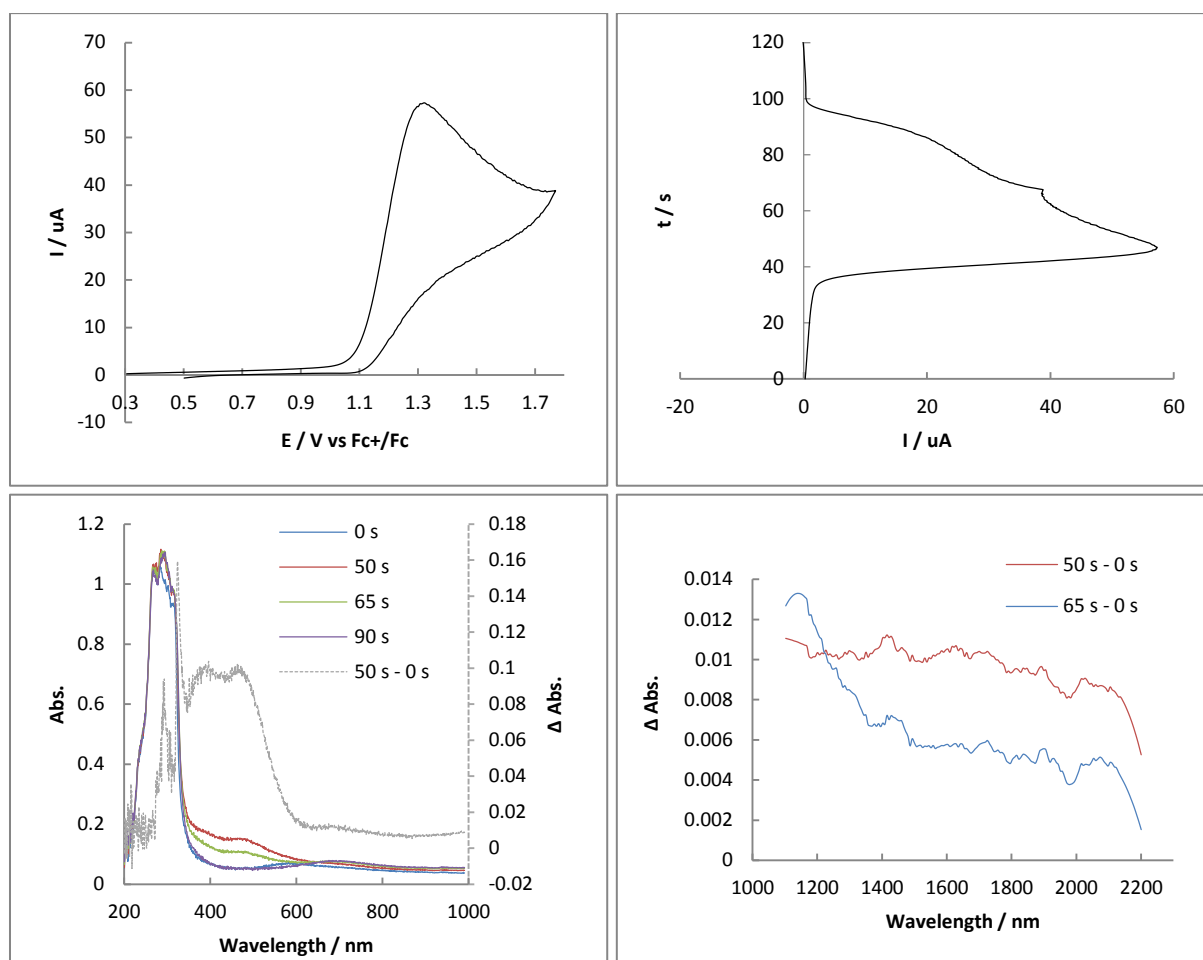
2. Spectra of the mono-oxidised species from complex $\text{Cu}^{\text{II}}\text{Ox}_4$ 

Figure 67: Room temperature spectroelectrochemistry of the complex $\text{Cu}^{\text{II}}\text{Ox}_4$. Top left: CV. Top right: Current vs. t for the CV. Bottom right: UV-vis spectra at different time intervals, along with the band obtained upon subtraction. Bottom right: NIR spectra obtained by subtraction. Parameters: concentration of complex = 6.8 mM; solvent: 0.1 M solution of NBu_4ClO_4 in acetonitrile; $v = 30 \text{ mV}\cdot\text{s}^{-1}$; $l = 0.2 \text{ mm}$; working electrode: Pt; room temperature.

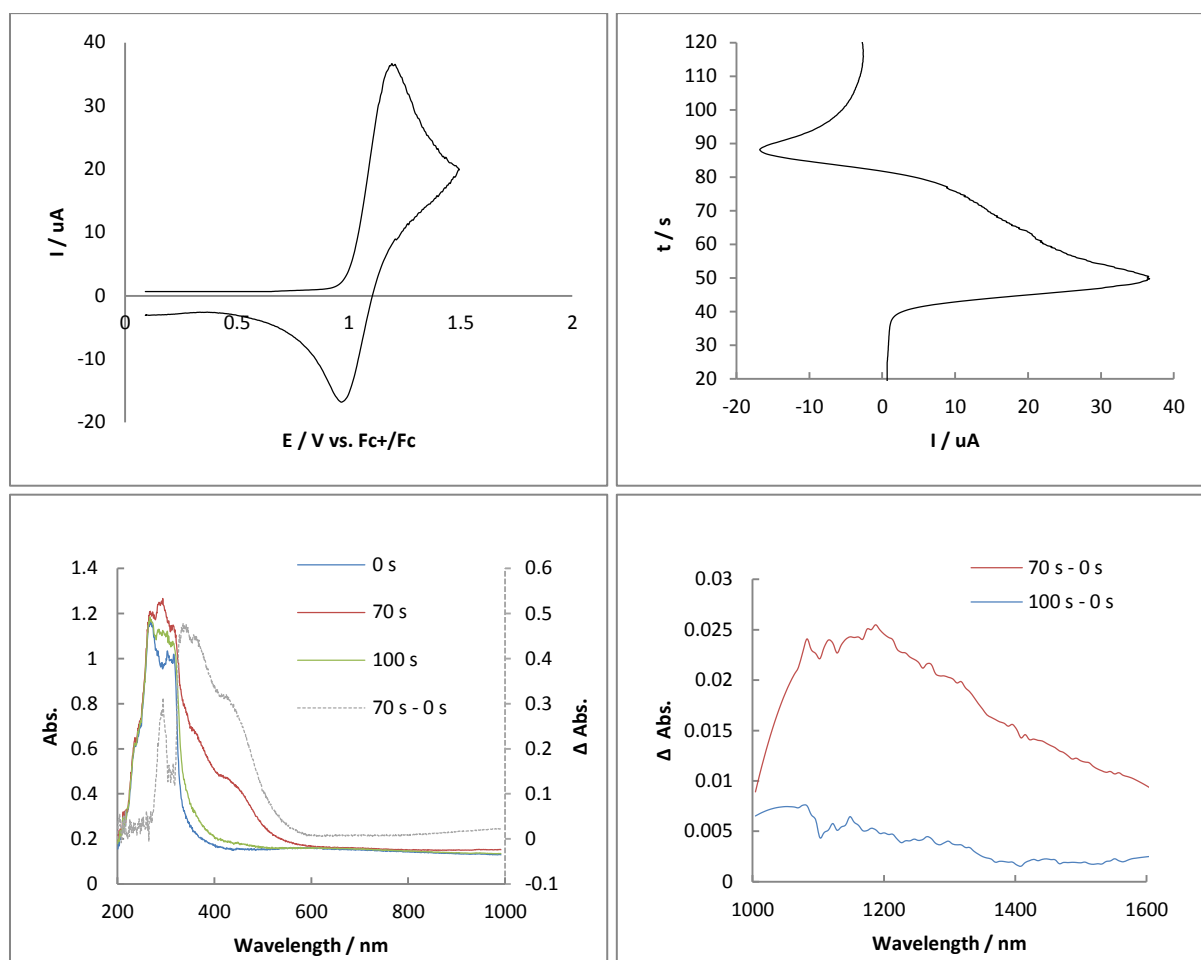
3. Spectra of the mono-oxidised species from complex $\text{Cu}^{\text{II}}_2\text{Py}_2\text{Ox}_2$ 

Figure 68: Room temperature spectroelectrochemistry of the complex $\text{Cu}^{\text{II}}_2\text{Py}_2\text{Ox}_2$. Top left: CV. Top right: Current vs. time. Bottom left: UV-vis at different time intervals. Bottom right: NIR spectra at different time intervals obtained by subtraction. Parameters: concentration of complex = 7.0 mM; solvent: 0.1 M NBu_4ClO_4 in acetonitrile; $v = 30 \text{ mV}\cdot\text{s}^{-1}$; $l = 0.2 \text{ mm}$; working electrode: Pt; room temperature.

4. Summary of the bands observed on the optical absorption spectra

All three complexes display similar features upon mono-oxidation. Bands in the NIR and UV-vis are summarised in Table 18. Bands on the UV-vis spectra of the mono-oxidised species are centred at 424 nm ($\epsilon = 1250 \text{ M}^{-1}\cdot\text{cm}^{-1}$) for $\text{Cu}^{\text{II}}_2\text{Py}_4$, 380 and 480 nm (both $735 \text{ M}^{-1}\cdot\text{cm}^{-1}$) for $\text{Cu}^{\text{II}}_2\text{Ox}_4$ and 360 nm ($3420 \text{ M}^{-1}\cdot\text{cm}^{-1}$) with a shoulder at 424 nm ($2140 \text{ M}^{-1}\cdot\text{cm}^{-1}$) for $\text{Cu}^{\text{II}}_2\text{Py}_2\text{Ox}_2$. Low intensity bands in the near infra-red (NIR) region centred at 1350 nm ($90 \text{ M}^{-1}\cdot\text{cm}^{-1}$), 1630 nm ($45 \text{ M}^{-1}\cdot\text{cm}^{-1}$) and 1185 nm ($120 \text{ M}^{-1}\cdot\text{cm}^{-1}$) were observed for the complexes $\text{Cu}^{\text{II}}_2\text{Py}_4$, $\text{Cu}^{\text{II}}_2\text{Ox}_4$ and $\text{Cu}^{\text{II}}_2\text{Py}_2\text{Ox}_2$ respectively and were attributed to the mono-oxidised species. This was confirmed by the observation that all bands described disappeared when the potential was reduced below the reduction potential of the complexes.

Table 18: Bands in the UV-vis and NIR with corresponding values of ϵ for the oxidised species of complexes $\text{Cu}^{\text{II}}_2\text{Py}_4$, $\text{Cu}^{\text{II}}_2\text{Ox}_4$, and $\text{Cu}^{\text{II}}_2\text{Py}_2\text{Ox}_2$.

Complex	UV-vis band wavelength / nm	UV-vis $\epsilon / \text{M}^{-1}.\text{cm}^{-1}$	NIR band wavelength / nm	NIR $\epsilon / \text{M}^{-1}.\text{cm}^{-1}$
$[\text{Cu}^{\text{II}}\text{Cu}^{\text{III}}\text{Py}_4]^+$	424	1250	1350	90
$[\text{Cu}^{\text{II}}\text{Cu}^{\text{III}}\text{Ox}_4]^+$	380, 480	735, 735	1630	45
$[\text{Cu}^{\text{II}}\text{Cu}^{\text{III}}\text{Py}_2\text{Ox}_2]^+$	360, (424)	3420, (2140)	1185	120

5. Determination of the localisation of the charge in the $\text{Cu}^{\text{II}}\text{Cu}^{\text{III}}$ species from complexes $\text{Cu}^{\text{II}}_2\text{Py}_4$, $\text{Cu}^{\text{II}}_2\text{Ox}_4$ and $\text{Cu}^{\text{II}}_2\text{Py}_2\text{Ox}_2$

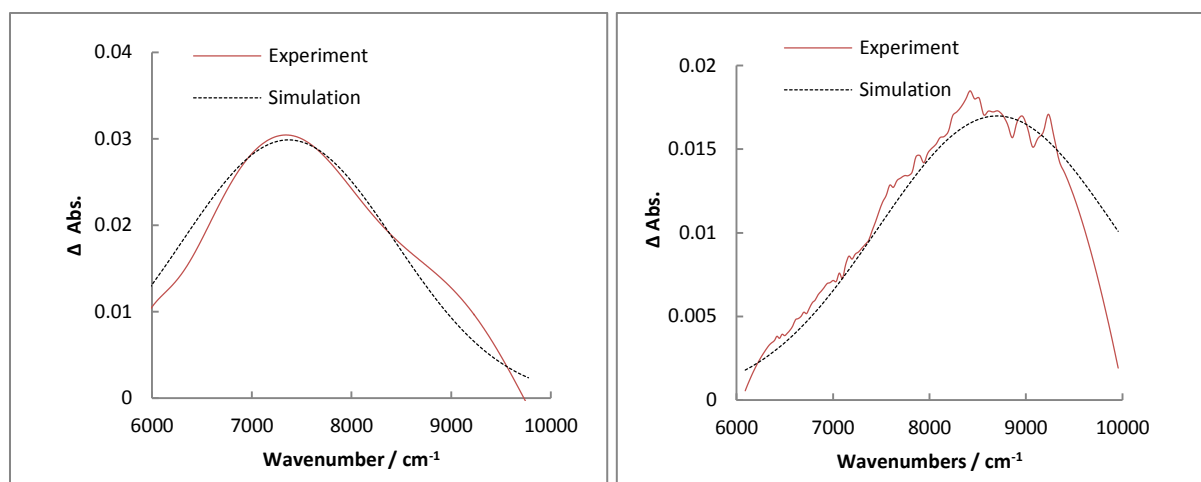


Figure 69: NIR bands of the oxidised species (obtained by subtraction of the spectrum of the oxidised species from the initial species) of the complexes $\text{Cu}^{\text{II}}_2\text{Py}_4$ (left) and $\text{Cu}^{\text{II}}_2\text{Py}_2\text{Ox}_2$ (right) along with fitted Gaussian distribution curves. Parameters for the simulation of a Gaussian distribution curve: $\text{Cu}^{\text{II}}_2\text{Py}_4$: $y_0 = 0$; $x_c = 7370$; $w = 2410$; $A = 80$. $\text{Cu}^{\text{II}}_2\text{Py}_2\text{Ox}_2$: $y_0 = 0$; $x_c = 8700$; $w = 2460$; $A = 52$.

The NIR bands observed upon oxidation of the complexes $\text{Cu}^{\text{II}}_2\text{Py}_2\text{Ox}_2$ and $\text{Cu}^{\text{II}}_2\text{Py}_4$ could be fitted with a Gaussian distribution curve (Equation 2) with the parameters $y_0 = 0$; $x_c = 7370$; $w = 2410$; $A = 80$ for the complex $\text{Cu}^{\text{II}}_2\text{Py}_4$ and $y_0 = 0$; $x_c = 8700$; $w = 2460$; $A = 52$ for the complex $\text{Cu}^{\text{II}}_2\text{Py}_2\text{Ox}_2$ (see Figure 69). Unfortunately the NIR band observed after oxidation of complex $\text{Cu}^{\text{II}}_2\text{Ox}_4$ could not be fitted, preventing more rigorous analysis.

Equation 2:

$$y = y_0 + \frac{A}{w\sqrt{\pi/2}} e^{-2\frac{(x-x_c)^2}{w^2}}$$

The electronic coupling matrix¹⁶⁶ element H_{AB} can be determined from Mulliken-Hush Equation 3.

Equation 3:

$$H_{AB} = \frac{0.0206 (\varepsilon_{max} \check{\nu}_{max} \Delta\check{\nu}_{1/2,exp})^{1/2}}{R_{AB}}$$

ε_{max} is the maximum absorption coefficient / $M^{-1}.cm^{-1}$

$\check{\nu}_{max}$ is the band energy at the maximum / cm^{-1}

$\Delta\check{\nu}_{1/2,exp}$ is the band width at half height / cm^{-1}

R_{AB} is the distance of electron transfer / Å

The value of $\varepsilon_{max} = 90 M^{-1}.cm^{-1}$, $\check{\nu}_{max} = 7370 cm^{-1}$, $\Delta\check{\nu}_{1/2,exp} = 2520 cm^{-1}$ and $R_{AB} = 2.75 \text{ Å}$ gave the value H_{AB} of $305 cm^{-1}$ for $[Cu^{II}Cu^{III}Py_4]^+$ and $\varepsilon_{max} = 120 M^{-1}.cm^{-1}$, $\check{\nu}_{max} = 8700 cm^{-1}$, $\Delta\check{\nu}_{1/2,exp} = 2460 cm^{-1}$ and $R_{AB} = 2.75 \text{ Å}$ gave the value H_{AB} of $380 cm^{-1}$ for $[Cu^{II}Cu^{III}Py_2Ox_2]^+$. As the values are both positive, there is a certain amount of delocalisation in both complexes indicating that the complexes are both class II or III in the Robin Day classification system (where class I is completely localised, class II is intermediate and class III is completely delocalised).¹⁶⁷

The Γ parameter also gives information on the degree of delocalisation of a mixed valent species: for class I $\Gamma = 0$, for class II $0 < \Gamma < 0.5$ and $\Gamma > 0.5$ for a class III system. The Γ parameter can be determined using Equation 4.

Equation 4:

$$\Gamma = 1 - \frac{(\Delta\check{\nu}_{1/2,exp})}{(\Delta\check{\nu}_{1/2,theo})}$$

Where $(\Delta\check{\nu}_{1/2,theo})$ is given by Equation 5.

Equation 5:

$$\Delta\check{\nu}_{1/2,theo} = (2310\check{\nu}_{max})^{1/2}$$

For the complex $[Cu^{II}Cu^{III}Py_4]^+$, $\check{\nu}_{max} = 7370 cm^{-1}$ giving the value $\Delta\check{\nu}_{1/2,theo} = 4125 cm^{-1}$. This value and the experimentally measured value $\Delta\check{\nu}_{1/2,exp} = 2520 cm^{-1}$ gave a value of $\Gamma = 0.39$, indicating that the complex is a class II (slightly delocalised) in the Robin Day classification system at a temperature of $-40^\circ C$. With a similar analysis for the complex $[Cu^{II}Cu^{III}Py_2Ox_2]^+$: $\check{\nu}_{max} = 8700 cm^{-1}$ so $\Delta\check{\nu}_{1/2,theo} = 4125 cm^{-1}$, $\Delta\check{\nu}_{1/2,exp} = 2460 cm^{-1}$ and hence $\Gamma = 0.45$, making the $Cu^{II}Cu^{III}$ complex on the class II/class III boundary at room temperature (Table 19).

Table 19: Summary of the values obtained for the electronic coupling matrix, the Γ parameter and the assignment of class in the Robin Day classification system from the bands observed in the NIR of the complexes $[\text{Cu}^{\text{II}}\text{Cu}^{\text{III}}\text{Py}_4]^+$ and $[\text{Cu}^{\text{II}}\text{Cu}^{\text{III}}\text{Py}_2\text{Ox}_2]^+$.

Complex	Temperature of measurement / °C	H_{AB} / cm^{-1}	Γ	Class
$[\text{Cu}^{\text{II}}\text{Cu}^{\text{III}}\text{Py}_4]^+$	-40	305	0.39	II
$[\text{Cu}^{\text{II}}\text{Cu}^{\text{III}}\text{Py}_2\text{Ox}_2]^+$	25	380	0.45	II/III

3.5.2.3. Theoretical calculations on the mono-oxidised species of complex $\text{Cu}^{\text{II}}_2\text{Py}_4$

Theoretical calculations were completed in order to determine the electronic structure, redox potential and UV-vis spectroscopic features of the mono-oxidised species.^j To determine the oxidation potential, the absolute oxidation potential was determined using Equation 6.

Equation 6:

$$E_{cal}^{abs} = \frac{-(\Delta G_{solv})}{nF}$$

E_{cal}^{abs} is the calculated absolute potential

ΔG_{solv} is the Gibbs free energy of the reaction in solution

n is the number of electrons

F is Faraday's constant

The absolute value of the oxidation potential can then be calibrated against a reference redox couple (RC) by calculating E_{cal}^{abs} for the reference and then subtracting the value of the reference (Fc^+/Fc) from the redox potential of the system in question as shown in Equation 7.¹⁶⁸ The value obtained for the complex $\text{Cu}^{\text{II}}_2\text{Py}_4$ using the M11-L functional and the IEFPCM continuum solvent model was 1.36 V vs. Fc^+/Fc , with a small discrepancy with the experimental value of 1.12 V vs. Fc^+/Fc .

Equation 7:

$$E_{calc}^0 (V \text{ vs. RC}) = E_{cal}^{abs} (V) - E_{cal,RC}^{abs} (V)$$

A spin density plot of the oxidised species is displayed in Figure 70, where the yellow colour indicates spin density (optimised using the PBE0 functional). The spin density is localised on one of

^j In collaboration with Dr. H. Jamet and Dr. R. David.

the coppers, indicating a Cu^{II} ion. The other copper has no spin density (therefore a Cu^{III} ion) and there is no spin density on the ligand indicating that the mono-oxidation is copper centred. Oxidation was also accompanied by geometric changes, with bond distances to the Cu^{III} being shorter (Cu-N_{py} and Cu-O distances of 1.88 Å and 1.85 Å compared to 1.97 Å and 2.00 Å for the Cu^{II}) as expected. The Cu...Cu distance increases to 2.83 Å for the mixed valent state compared to 2.78 Å and 2.75 Å for the computed and experimental values of the Cu^{II}₂ state.

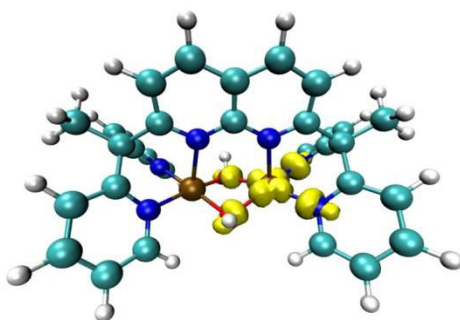


Figure 70: Spin density plot of the mono-oxidised species of complex Cu^{II}₂Py₄.

In order to assign the band observed experimentally by spectroelectrochemistry, time dependent density functional theory (TD-DFT) calculations were completed on the triplet state for the complex Cu^{II}₂Py₄ and the doublet state of the mono-oxidised species. Spin contamination can lead to errors in the transitions observed, therefore several functionals were used and the one with the lowest contamination of spin was selected (closest to the value of 0.75). No band was found for the complex Cu^{II}₂Py₄ at 430 nm. For the oxidised species, the best results with the lowest contamination of spin were obtained using the wB97XD level of theory, and gave a band with wavelength of 430 nm, coherent with experimental data with a band at 424 nm. Natural transition orbital analysis of the band indicated that it could be assigned to a ligand to metal charge transfer, from the pyridine groups to the Cu^{III} ion (Figure 71). Bands were calculated in the NIR region, however a high contamination of spin renders these results unreliable.

Table 20: TD-DFT data for absorption band detected at experimentally 424 nm after mono-oxidation of the complex Cu^{II}₂Py₄ for the doublet state at different levels.

Level of theory	Excited state	Energy / nm	Spin contamination <S ² >
PBE0	18	507	0.906
CAM-B3LYP	17	416	0.886
wB97XD	15	430	0.790

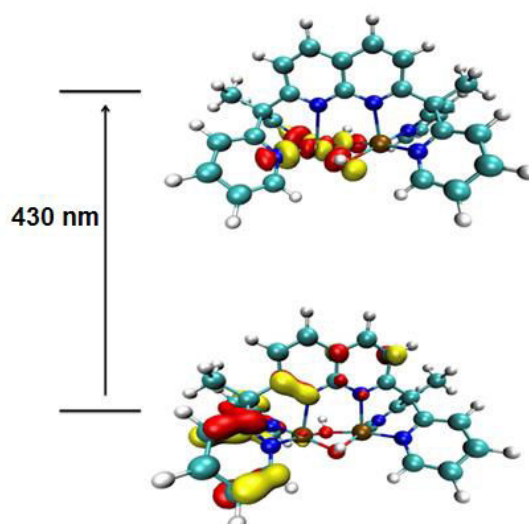


Figure 71: Natural transition orbitals of the excited state of the mono-oxidised species of $\text{Cu}^{\text{II}}\text{Py}_4$ associated with the absorption band detected at 424 nm.

In order to determine if the hydroxido bridges of the complex $\text{Cu}^{\text{II}}\text{Py}_4$ are deprotonated upon oxidation, the optimised structures of the $\text{bis}(\mu\text{-O})\text{Cu}^{\text{II}}\text{Cu}^{\text{III}}$ and $(\mu\text{-O})(\mu\text{-OH})\text{Cu}^{\text{II}}\text{Cu}^{\text{III}}$ species from complex $\text{Cu}^{\text{II}}\text{Py}_4$ were also determined. Only the $\text{bis}(\mu\text{-OH})\text{Cu}^{\text{II}}\text{Cu}^{\text{III}}$ core described above gave different bond distances to the copper depending on the oxidation state of the copper. The structures $\text{bis}(\mu\text{-O})\text{Cu}^{\text{II}}\text{Cu}^{\text{III}}$ and $(\mu\text{-O})(\mu\text{-OH})\text{Cu}^{\text{II}}\text{Cu}^{\text{III}}$ showed no differences in bond distances, consistent with a fully delocalised $\text{Cu}^{2.5}\text{Cu}^{2.5}$ species, which is not supported by experimental data. Thus the oxidised species from complex $\text{Cu}^{\text{II}}\text{Py}_4$ is tentatively assigned as a $\text{bis}(\mu\text{-OH})\text{Cu}^{\text{II}}\text{Cu}^{\text{III}}$ species.

3.6. Discussion

Three different $\text{bis}(\mu\text{-OH})\text{Cu}^{\text{II}}\text{Cu}^{\text{III}}$ complexes have been synthesised, two using symmetric ligands Py_4 and Ox_4 , and one using a dissymmetric ligand Py_2Ox_2 . All give access to the $\text{Cu}^{\text{II}}\text{Cu}^{\text{III}}$ state upon mono-oxidation. The oxidation potential of the complex $\text{Cu}^{\text{II}}\text{Ox}_4$ is the highest at 1.27 V vs. Fc^+/Fc . The oxidation potentials of the complexes $\text{Cu}^{\text{II}}\text{Py}_4$ and $\text{Cu}^{\text{II}}\text{Py}_2\text{Ox}_2$ are very similar at 1.12 V and 1.09 V vs. Fc^+/Fc . This is as expected as one can assume that mono-oxidation of the complex $\text{Cu}^{\text{II}}\text{Py}_2\text{Ox}_2$ would occur on the copper coordinated by the pyridine groups which seem to stabilise the Cu^{III} oxidation state slightly better than the oxazoline groups. The oxidation potentials are higher than other mixed valent $\text{Cu}^{\text{II}}\text{Cu}^{\text{III}}$ systems that have been characterised,^{126,127,159} which is because there are no negative charges on the ligands to stabilise the Cu^{III} oxidation state.

The bands observed by spectroelectrochemistry upon mono-oxidation of the complex $\text{Cu}^{\text{II}}_2\text{Ox}_4$ at 480 and 380 nm ($\epsilon = 735, 735 \text{ M}^{-1}\cdot\text{cm}^{-1}$) are much lower in intensity compared to bands at around 360 – 424 nm ($\sim 10^3 \text{ M}^{-1}\cdot\text{cm}^{-1}$) for complexes $\text{Cu}^{\text{II}}_2\text{Py}_4$ and $\text{Cu}^{\text{II}}_2\text{Py}_2\text{Ox}_2$. This could be due to the relative instability of $[\text{Cu}^{\text{II}}\text{Cu}^{\text{III}}\text{Ox}_4]^+$ (observable by CV) compared to the other two complexes which prevents full accumulation of the mono-oxidised species of $\text{Cu}^{\text{II}}_2\text{Ox}_4$. All the bands observed in the UV-vis for these $\text{Cu}^{\text{II}}\text{Cu}^{\text{III}}$ systems are consistent with values reported in the literature (between 386 nm and 517 nm)^{126,127,159} presumably because they are all ligand to metal charge transfer bands so the wavelength is strongly dependent on the nature of the ligand.

The NIR band observed upon mono-electronic oxidation of $\text{Cu}^{\text{II}}_2\text{Ox}_4$ at room temperature could not be fitted, however the lower energy of the maximum absorbance of the band indicates a more valence localised (class I/class II) $\text{Cu}^{\text{II}}\text{Cu}^{\text{III}}$ species.¹⁶⁹ The NIR band observed upon mono-oxidation of $\text{Cu}^{\text{II}}_2\text{Py}_2\text{Ox}_2$ at indicated that the mixed valent species is border line class II/class III (significant delocalisation), whether as the complex $\text{Cu}^{\text{II}}_2\text{Py}_4$ can be assigned to a class II (little delocalisation), consistent DFT calculations of the optimised structure. This can be explained by the differences in temperature of the spectroelectrochemical analysis of the complexes: $\text{Cu}^{\text{II}}_2\text{Py}_2\text{Ox}_2$ was analysed at room temperature (favouring delocalisation) whether as $\text{Cu}^{\text{II}}_2\text{Py}_4$ was analysed at -40 °C. However direct comparison of complexes $\text{Cu}^{\text{II}}_2\text{Ox}_4$ and $\text{Cu}^{\text{II}}_2\text{Py}_2\text{Ox}_2$ can be made as both were measured at the same temperature, but the result is surprising: the delocalisation is higher in the dissymmetric complex. This suggests that the different coordination sites of the ligand do not prevent delocalisation, *i.e.* the fact that pyridine groups stabilise the Cu^{III} better than the oxazoline groups does not trap the Cu^{III} on the side of the pyridine groups, and therefore other effects (such as reorganisation energy and solvent effects) are in fact larger.

3.7. Conclusions^k

The three complexes $\text{Cu}^{\text{II}}_2\text{Py}_4$, $\text{Cu}^{\text{II}}_2\text{Ox}_4$ and $\text{Cu}^{\text{II}}_2\text{Py}_2\text{Ox}_2$ have been synthesised. X-ray crystal diffraction of three complexes indicates that they all had a similar structure, containing the bis(μ -OH) Cu^{II}_2 core with very short Cu-Cu distances of 2.75-2.80 Å, similar to what was initially proposed for the enzyme pMMO.⁶⁰ Solution characterisation of these complexes indicates that their structures

^k All the work presented in this chapter on the complex $\text{Cu}^{\text{II}}_2\text{Py}_4$ has been published: Isaac, J. A.; Gennarini, F.; Lopez, I.; Thibon-Pourret, A.; David, R.; Gellon, G.; Gennaro, B.; Philouze, C.; Meyer, F.; Demeshko, S.; Le Mest, Y.; Reglier, M.; Jamet, H.; Le Poul, N.; Belle, C. *Inorg. Chem.* **2016**, 55 (17), 8263.

remain intact in acetonitrile with the exception of the complex $\text{Cu}^{\text{II}}_2\text{Py}_4$ for which the coordinated triflate group (observed by X-ray diffraction) may decoordinate in solution.

Electrochemical analysis of the complexes indicates that all three could be mono-oxidised. The species generated upon mono-oxidation of complexes $\text{Cu}^{\text{II}}_2\text{Py}_4$ and $\text{Cu}^{\text{II}}_2\text{Py}_2\text{Ox}_2$ could be assigned to a mixed valent localised $\text{Cu}^{\text{II}}\text{Cu}^{\text{III}}$ complex based on the EPR measurements (15 – 100 K). The EPR spectrum from the mono-oxidised species of $\text{Cu}^{\text{II}}\text{Ox}_4$ is less convincing, however similarities in the UV-vis with the other complexes ($\text{Cu}^{\text{II}}_2\text{Py}_4$ and $\text{Cu}^{\text{II}}_2\text{Py}_2\text{Ox}_2$) indicate that it also forms a $\text{Cu}^{\text{II}}\text{Cu}^{\text{III}}$ species. While the complexes $[\text{Cu}^{\text{II}}\text{Cu}^{\text{III}}\text{Py}_4]^+$ and $[\text{Cu}^{\text{II}}\text{Cu}^{\text{III}}\text{Py}_2\text{Ox}_2]^+$ are localised at 15-100 K, bands observed in the NIR indicate a slight delocalisation at higher temperatures (-40°C and RT respectively).

Theoretical calculations on the complex $\text{Cu}^{\text{II}}_2\text{Py}_4$ confirmed that mono-oxidation occurred on the copper, and that the charge was significantly localised on one of the coppers, consistent with a class II complex. TD-DFT allowed the assignment of the band experimentally observed at around 424 nm as a charge transfer from the pyridine groups to the metal. Optimised structures of various protonation states of the bridging groups suggested that the bridges remain protonated as hydroxido groups.

These results provide spectroscopic data for the $\text{Cu}^{\text{II}}\text{Cu}^{\text{III}}$ species, which until now has been relatively unknown, with only a handful of example in the literature. Our attempts at determining the reactivity of such species will be discussed in Part II Chapter 4.

4. Reactivity of mixed valent Cu^{II}Cu^{III} species

In the literature there is only one of example of a reactivity test of a Cu^{II}Cu^{III} species. Tolman *et al.*¹²⁶ demonstrated that the (μ-OH)Cu^{II}Cu^{III} species (described in Figure 17) reacted with DHA but neither the kinetics or the mechanism of the reaction are discussed. Theoretical calculations by Yoshizawa *et al.*^{71,72,74} have shown that it is likely that the bis(μ-OH)Cu^{II}Cu^{III} or a (μ-O)(μ-OH)Cu^{II}Cu^{III} core has a certain reactivity towards C-H bonds. It is therefore probable that there is a certain reactivity for each of the three Cu^{II}Cu^{III} species generated in Part II Chapter 3 (Figure 72). In this chapter our attempts probing the reactivity of such a species experimentally is discussed.

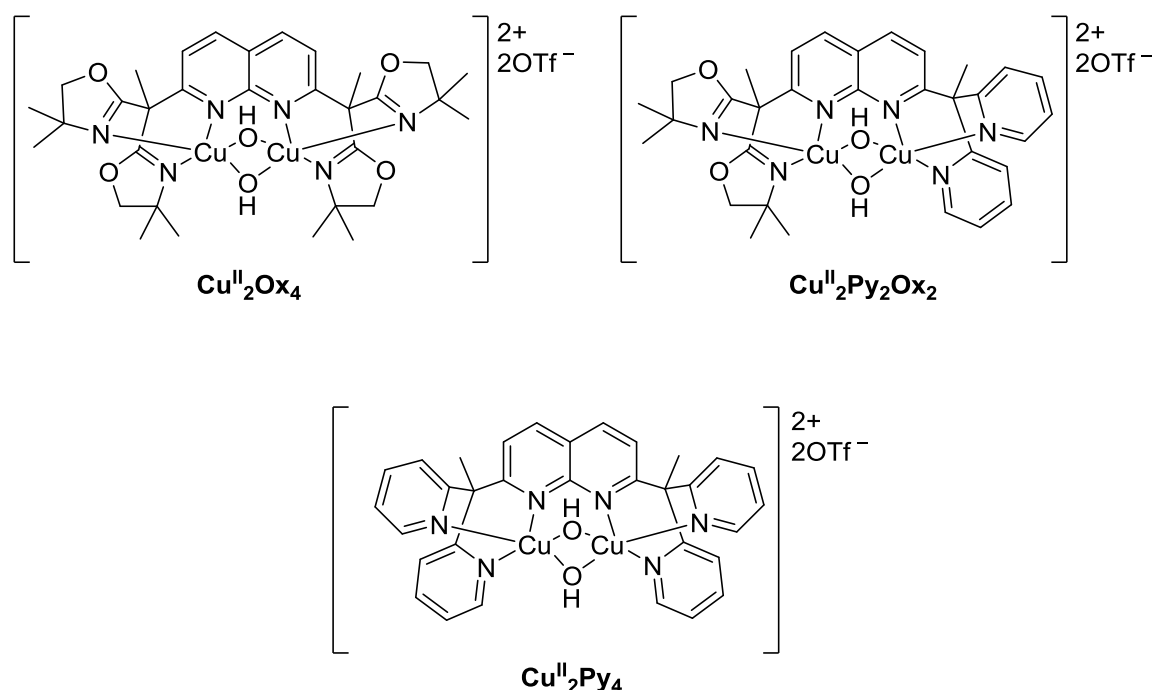


Figure 72: Complexes described in Chapter 3 for which the Cu^{II}Cu^{III} state is accessible.

The Cu^{II}Cu^{III} states in all three complexes have high oxidation potentials that are out of range of most commonly used oxidants. Only [N(C₆H₂Br₃-2,4,6)₃]⁺ (1.36 V vs. Fc⁺/Fc) or [N(C₆Cl₅)₃]⁺ (1.72 V vs. Fc⁺/Fc) could be used but electrochemical methods were chosen instead for generating the Cu^{II}Cu^{III} species due to the instability of the possible oxidising agents.¹⁶⁴

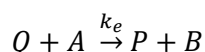
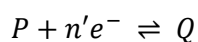
4.1. Brief introduction to electrocatalysis

Electrocatalysis (defined in this thesis as molecular catalysis where the catalyst is activated electrochemically) has recently become a method of choice for evaluating catalytic reactions, due to

the ease of extracting parameters from the reaction that can be used for benchmarking. It has been typically used for determining the performance of catalysts for H₂O oxidation and CO₂, H⁺ and O₂ reduction. In this section, idealised CVs of different types of electrocatalytic activity will be presented, explanations of what occurs at the electrode will be given as well as basic methods for extracting the rate constants from these CVs.^{170–173}

4.1.1. Typical shapes of CVs for electrocatalysis

An electrocatalytic reaction can be described as EC' where E is an electrochemical reaction, C is an irreversible chemical reaction and the prime symbol indicates a catalytic process (Scheme 45). The response of the CVs of such a catalytic process are dependent on the two parameter: the kinetic parameter (λ) (Equation 8) and the excess factor of the substrate (γ) (Equation 9). Both parameters are dimensionless.



Scheme 45: mechanism for a catalytic electrochemical reaction, where n' is the number of electrons transferred to the catalyst in the absence of a substrate.

Equation 8:

$$\lambda = \left(\frac{RT}{F}\right) \left(\frac{k_e C_P^0}{v}\right)$$

Equation 9:

$$\gamma = \left(\frac{C_A^0}{C_P^0}\right)$$

R = molar gas constant / J.K⁻¹.mol⁻¹

T = temperature / K

F = Faraday's constant / C.mol⁻¹

k_e = Rate of electron transfer of the oxidised (or reduced) catalyst Q to the substrate A / s⁻¹

C_P^0 = Bulk concentration of the catalyst P / M

C_A^0 = Bulk concentration of the substrate A / M

v = Scan rate / V.s⁻¹

Typical responses observed by CV for different types of electrocatalysis with respect to γ and λ are shown in Figure 73. The different zones are named D, KG, KD, KT1, KT2, KS and K and all have characteristic shapes. One can move between zones of the graph by increasing the bulk concentration of the substrate (C_A^0) or the catalyst (C_P^0), the scan rate (ν) or the rate constant for electron transfer from the catalyst to the substrate in solution (k_e) (see the arrows at the bottom left of Figure 73). For example if a CV in the shape of zone K is obtained, one can increase ν to obtain a CV in the shape of zone KS.

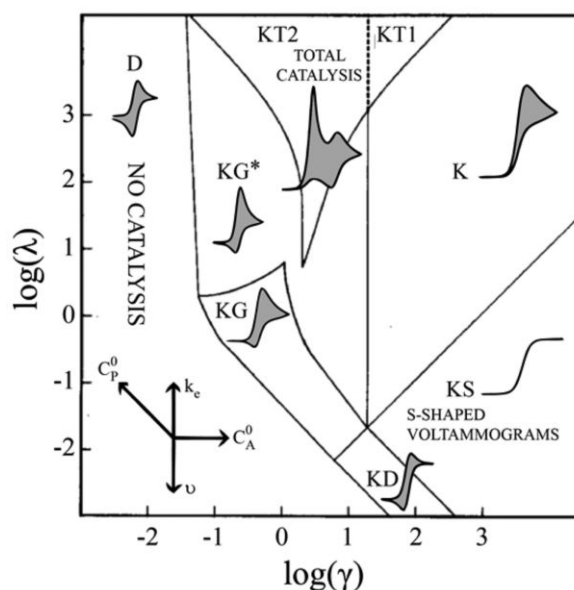


Figure 73: Idealised CVs depending on the kinetic parameter γ (the excess factor of the substrate) and λ (kinetic parameter). C_A^0 indicates the bulk concentration of the substrate, C_P^0 the bulk concentration of the catalyst, ν scan rate and k_e the rate constant for electron transfer from the catalyst to the substrate in solution. Figure from Dempsey *et al.*¹⁷⁴

4.1.2. Description of the occurrences at the electrode for each shape of CV

In terms of what occurs at the electrode in the case of each zone:

D represents no catalysis. This CV shape is a reversible wave where a substrate does not interfere.

KS (S shaped CV) occurs when there is an electrocatalytic reaction with no substrate depletion. This occurs when the relative concentration of the substrate is high compared i) the concentration of the catalyst and ii) the rate of the catalytic reaction.

K represents a similar situation to KS, but this time the faster rate of reaction leads to a drop in the current of the CV at the highest (or lowest if the catalytic process is in reduction) voltage. This is indicative of substrate depleting in the diffusion layer of the electrode.

The shape of KD also occurs in similar circumstances to KS (ie. there is no substrate depletion due to the large excess), but this time the kinetic parameter is much lower so that the current comes to a peak: the turnover reaction of the catalyst cannot keep up with the scan rate of the reaction. Thus lowering the scan rate would cause the case of KD to become more like KS. A peak can be observed on the reverse scan due to the accumulation of unreacted oxidised (or reduced) catalyst.

KG is indicative of both substrate depletion (drop in the maximum current, the same as zone K) and an accumulation of the oxidised catalyst (a peak on the reverse scan, the same as zone KD).

The zones KT1 and KT2 are also named “total catalysis”, and can easily be recognisable by the appearance of a pre-peak upon addition of a substrate before the reversible system of the catalyst. This occurs when there is a high kinetic parameter and substrate depletion occurs at the electrode leading to a sharp drop in the current. The reversible system of the catalyst can also be observed as there is no more substrate to react with the catalyst to form an electrocatalytic wave. KT2 has a more pronounced pre-peak, but as concentration of the substrate is increased the potential value of the pre-peak will approach the value of the redox system of the catalyst and increase in current (KT1) and will eventually become indistinguishable giving the CV shape of zone K.

4.1.3. Determining rate constants from the CV of an electrocatalytic reaction

4.1.3.1. Zone KS: Plateau current analysis:

KS is the most straightforward shape of CV to extract the rate constant from as the value of the observed rate constant (k_{obs}) can be directly related to the plateau current (i_{pl}), as i_{pl} is proportional to $\sqrt{k_{obs}}$ (see Equation 10).

Equation 10:

$$i_{pl} = nFAC_p^0 \sqrt{Dk_{obs}}$$

i_{pl} = plateau current / A

A = area of the electrode / dm²

D = the diffusion coefficient of the catalyst / dm².s⁻¹

k_{obs} = observed rate constant / $M^{-1}.s^{-1}$

n = total number of electrons for the conversion of the substrate

To avoid measuring the diffusion coefficient and the area of the electrode, Equation 10 can be divided by the Randles-Sevcik equation for the catalyst in the absence of a substrate (Equation 11), resulting in a much simpler Equation 12. For a catalytic system described as KS, the plateau current is independent of the scan rate (this should be verified by changing the scan rate) as it depends on the rate of the catalytic reaction. The value of i_p (peak current for scan rate v for the reversible redox process of the catalyst) can be extracted from a CV of the complex without the substrate, and thus the value of k_{obs} can be obtained. This equation is limited to the case of S shaped CVs (zone KS), and for other types of CV different approximations will have to be made.

Equation 11:

$$i_p = 0.4463n'FAC_p^0 \sqrt{\frac{n'FvD}{RT}}$$

Equation 12:

$$\frac{i_{pl}}{i_p} = \frac{n}{0.446n'} \sqrt{\left(\frac{RT}{n'Fv}\right) k_{obs}}$$

i_p = peak current / A (for scan rate v for the reversible redox process of the catalyst without a substrate)

4.1.3.2. Competing side phenomena (zones K, KG and KD). Foot of the wave analysis (FOWA):

When there are competing phenomena such as substrate depletion, catalyst deactivation, accumulation of the oxidised (or reduced if the catalytic process is in reduction) catalyst or passivation of the surface of the electrode, a current plateau cannot be achieved and the peak current will not be a real indicator of the k_{obs} of the catalyst. FOWA is therefore used to determine k_{obs} because the side phenomena do not come into play at the foot of the wave: the CV should follow the same path as a CV from the zone KS. As the voltage is increased, the catalytic performance will deviate away from the initial value of k_{obs} as the competing phenomena start to have an effect.

The equation for the foot of the wave approximation is shown below (Equation 13). The value of i_{pl}/i_p can be determined by plotting i_c / i_p against $1 / \left\{ 1 + \exp \left[\frac{nF}{RT} (E - E_{P/Q}^0) \right] \right\}$ and drawing a

tangent to the curve where i_c / i_p is close to zero (see Figure 74 for an example of a plot). The value of the gradient of the tangent (i_{pl}/i_p) can be substituted back into equation Equation 12 to obtain k_{obs} .

Equation 13:

$$\frac{i_c}{i_p} = \frac{i_{pl}/i_p}{1 + \exp\left[\frac{nF}{RT}(E - E_{P/Q}^0)\right]}$$

i_c = catalytic current / A

E = applied potential / V

$E_{P/Q}^0$ = standard potential for the reversible redox couple (P / Q) of the catalyst in the absence of a substrate / V

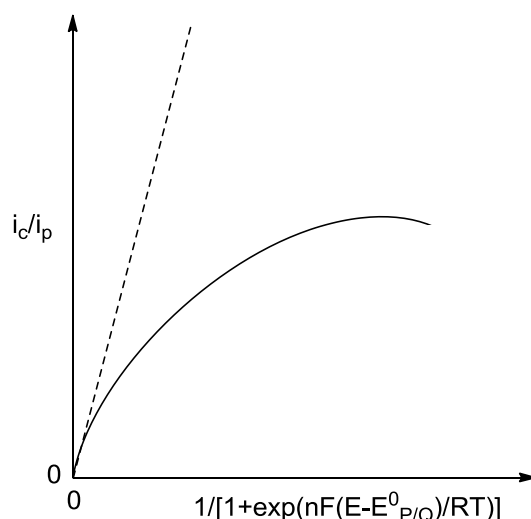


Figure 74: Example of FOWA analysis plot. The solid line indicates the experimental curve determined from the CV and the dotted line indicated the tangent for the first part of the curve, where competing phenomena with the electrocatalysis are at their lowest. Figure adapted from Dempsey *et al.*¹⁷¹

4.1.3.3. Zone KT2. The peak shift analysis:

For determining k_{obs} from the peak shift analysis, several CVs must be taken at different scan rates. The value of the first peak $E_{p,c}$ (catalytic peak) varies with the scan rate, but the value of $E_{P/Q}^0$ of the reversible system of the catalyst does not (Figure 75). The dependence of $E_{p,c}$ on the scan rate derived for one electron is shown in Equation 14. k_{obs} can be extracted from the gradient by plotting $\exp\left(\frac{2F}{RT}\left(E_{p,c} - E_{P/Q}^0 + 0.409\frac{RT}{F}\right)\right)$ against $1/v$.

Equation 14:

$$E_{p,c} = E_{P/Q}^0 - 0.409 \frac{RT}{F} + \frac{RT}{2F} \ln \left(\frac{RT}{F} \frac{k_{obs} D_P (C_P^0)^2}{v D_A (C_A^0)} \right)$$

$E_{p,c}$ = the potential of the catalytic peak / V

D_P = the diffusion coefficient of the catalyst / $\text{cm}^2 \cdot \text{s}^{-1}$

D_A = the diffusion coefficient of the substrate / $\text{cm}^2 \cdot \text{s}^{-1}$

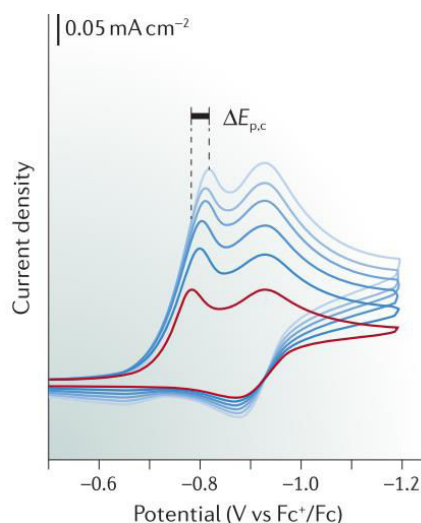


Figure 75: Variation of $E_{p,c}$ with increasing scan rate of CV in the case of total catalysis. Figure from Dempsey *et al.*¹⁷¹

4.1.3.4. Simulations

Often mechanisms are more complicated than the examples given above, so simulation of the CV can give an idea of the parameters in question. In general all parameters that can be measured experimentally should be measured. These parameters can be put into the simulation and then the mechanisms and/or rate constants can be changed in order to fit the experimental data. Fitting the experimental data exactly can be difficult, as small factors (for example catalyst degradation or inhibition of the catalyst by products) can have large effects on the CV shape.

4.1.4. Summary

The CVs demonstrating electrocatalysis can be wildly different from one another, and depend on a lot of factors. Modifying certain easily changeable parameters such as the scan rate or substrate concentration can lead to different shaped CVs, for which parameters can be extracted more easily. Different methods of analysis of the CV can be used for determining the kinetic parameters, by

making certain approximations, and for particularly complicated mechanisms simulations can be used.

4.2. Reactivity of complexes $\text{Cu}^{\text{II}}_2\text{Py}_2\text{Ox}_2$ and $\text{Cu}^{\text{II}}_2\text{Ox}_4$

4.2.1. Reactivity with an external substrate

The reactivity of the $\text{Cu}^{\text{II}}\text{Cu}^{\text{III}}$ species from complexes $\text{Cu}^{\text{II}}_2\text{Py}_2\text{Ox}_2$ and $\text{Cu}^{\text{II}}_2\text{Ox}_4$ were initially probed by CV. The first oxidation wave of both complexes (generation of the $\text{Cu}^{\text{II}}\text{Cu}^{\text{III}}$ species) is quasi-reversible (see Part II Chapter 3 Section 3.5.1.1). If a substrate is then added on which the $\text{Cu}^{\text{II}}\text{Cu}^{\text{III}}$ species reacts, the mechanism of the reaction will go from an E (electrochemical) to an EC (electrochemical coupled to a chemical reaction), and will be visible by a decrease in reversibility of the oxidation wave.

Certain points must be considered for the selection of a substrate:

- The oxidation potential of the substrate must be higher than that of the complex, so that the reactivity is measured on the substrate and not the electronically oxidised substrate.
- The bond dissociation energy (BDE) of the substrate must be lower than that of the solvent otherwise the reactivity cannot be observed by CV. Acetonitrile was chosen because of its large electrochemical window and due to insolubility in other, more robust solvents.

Table 21: Values of BDE for C-H oxidation for several commonly used substrates. Data obtained from Tolman *et al.*⁴⁴ and Dean *et al.*⁸⁹

Substrate	BDE / kcal.mol ⁻¹
DHA	77
Cyclohexene	81
Fluorene	82
Diphenylmethane	85
Toluene	88
THF	92
Acetonitrile	93
Cyclohexane	99

The values of BDE of several commonly used substrates for C-H oxidation are shown in Table 21. Cyclohexane has a higher BDE than that of acetonitrile, and therefore its oxidation is unlikely to be observed when acetonitrile is used as a solvent. All other substrates in Table 21 could be used as long as their oxidation potential is above that of the complex in question. The oxidation potential of

toluene was measured by CV in a 0.1 M solution of NBu_4ClO_4 in CH_3CN at room temperature. A value of 1.8 V vs. Fc^+/Fc was obtained and is therefore higher than that for the generation of the complexes discussed in Chapter 3 (between 1.1 and 1.3 V vs. Fc^+/Fc). Toluene was therefore chosen as a substrate.

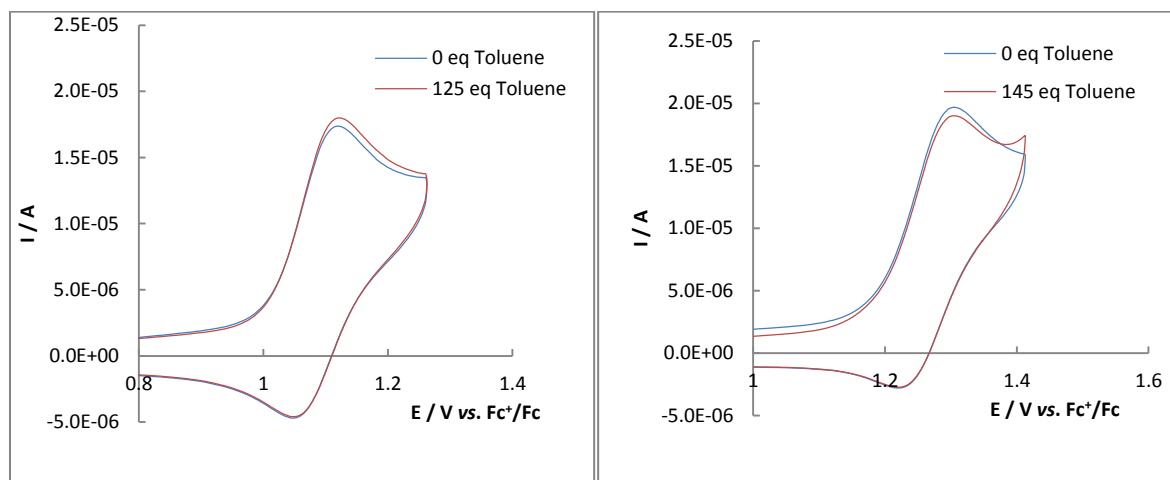


Figure 76 : CV of $\text{Cu}^{\text{II}}_2\text{Py}_2\text{Ox}_2$ (left) and $\text{Cu}^{\text{II}}_2\text{Ox}_4$ (right) with and without toluene. Parameters: CV, $\nu = 50$ mV/s; NBu_4ClO_4 in CH_3CN (0,1 M); concentration of $\text{Cu}^{\text{II}}_2\text{Py}_2\text{Ox}_2$ or $\text{Cu}^{\text{II}}_2\text{Ox}_4 = 1$ mM; concentration of toluene: left: 0 of 125 mM, right: 0 or 145 mM; under an atmosphere of air.

The CV of complexes $\text{Cu}^{\text{II}}_2\text{Py}_2\text{Ox}_2$ and $\text{Cu}^{\text{II}}_2\text{Ox}_4$ are shown in Figure 76 at a concentration of 1 mM in a solution of $\text{NBu}_4\text{ClO}_4/\text{CH}_3\text{CN}$ with and without the addition of over 100 eq of toluene. In the case of both complexes there is very little change in reversibility of the CV when toluene is added, meaning that the reactivity between the $\text{Cu}^{\text{II}}\text{Cu}^{\text{III}}$ species and the toluene added is negligible. There are several possible hypotheses to explain this lack of reactivity:

- The $\text{Cu}^{\text{II}}\text{Cu}^{\text{III}}$ species could be not reactive enough to oxidise toluene.
- The $\text{Cu}^{\text{II}}\text{Cu}^{\text{III}}$ species is sterically hindered by the methyl groups of the oxazoline motif, inhibiting the reactivity with an external substrate.
- The $\text{Cu}^{\text{II}}\text{Cu}^{\text{III}}$ species reacts with the methyl groups of the oxazoline on the ligand that are directed towards the bridging OH groups. In this case we would be highly unlikely to observe any reactivity towards an external substrate as the methyl groups of the ligand are pre-organised for reacting with the $\text{Cu}^{\text{II}}\text{Cu}^{\text{III}}$ centre, so the entropic component to reach the transition state of the reaction will be minimal.

Concerning hypothesis B, the crystals structures of the complexes $\text{Cu}^{\text{II}}_2\text{Py}_2\text{Ox}_2$ and $\text{Cu}^{\text{II}}_2\text{Ox}_4$ are shown in Figure 77 for comparison of the steric bulk between the complexes. In the case of the

complex $\text{Cu}^{\text{II}}\text{Ox}_4$ the bridging OH groups are more hindered than in the complex $\text{Cu}^{\text{II}}\text{Py}_2\text{Ox}_2$ as the bis-oxazoline groups are more bulky than the pyridine groups, making the approach of an external substrate to the reactive centre more difficult in the case of the complex $\text{Cu}^{\text{II}}\text{Ox}_4$. There is however no reactivity observed with the toluene in either case indicating that the steric hindrance is not the cause of the lack of reactivity.

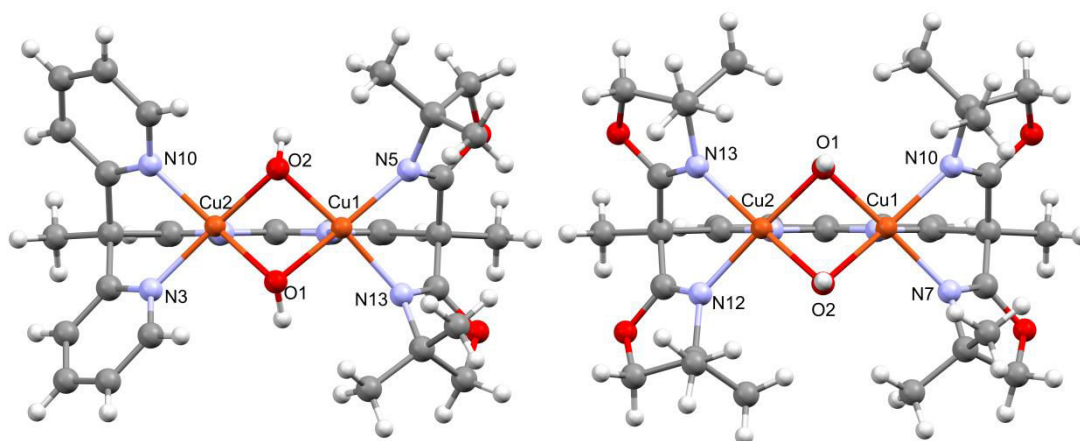


Figure 77 : Crystal structures of $\text{Cu}^{\text{II}}\text{Py}_2\text{Ox}_2$ (left) and $\text{Cu}^{\text{II}}\text{Ox}_4$ (right) shown along the plane of the naphthyridine group.

4.2.2. Internal reactivity

To determine whether the lack of reactivity of the $\text{Cu}^{\text{II}}\text{Cu}^{\text{III}}$ species of complexes $\text{Cu}^{\text{II}}\text{Py}_2\text{Ox}_2$ and $\text{Cu}^{\text{II}}\text{Ox}_4$ on an external substrate was due to lack of reactivity of the $\text{Cu}^{\text{II}}\text{Cu}^{\text{III}}$ species (hypothesis A) or the reactivity was masked by an internal reactivity (hypothesis C), the ligands were analysed after the $\text{Cu}^{\text{II}}\text{Cu}^{\text{III}}$ species was generated. The $\text{Cu}^{\text{II}}\text{Cu}^{\text{III}}$ species of both complexes were generated by exhaustive electrolysis of a 0.7 mM solution of each complex in $\text{NBu}_4\text{ClO}_4/\text{CH}_3\text{CN}$ at -40°C under air (to 1.26 V vs. Fc^+/Fc for complex $\text{Cu}^{\text{II}}\text{Py}_2\text{Ox}_2$ and 1.41 V vs. Fc^+/Fc for complex $\text{Cu}^{\text{II}}\text{Ox}_4$) then left to rise to room temperature. The solution was demetallated in concentrated potassium hydroxide, extracted in dichloromethane, and the NMR of the resulting residues were recorded. The starting $\text{Cu}^{\text{II}}\text{Cu}^{\text{II}}$ complexes of $\text{Cu}^{\text{II}}\text{Py}_2\text{Ox}_2$ and $\text{Cu}^{\text{II}}\text{Ox}_4$ were also demetallated in the same way but without prior electrolysis to ensure that any changes in the spectra of the ligand are not due to the harsh demetallation conditions. The ^1H -NMR spectra in CD_3CN of the ligands for the complexes that have i) been exposed to electrolysis followed by demetallation and ii) been exposed to demetallation alone are shown in Figure 78.

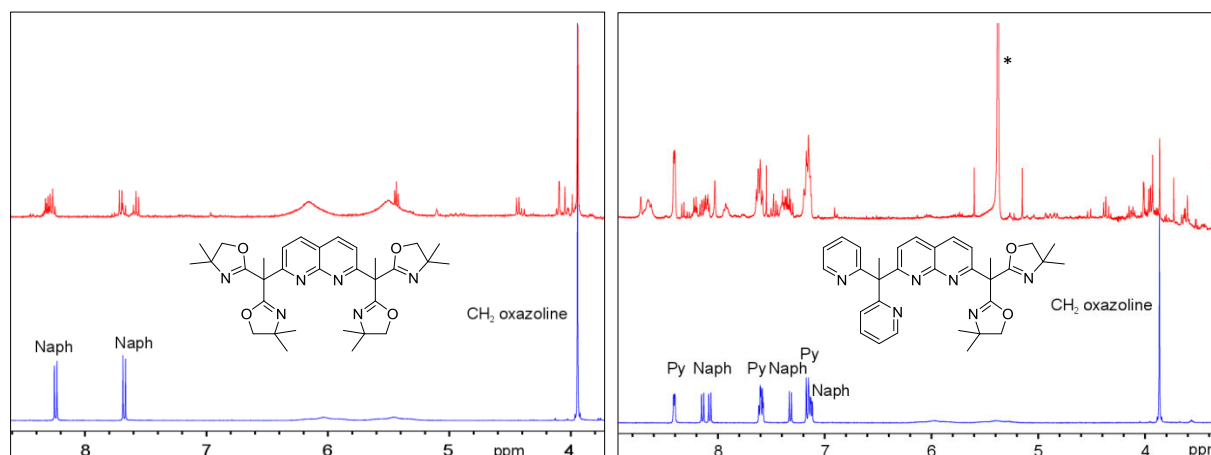


Figure 78: $^1\text{H-NMR}$ spectra in CD_3CN of the complexes after demetallation. Left: $\text{Cu}^{\text{II}}_2\text{Ox}_4$; right: $\text{Cu}^{\text{II}}_2\text{Py}_2\text{Ox}_2$. Red: demetallated complexes after electrolysis. Bleu: demetallated complexes without electrolysis. The starred peak is from CH_2Cl_2 remaining after purification (none present in the spectra from $\text{Cu}^{\text{II}}_2\text{Ox}_4$).

In the $^1\text{H-NMR}$ spectra from the ligand of $\text{Cu}^{\text{II}}_2\text{Py}_2\text{Ox}_2$ (Figure 78, right), the signals assigned to the pyridine groups are relatively unchanged after electrolysis. This is in contrast to peaks assigned to the naphthyridine group in the aromatic region and the single peak at 4 ppm assigned to the CH_2 group of the oxazoline, for which there are more peaks after electrolysis. This indicated a mix of products with changes occurring on the oxazoline entity. The fact that the signals attributed to the pyridine groups remain unchanged indicates that oxidation of the methyl group in the benzylic position on the side of the pyridines remains untouched, so it is unlikely that changes have occurred to the equivalent methyl group the side of the oxazolines. The increase in number of signals assigned to the CH_2 group most likely indicates various degrees of oxidation of the methyl groups next to the CH_2 where changes are observed. Unfortunately the methyl groups of the oxazoline and on the benzylic position of the naphthyridine cannot be observed after the electrolysis as they are in the region hidden by the large signals of the NBu_4ClO_4 salt (from 0.9 to 3.1 ppm). The spectra from the ligand of $\text{Cu}^{\text{II}}_2\text{Ox}_4$ (Figure 78, left) have similar changes in the aromatic region and the peak assigned to the CH_2 group of the oxazoline, indicating that similar changes have occurred as with the ligand from the complex $\text{Cu}^{\text{II}}_2\text{Py}_2\text{Ox}_2$ (Figure 78).

The $^{13}\text{C-NMR}$ spectra of both ligands indicate similar results (Figure 79). There are several peaks on the $^{13}\text{C-NMR}$ spectra of both ligands after electrolysis in the region of 80 ppm, compared to the single peaks of the respective ligands not having been exposed to the electrolysis. Unfortunately large peaks from the NBu_4ClO_4 electrolyte preclude further analysis of the $^{13}\text{C-NMR}$ spectra.

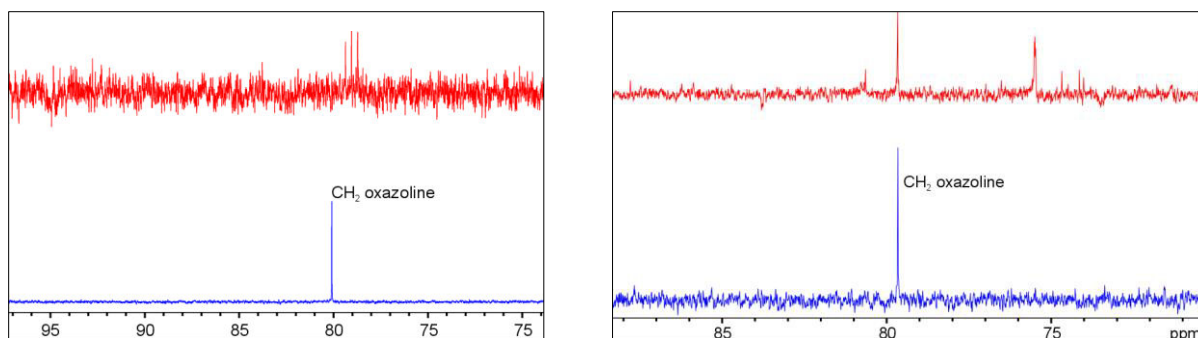
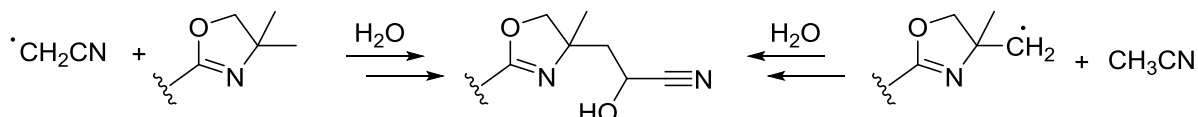


Figure 79: ^{13}C -NMR spectra in CD_3CN of the complexes after demetallation $\text{Cu}^{\text{II}}_2\text{Py}_2\text{Ox}_2$ left and $\text{Cu}^{\text{II}}_2\text{Ox}_4$ right. Red: demetallated complexes after electrolysis. Bleu: demetallated complexes without electrolysis.

To gain more insight into the oxidation products of each complex, the demetallated residues were purified by column chromatography (silica) using a 1:1 mixture of acetone and pentane to remove most of the 100 fold excess of NBu_4ClO_4 salt before analysis by ESI-MS (Figure 80 and Figure 81). In the case of the purified residue from the electrolysis of $\text{Cu}^{\text{II}}_2\text{Ox}_4$ the protonated ligand $[\text{LH}+\text{H}]^+$ (where LH is the ligand) is observed at $m/z = 575$, but also peaks at $m/z = 591$, 613 and 629 corresponding to the hydroxylated ligand $[\text{LOH}+\text{H}]^+$, $[\text{LOH}+\text{Na}]^+$ and $[\text{LOH}+\text{K}]^+$ respectively, indicating the addition of an oxygen atom and therefore possible transformation of the $\text{C}(\text{CH}_3)_2$ into $\text{C}(\text{CH}_3)(\text{CH}_2\text{OH})$. A peak at $m/z = 630$ was tentatively assigned to $[\text{LCHOHCN}+\text{H}]^+$, a product that could be formed by a radical coupling of the oxazoline groups with the solvent CH_3CN (Scheme 46).



Scheme 46: Possible mechanisms for the formation of LCHOHCN

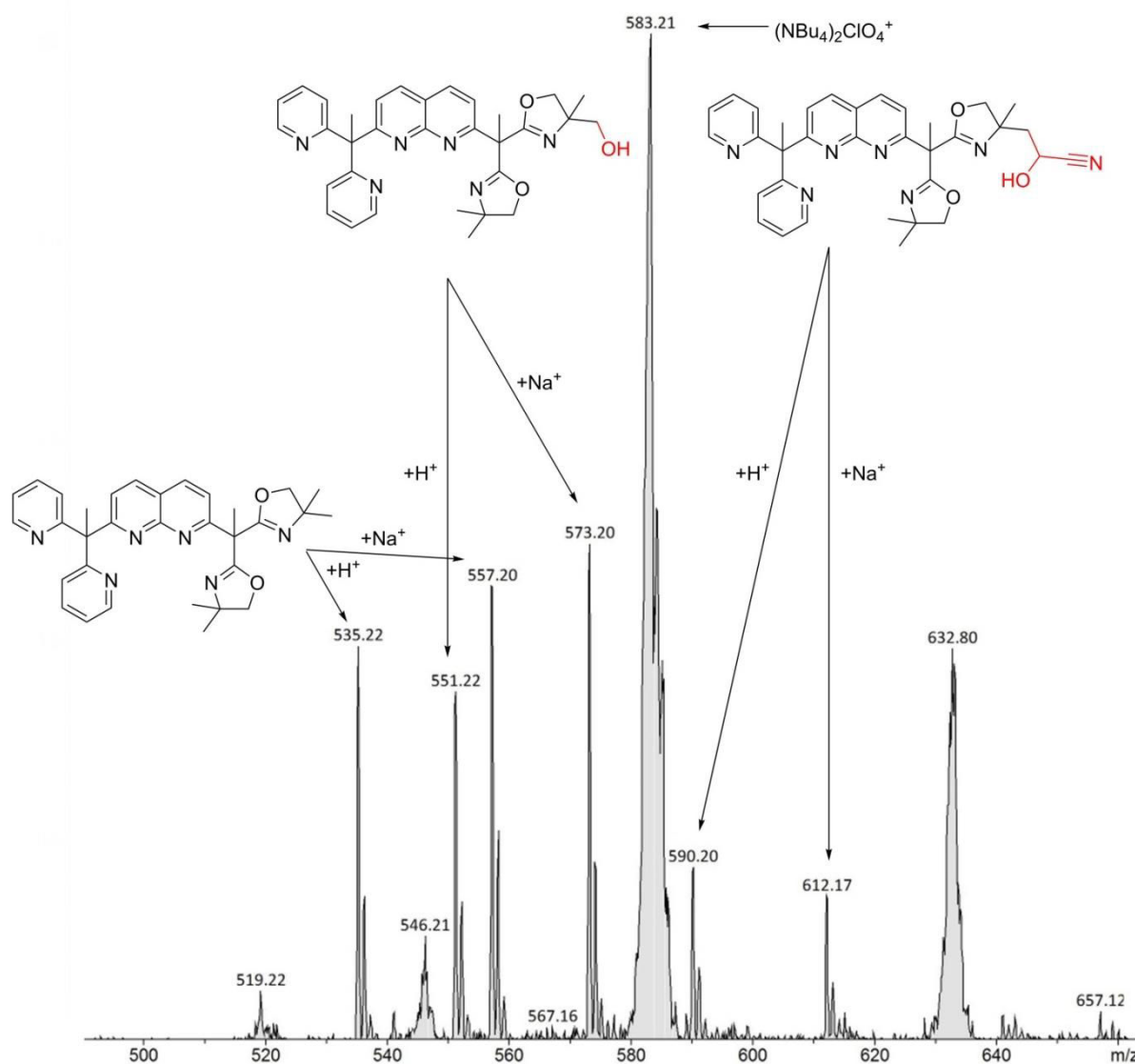


Figure 80: ESI spectrum of the complex $\text{Cu}^{\text{II}}\text{Py}_2\text{Ox}_2$ after electrolysis, demetallation and purification by column chromatography. The initial ligand and possible structures of the oxidised ligand are shown. The starred peak corresponds to the remaining $[(\text{NBu}_4)_2\text{ClO}_4]^+$.

Similar products were observed from the residue of $\text{Cu}^{\text{II}}\text{Py}_2\text{Ox}_2$: peaks at $m/z = 535$ and 557 from the ligand $[\text{LH}+\text{H}]^+$, $[\text{LH}+\text{Na}]^+$ respectively and peaks at $m/z = 551$ and 573 from the hydroxylated product $[\text{LOH}+\text{H}]^+$ and $[\text{LOH}+\text{Na}]^+$. Peaks $m/z = 590$ and 612 could tentatively be assigned to products $[\text{LCHOHCN}+\text{H}]^+$ and $[\text{LCHOHCN}+\text{Na}]^+$ respectively.

None of the hydroxylated products or the peaks assigned to the formation of LCHOHCN were observed on the residues from the complexes that were not electrolysed but went through the same treatment with concentrated potassium hydroxide, indicating that the changes to the ligand occurred because of the electrolysis and therefore the generation of the $\text{Cu}^{\text{II}}\text{Cu}^{\text{III}}$ species.

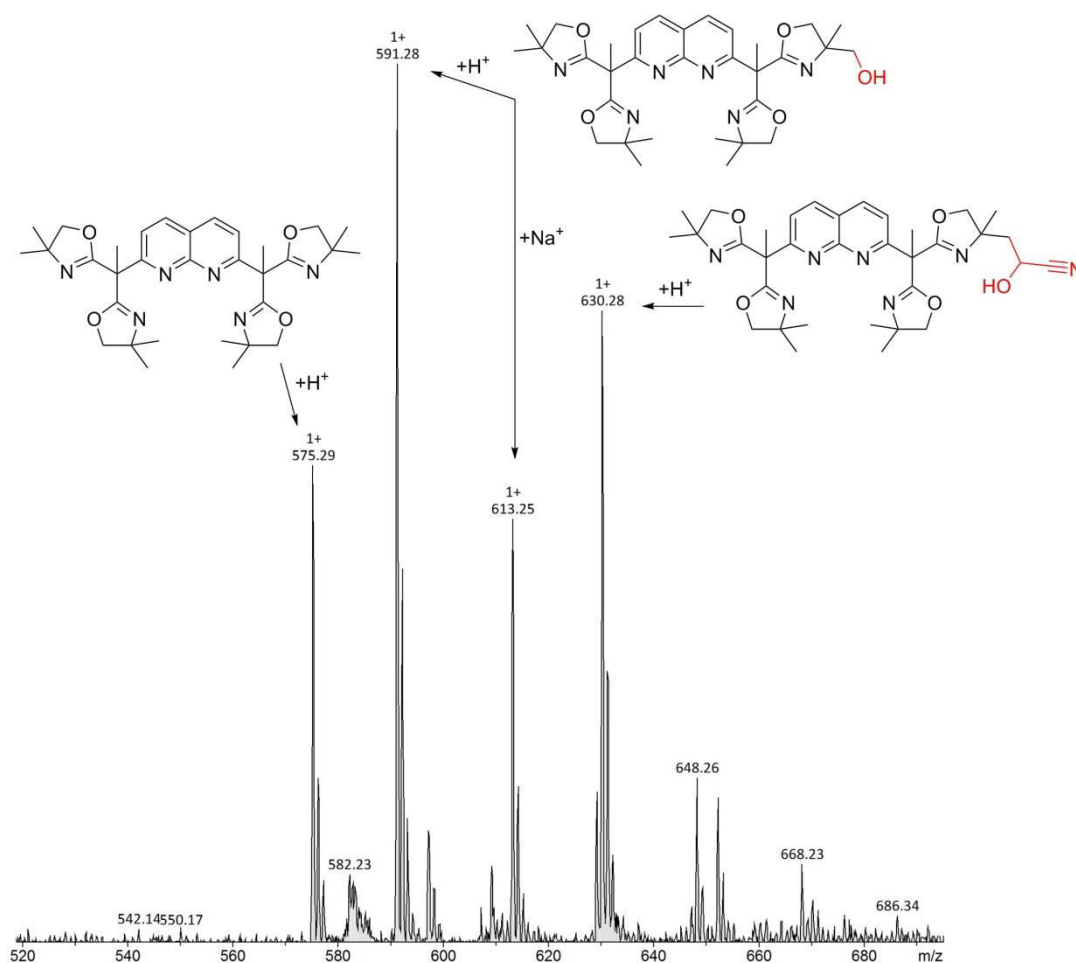


Figure 81: ESI spectrum of the complex $\text{Cu}^{\text{II}}\text{Ox}_4$ after electrolysis, demetallation and purification by column chromatography. The initial ligand and possible structures of the oxidised ligand are shown.

4.2.3. Conclusions

The $\text{Cu}^{\text{II}}\text{Cu}^{\text{III}}$ species from the complexes $\text{Cu}^{\text{II}}_2\text{Ox}_4$ and $\text{Cu}^{\text{II}}_2\text{Ox}_2\text{Py}_2$ (generated electrochemically with oxidation potentials of 1.27 and 1.09 V vs. Fc^+/Fc respectively) show no reactivity towards toluene. However NMR analysis of the electrochemical solution after electrolysis and demetallation indicates that changes have occurred on the ligand. ESI-MS evidences the presence of the hydroxylated ligand LOH, and the possible presence of LCHOHCN, a product that could be obtained by radical coupling of the ligand with a molecule of acetonitrile and water. The present study therefore indicates that the electrochemically generated $\text{Cu}^{\text{II}}\text{Cu}^{\text{III}}$ species is capable of intramolecular aliphatic oxidation of strong C-H bonds. In view of generating a catalytic system (or oxidation of an external

substrate) efforts were focussed on the reactivity of $\text{Cu}^{\text{II}}\text{Cu}^{\text{III}}$ species supported by less sterically hindered ligands with CH_3 that can easily be oxidised to avoid the intramolecular reactivity.

4.3. Reactivity of complex $\text{Cu}^{\text{II}}_2\text{Py}_4$

4.3.1. Reactivity of $\text{Cu}^{\text{II}}_2\text{Py}_4$ with an external substrate

4.3.1.1. Analysis of $\text{Cu}^{\text{II}}_2\text{Py}_4$ by CV with an external substrate

The reactivity of complex $\text{Cu}^{\text{II}}_2\text{Py}_4$ was examined in oxidation by CV with the addition of toluene as an external substrate (see section 4.2.1). The CV of the complex (0.95 mM) in a solution of 0.1 M NBu_4ClO_4 in acetonitrile without toluene and upon the addition of 140 eq of either toluene-H8 or toluene-D8 are shown in Figure 82.

The CV of $\text{Cu}^{\text{II}}_2\text{Py}_4$ on its own is quasi-reversible, but the reversibility decreases upon addition of toluene-H8. The effect is similar upon addition of toluene-D8 but less pronounced. This indicates that the $\text{Cu}^{\text{II}}\text{Cu}^{\text{III}}$ species that is formed on the positive scan then reacts with the toluene-H8 or toluene-D8, going from an EC_1 mechanism to an EC_1C_2 mechanism. A kinetic isotope effect (KIE) is present because of the significantly lower reversibility with toluene-H8 compare to toluene-D8. The results were the same under an inert atmosphere and under air, indicating that O_2 is not involved in the process.

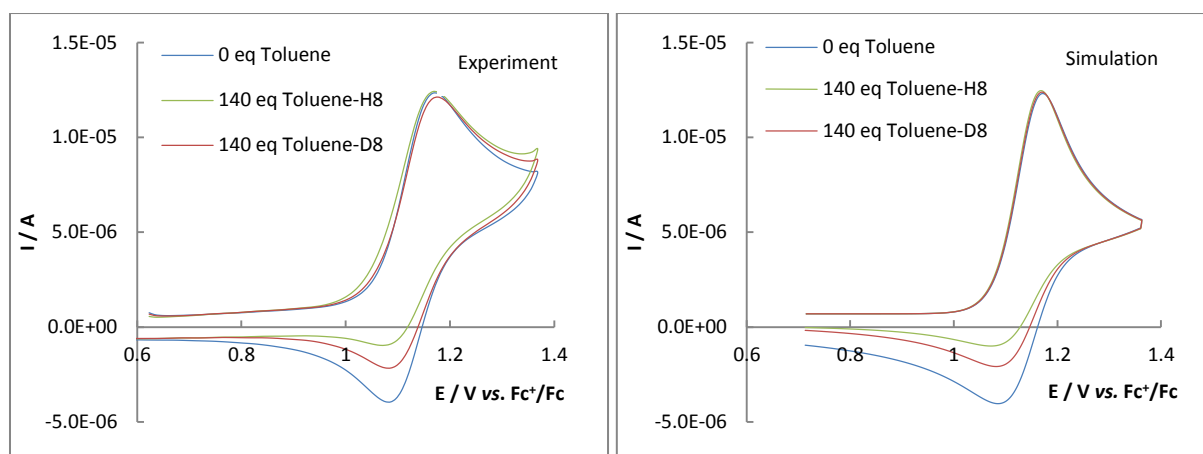
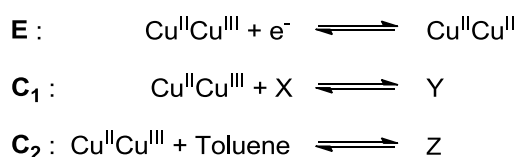


Figure 82 : CV of $\text{Cu}^{\text{II}}_2\text{Py}_4$ upon the addition of 140 equivalents of either toluene-H8 or toluene-D8. Left: experimental. Right: simulated. Experimental parameters: CV; $\nu = 50 \text{ mV/s}$; NBu_4ClO_4 in CH_3CN (0,1 M); concentration of $\text{Cu}^{\text{II}}_2\text{Py}_4 = 0.95 \text{ mM}$; glassy carbon as the working electrode; inert atmosphere. Simulation parameters: concentration of $\text{Cu}^{\text{II}}_2\text{Py}_4 = 0.95 \text{ mM}$; diffusion coefficient of $\text{Cu}^{\text{II}}_2\text{Py}_4 = 0.9 \cdot 10^{-5} \text{ cm}^2 \cdot \text{s}^{-1}$; Concentration of toluene = 0 or 135 mM; Area of electrode = 0.07 cm^2 ; heterogeneous standard rate constant for electron transfer $k^0 = 1 \text{ cm} \cdot \text{s}^{-1}$.

To quantify the differences in the CVs of $\text{Cu}^{\text{II}}\text{Py}_4$ upon the addition of toluene-H8 or toluene-D8, the CVs were simulated (Figure 82, right) using the software KISSA-1D.¹ The parameters used are close to those used for the experiment. The diffusion coefficient was determined by DOSY experiments (see Part II Chapter 3 Section 3.5.1.2). The heterogeneous standard rate constant for electron transfer (k^0) was defined as $1 \text{ cm}\cdot\text{s}^{-1}$ (*i.e.* relatively fast) as the peak to peak separation on the CV of the quasi reversible system is not that large (<100 mV).



Scheme 47 : Mechanism modelling the CV in oxidation displayed by $\text{Cu}^{\text{II}}\text{Py}_4$ in the presence of toluene. Parameters: E: [$E^0 = 1.11 \text{ V}$; $\alpha = 0.5$]; \mathbf{C}_1 : [$K_1 = 2 \text{ M}^{-1}$, $k_{f1} = 2 \text{ M}^{-1} \text{ s}^{-1}$]; \mathbf{C}_2 for toluene-H8 [$K_2 = 200 \text{ M}^{-1}$, $k_{f2} = 5 \text{ M}^{-1} \text{ s}^{-1}$]; for Toluene-D8 [$K_2 = 200 \text{ M}^{-1}$, $k_{f2} = 2 \text{ M}^{-1} \text{ s}^{-1}$].

The CV was modelled using an EC_1C_2 mechanism, where the complex on its own has an EC_1 mechanism (*i.e.* quasi-reversible, an unknown reaction occurs leading to compound Y), and upon the addition of toluene we get an extra chemical reaction C_2 , where the $\text{Cu}^{\text{II}}\text{Cu}^{\text{III}}$ species reacts with toluene. The mechanism is shown in Scheme 47. The following parameters were determined:

- E^0 denotes the oxidation potential (extracted from the experimental CV)
- α denotes the transfer coefficient (symmetry of the oxidation and reduction waves)
- K denotes equilibrium constants
- k denotes rate constants

By changing the rates of reaction of the C_2 reaction ($k_{f2\text{H}}$ for toluene-H8 and $k_{f2\text{D}}$ for toluene-D8) to fit the experimental data, the values $k_{f2\text{H}} = 5 \text{ M}^{-1}\cdot\text{s}^{-1}$ and $k_{f2\text{D}} = 2 \text{ M}^{-1}\cdot\text{s}^{-1}$ were obtained, giving a KIE value of $k_{f2\text{H}}/k_{f2\text{D}} = 2.5$. This is a primary kinetic isotope effect (although small), *i.e.* the partial rupture of the C-H bond in the transition state, which alludes to a possible hydrogen atom abstraction (HAT) as the rate determining step.

4.3.1.2. Determination of the oxidation products of toluene

In order to gain more insight into the reactivity of the $\text{Cu}^{\text{II}}\text{Cu}^{\text{III}}$ species on toluene, the determination of the oxidation products was attempted. Bulk electrolysis was performed on the complex $\text{Cu}^{\text{II}}\text{Py}_4$ (1mM) in a 0.1 M solution of $\text{NBu}_4\text{ClO}_4/\text{CH}_3\text{CN}$ to a potential of 1.3 V vs. Fc^+/Fc in the

¹ In collaboration with Dr. N. Le Poul.

presence of 490 equivalents of toluene-H8 at room temperature. Due to no differences in the response inside and outside the glovebox for the reactivity of the $\text{Cu}^{\text{II}}\text{Cu}^{\text{III}}$ species with toluene followed by CV, the electrolysis was performed outside the glovebox.

After exhaustive electrolysis the solution was concentrated, the large excess of NBu_4ClO_4 precipitated with diethyl ether and filtered, concentrated and precipitated a second time and the remaining diethyl ether solution was analysed by GCMS (see Figure 83, top) where the MS was probed by electron impact (EI).

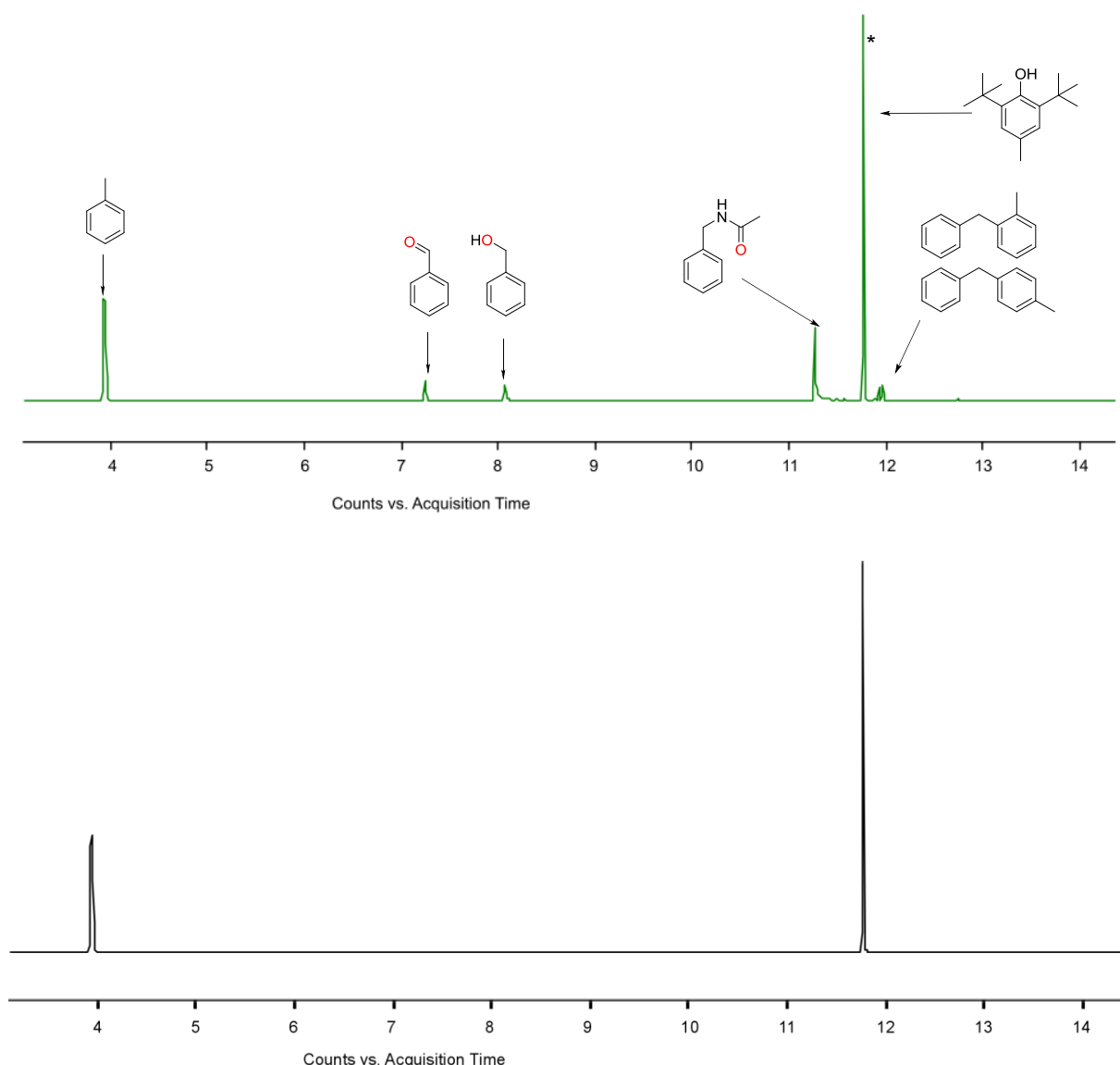


Figure 83 : Top: GCMS trace of the residue after bulk electrolysis of $\text{Cu}^{\text{II}}_2\text{Py}_4$ in the presence of toluene followed by treatment with diethyl ether. Starred peak: present in the diethyl ether. Bottom: GCMS trace of the blank electrolysis followed by treatment with diethyl ether.

A blank electrolysis was also completed as a control experiment – an electrochemical cell was set up in the same conditions but with no complex, and set at 1.3 V vs. Fc^+/Fc for the same amount of time (Figure 83, bottom). This was to ensure that no oxidation of toluene occurred at the electrode just because of the potential applied.

The GC trace presented in Figure 83 shows several peaks of which only the peaks at 3.9 min (toluene) and 11.8 (butylated hydroxytoluene, present in the diethyl ether) were observed after the electrolysis without the complex. The remaining products (determined by GC analysis of commercially available reference products or synthesised using literature procedures)¹⁷⁵ correspond to benzaldehyde, benzyl alcohol, benzylacetamide, 2-(methylphenyl)-toluene, and 4-(methylphenyl)-toluene were formed because of the presence of the $\text{Cu}^{\text{II}}\text{Cu}^{\text{III}}$ species generated by bulk oxidation of the complex $\text{Cu}^{\text{II}}_2\text{Py}_4$. Oxidation of toluene to benzoic acid was not observed. The products formed can be grouped into two categories: products with the insertion of an oxygen atom and products from C-C coupling.

Concerning the products for which the insertion of oxygen has occurred, the source of the oxygen atom was determined. The same reactions of the $\text{Cu}^{\text{II}}\text{Cu}^{\text{III}}$ species occur with toluene whether the electrolysis is carried out with or without the presence of O_2 (inside or outside the glove box). An exhaustive electrolysis of the complex $\text{Cu}^{\text{II}}_2\text{Py}_4$ (1mM) in the presence of 50 equivalents of H_2^{18}O in a glove box using a 0.1 M solution of $\text{NBu}_4\text{ClO}_4/\text{CH}_3\text{CN}$ dried over 3Å molecular sieves was also performed. Although the determination of the water content of the dried electrochemical solution was not attempted, the same procedure was used as that reported by Williams *et al.*¹⁷⁶ who determined a water content of less than 4 ppm (*i.e.* 1 mM of water in acetonitrile) which is far below the 50 mM of H_2^{18}O that was added. After electrolysis the solution was purified as previously described (precipitation of the NBu_4ClO_4 salt with diethyl ether) and analysed by GCMS. The counts vs. m/z are shown for specific retention times in Figure 84. Retention times, m/z and the assignment of peaks observed are displayed in Table 22.

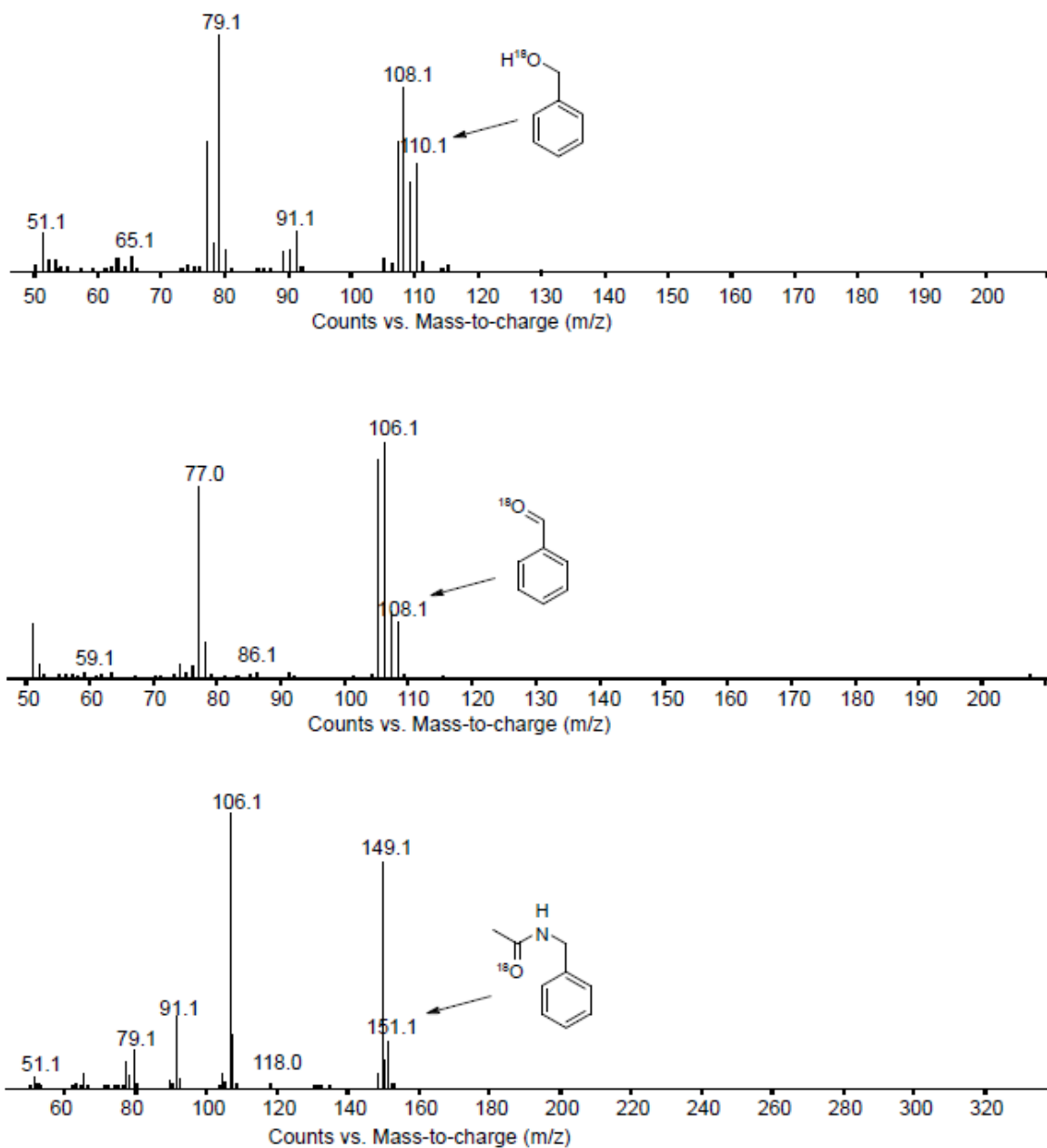


Figure 84 : EI spectra from the GCMS of the purified residue after the electrolysis of $\text{Cu}^{\text{II}}\text{Py}_4$ in the presence of toluene and H_2^{18}O . EI from retention times: Top: 8.03-8.06 min, middle 7.24-7.26 min, bottom 11.23-11.26 min.

Table 22: Retention time, m/z and assignment of peaks observed by GCMS after electrolysis of $\text{Cu}^{\text{II}}\text{Py}_4$ in the presence of toluene and H_2^{18}O .

Retention time / min	EI-MS / (m/z)	Assignment
8.03-8.06	108 and 110	$\text{PhCH}_2^{16}\text{OH}$ and $\text{PhCH}_2^{18}\text{OH}$
7.24-7.26	106 and 108	PhCH^{16}O and PhCH^{18}O
11.23-11.26	149 and 151	$\text{PhCH}_2\text{NHC}^{16}\text{OCH}_3$ and $\text{PhCH}_2\text{NHC}^{18}\text{OCH}_3$
11.87-11.90 and 11.93-11.95	182	2-(methylphenyl)-toluene and 4-(methylphenyl)-toluene

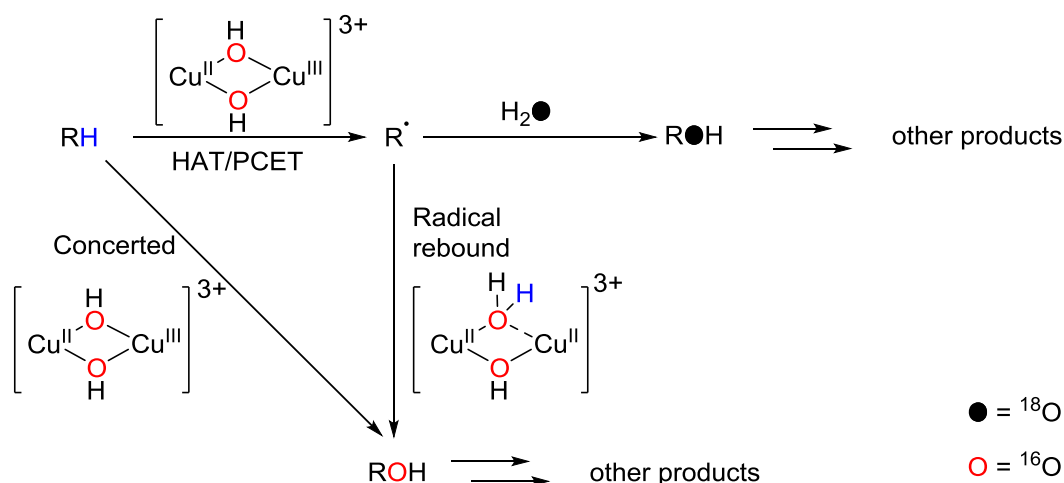
Despite the use of 50 eq of H_2^{18}O , there is still a significant amount of ^{16}O that has been incorporated into the oxidation products of toluene. This could be either the electrochemical solution was not properly dried. Another possibility that different mechanisms occur (Scheme 48) such as:

A. The $\text{Cu}^{\text{II}}\text{Cu}^{\text{III}}$ species oxidised toluene to form PhCH_2^\bullet that can then react with a molecule of water (forming products that incorporate ^{18}O).

B. The oxygen in the products comes from the hydroxido bridging groups, which if are not so labile (and do not exchange fast with the water in solution) will result in the incorporation of ^{16}O into the products. This can occur in two different ways:

- A radical rebound where the $\text{Cu}^{\text{II}}\text{Cu}^{\text{III}}$ species oxidised toluene to form PhCH_2^\bullet followed by a radical rebound with the bridging hydroxido group.
- A concerted mechanism, where the C-H bond is broken and oxygen is incorporated in a single step without the generation of radicals.

However a concerted/radical rebound cannot be the only mechanism due to the presence of 2-(methylphenyl)-toluene and 4-(methylphenyl)-toluene which have not incorporated an oxygen atom, and are clearly formed due to either a HAT or a sequential PCET.

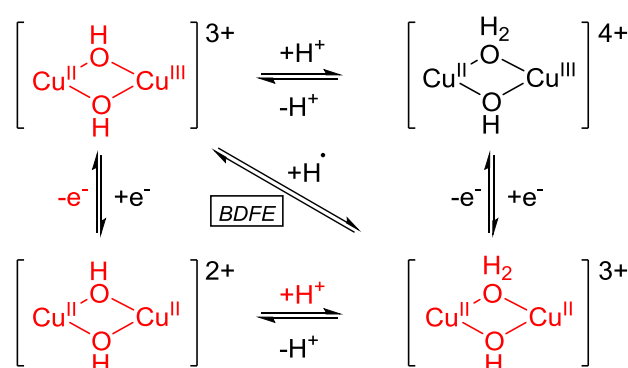


Scheme 48: Different mechanisms that could lead to the incorporation of ^{18}O and ^{16}O in the products.

4.3.1.3. Determination of the BDE of the $(\mu\text{-OH}) (\mu\text{-OH}_2)\text{Cu}^{\text{II}}\text{Cu}^{\text{III}}$ species

To fully determine the oxidising power of the $\text{bis}(\mu\text{-OH})\text{Cu}^{\text{II}}\text{Cu}^{\text{III}}$ species, the BDE of the HO-H bond formed upon HAT was determined by using a thermodynamic cycle.¹²² The $\text{bis}(\mu\text{-$

OH)Cu^{II}Cu^{III} species reacts either by HAT or by a sequential PCET, forming a (μ-OH)(μ-OH₂)Cu^{II}Cu^{II}. The transfer of a hydrogen radical can be equated to the transfer of an electron followed by a proton, and the free energy values of each of these can be determined from the oxidation potential and pK_a of the relevant species (see Scheme 49). The free energy of proton transfer (ΔG_{PT}) can be related to the pK_a via Equation 15 where R is the molar gas constant, T is the temperature and K_a is the association constant. Similarly the free energy of electron transfer (ΔG_{ET}) can be related to the oxidation potential via Equation 16 where F is Faraday's constant and E^0 is the reduction potential. The BDE can therefore be calculated using Equation 17 (where C_H is the H⁺/H[•] standard reduction potential in CH₃CN vs. Fc⁺/Fc) or the BDFE can be calculated simply by substituting C_H by C_G , similar to C_H but includes entropic effects.¹²²



Scheme 49 : Square scheme relating the species necessary for determining the BDFE of the bis(μ-OH)Cu^{II}Cu^{III} species. The processes in red were measure experimentally.

Equation 15:

$$\Delta G_{PT} = -RT \ln(K_a) = -1.37 \text{ kcal. mol}^{-1} \cdot pK_a$$

Equation 16:

$$\Delta G_{ET} = -FE^0 = -23.06 \text{ kcal. mol}^{-1} \cdot V^{-1} \cdot E^0$$

Equation 17:

$$BDE (\text{kcal. mol}^{-1}) = 1.37 pK_a + 23.06 E^0 + C_H$$

The pK_a for the (μ-OH) (μ-OH₂)Cu^{II}Cu^{II} species was determined by potentiometric titration of the complex (0.5 mM) in a 0.01 M solution of NaClO₄ in water, starting from a pH of 3.0 using HClO₄ and increasing the pH by sequential addition of a 0.01 M solution of NaOH in water. The pK_a was determined to be 3.9 ± 0.1 in water.^m This is consistent with the pK_a of a bridged water molecule (pK_a of 3.3) between two Cu^{II} ions obtained by Tilley *et al.*¹³⁶ using a very similar ligand 2,7-bis(di(2-pyridyl)fluoromethyl)-1,8-naphthyridine (DPFN), the only difference being the two methyl groups of

^m Personal communication from Dr. C. Belle.

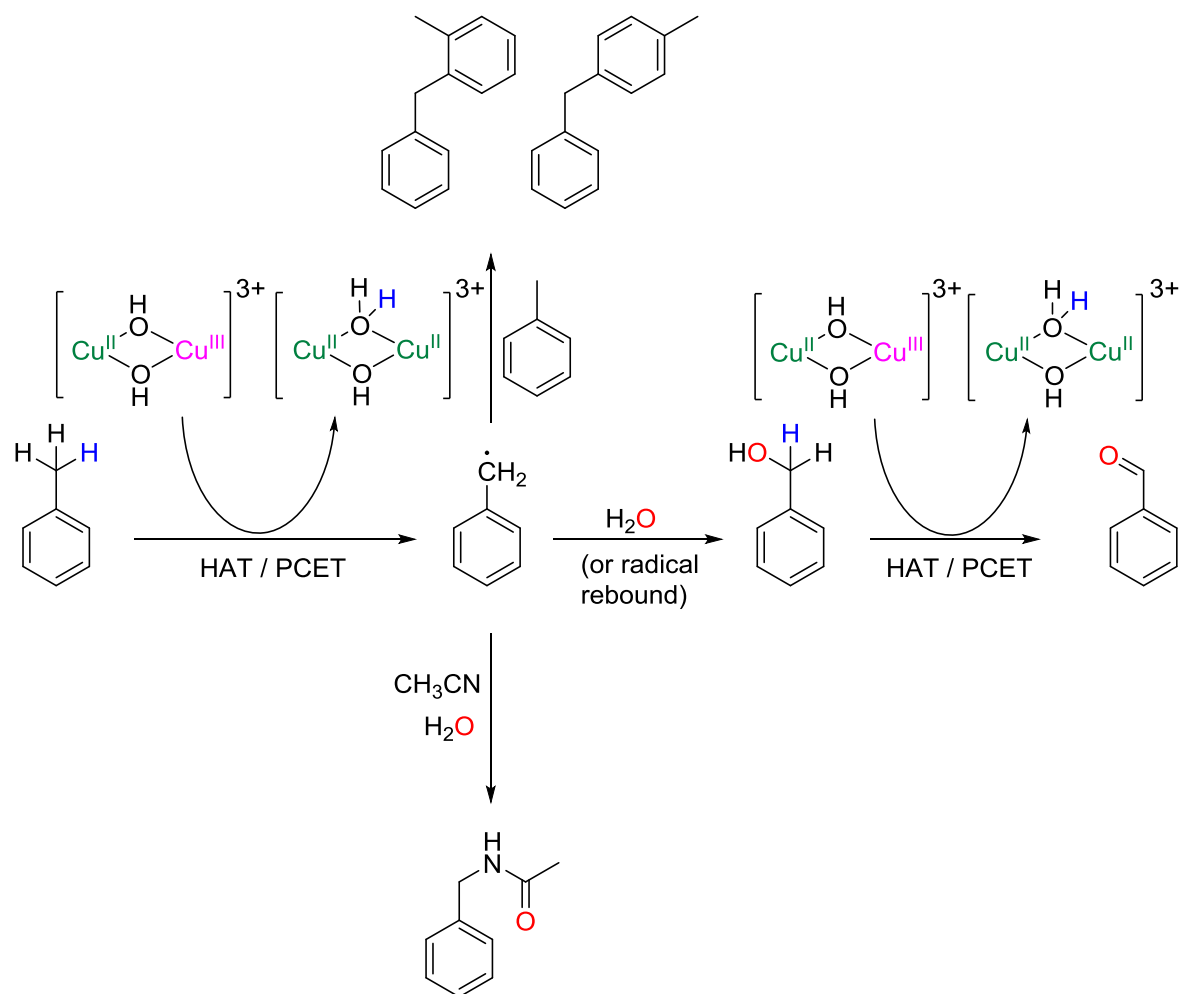
ligand Py_4 are replaced by fluorines. Although most of the characterisation of $\text{Cu}^{\text{II}}_2\text{Py}_4$ was in CH_3CN and not water, usually the pK_a is higher in organic solvents than in water¹⁷⁷ due to the charge stabilisation by the large dipole on water molecules, so the value of the pK_a value given in water is a lower estimation, making the estimated value for the BDE to be the lower limit. The values of $pK_a = 3.9$, $E_{1/2} = 1.11 \text{ V vs. Fc}^+/\text{Fc}$, and $C_H = 59.4 \text{ kcal.mol}^{-1}$ (or $C_G = 54.9 \text{ kcal.mol}^{-1}$),¹²² give a BDE of 90 kcal.mol^{-1} using Equation 17, and a bond dissociation free energy (BDFE) of 86 kcal.mol^{-1} .ⁿ

4.3.1.4. Discussion

A radical mechanism is probable due to the nature of the product, most likely a HAT from the methyl group of toluene to the bis(μ -OH) $\text{Cu}^{\text{II}}\text{Cu}^{\text{III}}$, however a sequential PCET cannot be ruled out with the available data. Correlations between rate of reaction and either bond strength or pK_a would have to be drawn, as was done by Tolman *et al.*⁴⁴ In either case it seems as though a PhCH_2^\bullet radical is formed which can then form (methylphenyl)-toluene by reaction with another molecule of toluene, or PhCH_2OH by reaction with water (or radical rebound of the OH group that originally bridges the two copper ions). The presence of PhCHO could be due to the further reaction of PhCH_2OH with the $\text{Cu}^{\text{II}}\text{Cu}^{\text{III}}$ centre and subsequent reaction with water, for which the kinetics will be faster because the C-H bond next to the OH group PhCH_2OH will be weaker than the equivalent CH_2 group in toluene. The presence of N-benzylacetamide could be either due to the PhCH_2^\bullet radical reacting with a molecule of acetonitrile and then water, or the $\text{Cu}^{\text{II}}\text{Cu}^{\text{III}}$ species directly oxidising the CN bond of the solvent. These proposals are summarised in Scheme 50. The relative yields of each species are variable, in part due to the procedure used for the purification of the electrochemical solution after electrolysis, and therefore quantification would not be accurate.

Oxidation of stronger C-H bonds than the methyl group of toluene are limited by the solvent. The methyl group of toluene has a bond dissociation energy (BDE) of 88 kcal.mol^{-1} ,¹⁷⁸ which is close to that of the CH_3 group of acetonitrile with a BDE of 93 kcal.mol^{-1} .⁸⁹ A change of solvent is therefore necessary for observing the oxidation of stronger bonds by CV, otherwise any attempts to oxidise stronger bonds will not be observed as the kinetics will be much faster for the oxidation of CH_3CN (which is also in a large excess as it is the solvent) than for the added substrate. The electrochemistry of the complex $\text{Cu}^{\text{II}}_2\text{Py}_4$ was attempted in benzonitrile as it is a more robust solvent with a large electrochemical window, however this resulted in the precipitation of the complex. The high oxidation potential of the complex rules out other commonly used electrochemical solvents such as DCM as the electrochemical window is too small.

ⁿ Both BDE and BDFE are reported for comparison with the literature.



Scheme 50: Summary of the reactions occurring between the Cu^{II}-Cu^{III} species and toluene.

Comparison to the literature:

The reactivity of no other Cu^{II}-Cu^{III} species has been characterised to this extent, so comparison to the literature is difficult. One of the most reactive Cu:O species in the literature is the Cu^{III}-OH unit characterised by Tolman *et al.*⁴⁴ which showed second order rate constant of 0.11 M⁻¹.s⁻¹ by reaction with THF (BDE = 92 kcal.mol⁻¹) at RT. We obtained the value of 5.0 M⁻¹.s⁻¹ for reaction of the bis(μ-OH)Cu^{II}-Cu^{III} unit with toluene (88 kcal.mol⁻¹), an order of magnitude faster for a reaction of C-H bonds of similar strength. Interestingly although the kinetics of the reaction are much faster with the bis(μ-OH)Cu^{II}-Cu^{III}, the energetics are very similar to Tolman's Cu^{III}-OH complex (Part 1 Chapter 2 complex **13**): both show a BDE of 90 kcal.mol⁻¹. This could be due to the bulk of the isopropyl groups on the ligand of Tolman's complex limiting access to the Cu^{III}-OH centre, slowing the reaction with an external substrate down. The high value of BDE for Tolman's complex is largely due to the high *pK_a*

of 19 for the $\text{Cu}^{\text{II}}\text{-OH}_2$ species which is very high compared to the value obtained for the $(\mu\text{-OH})(\mu\text{-OH}_2)\text{Cu}^{\text{II}}\text{Cu}^{\text{II}}$ ($pK_a = 3.9$) formed from the complex $\text{Cu}^{\text{II}}_2\text{Py}_4$. The high oxidation potential of the bis($\mu\text{-OH}$) $\text{Cu}^{\text{II}}\text{Cu}^{\text{II}}$ species in complex $\text{Cu}^{\text{II}}_2\text{Py}_4$ is therefore responsible for the high BDE.

Other known dicopper model complexes that form O-H bonds upon reaction with a substrate have shown lower O-H bond strengths. Meyer's $\text{Cu}^{\text{II}}_2(\text{O}_2^-)$ species (Part I Chapter 2 complex **42**) abstracts a hydrogen atom from TEMPO-H to form $\text{Cu}^{\text{II}}_2(\text{O}_2\text{H})$ (which is therefore a weaker oxidant) with the value of BDFE° ,^{122,179} given as $72 \text{ kcal}\cdot\text{mol}^{-1}$.¹²⁰ Karlin's bis($\mu\text{-O}$) $\text{Cu}^{\text{III}}\text{Cu}^{\text{III}}$ complexes (Part I Chapter 2 complexes **30** and **33**) react only with weak C-H bonds *via* HAT, there is no significant reaction of this species with DHA ($\text{BDE} = 76 \text{ kcal}\cdot\text{mol}^{-1}$).⁹⁹ Other $\text{Cu}_2:\text{O}_2$ adducts formed upon reaction of O_2 with Cu^{I} have been shown to oxidise toluene, but the active species is ambiguous due to equilibriums of $[\text{Cu}_2\text{O}_2]^+$ (and even mononuclear) species.¹¹⁷ The OH bond in $\text{Cu}^{\text{I}}\text{Cu}^{\text{II}}\text{OH}$ of the zeolite Cu-ZSM-5 has been calculated at $90 \text{ kcal}\cdot\text{mol}^{-1}$,⁷⁷ and has therefore been proposed to be one of the driving forces for the oxidation of methane by the $\text{Cu}^{\text{II}}_2\text{O}$ species, but the $\text{Cu}^{\text{II}}_2\text{O}$ species has yet to be demonstrated to react with strong CH bonds in solution (so far only reactivity with water, PPh_3 , CO_2 and oxidative coupling of 2,4-di-tert-butylphenol with a BDE of $82 \text{ kcal}\cdot\text{mol}^{-1}$ have been demonstrated).^{125,180} The bis($\mu\text{-OH}$) $\text{Cu}^{\text{II}}\text{Cu}^{\text{III}}$ species is therefore of interest because the strong OH bond strength of the $(\mu\text{-OH})(\mu\text{-OH}_2)\text{Cu}^{\text{II}}\text{Cu}^{\text{II}}$ species is high and therefore can help HAT/PCET from alkanes with strong C-H bonds.

4.3.1.5. Conclusions

The $\text{Cu}^{\text{II}}\text{Cu}^{\text{III}}$ species generated is capable at room temperature of oxidising the CH bond of the methyl group of toluene, a bond strength of $88 \text{ kcal}\cdot\text{mol}^{-1}$,¹⁷⁸ with the driving force likely to be the formation of the strong OH bond of the $(\mu\text{-OH})(\mu\text{-OH}_2)\text{Cu}^{\text{II}}\text{Cu}^{\text{II}}$ species ($\text{BDE} \sim 90 \text{ kcal}\cdot\text{mol}^{-1}$). A KIE of 2.5 was evidenced by CV indicating the partial rupture of the C-H bond in the rate determining step. Several oxidation products are observed which are all consistent with a radical mechanism. The oxygen atoms incorporated into some of the oxidation products are most likely from a radical PhCH_2^\bullet reacting with a water molecule in solution and not a direct insertion of the hydroxido bridging group into the C-H bond, as this would not explain the presence of (methylphenyl)-toluene. From the data available, a HAT reaction or a sequential PCET cannot be distinguished.

^o BDE (bond dissociation enthalpy) and BDFE (bond dissociation free energy) are not strictly the same, as the former misses out the entropic contribution. The entropic contribution in the case of a PCET is low, typically 2 to $5 \text{ kcal}\cdot\text{mol}^{-1}$ so for the purpose of this discussion BDEs and BDFEs are compared.

4.3.2. Electrocatalytic activity of $\text{Cu}^{\text{II}}\text{Py}_4$

Up to this point, the capabilities of reactivity of the mixed valent $\text{Cu}^{\text{II}}\text{Cu}^{\text{III}}$ species has been demonstrated by a non-catalytic reaction of the species with toluene. After HAT/PCET by the bis($\mu\text{-OH}$) $\text{Cu}^{\text{II}}\text{Cu}^{\text{III}}$ species it is likely that the resulting product is a $(\mu\text{-OH})(\text{OH}_2)\text{Cu}^{\text{II}}_2$ species so the protonation states of the bridges need to be controlled to make the reaction electrocatalytic. Bases must therefore be used, however the addition of a base may actually deprotonate the bridging OH groups of the starting bis($\mu\text{-OH}$) $\text{Cu}^{\text{II}}\text{Cu}^{\text{II}}$ complex.

4.3.2.1. The effect of base on the CV of $\text{Cu}^{\text{II}}\text{Py}_4$

The effect of a base on $\text{Cu}^{\text{II}}\text{Py}_4$ was investigated to see if the hydroxido bridges could be deprotonated. This should be observable by a lowering of the oxidation potential of the complex, as an O^{2-} (more negatively charged) bridge would stabilise the formation of a Cu^{III} , and thus the formation of a mixed valent $[\text{Cu}^{\text{II}}\text{Cu}^{\text{III}}\text{Py}_4]^+$ species. The bases 2,6-lutidine and pyridine were investigated, as their oxidation potential is higher than that of the complex $\text{Cu}^{\text{II}}\text{Py}_4$ (1.8 V vs. Fc^+/Fc for 2,6-lutidine, and 1.45 V vs. Fc^+/Fc for pyridine). 2,6-lutidine or pyridine (0-5 eq) was added sequentially to the complex (0.1 mM) in solution of 0.1 M $\text{NBu}_4\text{ClO}_4/\text{CH}_3\text{CN}$ and the CVs were recorded after each addition. The results are shown below in Figure 85.

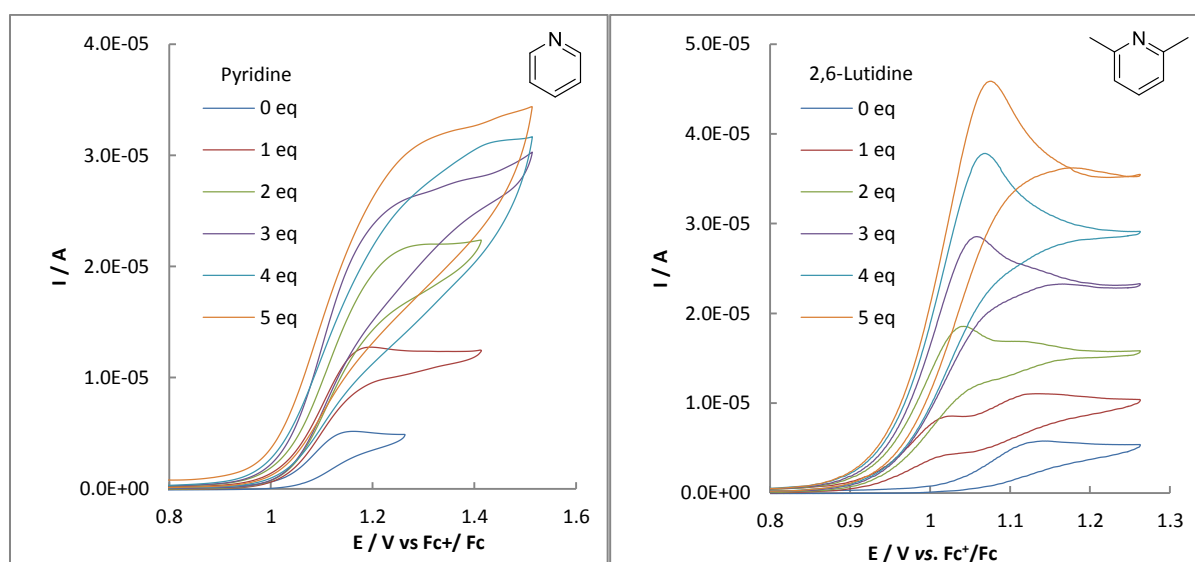


Figure 85 : Addition of Pyridine (left) and 2,6-lutidine (right) to the complex $\text{Cu}^{\text{II}}\text{Py}_4$ followed by CV. Parameters: $\nu = 5$ mV/s; NBu_4ClO_4 in CH_3CN (0,1 M); concentration of $\text{Cu}^{\text{II}}\text{Py}_4 = 1$ mM; glassy carbon as the working electrode; presence of air.

A. Pyridine as a base:

A dramatic increase in the current is observable upon addition of pyridine indicating an electrocatalytic activity. There is no real plateau in the current above 1 equivalent of pyridine, which could be due to the grafting of the pyridine base onto the electrode. The curves of addition of 3 and 4 equivalents are very similar, also indicating that the pyridine interferes with the surface of the electrode. The oxidation potential of the pyridine at 1.45 vs. Fc^+/Fc is close to the oxidation potential of the complex and could be the source of these problems. Studies using pyridine were not taken any further due to these problems, and also due to the possibility that it can coordinate to the copper (although in this case there seems to be no coordination, which would be observable by a change in oxidation potential).

B. 2,6-Lutidine as a base:

The addition of 2,6-lutidine also causes a dramatic increase in current. A pre-peak is observed upon addition of 1 eq of 2,6-lutidine at 1.0 V vs. Fc^+/Fc . The potential of this pre-peak increases with addition of further equivalents of 2,6-lutidine, whereas the second peak at $E_p = 1.13$ V vs. Fc^+/Fc attributed to the oxidation of $\text{Cu}^{\text{II}}_2\text{Py}_4$ to $[\text{Cu}^{\text{II}}\text{Cu}^{\text{III}}\text{Py}_4]^+$ stays at the same potential. This is the classic case of “total catalysis” (described in Section 4.1), where upon addition of a small amount of a substrate, all the substrate gets consumed at the surface of the electrode on the timescale of the forward scan leading to a peak, but there is still some un-oxidised catalyst present so the oxidation of the catalyst is still observable (the second peak).^{170,171} This indicates that the presence of a base causes the electrocatalysis of either the base itself, the solvent (CH_3CN), the supporting electrolyte NBu_4ClO_4 or of water which is present in the solution.

4.3.2.2. Determination of the effect of water on the electrocatalysis of $\text{Cu}^{\text{II}}_2\text{Py}_4$

In order to determine if it is the electrocatalytic wave that is observed upon addition of 2,6-Lutidine, the electrocatalytic activity was investigated in the presence of various amounts of water. The electrochemical solution (0.1 M $\text{NBu}_4\text{ClO}_4/\text{CH}_3\text{CN}$) was prepared by drying over 3Å molecular sieves,¹⁷⁶ and the CV of $\text{Cu}^{\text{II}}_2\text{Py}_4$ (1 mM) in the presence of 1 eq of 2,6-Lutidine was investigated upon addition of water (0-50 eq). The results are shown in Figure 86. A boron doped diamond (BDD) electrode was used because of the minimal residual current in the presence of water (and therefore the results are not comparable to those shown in Figure 85 using a glassy carbon electrode). The CVs of 1 mM 2,6-lutidine and different quantities of water were subtracted from the CVs of the complex

with 2,6-lutidine and the respective amount of water, so that any changes to the current are not due to the oxidation of water (or 2,6-lutidine) at the electrode.

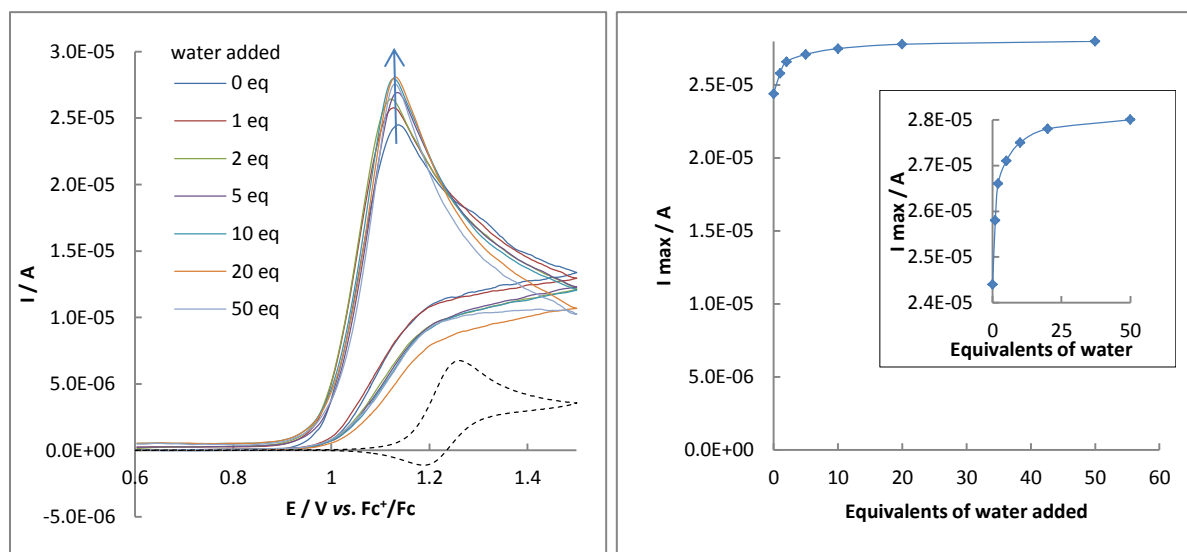


Figure 86 : Left : CV of the addition of water to Cu^{II}₂Py₄ in the presence of 1 eq of 2,6-lutidine. The CV curves of 2,6-lutidine and water were subtracted from the respective CVs of Cu^{II}₂Py₄, 2,6-lutidine and water. Dotted line: 0 eq 2,6-lutidine, 0 eq H₂O. Coloured lines: 1 eq 2,6-lutidine, 0-50 eq H₂O. Parameters: $\nu = 20$ mV/s; NBu₄ClO₄ in CH₃CN (0,1 M); concentration of Cu^{II}₂Py₄ = 1 mM; concentration of 2,6-lutidine = 0 or 1 mM; boron doped diamond (BDD) used as the working electrode; inert atmosphere. Right: maximum current of each of the CV curves Cu^{II}₂Py₄ with 1 eq 2,6-Lutidine upon addition of 0-50 eq H₂O.

There is a dramatic increase in the maximum current upon addition of 1 eq of 2,6-lutidine, even without the presence of water, ruling out the hypothesis that electrocatalysis of water by the complex Cu^{II}₂Py₄ occurs. Slight increases in the current are observable upon an increase in water concentration at a constant concentration of 2,6-lutidine: the increase with the first equivalent of water is relatively significant and the increase in current is reduced on each subsequent addition. This indicates that water does have an effect, but the effect is minimal. Interpretation of this result is difficult: it could either be that the water helps regenerate the starting Cu^{II}₂Py₄, or that the mechanism of the electrocatalytic oxidation changes upon addition of water. Simulations would not be rigorous as there are too many unknown parameters (such as which is the substrate to be oxidised by the Cu^{II}Cu^{III} species). Water is therefore not the substrate for the electrocatalysis caused by Cu^{II}₂Py₄ but does have a small effect.

4.3.2.3. Determination of the oxidation products of the electrocatalysis by Cu^{II}₂Py₄

Suspecting that the 2,6-lutidine was acting to regenerate the catalyst and as a substrate (oxidation of the methyl groups), analysis of the oxidation products was attempted by NMR. Bulk

electrolysis in a 0.1 M solution $\text{CH}_3\text{CN}/\text{NBu}_4\text{ClO}_4$ of $\text{Cu}^{\text{II}}\text{Py}_4$ (1mM) in the presence of 8 equivalents of 2,6-Lutidine was completed until a total of eight electrons. mol^{-1} of catalyst had been passed (4 Coulombs). The ^1H -NMR of the resulting residue is shown in Figure 87.

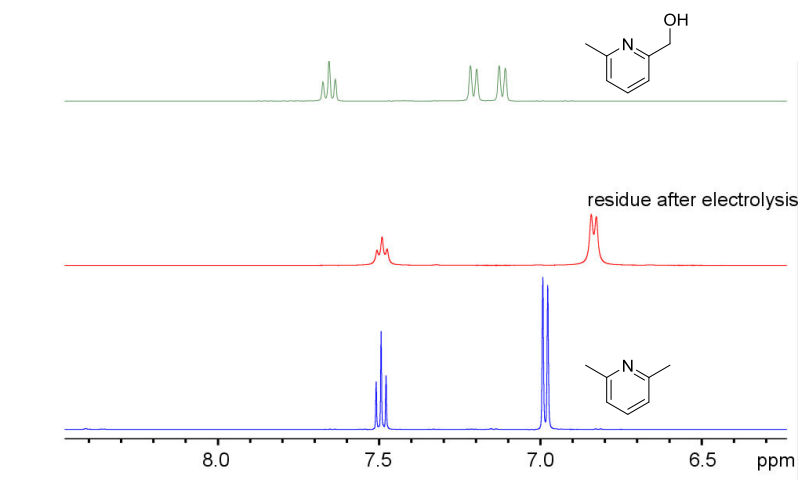


Figure 87: ^1H -NMR spectra in CD_3CN of the aromatic regions of 2,6-lutidine (blue), 2,6-lutidine after electrolysis in the presence of $\text{Cu}^{\text{II}}\text{Py}_4$ (red) and 6-methyl-2-pyridinemethanol (green).

The ^1H -NMR of the residue after electrolysis shows very few changes compared to the spectrum of 2,6-lutidine: there is only a slight change in chemical shift. The pattern in the aromatic region is not at all the same as 6-methyl-2-pyridinemethanol, the expected oxidation product. 6-methyl-2-pyridinemethanol also has a peak assigned to the CH_2OH at 4.60 ppm (not shown) which is not present in the residue after electrolysis. The lack of a CH_2OH peak at 4-5 ppm also eliminates the possibility that 2,6-lutidine has been oxidised on both methyl groups to form 2,6-pyridinedimethanol.

For further analysis, the residue was taken up in ether to remove the NBu_4ClO_4 and analysed by ESI and GCMS. Both of these techniques revealed only the presence of 2,6-lutidine and no oxidation products of either the 2,6-lutidine or the solvent CH_3CN . It is clear therefore that the electrocatalytic oxidation that is observed is not that of the methyl groups of the 2,6-lutidine (or at least only undetectable amounts of the product are formed, and therefore oxidation of something else in solution occurs as well).

As the electrocatalytic oxidation is not that of water or of the base itself, the only other possibilities for substrates in the electrochemical cell are the solvent CH_3CN or the supporting electrolyte NBu_4ClO_4 , the oxidation products of which both are difficult to characterise. Chan *et al.* observed the oxidation of CH_3CN into CH_2OHCN by adducts of CH_2OHCN and their complex by ESI and by a shift in the CN stretching band by IR.⁸² In our case these methods would not be possible because

of the presence of a large excess of NBu_4ClO_4 . It is very probable that the electrocatalytic oxidation is that of the CH_3CN solvent and the oxidation products have not been observed.

To determine if the electrocatalytic oxidation of C-H bonds of an external substrate occurs, the electrolysis of the complex $\text{Cu}^{\text{II}}\text{Py}_4$ was attempted in the presence of 8 equivalents of 2,6-lutidine and 490 equivalents of toluene in the hope that oxidation of toluene would occur instead of the acetonitrile solvent because of the lower BDE of toluene. The electrolysis was performed using a 0.8 mM of the complex $\text{Cu}^{\text{II}}\text{Py}_4$ in a solution of 0.1 M $\text{NBu}_4\text{ClO}_4/\text{CH}_3\text{CN}$ to a potential of 1.3 V vs. Fc^+/Fc under an atmosphere of air. A blank electrolysis in the same conditions (the same potential for the same amount of time) but without the complex was also completed to ensure that there was no oxidation of toluene catalysed by the 2,6-lutidine at the electrode. The residues were purified by precipitation with diethylether to remove the NBu_4ClO_4 and then analysed by GCMS (Figure 88).

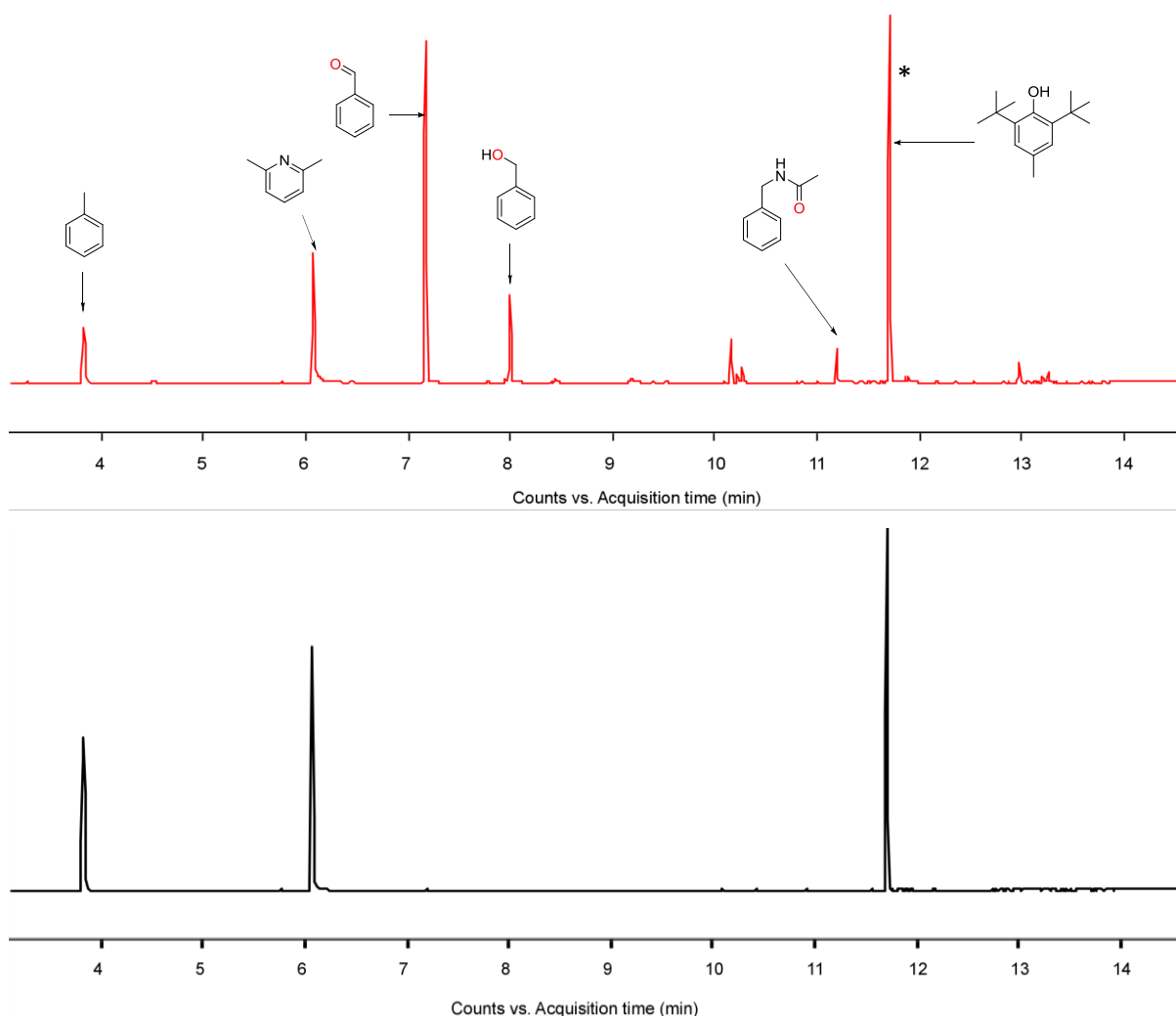


Figure 88: Top: GCMS trace of the purified solution after bulk electrolysis of $\text{Cu}^{\text{II}}\text{Py}_4$ in the presence of 2,6-lutidine and Toluene that has been taken up in diethyl ether. Bottom: GCMS trace of the blank electrolysis performed under the same conditions but with no complex. The starred peak is present in the diethyl ether used.

The GC trace shown in Figure 88 reveals several peaks of which only the peaks at 3.9 min (toluene), 6.1 min (2,6-lutidine) and 11.6 min (butylated hydroxytoluene, present in the diethyl ether) were observed after the electrolysis without the complex. This indicates that the remaining products benzaldehyde, benzylalcohol and N-benzylacetamide are formed because of the electrocatalysis of $\text{Cu}^{\text{II}}_2\text{Py}_4$, indicating that the species formed upon oxidation in the presence of a base is capable of C-H oxidation.

4.3.2.4. Determination of kinetic parameters of the electrocatalysis by the complex $\text{Cu}^{\text{II}}_2\text{Py}_4$ ^P

A. Determination of the “total catalysis” regime

When small quantities of 2,6-Lutidine are added to the complex (Figure 85), a double peak is observed indicating a possible “total catalysis” regime (a pre-peak corresponding to the catalytic reaction consuming all the substrate, followed by the reversible system of the leftover catalyst, see Section 4.1.3.3). To confirm if the limits of the total catalysis regime (where the catalytic peak is dependent on the diffusion of the (co)substrate), CVs were recorded in a glove box of the complex $\text{Cu}^{\text{II}}_2\text{Py}_4$ (0.8 mM) in dried acetonitrile/ NBu_4ClO_4 with:

- i) A constant scan rate ($20 \text{ mV}\cdot\text{s}^{-1}$) and changing the concentration of 2,6-lutidine
- ii) A constant concentration of 2,6-lutidine (0.6 mM) and variable scan rate.

The results are displayed in Figure 89 and Figure 90 respectively.

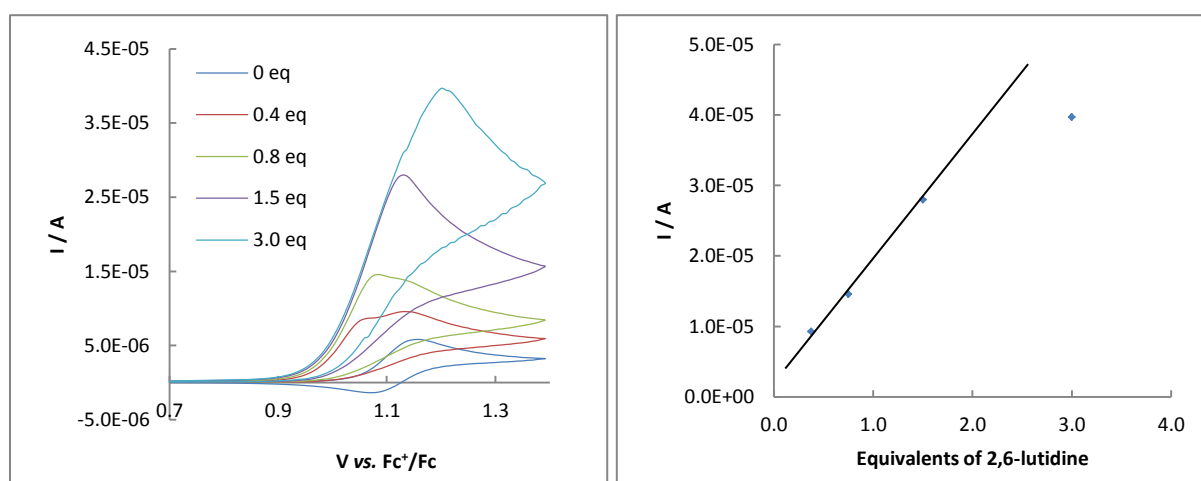


Figure 89: left: CV of the addition of different concentrations of 2,6-lutidine to the complex $\text{Cu}^{\text{II}}_2\text{Py}_4$. Right: peak current against the concentration of 2,6-lutidine added. Parameters: solvent: 0.1 M NBu_4ClO_4 in CH_3CN , dried over molecular sieves; concentration of complex: 0.8 mM; concentration of 2,6-lutidine: 0.3, 0.6, 1.2 and 2.4 mM; scan rate: $20 \text{ mV}\cdot\text{s}^{-1}$, working electrode: BDD; room temperature; under Ar.

^P In collaboration with Dr. N. Le Poul.

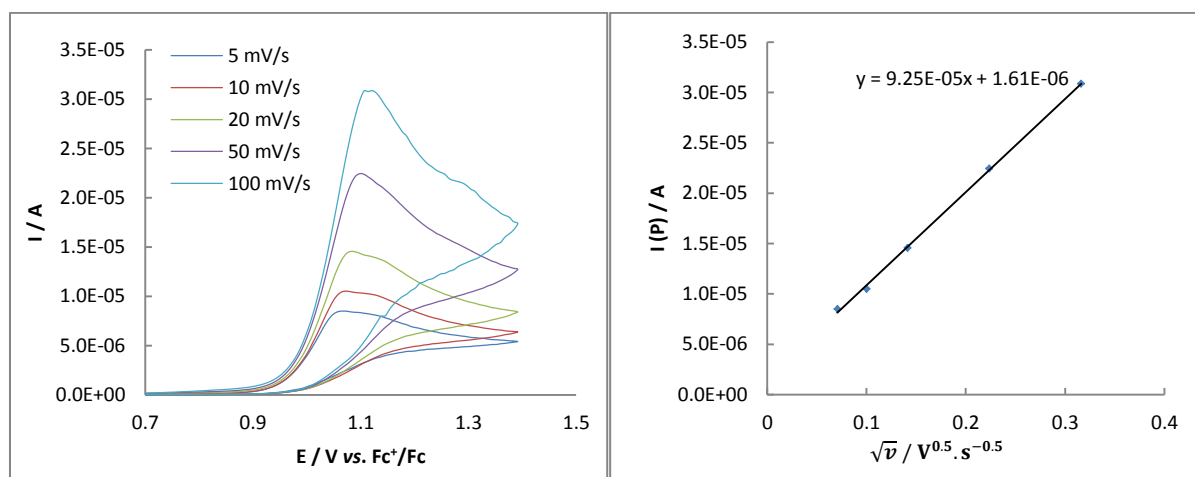


Figure 90: Left: CV of the Cu^{II}₂Py₄ with 0.6 mM of 2,6-lutidine at different scan rates. Right: corresponding plot of the peak current as a function of \sqrt{v} . Parameters: solvent: 0.1 M NBu₄ClO₄/CH₃CN dried over molecular sieves; concentration of Cu^{II}₂Py₄: 0.8 mM; concentration of 2,6-lutidine: 0.6 mM; working electrode: BDD; room temperature; under Ar.

The plot of peak current as a function of concentration of 2,6-lutidine (Figure 89, right) displays a straight line below 1.5 eq of 2,6-lutidine, indicating that below this value the peak current is limited by the diffusion of the 2,6-lutidine into the reaction layer.¹⁸¹ The plot of the peak current against the square root of the scan rate for a concentration in 2,6-lutidine of 0.6 mM also displays a straight line (Figure 90, right), confirming that no other effects occur in the range of $5 < v < 100 \text{ mV}\cdot\text{s}^{-1}$. Thus the total catalysis regime is within these conditions, allowing the use of approximations valid for this regime.

B. Determining the number of electrons in the catalytic reaction

In the case of a single electron catalytic reaction, the peak current is determined by Equation 18,¹⁷³

Equation 18:

$$I_p = 1 \times 0.609 F A C_A^0 \sqrt{D \frac{Fv}{RT}}$$

In the case of a two electron, two substrate reaction where the excess factor of the substrate (Z, in this case the solvent acetonitrile) is in a large excess of the co-substrate (A, in this case the co-substrate 2,6-lutidine) (and therefore $\gamma_Z/\gamma_A \rightarrow \infty$), the peak current is determined by Equation 19, for all possible mechanisms.¹⁸² It differs only by a factor of 2 from the equation for a single electron.

Equation 19:

$$I_p = 2 \times 0.609 F A C_A^0 \sqrt{D \frac{Fv}{RT}}$$

C_A^0 = is the bulk concentration of the substrate / M

$D = D_A = D_Z$ = the diffusion coefficients of the co-substrate and the substrate / $\text{dm}^2 \cdot \text{s}^{-1}$

As the area of the electrode ($A = 0.07 \text{ cm}^2$) and the diffusion coefficient of the 2,6-lutidine (measured to be $4.4 \times 10^{-5} \text{ cm}^2 \cdot \text{s}^{-1}$ by DOSY NMR in a 0.1 M solution of KPF_6 in CD_3CN) are already known, the plot of the peak current against the square root of the scan rate shown in Figure 90 (right) gives access to the factor displayed in red in Equation 18 and Equation 19. A factor of 0.9 was obtained, consistent with a one electron mechanism.

C. Determination of the observed rate constant from experimental data

In the case of total catalysis, the kinetics of the reaction can be extracted from the potential of the pre-peak observed upon total catalysis (related *via* Equation 20, introduced in Section 4.1.3.3).

Equation 20:

$$E_{p,c} = E_{\text{Cu}_2^{\text{II}}/\text{Cu}^{\text{II}}\text{Cu}^{\text{III}}}^0 - 0.409 \frac{RT}{F} + \frac{RT}{2F} \ln \left(\frac{RT}{F} \frac{k_{\text{obs}} D_{\text{Cu}_2^{\text{II}}} (C_{\text{Cu}_2^{\text{II}}}^0)^2}{v D_{\text{lut}} (C_{\text{lut}}^0)} \right)$$

$E_{\text{Cu}_2^{\text{II}}/\text{Cu}^{\text{II}}\text{Cu}^{\text{III}}}^0$ = the oxidation potential of the catalyst $\text{Cu}^{\text{II}}_2\text{Py}_4 = 1.12 \text{ V vs. Fc}^+/\text{Fc}$

$D_{\text{Cu}_2^{\text{II}}}$ = the diffusion coefficient of the catalyst $\text{Cu}^{\text{II}}_2\text{Py}_4 = 1.0 \times 10^{-5} \text{ cm}^2 \cdot \text{s}^{-1}$

D_{lut} = the diffusion coefficient of 2,6-lutidine = $4.4 \times 10^{-5} \text{ cm}^2 \cdot \text{s}^{-1}$

$C_{\text{Cu}_2^{\text{II}}}^0$ = the bulk concentration of the catalyst $\text{Cu}^{\text{II}}_2\text{Py}_4 = 0.8 \text{ mM}$

C_{lut}^0 = the bulk concentration of 2,6-lutidine = 0.6 mM

A plot of $\exp \frac{2F}{RT} \left(E_{p,c} - E_{\text{Cu}_2^{\text{II}}/\text{Cu}^{\text{II}}\text{Cu}^{\text{III}}}^0 + 0.409 \frac{RT}{F} \right)$ against $1/v$ is displayed in Figure 91, corresponding to the CVs displayed in Figure 90.

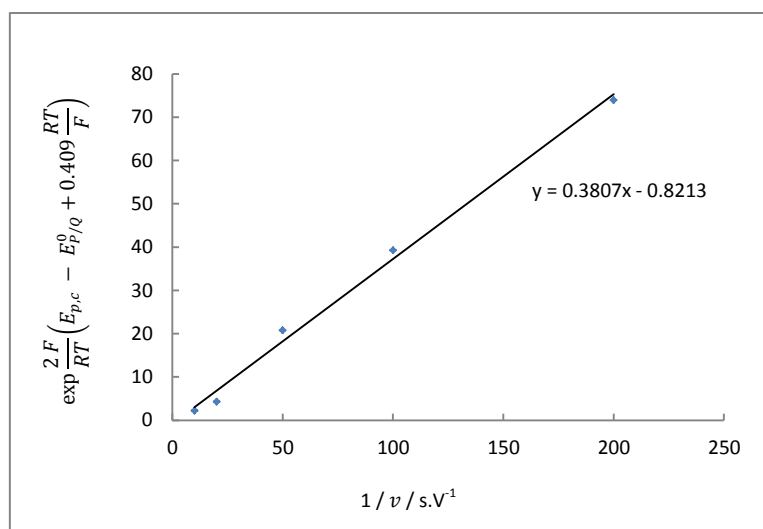


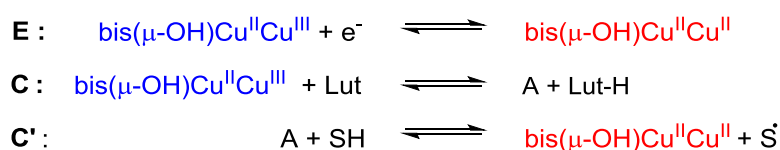
Figure 91: Plot of $\exp\left(\frac{2F}{RT}\left(E_{p,c} - E_{p/Q}^0 + 0.409\frac{RT}{F}\right)\right)$ against $1/v$ corresponding to the CVs displayed in Figure 90 for determining the rate constant k_{obs} .

A gradient of 0.381 was obtained from the plot in Figure 91. Using the previously determined values of $D_{Cu_2^{II}Py_4}$ of $1.0 \times 10^{-5} \text{ cm}^2 \cdot \text{s}^{-1}$ (determined by DOSY NMR in Part II Chapter 3) and $D_{lut} = 4.4 \times 10^{-5} \text{ cm}^2 \cdot \text{s}^{-1}$ (see above in this Section), the concentrations of $C_{Cu_2^{II}}^0$ and C_{lut}^0 as 0.8 and 0.6 mM respectively and a temperature of 293 K, second order rate constant k_{obs} was determined to be $6 \times 10^4 \text{ M}^{-1} \cdot \text{s}^{-1}$.

D. Refining the value of the rate constant with simulations

The value of $k_{obs} = 6 \times 10^4 \text{ M}^{-1} \cdot \text{s}^{-1}$ obtained for the catalytic reaction is far greater than the value of $k_{r2H} = 5 \text{ M}^{-1} \cdot \text{s}^{-1}$ obtained by stoichiometric reaction of $[Cu^I Cu^{III} Py_4]^+$ with toluene-H8. The difference in substrate (toluene vs. the solvent acetonitrile) would not account for the difference in k of 4 orders of magnitude, indicating that the active species for the catalytic reaction is not the same as the stoichiometric reaction characterised in section 4.3.1.

Simulations were therefore completed using a simple ECC' mechanism, displayed in Scheme 51, where the catalysts is oxidised followed by a reaction with 2,6-lutidine to form active species **A** that subsequently reacts quickly with the solvent SH to re-generate the Cu_2^{II} catalyst.



Scheme 51: Simple mechanism used for the simulation of CVs upon the addition of 2,6-lutidine (Lut) to the complex $Cu_2^{II}Py_4$ (represented as the $\text{bis}(\mu\text{-OH})\text{Cu}^{\text{II}}\text{Cu}^{\text{II}}$ core) in the solvent acetonitrile (SH).

When the parameters determined experimentally were used for the simulations using the simple mechanism displayed in Scheme 51 ($k_{obs} = 6 \times 10^4 \text{ M}^{-1}\cdot\text{s}^{-1}$ along with measured diffusion coefficients and concentrations), the simulated CV did not fit well with the experimental CVs. This could be due to side reactions that occur, which might interfere with the CV features (peak potential and peak current). Certain features of the experimental CV give evidence for side reactions:

- i) The CV of the catalyst $\text{Cu}^{\text{II}}\text{Py}_4$ with no base is chemically not fully reversible ($I_{pa} \neq I_{pc}$), indicating that the oxidised form also has a side reaction without the presence of 2,6-lutidine (an EC mechanism).
- ii) There is a complete loss of reversibility upon the addition of only 0.4 eq of 2,6-lutidine (see Figure 89, left). This is unusual for the case of total catalysis, as generally the reversible system of the catalyst is still observable after the catalytic peak (see Figure 75, Section 4.1.3.3).

A more elaborate mechanism was therefore required to simulate the CVs.

The cyclic voltammetry of the addition of sub-stoichiometric amounts of 2,6-lutidine is shown below in Figure 92, left. 2,6-lutidine (0 to 0.4 eq) was added sequentially to $\text{Cu}^{\text{II}}\text{Py}_4$ (0.8 mM) in a 0.1 M solution of $\text{NBu}_4\text{ClO}_4/\text{CH}_3\text{CN}$ (dried over 3 Å molecular sieves) in a glove box. Simulations using a more elaborate mechanism (Scheme 52) are displayed in Figure 92, right.

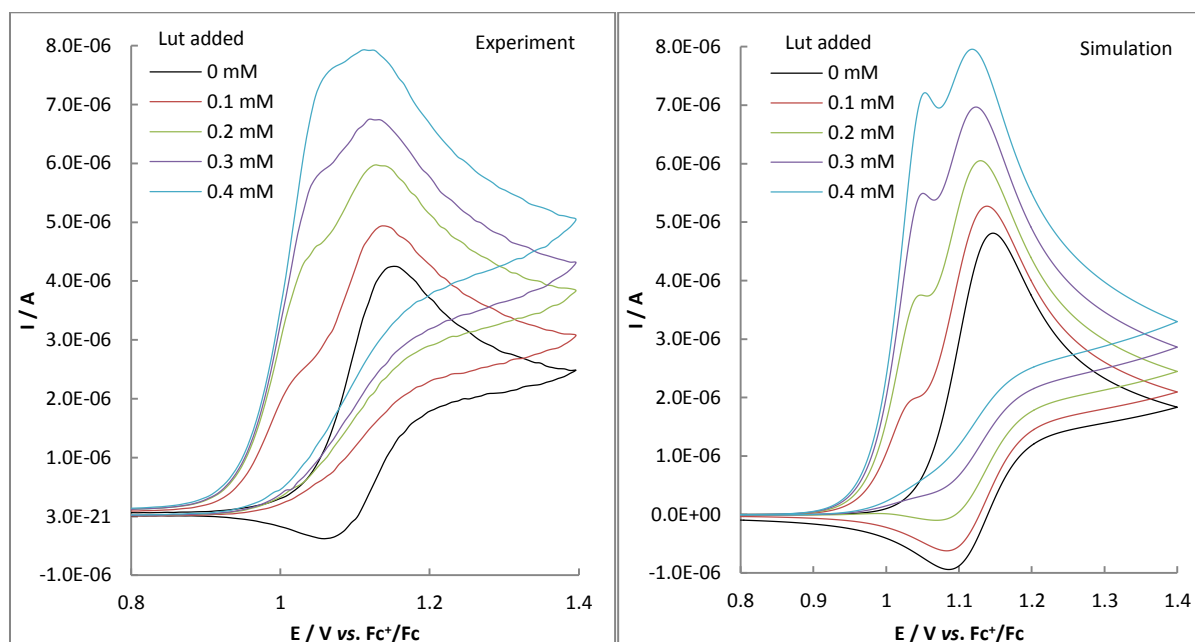
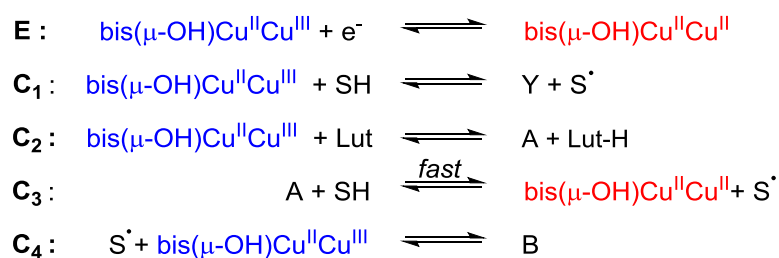


Figure 92: CV of the addition of sub-stoichiometric amounts of 2,6-lutidine to $\text{Cu}^{\text{II}}\text{Py}_4$. Left: experiment. Parameters: $\nu = 10$ mV/s; NBu_4ClO_4 in CH_3CN (0.1 M) dried over 3 Å molecular sieves; concentration of $\text{Cu}^{\text{II}}\text{Py}_4 = 0.8$ mM; working electrode: BDD; inert atmosphere. Right: simulation. Parameters: see Scheme 52.



Scheme 52: Mechanism of the electrocatalysis by complex $[\text{Cu}^{\text{II}}\text{Cu}^{\text{II}}\text{Py}_4]^+$ used for simulating the CV curves. Parameters: \mathbf{E}_1 : $[v = 10 \text{ mV/s}, \alpha = 0.5, E^\circ = 1.12 \text{ V vs. Fc}^+/\text{Fc}]$; \mathbf{C}_1 : $[k_{f1} = 1 \times 10^{-3} \text{ M}^{-1}\cdot\text{s}^{-1}, K_1 = 10]$; \mathbf{C}_2 : $[k_{f2} = 7 \times 10^5 \text{ M}^{-1}\cdot\text{s}^{-1}, K_2 = 10^7]$; \mathbf{C}_3 : $[k_{f3} = 1 \times 10^6 \text{ M}^{-1}\cdot\text{s}^{-1}, K_3 = 10^7]$; \mathbf{C}_4 : $[k_{f4} = 5 \times 10^3 \text{ M}^{-1}\cdot\text{s}^{-1}, K_4 = 1 \times 10^6 \text{ M}^{-1}]$. Concentration: $[\text{Cu}^{\text{II}}_2\text{Py}_4] = 0.8 \text{ mM}$, $[\text{SH}] = 20 \text{ M}$, $[2,6\text{-lutidine}] = 0, 0.1 \text{ mM}, 0.2 \text{ mM}, 0.3 \text{ mM}, 0.4 \text{ mM}$. Diffusion coefficients: $D([\text{Cu}_2\text{Py}_4]^{n+}) = 1 \times 10^{-5} \text{ cm}^2\cdot\text{s}^{-1}$; $D(\text{SH}), D(\text{S}^\bullet), D(\text{Lut})$ and $D(\text{Lut-H}) = 4.4 \times 10^{-5} \text{ cm}^2\cdot\text{s}^{-1}$; $D(\text{A})$ and $D(\text{B}) = 1 \times 10^{-5} \text{ cm}^2\cdot\text{s}^{-1}$.

The mechanism used for simulating the electrocatalysis by the complex $\text{Cu}^{\text{II}}_2\text{Py}_4$ is shown in Scheme 52. In terms of the parameters, values chosen were as close to the experimental values as possible (concentration and E° of the catalyst, concentration of the 2,6-lutidine). The concentration of the solvent SH was calculated from its density to give a value of around 20 M. The measured value of the diffusion of the catalyst $\text{Cu}^{\text{II}}_2\text{Py}_4$ ($1 \times 10^{-5} \text{ cm}^2\cdot\text{s}^{-1}$) was used for all oxidation/protonation states of the catalyst. The measured diffusion coefficient of the 2,6-lutidine ($4.4 \times 10^{-5} \text{ cm}^2\cdot\text{s}^{-1}$) was also used for other small molecules (the solvent SH, the oxidised solvent S^\bullet and the protonated 2,6-lutidine Lut-H). Rate constants and equilibrium constants were then changed until the simulated values of the catalytic peak current and potential fitted the experimental CVs.

The mechanism is as follows:

- The first two steps (**E** and **C₁**) of the electrocatalytic mechanism (Scheme 52) are the same as shown in Scheme 47 (stoichiometric reaction of $[\text{Cu}^{\text{II}}\text{Cu}^{\text{III}}\text{Py}_4]^+$ with toluene), where $\text{Cu}^{\text{II}}_2\text{Py}_4$ is electrochemically oxidised to $[\text{Cu}^{\text{II}}\text{Cu}^{\text{III}}\text{Py}_4]^+$, followed by a slow chemical reaction **C₁** making the system in the absence of 2,6-Lutidine quasi-reversible. As the $\text{bis}(\mu\text{-OH})\text{-Cu}^{\text{II}}\text{Cu}^{\text{III}}$ reacts with the C-H bonds of toluene (Section 4.3.1.5) presumably in the absence of toluene the reaction **C₁** is with the acetonitrile solvent (and therefore SH is given a high concentration of 20 M).
- Upon addition of 2,6-lutidine (Lut) a new species is formed from $[\text{Cu}^{\text{II}}\text{Cu}^{\text{III}}\text{Py}_4]^+$ (denoted **A**) through the reaction **C₂** with a rate constant of $7 \pm 1 \times 10^5 \text{ M}^{-1}\cdot\text{s}^{-1}$.
- In reaction **C₃** the new species **A** reacts with a substrate SH (presumably the CH_3CN solvent), with a rate constant of $1 \pm 0.1 \times 10^6 \text{ M}^{-1}\cdot\text{s}^{-1}$. This reaction regenerates the $\text{bis}(\mu\text{-OH})\text{-Cu}^{\text{II}}\text{Cu}^{\text{II}}$ species making the system catalytic.

- In the case of “total catalysis” the second wave corresponds to the oxidation of the remaining complex which in this case is quasi-reversible. However in the experimental CV in Figure 92, the second oxidation system ($E_p = 1.13$ V vs. Fc^+/Fc) becomes completely irreversible upon the addition of 2,6-lutidine indicating that another chemical reaction occurs with the $\text{bis}(\mu\text{-OH})\text{-Cu}^{\text{II}}\text{Cu}^{\text{III}}$ that is dependent on the concentration of 2,6-lutidine. An additional reaction was therefore added (C_4) where the radical product of the electrocatalysis (S^*) reacts with the $\text{bis}(\mu\text{-OH})\text{-Cu}^{\text{II}}\text{Cu}^{\text{III}}$ species making the redox system of the complex irreversible.

Thus when simulations are used to model the side reactions that occur during the electrocatalytic process, a higher value of k_{obs} is obtained ($7 \pm 1 \times 10^5 \text{ M}^{-1} \cdot \text{s}^{-1}$ compared to the experimental value of $k_{obs} = 6 \times 10^4 \text{ M}^{-1} \cdot \text{s}^{-1}$).

4.3.2.5. Discussion

The addition of a base to the complex $\text{Cu}^{\text{II}}_2\text{Py}_4$ leads to an electrocatalytic wave observed on the CV in oxidation. Our initial suspicion was that the electrocatalysis of water was taking place, so the effect of water was measured. The addition of water causes a slight increase in the catalytic current indicating a possible change in mechanism, but a catalytic current still occurs in a minimum concentration of water, indicating that the electrocatalysis was not that of the water. A radical mechanism is likely due to the mixture of products (for explanation see section 4.3.1.4). As the reaction proceeds by either a HAT or PCET, alkane radicals will be generated (most likely $^{\bullet}\text{CH}_2\text{CN}$) which in the presence of water would form the alcohol for which the CH bonds next to the OH groups will have a much lower BDE making the rate of HAT/PCET for the alcohol faster than the alkane. If the HAT/PCET is the rate determining step, an accumulation of the alcohol at the electrode should cause an increase in the catalytic current.

The current rapidly stabilising upon addition of water with no increase after 50 equivalents of water could indicate that another step in the reaction mechanism becomes the rate determining step. Indeed in the simulations (Scheme 52), the deprotonation of the $\text{bis}(\mu\text{-OH})\text{-Cu}^{\text{II}}\text{Cu}^{\text{III}}$ to form **A** and the rate of HAT/PCET from the solvent SH by **A** have similar rate constants of $7 \pm 1 \times 10^5 \text{ M}^{-1} \cdot \text{s}^{-1}$ and $1 \pm 0.1 \times 10^6 \text{ M}^{-1} \cdot \text{s}^{-1}$ respectively. While the simulations are an approximation, it is possible that the rate constants of these two reactions are very close so that slight changes in the conditions leads to a change in the rate determining step.

In terms of the nature of the species **A**, spectroscopic data would be difficult to obtain due to the high reactivity of this species with the solvent (and therefore no accumulation occurs). Very low

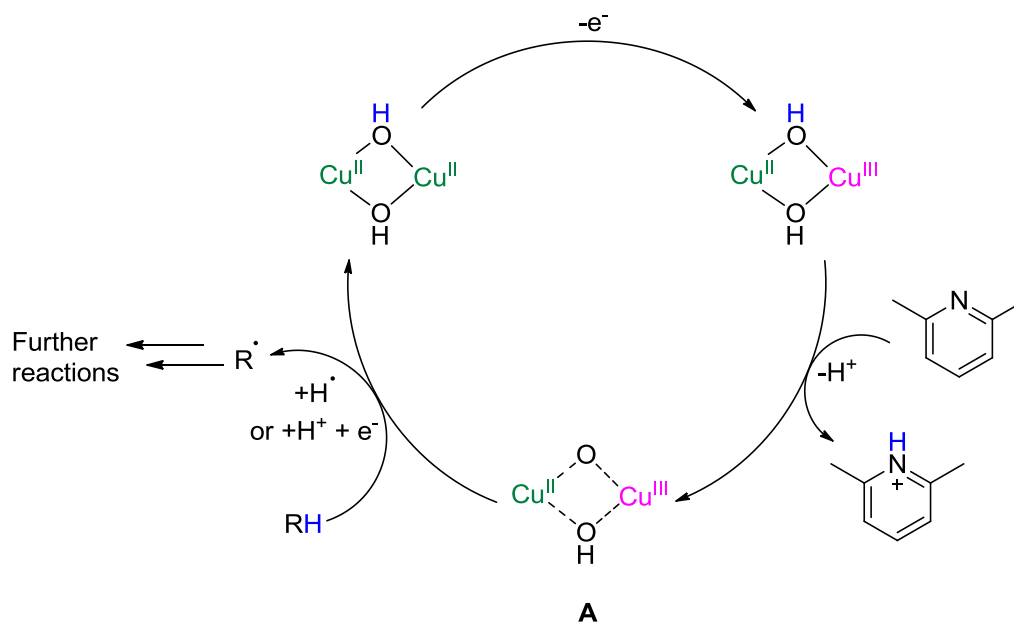
temperature spectroelectrochemistry would have to be completed. **A** is generated upon oxidation of the complex, and requires a base for deprotonation. The deprotonation only occurs after oxidation because the higher oxidation state of the copper will cause a decrease in the pK_a of the bridging OH groups. A possible species could therefore be the $(\mu\text{-OH})(\mu\text{-O})\text{Cu}^{\text{II}}\text{Cu}^{\text{III}}$ proposed by Yoshizawa *et al.*⁷⁴ for the oxidation of methane by a binuclear copper centre. One or several of the Cu-O bonds to the bridging O(H) groups could also be broken. Theoretical calculations could give an insight into which species is responsible for the oxidation of alkanes in the electrocatalytic cycle of the complex $\text{Cu}^{\text{II}}_2\text{Py}_4$.

4.3.2.6. Conclusions.

The addition of a base has a dramatic effect on the CV of $\text{Cu}^{\text{II}}_2\text{Py}_4$ by making an oxidation process catalytic. Due to the difficulties involved in detection the oxidation products of the solvent acetonitrile, bulk oxidation of the complex $\text{Cu}^{\text{II}}_2\text{Py}_4$ was completed in the presence of 2,6-lutidine and toluene, leading to the oxidation of toluene into benzylalcohol, benzaldehyde and N-benzylacetamide consistent with a radical mechanism. This strongly suggests that the electrocatalytic oxidation of the solvent CH_3CN occurs in the absence of toluene.

*The oxidation potential of the complex remains unchanged upon addition of a base, so the initial oxidation is still the formation of a bis $(\mu\text{-OH})\text{Cu}^{\text{II}}\text{Cu}^{\text{III}}$ species. DFT studies indicate that the hydroxido bridges remain intact in the mixed valent species (see Part II Chapter 3 Section 3.5.2.3). The addition of a base could then cause the deprotonation of one of the hydroxido bridges leading to the formation of a $(\mu\text{-OH})(\mu\text{-O})\text{Cu}^{\text{II}}\text{Cu}^{\text{III}}$ (or similar) species **A**. The electrocatalysis occurs in the absence of water, but addition of water does cause a slight increase in the catalytic current indicating that water can alter the mechanism, presumably by reacting with the alkane radical to form the alcohol that can then be oxidised by the species **A**.*

*The number of electrons for the catalytic reaction was determined to be $n = 1$. The rate constant for the catalytic reaction was determined experimentally to be $k_{\text{obs}} = 6 \times 10^4$ and from simulation to be $k = 7 \times 10^5 \text{ M}^{-1} \cdot \text{s}^{-1}$ (both for the deprotonation step **C**₂ and for the HAT/PCET step **C**₃) a factor of 10^5 greater than that of the stoichiometric reaction of $[\text{Cu}^{\text{II}}\text{Cu}^{\text{III}}\text{Py}_4]^+$ with toluene. The proposed mechanism is summarised in Scheme 53.*



Scheme 53 : Proposed mechanism for the electrocatalysis that occurs upon addition of 2,6-lutidine to $\text{Cu}^{\text{II}}_2\text{Py}_4$ in the presence of a substrate.

4.4. Conclusions on the reactivity of a $\text{Cu}^{\text{II}}\text{Cu}^{\text{III}}$ species.

Initial attempts at probing the reactivity of the mixed valent $\text{Cu}^{\text{II}}\text{Cu}^{\text{III}}$ species using the ligands Py_2Ox_2 and Ox_4 displayed an intramolecular oxidation on the ligand. This has implications for the choice of ligand that are to be used to study mixed valent $\text{Cu}^{\text{II}}\text{Cu}^{\text{III}}$ systems as C-H bonds near the metal centre are likely to be oxidised, preventing any reactivity towards an external substrate.

The ligand Py_4 was therefore used to characterise the reactivity of the bis($\mu\text{-OH}$) $\text{Cu}^{\text{II}}\text{Cu}^{\text{III}}$ species formed due to its robust nature. The bis($\mu\text{-OH}$) $\text{Cu}^{\text{II}}\text{Cu}^{\text{III}}$ species was shown to oxidise toluene into benzaldehyde, benzylalcohol, N-benzylacetamide, 2-(methylphenyl)-toluene, and 4-(methylphenyl)-toluene, indicating a radical mechanism. A small primary kinetic isotope effect of 2.5 was observed upon addition of toluene- D_8 instead of toluene- H_8 indicating a C-H rupture in the rate determining step, alluding to a HAT/PCET mechanism. Approximations of the strength of the ($\mu\text{-OH}$)($\mu\text{-HO-H}$) $\text{Cu}^{\text{II}}\text{Cu}^{\text{II}}$ bond formed upon oxidation of alkanes indicates that this species is among the most powerful oxidants in the literature, with a similar BDE to the $\text{Cu}^{\text{II}}\text{-HO-H}$ species characterised by Tolman et al.⁴⁴

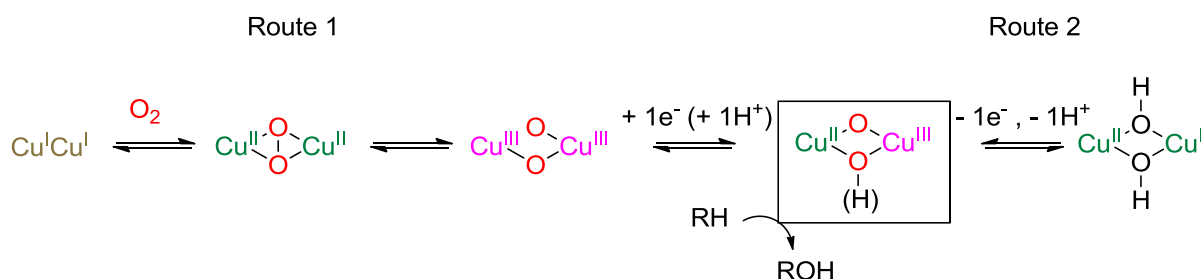
Oxidation of the bis(μ -OH)Cu^{II}Cu^{II} complex Cu^{II}₂Py₄ in the presence of a base renders the system electrocatalytic, oxidising alkanes such as toluene. While the active species responsible for the oxidation of alkanes is unknown, the difference in the rates between the stoichiometric reaction and the catalytic reaction of a factor of 10⁵ indicates that it is not the bis(μ -OH)Cu^{II}Cu^{III} species, and the necessity of a base eludes to a possible (μ -OH)(μ -O)Cu^{II}Cu^{III} intermediate. Spectroscopic studies of such an intermediate would be difficult because of the rate at which the species reacts with the solvent. DFT calculations could hint at the nature of this species. Optimised geometries of various terminal or bridging oxo and hydroxido Cu^{II}Cu^{III} species could indicate the stability of such species. The BDEs of the O-H bonds formed upon HAT/PCET could also provide some insight. Further studies with the electrocatalytic system could also be completed to determine the source of the oxygen atom in the products obtained and to attempt quantification of the electrocatalytic reactivity.

While the high oxidation potential is related to the oxidising power of these complexes, the potentials required to generate the mixed valent Cu^{II}Cu^{III} species have been problematic. The generation of the mixed valent Cu^{II}Cu^{III} species has been limited to electrochemistry, which has implications on solvent choice because of the electrochemical window (limited by oxidation of the solvent at the electrode). Lower temperatures could be achieved without the presence of the electrochemical salt, stabilising intermediates. A whole range of substrates could also be tested if a chemical oxidant could be used allowing the determination of the mechanism. Complexes should therefore be synthesised with lower oxidation potentials to allow further characterisation of the Cu^{II}Cu^{III} species.

Despite recent results in the literature going against the possibility that one of nature's most potent oxidants, the enzyme pMMO, is a dinuclear copper enzyme,^{3,63} the results in this chapter demonstrate for the first time experimentally that the bis(μ -OH)Cu^{II}Cu^{III} species is a promising species to study as an oxidant. With the literature still very much depleted in the area of synthetic Cu^{II}Cu^{III} systems, there is room for much spectroscopic and catalytic study.

5. General conclusions and perspectives

The conversion of methane (natural gas) into a more easy-to-use liquid fuel such as methanol is of industrial interest for multiple reasons, however current methods of doing this conversion are costly. The design of catalysts that can do the selective C-H activation necessary for this reaction is therefore an important topic in current research. The work in this thesis has been realised considering this context using a bio-inspired approach. Several enzymes are able to functionalise strong C-H bonds at ambient temperature. The first part of this thesis is therefore devoted to a literature review of copper-oxygen enzymes that can hydroxylate C-H bonds (copper mono-oxygenases) and of model complexes of suggested active species. Among these, mixed valent $\text{Cu}^{\text{II}}\text{Cu}^{\text{III}}$ species have been proposed. It was therefore the aim of this thesis to synthesise $\text{Cu}^{\text{II}}\text{Cu}^{\text{III}}$ systems and to probe their reactivity. To achieve the synthesis of these $\text{Cu}^{\text{II}}\text{Cu}^{\text{III}}$ species, our work has been based on two approaches illustrated in Scheme 54.



Scheme 54: Two synthetic routes to the generation of $\text{Cu}^{\text{II}}\text{Cu}^{\text{III}}$ species.

- In the first chapter, we have investigated Route 1 in order to generate $\text{Cu}_2\text{:O}_2$ species *via* the activation of O_2 by Cu_2^{I} complexes followed by mono-electronic reduction. Three ligands (Py_4 , Ox_4 and Py_2Ox_2) made up of either pyridine (Py) or oxazoline (Ox) moieties attached *via* a 1,8-naphthyridine spacer were synthesised as well as their corresponding Cu_2^{I} complexes. The Cu_2^{I} complexes from the ligands Ox_4 and Py_2Ox_2 generated $\mu\text{-}\eta^2\text{:}\eta^2\text{-peroxo-Cu}_2^{\text{II}}$ complexes (characterised by UV-vis, rR and DFT) when O_2 was bubbled through solutions of the complexes in acetone at -80°C . The reactivity of both of the $\mu\text{-}\eta^2\text{:}\eta^2\text{-peroxo-Cu}_2^{\text{II}}$ towards external substrates was relatively limited, coupling 2,4-di-*tert*-butylphenol to form 3,3',5,5'-tetra-*tert*-butyl-2,2'-biphenol (presumably an outer-sphere electron transfer), but no oxygen insertion was observed towards PPh_3 and benzaldehyde. The limited reactivity towards external substrates could be due to the steric bulk of

the oxazoline groups protecting the $\text{Cu}_2\text{:O}_2$ core. While this limits the use of these $\mu\text{-}\eta^2\text{:}\eta^2\text{-peroxo-Cu}^{\text{II}}_2$ species for catalysis, these species could be used to attempt the mono-reduction to generate bis($\mu\text{-O}$) $\text{Cu}^{\text{II}}\text{Cu}^{\text{III}}$ species (which has yet to be synthesised in a model complex) because of their relative stability at -80°C .

The remainder of the thesis is focused on the generation of $\text{Cu}^{\text{II}}\text{Cu}^{\text{III}}$ species *via* oxidation of Cu^{II}_2 complexes *via* synthetic Route 2.

- In the second chapter the synthesis of several dissymmetric complexes are discussed, with the aim of forming localised $\text{Cu}^{\text{II}}\text{Cu}^{\text{III}}$ systems. The naphthyridine spacer was chosen because previous studies with a phenoxido spacer have shown that most of the time, mono-electronic oxidation was ligand centred instead of metal centred. Consequently dissymmetric ligands separated by a naphthyridine spacer were used with pyridine moieties forming one binding pocket and a variable group forming the other (aniline, benzimidazole, indole and bis pyrazole). A variety of structures were obtained (dinuclear, tetranuclear and hexanuclear), demonstrating the difficulties of controlling the formation of a dinuclear species. Despite the presence of negatively charged ligands coordinating the copper, the oxidation potentials of these complexes are all very high. This is essentially due to the design of the ligand: the geometry the side of the pyridine groups is far more favourable as they are in a “pincer” shape, which (assuming two bridging hydroxido groups) would have negative charges in the equatorial positions of the copper forming a square based pyramid perpendicular of the plane of the naphthyridine (Figure 93). All the ligands from the synthon **I** used in this chapter have the amide in the plane of the naphthyridine, precluding the formation of the square based pyramid with bridging groups in the equatorial positions. A preferable type of ligand would have the negative charges on the pincer group, and could therefore be synthesised from a different precursor (Figure 94).

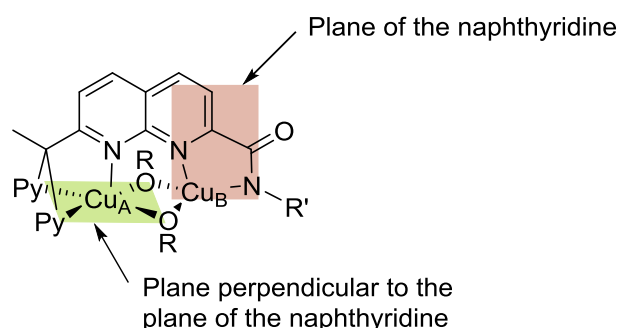


Figure 93: Schematic representation of the coordination geometry with the ligands used in Chapter 2.

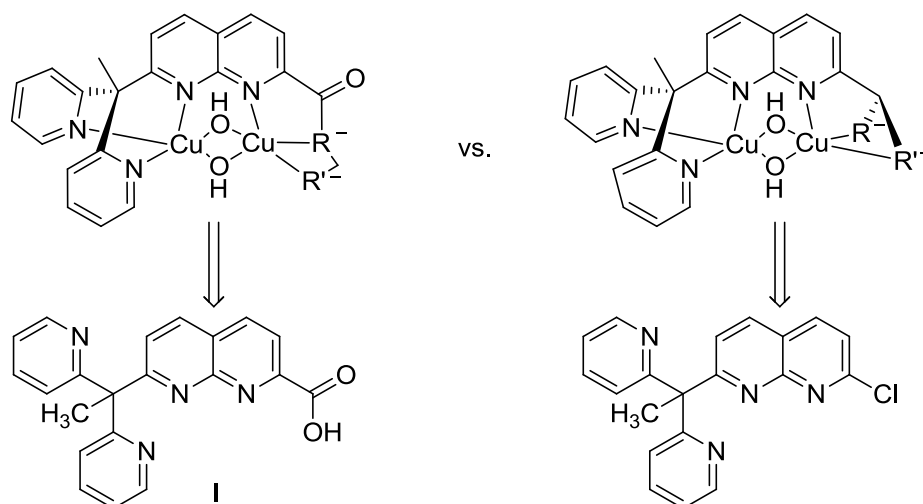


Figure 94: Left: design and precursor of ligands in Chapter 2. Right: a preferential ligand design and precursor for a dissymmetric complex.

- The third chapter describes the successful synthesis of three Cu_2^{II} complexes (two symmetrical and one dissymmetric) supported by the ligands Py_4 , Ox_4 and Py_2Ox_2 , which upon mono-electronic oxidation form $\text{Cu}^{\text{II}}\text{Cu}^{\text{III}}$ complexes. The mono-oxidation of the Cu_2^{II} complexes all occur at high potentials (1.09-1.27 V vs. Fc^+/Fc) limiting the study the oxidised species to electrochemical methods. Spectroelectrochemical methods enabled the determination UV-vis and NIR of the oxidised species. All of the $\text{Cu}^{\text{II}}\text{Cu}^{\text{III}}$ complexes display bands in the UV-vis between 330 and 480 nm with values of around $\epsilon \approx 10^3 \text{ M}^{-1}\cdot\text{cm}^{-1}$. The EPR signals (15-100 K) of the oxidised species of all three complexes were consistent with localised $\text{Cu}^{\text{II}}\text{Cu}^{\text{III}}$ species, but a slight delocalisation was observed for the complexes $[\text{Cu}^{\text{II}}\text{Cu}^{\text{III}}\text{Py}_4]^+$ and $[\text{Cu}^{\text{II}}\text{Cu}^{\text{III}}\text{Py}_2\text{Ox}_2]^+$ at higher temperatures (-40°C and room temperature respectively). TD-DFT studies of the complex $[\text{Cu}^{\text{II}}\text{Cu}^{\text{III}}\text{Py}_4]^+$ allowed the assignment of the band observed in the UV-vis as an ligand to metal charge transfer and DFT confirmed that the mono-electronic oxidation was metal centred. Optimisation of the geometry of $[\text{Cu}^{\text{II}}\text{Cu}^{\text{III}}\text{Py}_4]^+$ also indicated that it is likely that the OH bridges remain protonated.

- Our efforts to probe the reactivity of mixed valent systems from the complexes $\text{Cu}_2^{\text{II}}\text{Py}_4$, $\text{Cu}_2^{\text{II}}\text{Ox}_4$, and $\text{Cu}_2^{\text{II}}\text{Py}_2\text{Ox}_2$ are discussed in Chapter 4. When oxazoline groups are present on the ligand, intramolecular aliphatic oxidation is observed. When the ligand Py_4 is used, the mixed valent species is able to oxidise toluene at room temperature to form a series of products indicating a radical mechanism. While the source of the oxygen atom in the products is unknown, it is clear that it does not come from O_2 . The mechanism of C-H activation cannot be determined from the data

within, and a series of substrates should be tested to determine if the mechanism proceeds *via* HAT or a sequential PCET.

The addition of a base made the oxidation of toluene (and acetonitrile) catalytic at room temperature. The reactive intermediate for the catalytic reaction is different to the bis(μ -OH)Cu^{II}Cu^{III} species responsible for the stoichiometric reaction (because the difference in rates of reaction of several orders of magnitude), and may involve a (O)(OH)Cu^{II}Cu^{III} species. Spectroscopy of such a species would be difficult due to the high rates of reaction, however DFT studies may help to elucidate the nature of the intermediate.

Lowering the oxidation potential for the generation of Cu^{II}Cu^{III} would allow their study with chemical oxidants. Comparative studies with similar mixed valent systems with a lower oxidation potential would be interesting to determine the effect of the relative oxidation potentials and pK_a on the reactivity of such mixed valent systems. The oxidation potential of the complex Cu^{II}₂Py₄ could be decreased by adding electron donor groups *para* to the nitrogen atoms of the pyridine groups (Figure 95).

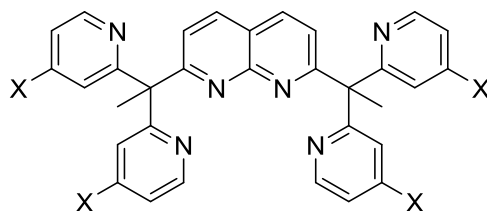


Figure 95: Representation of a possible ligand design to decrease the oxidation potential of Cu^{II}₂ species, where X indicates an electron donor.

To further probe the reactivity of the mixed valent species, a change of solvent is necessary. A reaction of the Cu^{II}Cu^{III} species with the solvent would likely mask the reactivity with substrates containing C-H bonds with higher BDEs. The solubility of the system would have to be improved so that it could be studied in solvents such as DCM or benzonitrile.

This thesis provides the first comprehensive study of the reactivity of synthetic Cu^{II}Cu^{III} species, and sets a unique precedent for future work as such mixed valent systems are indeed potentially strong oxidants. A rare example of the molecular electrocatalytic oxidation of alkanes is also presented, and while the reactive intermediate has not been determined, we have illustrated the need of a sacrificial base to regenerate the catalyst after a HAT/PCET process.

Part III: Experimental Section

1. General methods

1.1. X-ray crystallography

Crystals were mounted on a Kappa APEXII Bruker-Nonius diffractometer equipped with an Incoatec high brilliance microsource with multilayers mirrors monochromated Mo-K α radiation ($\lambda = 0.71073 \text{ \AA}$) and an Oxford cryosystem cryostream cooler. The collected reflections were corrected for Lorentz and polarization effects (EVAL14) and for absorption (SADABS). Crystal structural solution (direct method (SIR97) or the charge flipping method (Superflip)) and refinement (by full-matrix least squares on F^2 (SHELX2013)) was performed using the OLEX 2 analysis package.¹⁸³ All non-hydrogen atoms were refined with anisotropic thermal parameters. Hydrogen atoms were generated in idealized positions (except for the hydroxido bridges and the thiol which were found on the difference Fourier map), riding on the carrier atoms, with isotropic thermal parameters.

1.2. EPR spectroscopy

X-band EPR spectra were recorded at 100K with a EMX Bruker spectrometer equipped with a standard ER4102ST Bruker cavity. At helium temperature the spectrometer is equipped with a ER4116DM Bruker cavity, a ESR900 continuous-flow Oxford Instrument cryostat and a ER4131VT Bruker temperature controller. All spectra presented were recorded under non-saturating conditions. Simulation of EPR spectra was carried out with the software Simfonia or Easyspin.

1.3. NMR spectroscopy

1.3.1. NMR of paramagnetic complexes

A Unity Plus 500 MHz Varian or 400 MHz spectrometer equipped with a Variable Temperature Control was used for collection of 1D, 2D ^1H -NMR, ^{19}F -NMR and DOSY spectra at the required temperature. The spectral window for ^1H NMR data acquisition was adjusted. A typical spectrum consisted of 100 scans on the whole spectral bandwidth and a 0.2 second relaxation delay. An exponential weighting function ($lb = 20 \text{ Hz}$) was used during the processing. Baseline correction was used in 1D spectra. Chemical shifts (in ppm) were referenced to the residual solvent peak.

1.3.2. NMR general

All chemical shifts are reported in ppm. Coupling (J) values are given in Hz.

1.4. ESI-MS

ESI-MS were recorded at a concentration of $1 \times 10^{-5} \text{ M}$ on the mass spectrometer Esquire 3000 plus Bruker Daltonics with a nanospray inlet.

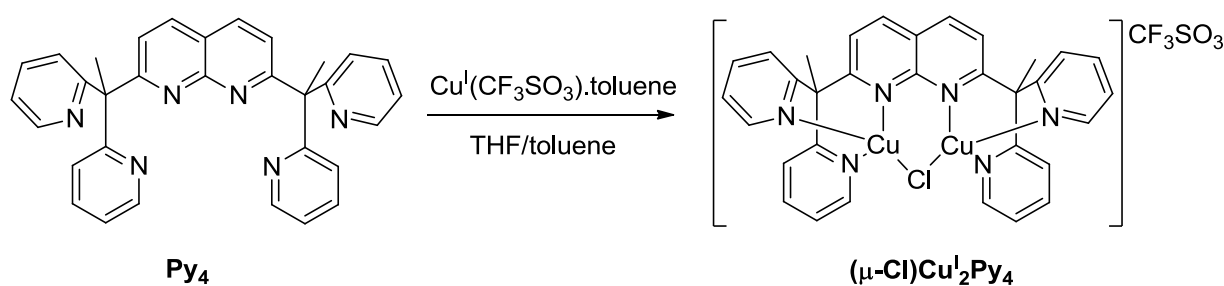
2. Part II Chapter 1

2.1. Synthesis of Cu^I complexes

2.1.1. Synthesis of the complex (μ-NCCH₃)Cu₂Py₄

The ligand Py₄ was synthesised in four steps using published literature procedures.^{133,146,149} The complex (μ-NCCH₃)Cu₂Py₄ was synthesised using the procedure published by Tilley *et al.*¹³³

2.1.2. Synthesis of complex Cu₂Py₄



In a glove box the ligand Py₄ (0.050 g, 1.0 × 10⁻⁴ mol) was dissolved in a mixture of 10 mL of toluene and 4 mL of THF and added to a solution of Cu^I(SO₃CF₃)₂·C₇H₈ (0.107 g, 2.1 × 10⁻⁴ mol, 2.1 eq) in 10 mL of toluene. The resulting suspension was stirred for 12 h then filtered giving a grey solid in quantitative yields. A few crystals were obtained by slow diffusion of DIPE into a solution of DMF.

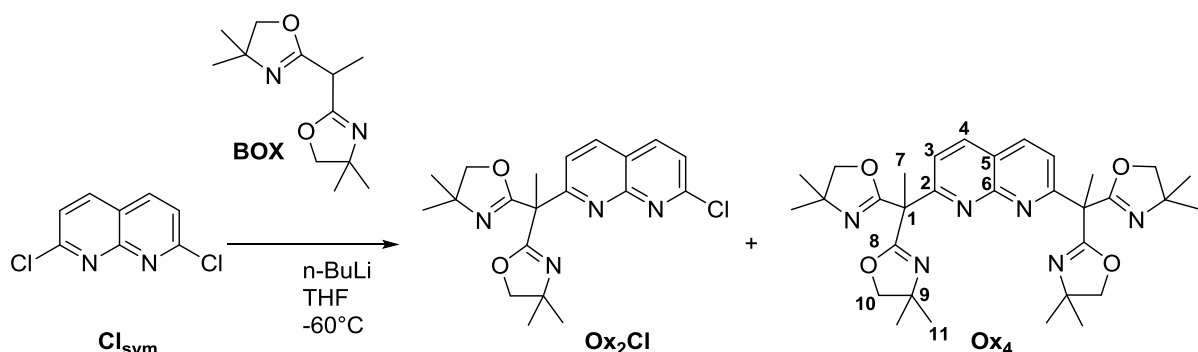
¹H-NMR (400 MHz, acetone-d₆), δ_H: 8.93 (4H, br, s, PyH), 8.74 (2H, br, d, *J* 9.3, NaphthH), 8.23 (4H, br, d, *J* 8.0, PyH), 8.84 (4H, br, t, *J* 7.4, PyH), 7.75 (2H, br, s, NaphthH), 2.73 (6H, br, s, CH₃).

2.1.3. Crystallographic data for the complex $\text{Cu}^{\text{I}}_2\text{Py}_4$ **Table 23:** Crystallographic data for the complex $\text{Cu}^{\text{I}}_2\text{Py}_4$.

Complex	$\text{Cu}^{\text{I}}_2\text{Py}_4$
Formula	$\text{C}_{32}\text{H}_{26}\text{ClCu}_2\text{N}_6 \cdot \text{CF}_3\text{SO}_3 \cdot 0.5(\text{C}_3\text{H}_6\text{O})$
M	923.5
Crystal system	monoclinic
Space group	$P 2_1/n$
a / Å	12.395(3)
b / Å	14.890(3)
c / Å	18.424(4)
$\alpha / ^\circ$	90
$\beta / ^\circ$	102.11(3)
$\gamma / ^\circ$	90
V / Å ³	3324.8(12)
Z	4
T / K	293(2)
$\rho_c / \text{g}\cdot\text{cm}^{-3}$	1.845
μ / mm^{-1}	0.5465
Total reflections	33697
Independent reflections	7548
Observed reflections	5573 ($I > 2\sigma(I)$)
R	0.0544
R_w	0.1238

2.1.4. Complexes $(\mu\text{-CH}_3\text{CN})\text{Cu}^{\text{I}}_2\text{Ox}_4$ and $(\mu\text{-CH}_3\text{CN})\text{Cu}^{\text{I}}_2\text{Py}_2\text{Ox}_2$ 2.1.4.1. Synthesis of ligands Ox_4 and Py_2Ox_2

The intermediates Cl_{sym} and BOX were synthesised according to the literature procedures.^{145,146}



1.25 g (5.56×10^{-3} mol, 2.2 eq) of BOX was dissolved in 40 mL of freshly distilled THF under argon and cooled to -60°C , followed by slow addition of 2.5 mL (5.56×10^{-3} mol, 2.2 eq) of 2.4 M n-

BuLi and the colourless solution was stirred for 30 min. 0.526 g of 2,7-dichloro-1,8-naphthyridine was added using a powder finger resulting in an orange solution with a beige precipitate. The solution was stirred overnight and allowed to rise to room temperature resulting in the solubilisation of the precipitate. 5 mL of water was added, the THF evaporated and a further 40 mL of water was added. The solution was extracted with DCM and dried over Na₂SO₄. The residue was purified by column chromatography (gradient of acetone/pentane) over silica to give products Ox₂Cl and Ox₄ (79 % and 20 % respectively).

The characterisation of Ox₄ is as follows:

¹H-NMR (400 MHz, CDCl₃), δ_H: 8.08 (2H, d, *J* 8.8, C₄H), 7.67 (2H, d, *J* 8.4, C₃H), 4.00 (8H, s, C₁₀H), 2.10 (6H, s, C₇H), 1.32 (24H, d, *J* 8.0, C₁₁H).

¹³C-NMR (101 MHz, CDCl₃), δ_C: 165.44 (C₆), 162.71 (C₂), 154.16 (C₈), 136.10 (C₄), 122.14 (C₃), 120.66 (C₅), 79.47 (C₁₀), 67.36 (C₉), 50.58 (C₁), 27.95 (C₁₁), 23.15 (C₇).

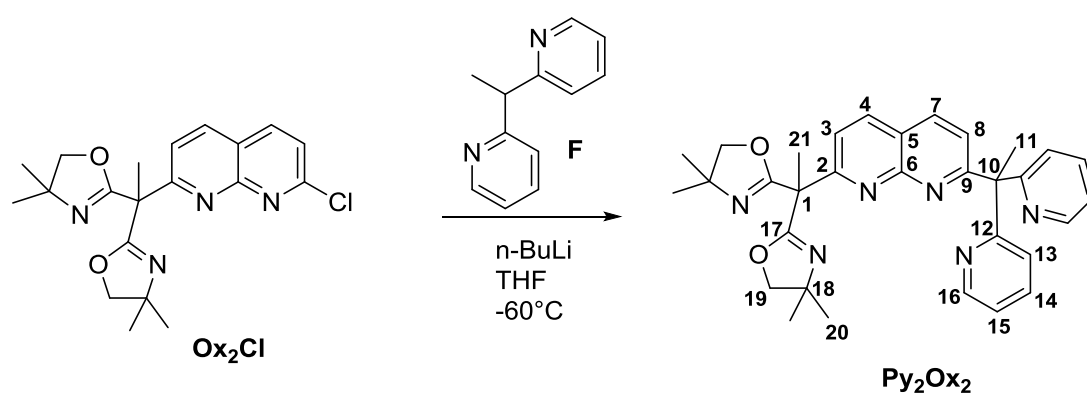
Elemental analysis: C₃₆H₄₂N₆O₄•1.75(H₂O). Theoretical (%): C: 63.40, H: 7.57 and N: 13.86. Obtained: C: 63.37, H: 7.24 and N: 13.77.

ESI-MS: *m/z* 575.4 [M+H]⁺.

The characterisation of Ox₂Cl is as follows:

¹H-NMR (400 MHz, CDCl₃) δ_H: 8.14 (1H, d, *J* 8.4, ArH), 8.11 (1H, d, *J* 8.4 Hz, ArH), 7.79 (1H, d, *J* 8.4, ArH), 7.47 (1H, d, *J* 8.4, ArH), 3.66 (4H, s, CH₂), 1.30 (12, d, *J* 8.0, CH₃).

ESI-MS: *m/z* 409.2 [M+Na]⁺, 387.2 [M+H]⁺.



0.70 g (0.38 x 10⁻³ mol, 1.1 eq) of 1,1-di-(2-pyridyl)ethane¹⁴⁹ was dissolved in 15 mL of freshly distilled THF under argon and cooled to -50°C, followed by slow addition of 0.26 mL (0.38 x 10⁻³ mol,

1.1 eq) of 1.4 M n-BuLi and the red solution was stirred for 30 min. 0.133 g of 2,7-dichloro-1,8-naphthyridine was added using a powder finger. The solution was stirred overnight and allowed to rise to room temperature resulting in the formation of a precipitate. 1 mL of water was added dissolving the precipitate, the THF evaporated and a further 20 mL of water was added, the solution extracted with DCM (4 x 15 mL) and dried over MgSO₄. The residue was purified by column chromatography (gradient of acetone/pentane) over silica to give the ligand Py₂Ox₂ (140 mg, 76%).

¹H-NMR (400 MHz, CD₃CN), δ_H: 8.48 (2H, d, *J* 3.9, C₁₆H), 8.22 (1H, d, *J* 8.5, C₇H), 8.15 (1H, d, *J* 8.5, C₄H), 7.67 (1H, d, *J* 8.5, C₈H), 7.66 (2H, dt, *J*₁ 8.0, *J*₂ 2.0, C₁₄H), 7.40 (1H, d, *J* 8.5, C₃H), 7.23 (2H, d, *J* 8.0, C₁₃H), 7.19 (2H, dd, m, C₁₅H), 3.95 (4H, s, C₁₉H), 2.35 (3H, s, C₁₁H), 1.92 (3H, s, C₂₁H), 1.21 (12H, d, *J* 4.6, C₂₀H).

¹³C-NMR (101 MHz, CD₃CN), δ_C: 170.73 (C₆), 166.57 (C₂), 166.22 (C₉), 163.51 (C₁₇), 154.85 (C₁₂), 149.48 (C₁₆), 137.66 (C₄), 137.24 (C₁₄), 137.00 (C₇), 126.41 (C₃), 124.80 (C₁₃), 123.15 (C₈), 122.61 (C₁₅), 121.01 (C₅), 80.10 (C₁₉), 68.21 (C₁₈), 62.03 (C₁₀), 51.42 (C₁), 30.70 (C₁₁), 28.17 (C₂₀), 23.07 (C₂₁).

Elemental analysis: C₃₂H₃₄N₆O₂•0.6(CH₂Cl₂). Theoretical: C: 66.86, H: 6.06 and N: 14.35. Obtained: C: 66.91, H: 6.27 and N: 14.08.

ESI-MS: *m/z* 557 [M+Na]⁺, 535 [M+H]⁺.

2.1.4.2. Synthesis of complex (μ-CH₃CN)Cu^I₂Py₂Ox₂

In a glove box the ligand Py₂Ox₂ (0.073 g, 1.4 x 10⁻⁴ mol, 1 eq) was dissolved in 4 mL of distilled THF and added to a solution of [Cu^I(CH₃CN)₄]OTf (0.11 g, 2.9 x 10⁻⁴ mol, 2.1 eq) in 10 mL of THF. The resulting suspension was stirred for 12 h then filtered. The solid was recovered and dried under vacuum giving a bright orange solid (0.127 g, 92%).

¹H-NMR (400 MHz, CD₃CN), δ_H: 8.56 (2H, br, PyH), 8.35 (2H, m, NaphthH), 7.90 (2H, m, NaphthH), 7.77 (2H, br, PyH), 7.50 (2H, br, PyH), 7.37 (2H, br, PyH), 4.07 (2H, d, *J* 8.2, CH₂), 3.90 (2H, d, *J* 8.2, CH₂), 2.43 (3H, s, CH₃), 2.13 (3H, s, CH₃), 1.39 (6H, s, CH₃), 1.32 (6H, s, CH₃).

Elemental analysis: C₃₆H₃₇Cu₂F₆N₇O₈S₂•2(H₂O)•1.5(CH₃CN). Theoretical: C: 42.64, H: 4.17 and N: 10.84. Obtained: C: 42.32, H: 4.03 and N: 10.82.

2.1.4.3. *Synthesis of complex (μ -CH₃CN)Cu^I₂Ox₄*

In a glove box the ligand Ox₄ (0.041 g, 7.5×10^{-5} mol, 1 eq) was dissolved in 4 mL of distilled THF and added to a solution of [Cu^I(CH₃CN)₄]OTf (0.057 g, 1.5×10^{-4} mol, 2.1 eq) in 10 mL of THF. The resulting suspension was stirred for 12 h then filtered and the solid was dried under vacuum giving a bright orange solid (0.050 g, 70%).

¹H-NMR (400 MHz, CD₃CN), δ_H : 8.44 (2H, d, *J* 8.5, NaphthH), 7.61 (2H, *J* 8.5, NaphthH), 4.10 (4H, *J* 8.6, CH₂), 3.96 (4H, d, *J* 8.6, CH₂), 2.09 (6H, s, CH₃), 1.40 (12H, s, CH₃), 1.36 (12H, s, CH₃).

Elemental analysis: C₃₆H₄₅Cu₂F₆N₇O₁₀S₂•3(H₂O)•(CH₃CN)•(CH₂Cl₂). Theoretical: C: 39.24, H: 4.70 and N: 9.51. Obtained: C: 39.16, H: 4.35 and N: 9.41.

2.2. Other procedures

2.2.1. Addition of O₂ to Cu^I₂ complexes followed by UV-vis

A 3 mL solution of the relevant Cu^I₂ complex was generated inside the glove box (Jacomex). The solution was placed inside a schlenk flask for which the bottom has a path-length of 1 cm. The schlenk flask was removed from the glove box and placed under a pressure of nitrogen before being cooled using a Lauda Pro-line cryostated-system. The time-resolved UV-vis spectra could be detected directly from the schlenk flask using a QEPro spectrometer (Ocean optics). Oxygen was added by bubbling directly into the solution of the complex continuously.

2.2.2. Raman spectroscopy

2.2.2.1. *Raman spectroscopy of the Cu^I₂ complexes (μ -CH₃CN)Cu^I₂Py₂Ox₂ and (μ -CH₃CN)Cu^I₂Ox₄ in the solid state*

Samples were prepared inside the glove box, removed in a sealed container that was only opened at the time of measuring. Spectra measured using a Perkin Elmer Raman station using a laser excitation of 532 nm.

2.2.2.2. *Resonance Raman of the Cu₂:O₂ species formed from the reaction of (μ -CH₃CN)Cu^I₂Py₂Ox₂ or (μ -CH₃CN)Cu^I₂Ox₄ with O₂*

5 mg of the respective Cu^I₂ complex was placed inside an NMR tube (1 cm diameter) in the glovebox and sealed with a septum. The sample was removed from the glove box and 1 mL of

acetone that had been degassed (freeze-pump-thaw) was cannulated to form a 5 mM solution of the Cu_2^{I} complex. The sample was cooled to -80°C still under a pressure of Ar then O_2 was bubbled through the sample for 1 minutes (10 s at a time, then allowing to stir for 10 s). The samples were then frozen in liquid nitrogen, and the rR spectra recorded at 77K using a home built open bench rR apparatus using SOLIS (Andor Technology) and a wavelength of 355 nm. The spectra of the solvent were subtracted from the spectra obtained of the $\text{Cu}_2:\text{O}_2$ species.

2.2.3. ESI-MS of complex $(\mu\text{-CH}_3\text{CN})\text{Cu}_2^{\text{I}}\text{Ox}_4$

A 0.1 mM solution of $(\mu\text{-CH}_3\text{CN})\text{Cu}_2^{\text{I}}\text{Ox}_4$ (2.5 mg in 25 mL of acetone) was generated inside the glovebox, removed from the box and kept under a pressure of Ar. A separate solution of acetone was degassed using schlenk technique. The degassed acetone was injected into the spectrometer (esquire 3000 plus) to purge the spectrometer of most of the oxygen. The sample was injected and analysed immediately after.

2.2.4. $^1\text{H-NMR}$ of $(\mu\text{-CH}_3\text{CN})\text{Cu}_2^{\text{I}}\text{Ox}_4$ and $(\mu\text{-CH}_3\text{CN})\text{Cu}_2^{\text{I}}\text{Py}_2\text{Ox}_2$

An approximately 2 mM (1.5 mg in 0.75 mL) solution of each complex was generated in CD_3CN in the glove box. The samples were placed in a sealed NMR tube and recorded using the NMR spectrometer Advance 400 (Bruker) at a frequency of 400 MHz.

2.2.5. Reactivity of the $\text{Cu}_2:\text{O}_2$ species formed from the complexes $(\mu\text{-CH}_3\text{CN})\text{Cu}_2^{\text{I}}\text{Ox}_4$ and $(\mu\text{-CH}_3\text{CN})\text{Cu}_2^{\text{I}}\text{Py}_2\text{Ox}_2$: screening by GCMS

A 0.3 mM solution (3 mg in 10 mL) of each complex was generated inside the glovebox (Jacomex) using acetone (Aldrich) that had been degassed by bubbling Ar. Samples of 1 mL were placed inside schlenk tubes and removed from the glove box and placed under Ar on a schlenk line and cooled to -80°C using a bath of ethanol/liquid nitrogen. O_2 was bubbled for 2 minutes through each sample, then a substrate was added (5-10 eq in a 0.1 mL solution of acetone), then the solution was immediately degassed by 10 cycles of vacuum/Ar. The solution was stirred for 30 min at -80°C then heated to room temperature (still under Ar) then filtered over silica. The sample was then analysed by GCMS (AGILENT 5977A-7890B) (EI with an ionisation source of 70 eV coupled to a gas phase chromatograph using the software Mass Hunter). The temperature sequence used for the gas chromatogram was as follows: the temperature was held at 40°C for 4 min then increased at $20^\circ\text{C}/\text{min}$ to a temperature of 280°C , for which the temperature was held for 4 min.

2.2.6. DFT calculations

All calculations were performed using the GAUSSIAN 09 package.¹⁸⁴ All geometry optimisations were carried using the pure functional BLYP in gas phase. A mixed basis comprised of Lanl2dz for copper atoms and the 6-311G(d,p) for other atoms. The use of pure DFT functionals for the modelling of Cu₂:O₂ systems, especially if larger ligands are to be modelled, was justified by Cramer *et al.*¹⁸⁵ Optimisations were done on a triplet state but broken symmetry state calculations were also performed to characterise the ground state. Vibrational frequency calculations were performed to ensure that all geometry optimisations converged.

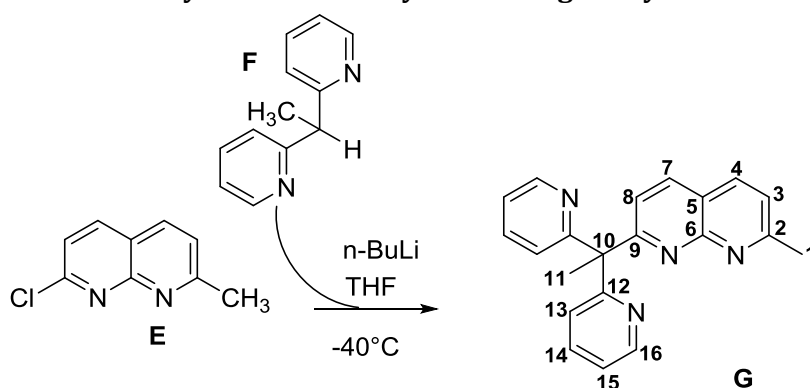
3. Part II Chapter 2

3.1. Complexes with a phenoxido spacer

The synthesis of ligands and complexes along with their characterisation have recently been published.^{128,131}

3.2. Syntheses of dissymmetric ligands

3.2.1. Synthesis of the synthon I for dissymmetric ligand synthesis



A solution of 1,1-di-(2-pyridyl)ethane (F) (1.1 g, 6.0×10^{-3} mol, 1.1 eq) in dry THF (75 mL) was placed under argon and cooled to -40°C . A 2.5 M solution of n-BuLi (2.4 mL, 6.0×10^{-3} mol, 1.1 eq) was added slowly and the resulting red solution stirred for 20 min before adding 1.0 g of E (5.6×10^{-3} mol, 1.0 eq, synthesised using a published literature procedure¹⁵⁷) slowly. The solution was left to stir over night and the temperature allowed to rise to room temperature. The red solution was then evaporated to 30 mL, cooled over ice and 70 mL H₂O was added slowly. The solution was extracted

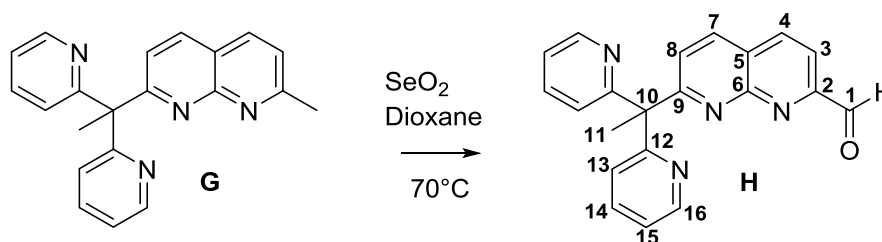
with DCM (3 x 100 mL), the organic phase dried over MgSO_4 , filtered, evaporated and purified by column chromatography (aluminium oxide, neutral, with a gradient of pentane/ethyl acetate) to yield **G** as an orange solid (1.3g, 4.1×10^{-3} mol, 72 %).

$^1\text{H-NMR}$ (400 MHz, DMSO), δ_{H} : 8.51 (2H, d, J 4.9, C_{16}H), 8.26 (1H, d, J 8.2, C_7H), 8.22 (1H, d, J 8.5, C_4H), 7.72 (2H, td, J 1.6, 7.7, C_{14}H), 7.48 (1H, d, J 8.3, C_8H), 7.28 (1H, d, J 8.4, C_3H), 7.25 (2H, m, C_{15}H), 7.18 (2H, d, J 8.0, C_{13}H), 2.67 (3H, s, C_1H_3), 2.30 (3H, s, C_{11}H_3).

$^{13}\text{C-NMR}$ (101 MHz, DMSO), δ_{C} : 169.23 (C_6), 165.65 (C_{12}), 162.43 (C_9), 154.69 (C_2), 148.87 (C_{16}), 137.42 (C_7), 136.79 (C_{14}), 136.59 (C_4), 123.75 (C_{13}), 123.14 (C_8), 122.73 (C_3), 122.02 (C_{15}), 119.22 (C_5), 61.19 (C_{10}), 27.63 (C_1), 25.39 (C_{11}).

Elemental analysis: $\text{C}_{21}\text{H}_{18}\text{N}_4 \cdot 0.5(\text{CH}_3\text{COOCH}_2\text{CH}_3)$. Theoretical: C: 74.47, H: 5.99 and N: 15.12. Obtained: C: 74.37, H: 5.68 and N: 15.33.

ESI-MS: m/z 465 ($\text{M}+\text{K}$) $^+$, 349 ($\text{M}+\text{Na}$) $^+$, 327 ($\text{M}+\text{H}$) $^+$.

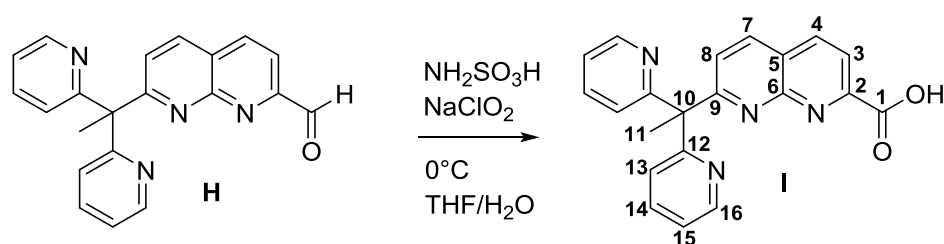


Dioxane (40 mL) was added to a mixture of **G** (0.4 g, 1.2×10^{-3} mol, 1 eq) and SeO_2 (0.25g, 2.3×10^{-3} , 1.9 eq), heated to 70°C and stirred overnight. The purple precipitate was filtered and the filtrate was evaporated. 60 mL of water was added, the pH increased to pH 7 with NaHCO_3 and then extracted with DCM (4 x 75 mL). The organic phase was dried over MgSO_4 , filtered, evaporated and dried under a vacuum line to give **H** as a beige solid (0.35 g, 1.0×10^{-3} mol, 82%).

$^1\text{H-NMR}$ (300 MHz, CDCl_3), δ_{H} : 10.35 (1H, s, C_1H), 8.55 (2H, d, J 4.8, C_{16}H), 8.30 (1H, d, J 8.2, C_3H), 8.09 (1H, d, J 8.3, C_4H), 8.06 (1H, d, J 8.4, C_7H), 7.70 (1H, d, J 8.6, C_8H), 7.64 (2H, td, J 1.9, J_2 7.9, C_{14}H), 7.28 (2H, d, J 7.9, C_{13}H), 7.14 (2H, dd, J 4.8, 7.3 C_{15}H), 2.52 (3H, s, C_{11}H_3).

$^{13}\text{C-NMR}$ (75 MHz, CDCl_3), δ_{C} : 193.83 (C_1), 171.19 (C_6), 165.34 (C_{12}), 154.84 (C_2), 154.24 (C_9), 148.88 (C_{16}), 138.31 (C_4), 136.42 (C_{14}), 135.11 (C_7), 127.19 (C_8), 123.98 (C_5), 123.06 (C_{13}), 121.54 (C_{15}), 117.91 (C_3), 61.09 (C_{10}), 27.29 (C_{11}).

Elemental analysis: $\text{C}_{21}\text{H}_{16}\text{N}_4\text{O} \cdot 0.125\text{CH}_3\text{COOCH}_2\text{CH}_3$. Theoretical: C: 73.40, H: 4.90 and N: 15.87. Obtained: C: 73.21, H: 4.89 and N: 16.13.

ESI-MS: m/z 341 (M+H)⁺ 50%

H (0.50 g, 1.5×10^{-3} mol, 1 eq) was dissolved in a mixture of 18 mL of THF and 10 mL of water then cooled to 0°C. $\text{NH}_2\text{SO}_3\text{H}$ (0.19 g, 1.9×10^{-3} mol, 1.3 eq) was added, and the mixture was stirred for 10 minutes before the addition of NaClO_2 (0.23 g, 1.9×10^{-3} mol, 1.3 eq). The solution was stirred for a further 2h30. The THF evaporated, the remaining aqueous phase extracted with DCM (4 x 40 mL), the organic fraction dried over MgSO_4 and evaporated to give **I** as a beige solid (0.61 g, 75%) that was used without further purification.

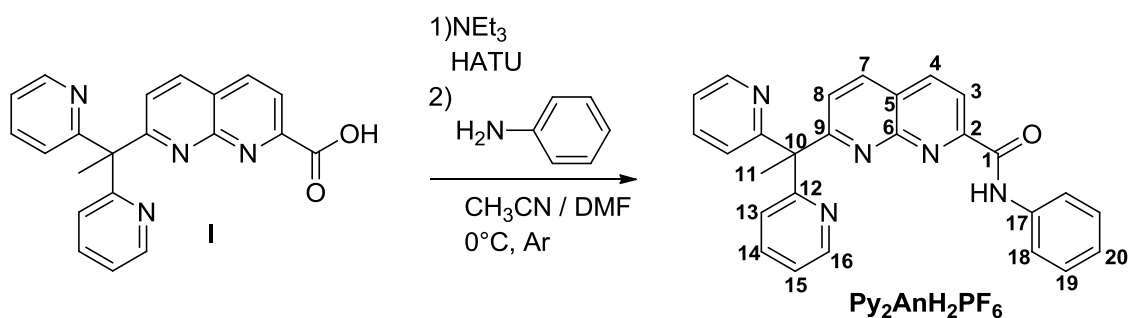
$^1\text{H-NMR}$ (300 MHz, CD_3CN), δ_{H} : 8.79 (2H, d, J 6.6 C_{16}H), 8.64 (1H, d, J 8.4, C_3H), 8.51 (1H, d, J 8.5, C_7H), 8.33 (1H, d, J 8.4, C_4H), 8.27 (2H, dd, J 8.2, 7.1, C_{14}H), 7.76 (2H, d, J 8.2, C_{15}H), 7.74 (2H, d, J 7.1, C_{13}H), 7.52 (1H, d, J 8.5, C_8H), 2.48 (3H, s, C_{11}H_3).

$^{13}\text{C-NMR}$ (126 MHz, CD_3CN), δ_{C} : 167.98 (C_6), 165.51 (C_1), 159.40 (C_{12}), 152.94 (C_2), 151.44 (C_9), 145.62 (C_{16}), 144.13 (C_{14}), 141.06 (C_3), 140.26 (C_7), 128.82 (C_5), 126.37 (C_{13}), 125.68 (C_{15}), 124.15 (C_8), 123.03 (C_4), 56.52 (C_{10}), 26.90 (C_{11}).

ESI: m/z 379 (M+Na)⁺, 357 (M+H)⁺.HRMS: Theoretical ($\text{C}_{21}\text{H}_{17}\text{N}_4\text{O}_2$) m/z 357.1352, found 357.1357

3.2.2. Synthesis of dissymmetric ligands

3.2.2.1. Synthesis of the ligand $\text{Py}_2\text{AnH}_2\text{PF}_6$



Compound **I** (0.10 g, 0.28×10^{-3} mol, 1 eq) was put in a schlenk tube, and 10 mL of dry acetonitrile was added. The solution was degassed, and around 1mL DMF (dry) was added via syringe

chromatography (silica, 92% DCM, 7% CH₃OH, 1% NH₄OH) to give Py₂BenzimH₂ as yellow/brown solid (0.13 g, 37%).

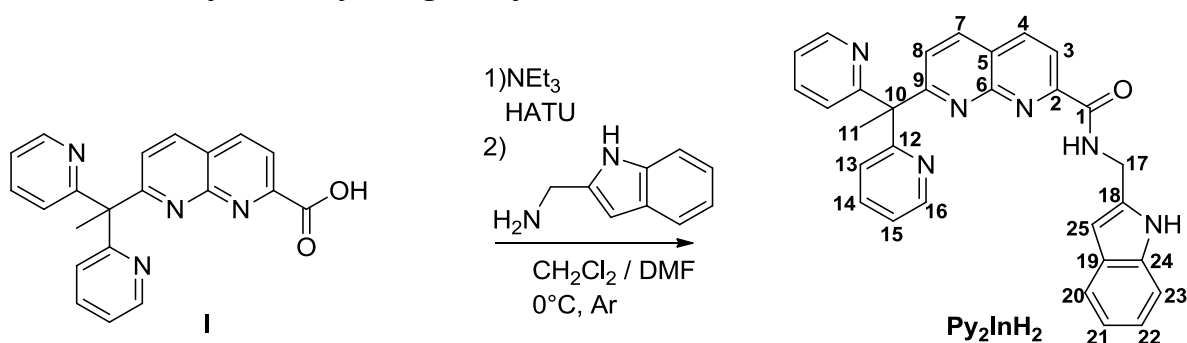
¹H-NMR (500 MHz, CDCl₃), δ_H: 9.49 (1 H, t, *J* 6.0 CONH), 8.55 – 8.49 (2 H, m, C₁₆H), 7.93 – 7.85 (3 H, m, C₃H, C₄H, C₇H), 7.67 – 7.61 (2 H, m, C₁₄H), 7.54 (1 H, d, *J* 8.6 C₈H), 7.32 (2 H, d, *J* 6.6, C₁₃H), 7.21 (2 H, m, C₂₃H, C₂₀H), 7.17 – 7.11 (2 H, m, C₁₅H), 7.00 – 6.92 (2 H, m, C₂₁H, C₂₂H), 4.83 (2 H, d, *J* 6.1 C₁₇H₂), 2.39 (3 H, s, C₁₁H₃).

¹³C-NMR (101 MHz, CDCl₃), δ_C: 170.13 (C₁), 165.20 (C₁₂), 164.96 (C₆), 153.00 (C₂), 151.70 (C₁₈), 151.21 (C₉), 148.67 (C₁₆), 137.68 (C₃), 136.65 (C₁₄), 135.66 (C₇), 125.45 (C₈), 123.38 (C₁₃), 122.53 (C₅), 121.94 (C₂₁), 121.93 (C₂₂), 121.83 (C₁₅), 120.24 (C₁₉), 119.35 (C₄), 116.74 (C₂₄), 114.70 (br, C₂₀, C₂₃), 60.94 (C₁₀), 38.25 (C₁₇), 27.50 (C₁₁).

ESI: *m/z* 486 (M+H)⁺.

Elemental analysis: C₂₉H₂₃N₇O·CH₃OH·0.8CH₂Cl₂ Theoretical: C: 63.18, H: 4.92 and N: 16.75. Obtained: C: 63.10, H: 4.94 and N: 16.79.

3.2.2.3. Synthesis of the ligand Py₂InH₂



Compound **I** (0.30 g, 8.4 × 10⁻⁴ mol, 1 eq) was put in a dry schlenk tube under argon and 20 mL of dry CH₂Cl₂ was added. NEt₃ (1.1 mL, 7.6 × 10⁻³ mol, 9 eq) was added and the solution cooled to 0°C. HATU (0.42 g, 1.1 × 10⁻³ mol, 1.3 eq) was dissolved in 8 mL dry DMF then added to the first schlenk. The solution was allowed to stir for 45 min at 0°C. In a second schlenk 15 mL dry DMF was added to 2-(aminomethyl)indole (0.16 g, 1.1 × 10⁻³ mol, 1.3 eq) and the mixture cannulated into the first schlenk. The solution was left to stir overnight and allowed to rise to room temperature, then the solvent evaporated and the product dried under a high vacuum line. The product was purified by column chromatography (silica, 97% DCM, 3% CH₃OH, 1% NH₄OH) to give Py₂InH₂ as yellow/brown solid (0.25 g, 61%).

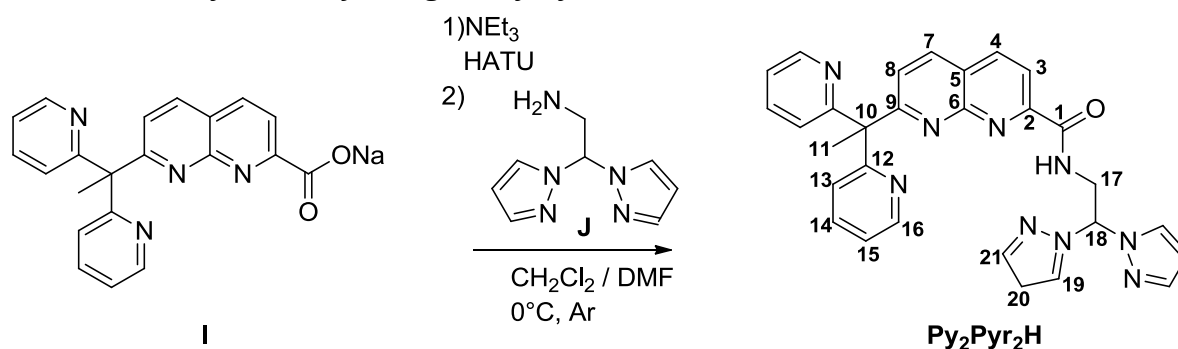
$^1\text{H-NMR}$ (400 MHz, CDCl_3), δ_{H} : 9.29 (1H, s, NH), 8.79 (1H, t, J 6.0, CONH), 8.54 (2H, d, J 4.6, C_{16}H), 8.26 (1H, d, J 8.2, C_4H), 8.20 (1H, d, J 8.2, C_3H), 8.02 (1H, d, J 8.5, C_7H), 7.62 (2H, t, J 7.8, C_{14}H), 7.55 (1H, d, J 8.2, C_8H), 7.55 (1H, d, J 8.2, C_{23}H), 7.30 (1H, d, J 8.0, C_{20}H), 7.25 (2H, d, J 8.0, C_{13}H), 7.12 (2H, t, J 7.8, C_{15}H), 7.11 (1H, m, C_{21}H), 7.06 (1H, t, J 7.2, C_{22}H), 6.36 (1H, s, C_{25}H), 4.68 (2H, d, J 6.0, C_{17}H), 2.46 (3H, s, C_{11}H).

$^{13}\text{C-NMR}$ (101 MHz, CDCl_3), δ_{C} : 171.04 (C_1), 165.23 (C_{12}), 165.21 (C_6), 153.49 (C_2), 151.64 (C_9), 148.92 (C_{16}), 138.35 (C_3), 136.43 (C_{14}), 135.78 (C_{18}), 135.49 (C_7), 127.88 (C_{19}), 125.93 (C_{23}), 123.94 (C_{13}), 122.82 (C_5), 121.78 (C_{21}), 121.60 (C_{15}), 120.34 (C_8), 119.56 (C_{22}), 119.53 (C_4), 111.06 (C_{20}), 101.03 (C_{25}), 61.08 (C_{10}), 37.21 (C_{17}), 27.37 (C_{11}).

ESI: m/z 485 ($\text{M}+\text{H}$) $^+$.

Elemental analysis: $\text{C}_{30}\text{H}_{24}\text{N}_6\text{O}\cdot\text{C}_3\text{H}_7\text{NO}\cdot 0.33\text{CH}_3\text{OH}$. Theoretical: C: 70.45, H: 5.73 and N: 17.25. Obtained: C: 70.37, H: 5.83 and N: 17.45.

3.2.2.4. Synthesis of the ligand $\text{Py}_2\text{Pyr}_2\text{H}$



Compound **I** (0.30 g, 8.4×10^{-4} mol, 1 eq) was put in a dry schlenk line under argon and 20 mL of dry CH_2Cl_2 was added. NEt_3 (0.5 mL, 3.7×10^{-3} mol, 4.4 eq) was added and the solution cooled to 0°C . HATU (0.43 g, 1.1×10^{-3} mol, 1.3 eq) was dissolved in 5 mL dry DMF then added to the first schlenk. The solution was allowed to stir for 45 min at 0°C . In a second schlenk 20 mL dry DCM was added to **J** (0.21 g, 1.1×10^{-3} mol, 1.3 eq, synthesised according to the literature procedure¹⁶⁰) and the mixture cannulated into the first schlenk. The solution was stirred for 30 min then a further 0.4 mL (3.0×10^{-3} mol, 3.5 eq) of NEt_3 was added. The solution was left to stir overnight and allowed to rise to room temperature, then the solvent evaporated and the product dried under a vacuum line. The product was purified by column chromatography (silica, 91% DCM, 8% CH_3OH , 1% NH_4OH) to give $\text{Py}_2\text{Pyr}_2\text{H}$ as yellow oil (0.39 g, 88%).

$^1\text{H-NMR}$ (400 MHz, CDCl_3), δ_{H} : 8.58 (1H, t, J 6.1 NH), 8.36 (2H, d, J 4.2, C_{16}H), 8.12 (1H, d, J 8.2, C_4H), 8.05 (1H, d, J 8.2, C_3H), 7.86 (1H, d, J 8.8, C_7H), 7.51 (2H, s, C_{19}H), 7.43 (2H, t, J 7.8, C_{14}H), 7.38 (1H, d, J 6.1, C_8H), 7.37 (2H, s, C_{21}H), 7.07 (2H, d, J 7.8 C_{13}H), 6.95 (2H, dd, J 5.0, C_{15}H), 6.74 (1H, t, J 6.8, C_{18}H), 6.04 (2H, s, C_{20}H), 4.45 (2H, t, J 6.8, C_{17}H), 2.30 (3H, s, C_{11}H).

$^{13}\text{C-NMR}$ (101 MHz, CDCl_3), δ_{C} : 170.41 (C_1), 165.07 (C_{12}), 165.02 (C_6), 153.03 (C_2), 150.99 (C_9), 148.39 (C_{16}), 140.03 (C_{21}), 138.02 (C_4), 136.00 (C_{14}), 135.09 (C_7), 128.72 (C_{19}), 125.51 (C_8), 122.89 (C_{13}), 122.47 (C_5), 121.18 (C_{15}), 119.23 (C_3), 106.23 (C_{20}), 72.61 (C_{18}), 60.62 (C_{10}), 41.97 (C_{17}), 26.89 (C_{11}).

ESI: m/z 538 ($\text{M}+\text{Na}$) $^+$, 516 ($\text{M}+\text{H}$) $^+$.

Elemental analysis: $\text{C}_{29}\text{H}_{25}\text{N}_9\text{O}\cdot 1.5\text{H}_2\text{O}$. Theoretical: C: 64.19, H: 5.20 and N: 23.23. Obtained: C: 64.15, H: 5.40 and N: 23.25.

3.3. Syntheses of dissymmetric complexes

3.3.1. Syntheses of complexes with the ligand $\text{Py}_2\text{AnH}_2\text{PF}_6$

50 mg of the ligand $\text{Py}_2\text{AnH}_2\text{PF}_6$ (8.7×10^{-5} mol, 1 eq) was dissolved in 5 mL THF. H_2O (21 μl , 1.2×10^{-3} mol, 14 eq) and NEt_3 (48 μl , 3.6×10^{-4} mol, 4 eq) were added followed by a solution of $\text{Cu}(\text{OTf})_2$ (93 mg, 2.6×10^{-4} mol, 3 eq) in 5 mL THF. A green precipitate immediately appeared and the mixture was stirred for 3 hours. The mixture was allowed to stand, then the THF decanted. The solid was washed twice with THF. The green solid was recrystallized by slow diffusion of DIPE into a either a solution of methanol to give a few crystals of the tetranuclear complex.

10 mg of the green precipitate was dissolved in 5 mL of CH_3CN and 13 mg of sodium perchlorate (approximately a 10 fold excess) was added, resulting in a green precipitate that was filtered. Slow diffusion of DIPE into a solution of DMF resulted in a few crystals of the hexanuclear complex.

Elemental analysis: Unfortunately an elemental analysis corresponding to the structures determined could not be obtained.

3.3.2. Synthesis of the complex $\text{Cu}^{\text{II}}_4(\text{Py}_2\text{Benzim})_2$

50 mg of the ligand $\text{Py}_2\text{BenzimH}_2$ (1.0×10^{-4} mol, 1 eq) was dissolved in 5 mL THF. H_2O (18 μl , 1.0×10^{-3} mol, 10 eq) and NEt_3 (75 μl , 5.4×10^{-4} mol, 5.4 eq) were added followed by a solution of $\text{Cu}(\text{OTf})_2$ (78 mg, 2.2×10^{-4} mol, 2.1 eq) in 5 mL THF. A dark green precipitate immediately appeared

and the mixture was stirred for 2 hours. The precipitate was filtered and recrystallized by slow diffusion of THF into a solution of CH₃OH, to give 54 mg of the complex Cu^{II}₄(Py₂Benzim)₂ (24%).

Elemental analysis: C₆₀H₄₄Cu₄F₆N₁₄O₁₀S₂·6H₂O. Theoretical: C: 43.40, H: 3.10 and N: 11.98. Obtained: C: 43.37, H: 3.40 and N: 11.80.

ESI-MS: m/z 1553 (M+H)⁺, 1403 (M-OTf)⁺, 627 (M-(OTf)₂)²⁺.

UV-Vis (acetonitrile) λ /nm ($\epsilon/M^{-1} \text{ cm}^{-1}$): 323 (21000), 312 (19500), 588 (421), 681 (362).

3.3.3. Attempted syntheses of complexes with the ligand Py₂InH₂

3.3.3.1. Synthesis in THF with triethylamine as the base

50 mg of the ligand Py₂InH₂ (1.0×10^{-4} mol, 1.0 eq) was dissolved in 5 mL of THF. H₂O (10 μ l, 5.5×10^{-4} mol, 5.5 eq) and NEt₃ (150 μ l, 1.0×10^{-3} mol, 10 eq) were added followed by a solution of Cu(OTf)₂ (80 mg, 2.1×10^{-4} mol, 2.1 eq) in 5 mL of THF. The solution was stirred for 2 h and a dark green precipitate was formed that was filtered and washed in THF. No crystals could be obtained following several attempts.

3.3.3.2. Synthesis in acetonitrile with triethylamine as the base

50 mg of the ligand Py₂InH₂ (1.0×10^{-4} mol, 1.0 eq) was dissolved in 5 mL of acetonitrile. H₂O (10 μ l, 5.5×10^{-4} mol, 5.5 eq) and NEt₃ (150 μ l, 1.0×10^{-3} mol, 10 eq) were added followed by a solution of Cu(OTf)₂ (80 mg, 2.1×10^{-4} mol, 2.1 eq) in 5 mL of acetonitrile. The solution was stirred overnight then concentrated to 2 mL, THF was added forming a brown precipitate that was filtered. No crystals could be obtained following several attempts.

3.3.3.3. Synthesis in methanol with tetramethylammonium hydroxide as the base

50 mg of the ligand Py₂InH₂ (1.0×10^{-4} mol, 1.0 eq) was dissolved in 10 mL of methanol and 174 μ l of a solution of 25 wt. % [(CH₃)₄N]OH in methanol was added followed by a solution of 79 mg of Cu^{II}(ClO₄)₂·6H₂O and stirred for 2 h during which a dark green/brown precipitate was formed which was filtered. No crystals could be obtained following several attempts.

3.3.3.4. Synthesis in THF using n-BuLi as the base

20 mg of the ligand Py₂InH₂ (4.1×10^{-5} mol, 1.0 eq) was dissolved in 5 mL of freshly distilled THF and placed under Ar in a schlenk tube. The solution was cooled to -35 °C, and 65 μ l of 1.4 M n-BuLi

(9.0×10^{-5} mol, 2.2 eq) was added slowly. In a second schlenk tube 32 mg of $\text{Cu}(\text{OTf})_2$ was dissolved in 5 mL of freshly distilled THF (under Ar), cooled to -35°C and cannulated into the first schlenk. The green solution was stirred for 30 min allowing the temperature to rise to room temperature, then 15 μl of water was added. The solution was filtered and the filtrate concentrated. Pentane was added until a precipitate started to appear and the mixture was placed in the freezer (-20°C) for 12 h then filtered and washed with pentane to give a dark green solid. No crystals could be obtained following several attempts.

3.3.4. Synthesis of the complex $\text{Cu}^{\text{II}}_2\text{Py}_2\text{Pyr}_2$

50 mg of the ligand $\text{Py}_2\text{Pyr}_2\text{H}$ (9.8×10^{-5} mol, 1 eq) was dissolved in 10 mL of acetonitrile. H_2O (18 μl , 1.0×10^{-3} mol, 10 eq) and NEt_3 (26 μl , 1.9×10^{-4} mol, 2 eq) were added followed by a solution of $\text{Cu}(\text{OTf})_2$ (70 mg, 2.0×10^{-4} mol, 2.05 eq) in 5 mL of acetonitrile. The dark green solution was stirred for 1 h, then concentrated and precipitated with THF. The mixture was placed in the freezer (-20°C) for 12 h, then filtered and washed with THF to give a green solid that was crystallised by slow diffusion of THF into a solution of acetonitrile. Green crystals were obtained (50 mg, 53%).

ESI-MS: m/z 806 ($\text{M}(\text{OTf}-\text{H}_2\text{O})^+$), 328.5 ($\text{M}(\text{OTf})_2-\text{H}_2\text{O})^{2+}$.

Elemental analysis: $\text{C}_{31}\text{H}_{27}\text{Cu}_2\text{F}_6\text{N}_9\text{O}_9\text{S}_2 \cdot 1.33\text{H}_2\text{O}$. Theoretical: C: 37.28, H: 2.99 and N: 12.62. Obtained: C: 37.09, H: 2.75 and N: 12.37.

UV-Vis (acetonitrile) λ /nm ($\epsilon/\text{M}^{-1} \text{cm}^{-1}$): 263 (19000), 310 (10000), 322 (10000), 640 (110).

3.3.5. Crystallographic data complexes

Table 24: Crystallographic data for the complexes $\text{Cu}^{\text{II}}_4(\text{Py}_2\text{An})_2$, $\text{Cu}^{\text{II}}_6(\text{Py}_2\text{An})_2$, $\text{Cu}^{\text{II}}_4(\text{Py}_2\text{Benzim})_2$ and $\text{Cu}^{\text{II}}_2\text{Py}_2\text{Pyr}_2$.

Complex	$\text{Cu}^{\text{II}}_4(\text{Py}_2\text{An})_2$	$\text{Cu}^{\text{II}}_6(\text{Py}_2\text{An})_2$	$\text{Cu}^{\text{II}}_4(\text{Py}_2\text{Benzim})_2$	$\text{Cu}^{\text{II}}_2\text{Py}_2\text{Pyr}_2$
Formula	$\text{C}_{29}\text{H}_{26}\text{Cu}_2\text{N}_5\text{O}_3\cdot\text{F}_6\text{P}\cdot\text{CH}_4\text{O}$	$\text{C}_{33}\text{H}_{37}\text{Cu}_3\text{N}_7\text{O}_6\cdot 2(\text{ClO}_4)\cdot\text{C}_3\text{H}_7\text{NO}$	$\text{C}_{29}\text{H}_{22}\text{Cu}_2\text{N}_7\text{O}_2\cdot\text{CF}_3\text{O}_3\text{S}\cdot 2.25(\text{H}_2\text{O})\cdot 0.5(\text{C}_4\text{H}_8\text{O})$	$\text{C}_{29}\text{H}_{27}\text{Cu}_2\text{N}_9\text{O}_3\cdot 2(\text{CF}_3\text{O}_3\text{S})\cdot 0.83(\text{C}_4\text{H}_8\text{O})$
M	796.64	1090.31	861.53	1042.66
Crystal system	monoclinic	triclinic	monoclinic	monoclinic
Space group	$P 2_1/n$	$P - 1$	$P 2_1/n$	$P 2_1/n$
a / Å	11.149(2)	12.389(3)	11.839(2)	10.036(2)
b / Å	17.536(4)	12.436(3)	11.857(2)	24.598(5)
c / Å	15.966(3)	14.988(3)	28.305(6)	16.487(3)
$\alpha / ^\circ$	90.00	88.57(3)	90.00	90.00
$\beta / ^\circ$	91.21(3)	72.01(3)	101.23(3)	95.68(3)
$\gamma / ^\circ$	90.00	81.25(3)	90.00	90.00
v / Å ³	3120.6(11)	2170.0(8)	3897.3(14)	4050.0(14)
Z	4	2	4	4
T / K	200	200	200	200
$\rho_c / \text{g}\cdot\text{cm}^{-3}$	1.845	1.669	1.468	1.710
μ / mm^{-1}	0.5465	1.657	1.215	1.250
Total reflections	36034	49692	34776	32339
Independent reflections	5455	9802	8690	7045
Observed reflections	3914 ($I > 2\sigma(I)$)	7105 ($I > 2\sigma(I)$)	6186 ($I > 2\sigma(I)$)	4225 ($I > 2\sigma(I)$)
R	0.0713	0.0503	0.0985	0.0793
R_w	0.1483	0.1043	0.2559	0.1462

3.4. Other procedures

3.4.1. Cyclic voltammetry

The CVs of the complexes from ligands $\text{Py}_2\text{AnH}_2\text{PF}_6$, $\text{Py}_2\text{BenzimH}_2$ and $\text{Py}_2\text{Pyr}_2\text{H}$ were completed in commercially available HPLC grade solvents CH_3CN (Fisher), CH_3OH (Fisher) or DMF (Arcos) using NBu_4ClO_4 (Sigma Aldrich). A three electrode cell was used with glassy carbon (working

electrode), Pt wire (counter electrode) and an Ag wire in a 0.01 M solution of AgNO_3 (in 0.1 M $\text{NBu}_4\text{OH}/\text{CH}_3\text{CN}$) as the reference electrode, and the potential was calibrated against Fc^+/Fc by addition of Fc at the end of the experiment. The potentiostat used was purchased from CH Instruments.

3.4.2. UV-vis: Titration of the ligand Py_2InH_2 with $\text{Cu}(\text{OTf})_2$

1.08 mg (2.2×10^{-6} mol, 1 eq) of the ligand Py_2InH_2 was dissolved in 60 mL CH_3CN (to give a concentration of 3.7×10^{-5} mol. dm^{-3}). 31 μl (2.2×10^{-4} mol, 100 eq) of triethylamine was dissolved in 10 mL of acetonitrile. The ligand was titrated with 4 x 50 μl of the solution of NEt_3 (a total of 2 eq). After each addition, a 3 mL sample was removed and placed in a cuvette ($l = 1$ cm) and the UV-vis spectrum recorded using the spectrometer Cary 50. 2.28 mg of $\text{Cu}(\text{OTf})_2$ (2.8 eq, 6.2×10^{-6} mol) was dissolved in 1.4 mL of CH_3CN . 100 μl (0.2 eq) of the copper solution was added at a time to the mixture of base and ligand, and a UV-vis spectrum was recorded after each addition by removing a 3 mL sample and placing inside the cuvette. The experiment was repeated at a higher concentration of the ligand (1.0×10^{-3} mol. dm^{-3}), adding the same number of equivalents of triethylamine and $\text{Cu}(\text{OTf})_2$ and recording the UV-vis spectra after each addition.

4. Part II Chapter 3

4.1. Synthesis

4.1.1. Synthesis of the ligands Py_4 , Ox_4 and Py_2Ox_2

The synthesis of the ligand Py_4 was carried out using a published literature procedure.¹³³

The synthesis of ligands Ox_4 and Py_2Ox_2 is described in Section 2.1.4.1.

4.1.2. Syntheses of the complexes $\text{Cu}^{\text{II}}\text{Py}_4$, $\text{Cu}^{\text{II}}\text{Ox}_4$ and $\text{Cu}^{\text{II}}\text{Py}_2\text{Ox}_2$

4.1.2.1. Synthesis of the complex $\text{Cu}^{\text{II}}\text{Py}_4$

150 mg of the ligand Py_4 (3.0×10^{-4} mol, 1 eq) was dissolved in 15 mL of THF. H_2O (54 μl , 3.0×10^{-3} mol, 10 eq) and triethylamine (85 μl , 6.1×10^{-4} mol, 2.05 eq) were added followed by a solution of $\text{Cu}(\text{OTf})_2$ (231 mg, 6.4×10^{-4} mol, 2.1 eq) in 15 mL THF. A blue precipitate formed immediately, which after 2 h was filtered and washed with THF. The blue solid was dissolved in 3 mL of CH_3CN , 70

mL of THF was added and the mixture placed in the freezer (-20°C) for one week after which crystals had formed. These were collected, and dried under vacuum (290 mg, quantitative yield). X-ray diffraction quality crystals were obtained by slow diffusion of DIPE into a solution of CH₃CN.

ESI (acetonitrile): m/z 803 (M-OTf)⁺, 327 (M-(OTf)₂)²⁺.

Elemental analysis: C₃₄H₂₈Cu₂F₆N₆O₈S₂•0.5H₂O•0.2C₄H₈O. Theoretical: C: 42.77, H: 3.16 and N: 8.60. Obtained: C: 43.02, H: 3.31 and N: 8.35.

UV-Vis (acetonitrile) λ /nm (ϵ /M⁻¹ cm⁻¹): 262 (4520), 306 (4080), 312 (4080), 320 (4230) 580 (77).

4.1.2.2. *Synthesis of the complex Cu^{II}Ox₄*

130 mg of the ligand Py₂Ox₂ (2.2 x 10⁻⁴ mol, 1 eq) was dissolved in 10 mL of THF. Triethylamine (66 μ l, 4.7 x 10⁻⁴ mol, 2.1 eq) was added followed by a solution of Cu(OTf)₂ (170 mg, 4.6 x 10⁻⁴ mol, 2.1 eq) in 5 mL THF. A blue precipitate gradually formed, and after 3 h the solution was decanted and the solid washed in THF. The blue solid was recrystallized by slow diffusion of DIPE into a solution of CH₃CN to give blue crystals (160 mg, 71%) suitable for X-ray diffraction.

ESI (acetonitrile): m/z 883 (M-OTf)⁺, 359 (M-(OTf)₂)²⁺.

Elemental analysis: C₃₄H₄₆Cu₂F₆N₆O₁₃S₂•H₂O. Theoretical: C: 38.82, H: 4.41 and N: 7.99. Obtained: C: 38.85, H: 4.51 and N: 8.34.

UV-Vis (acetonitrile) λ /nm (ϵ /M⁻¹ cm⁻¹): 253 (9700), 305 (8300), 310 (8600), 317 (10000) 580 (94).

4.1.2.3. *Synthesis of the complex Cu^{II}Py₂Ox₂*

50 mg of the ligand Py₂Ox₂ (9.4 x 10⁻⁵ mol, 1 eq) was dissolved in 5 mL of THF. H₂O (17 μ l, 9.4 x 10⁻⁴ mol, 10 eq) and triethylamine (27 μ l, 1.9 x 10⁻⁴ mol, 2.1 eq) were added followed by a solution of Cu(OTf)₂ (71 mg, 2.0 x 10⁻⁴ mol, 2.1 eq) in 5 mL THF. A blue precipitate gradually formed, and after 3 h the solution was decanted and the solid washed in THF. The blue solid was dissolved in 1 mL of CH₃CN, 40 mL of THF was added and the mixture placed in the freezer (-20°C) for one week after which crystals had formed. These were collected, and dried under vacuum (73 mg, 75%). X-ray diffraction quality crystals were obtained by slow diffusion of DIPE into a solution of CH₃CN.

ESI (acetonitrile): m/z 843 (M-OTf)⁺, 338 (M-(OTf)₂-H₂O)²⁺.

Elemental analysis: C₃₄H₃₆Cu₂F₆N₆O₁₀S₂·0.5H₂O. Theoretical: C: 40.72, H: 3.72 and N: 8.38. Obtained: C: 40.69, H: 3.60 and N: 8.58.

UV-Vis (acetonitrile) λ /nm (ϵ /M⁻¹ cm⁻¹): 268 (8200), 303 (7400), 306 (8600), 317 (7300) 570 (100).

4.1.3. Crystallographic data

Table 25: Crystallographic data for the complexes Cu^{II}Py₄, Cu^{II}Py₂Ox₂ and Cu^{II}Ox₄.

Complex	Cu ^{II} Py ₄	Cu ^{II} Py ₂ Ox ₂	Cu ^{II} Ox ₄
Formula	C ₃₃ H ₂₈ Cu ₂ N ₆ F ₃ O ₅ S·CF ₃ O ₃ S·1.8CH ₃ CN	2(C ₃₂ H ₃₆ Cu ₂ N ₆ O ₄)·4(CF ₃ O ₃ S)·CH ₃ CN	C ₃₂ H ₄₄ Cu ₂ N ₆ O ₆ ·2(CF ₃ O ₃ S)
M	1028.05	2028.83	1033.95
Crystal system	triclinic	triclinic	monoclinic
Space group	P -1	P -1	P 2 ₁ /n
a / Å	14.783(3)	12.377(3)	10.332(2)
b / Å	17.300(4)	14.361(3)	30.427(6)
c / Å	18.904(4)	23.657(5)	13.415(3)
α / °	70.13(3)	84.30(3)	90
β / °	68.96(3)	82.98(3)	92.80(3)
γ / °	76.69(3)	83.00(3)	90
V / Å ³	4211.3(15)	4127.1(15)	4212.2(15)
Z	4	2	4
T / K	200	200	200
ρ_c / g·cm ⁻³	1.621	1.633	1.630
μ / mm ⁻¹	1.197	1.222	1.202
Total reflections	82271	77009	68415
Independent reflections	19295	18827	12173
Observed reflections	10403 (I > 2 σ (I))	11658 (I > 2 σ (I))	9889 (I > 2 σ (I))
R	0.0474	0.0868	0.0400
R _w	0.1082	0.2176	0.0872

4.2. Other procedures

4.2.1. Room temperature CV

The CVs were completed in commercially available HPLC grade solvents CH₃CN (Fisher) using NBu₄ClO₄ (Sigma Aldrich) as the supporting electrolyte. A three electrode cell was used with glassy carbon (working electrode), Pt wire (counter electrode) and an Ag wire in a 0.01 M solution of AgNO₃ (in 0.1 M NBu₄OH/CH₃CN) (reference electrode), and the potential was calibrated against Fc⁺/Fc by addition of Fc at the end of the experiment. The potentiostat used was purchased from CH Instruments.

4.2.2. Spectroelectrochemistry

Thin layer room and low-temperature UV-Vis-NIR spectro-electrochemistry were performed with a specific home-designed cell in a reflectance mode (working electrode: glassy carbon, reference electrode: Pt wire, counter electrode: Pt wire) in a glove box (Jacomex). Ferrocene was added at the end of the experiments to determine redox potential values vs. Fc⁺/Fc. The potential of the cell was controlled by an AUTOLAB PGSTAT 100 (Metrohm) potentiostat monitored by the NOVA software. HPLC-grade acetonitrile was degassed under argon and stored into the glovebox. The supporting salt NBu₄PF₆ was synthesized from NBu₄OH (Acros) and HPF₆ (Aldrich). It was then purified, dried under vacuum for 48 hours at 100° C, then kept under argon in the glovebox. The supporting salt NBu₄ClO₄ was purchased from Sigma Aldrich. The UV-Vis and Vis-NIR optic fibre probes were purchased from Ocean Optics. Time-resolved UV-Vis-NIR detection was performed with QEPro and NIRQuest spectrometers (Ocean optics). Cooling down of the solution was operated with a Lauda Pro-line cryostated-system.

4.2.3. Low temperature electrolysis

Low-temperature electrolyses were carried out with a home-designed 3-electrodes cell (working electrode: Carbon felt, reference electrode: Ag wire in a 0.01 M solution of AgNO₃ (in 0.1 M NBu₄OH/CH₃CN), counter electrode: Pt plate) dipped in an ethanol/liquid N₂ bath at -40°C for 45 minutes. CH₃CN (Fisher) was used as the solvent with NBu₄ClO₄ (Sigma Aldrich) as the supporting electrolyte.

4.2.4. EPR of the complexes $\text{Cu}^{\text{II}}_2\text{Py}_4$, $\text{Cu}^{\text{II}}_2\text{Ox}_4$ and $\text{Cu}^{\text{II}}_2\text{Py}_2\text{Ox}_2$ and their mono-electronic-oxidised species

Samples of the mono-electronic oxidised species were obtained as follows: samples were taken out every 10 min during the course of the electrolysis using a pre-cooled syringe and EPR tube, and the sample was immediately frozen in liquid nitrogen for EPR analysis.

4.2.5. Theoretical calculations on the complex $\text{Cu}^{\text{II}}_2\text{Py}_4$ and its oxidised species

All calculations were performed using the GAUSSIAN 09 package. Geometry optimisations were carried out for all systems using the hybrid exchange-correlation PBE0 functional accounting for CH_3CN solvation effects using the IEF-PCM continuum solvent model. A mixed basis set comprised of the Def2-TZVDP for copper atoms, the 6-311+G(d,p) for N and O atoms and 6-311G(d,p) for C and H atoms as it was already described.¹²⁶ Vibrational frequency calculations were performed to ensure that each geometry optimisation converged to a real minimum.

To compute redox potentials, energetic calculations were carried from additional single point calculations on the previously optimized geometries using the M11-L functional and always the IEF-PCM continuum solvent model. For $\text{Cu}^{\text{II}}_2\text{Py}_4$, two spin states (a triplet or a singlet ground state) are possible. However the energy difference between these two states is very small compared to that between the two redox states. So we choose to work only on the triplet state.

Finally TD-DFT calculations were performed for the doublet state of the $\text{Cu}^{\text{II}}\text{Cu}^{\text{III}}$ species from $\text{Cu}^{\text{II}}_2\text{Py}_4$. In the case of open shell systems such as the mono-oxidized $\text{Cu}^{\text{II}}\text{Cu}^{\text{III}}$ species, spin contamination problems can induce errors on the nature of the excited states.¹⁸⁶ Thus, benchmarks were tested using different functionals. We used the PBE0 functional and the two long range corrected CAM-B3LYP and wB97XD functionals. These three functionals were associated with the IEF-PCM solvent model and the same basis set as before. Solutions for the 50 lowest states were computed.

5. Part II Chapter 4

5.1. Cyclic Voltammetry

5.1.1. CVs of complexes $\text{Cu}^{\text{II}}_2\text{Py}_4$, $\text{Cu}^{\text{II}}_2\text{Ox}_4$ and $\text{Cu}^{\text{II}}_2\text{Py}_2\text{Ox}_2$ with toluene

The CVs were performed either opened to an atmosphere of air or in a Jacomex glove box (specified in the text). The CVs were completed in commercially available HPLC grade solvents CH_3CN (Fisher) using NBu_4ClO_4 (Sigma Aldrich) as the supporting electrolyte. A three electrode cell was used with glassy carbon (working electrode), Pt wire (counter electrode) and an Ag wire in a 0.01 M solution of AgNO_3 (in 0.1 M $\text{NBu}_4\text{OH}/\text{CH}_3\text{CN}$) (reference electrode), and the potential was calibrated against Fc^+/Fc by addition of Fc at the end of the experiment. The potentiostat used was purchased from CH Instruments (CHI260B) or BioLogic using the software EC-lab when experiments were performed inside the glove box.

5.1.2. CVs of complex $\text{Cu}^{\text{II}}_2\text{Py}_4$ with greater than one equivalent of pyridine or 2,6-lutidine

Experiments were performed open to air. The same systems solvents and electrodes were used as described in Section 5.1.1. The potentiostat used was purchased from CH Instruments.

5.1.3. CVs of complex $\text{Cu}^{\text{II}}_2\text{Py}_4$ with 2,6-lutidine: addition of substoichiometric quantified of 2,6-lutidine and addition of water

Studies were performed in a glovebox (Jacomex) with a home-designed 3-electrodes cell (working electrode: BDD, reference electrode: Pt wire in a solution of Fc^+/Fc , counter electrode: Pt wire). Ferrocene was added at the end of the experiments to determine redox potential values. The potential of the cell was controlled by an AUTOLAB PGSTAT 100 (Metrohm) potentiostat monitored by the NOVA software. HPLC-grade acetonitrile was degassed under argon and stored into the glovebox. The supporting salt NBu_4ClO_4 was purchased from Sigma Aldrich. The electrolyte solution was dried over 3 Å molecular sieves for 24 h before use (the 3 Å sieves were activated at 350°C for 24 h prior to use then stored in the glove box).

5.1.4. Simulations

Simulations were completed using the software KISSA-1D.

5.2. Determination of oxidation products

5.2.1. Determination of the internal reactivity of complexes $\text{Cu}^{\text{II}}_2\text{Py}_2\text{Ox}_2$ and $\text{Cu}^{\text{II}}_2\text{Ox}_4$

5 mg of the complex was used in 7 mL of electrolyte (concentration of complex = 0.7 mM).

The electrolyses were carried out at -40°C using a bath of ethanol/ liquid N_2 with a home-designed 3-electrodes cell (working electrode: reticulated vitreous carbon, reference electrode: Ag wire in a 0.01 M solution of AgNO_3 (in 0.1 M $\text{NBU}_4\text{OH}/\text{CH}_3\text{CN}$), counter electrode: Pt plate). CH_3CN (Fisher) was used as the solvent with NBU_4ClO_4 (Sigma Aldrich) as the supporting electrolyte, and the potential controlled by a potentiostat purchased from CH Instruments (CHI260B).

After electrolysis the solution was allowed to rise to room temperature, concentrated to 1 mL and 5 mL of concentrated KOH was added. The solution was stirred for 4h, extracted with DCM (3 x 5 mL) and the organic phase dried over MgSO_4 . The residue was dissolved in the minimum amount of acetone:pentane (1:1) and purified over a column of silica using the same eluent. The purified residue was analysed by NMR (A Unity Plus 500 MHz Varian or 400 MHz spectrometer) and ESI-MS (mass spectrometer amaZon speed).

5.2.2. Determination of the reactivity of complex $\text{Cu}^{\text{II}}_2\text{Py}_4$ with Toluene

5.2.2.1. *Determination of the oxidation products*

4.8 mg of the complex was added to 6 mL of electrolyte (concentration of complex = 0.8 mM). 260 μL of toluene was added to this solution (490 eq). An exhaustive electrolysis was performed at room temperature using the same equipment described in Section 5.2.1, but this time at room temperature.

The solution from the electrolysis was then concentrated to 1 mL, and 25 mL of diethyl ether was added, resulting in the precipitation of the NBU_4ClO_4 salt which was filtered off. The solution was concentrated again almost to dryness and the residue taken up in diethyl ether (1 mL).

The sample was then analysed by GCMS (AGILENT 5977A-7890B) (EI with an ionisation source of 70 eV coupled to a gas phase chromatograph using the software Mass Hunter). The temperature sequence used for the gas chromatograph was as follows: the temperature was held at 40°C for 4 min then increased at $20^\circ\text{C}/\text{min}$ to a temperature of 280°C , for which the temperature was held for 4 min.

5.2.2.2. Determination of the source of the oxygen atom

The electrolysis was performed in a glove box (Jacomex). The solvent CH₃CN (Fisher) with NBu₄ClO₄ (Sigma Aldrich) as the supporting electrolyte was dried over 3 Å molecular sieves for 24 h (sieves activated at 350°C for 24 and stored in the glove box before use). 4.9 mg of the complex was dissolved in 6 mL of the solvent (concentration of the complex = 0.8 mM) and toluene (260 µl, 490 eq) and H₂¹⁸O (5 µl, 50 eq) were added. The electrolysis was performed at room temperature using a home-designed 3-electrodes cell (working electrode: reticulated vitreous carbon, reference electrode: Ag wire in a 0.01 M solution of AgNO₃ (in 0.1 M NBu₄OH/CH₃CN), counter electrode: Pt plate). The potentiostat AUT86078 (Metrohm) was used monitored by the software NOVA.

After electrolysis the solution was removed from the glove box, purified and analysed by GCMS using the same procedure described in Section 5.2.2.1.

5.2.3. Determination of the products from the electrocatalytic reactivity of complex Cu^{II}₂Py₄ with 2,6-lutidine and toluene

5.2.3.1. Electrolysis of Cu^{II}₂Py₄ with 2,6-lutidine

The materials for electrolysis are described in Section 5.2.1, with the exception of the potentiostat which was purchased from BioLogic using the software EC-lab. The procedure for purification and analysis by GCMS are the identical to the procedure in Section 5.2.2.1. The purified residue was additionally analysed by ¹H-NMR (Unity Plus 400 MHz Varian spectrometer).

4.9 mg of the complex was added to the electrolyte solution (concentration = 0.8 mM) and 4.8 µl (8 eq) of 2,6-lutidine was added. The electrolysis was completed in steps gradually increasing the potential to avoid an overload.

5.2.3.2. Electrolysis of Cu^{II}₂Py₄ with 2,6-lutidine and toluene

The same experiment was performed as described in Section 5.2.3.1 but this time in the presence of toluene (245 µL, 490 eq).

Bibliography

- (1) Bibler, C. J.; Marshall, J. S.; Pilcher, R. C. *Int. J. Coal Geol.* **1998**, *35* (4), 283.
- (2) Tilman, D.; Balzer, C.; Hill, J.; Befort, B. L. *Proc. Natl. Acad. Sci.* **2011**, *108* (50), 20260.
- (3) Ross, M. O.; Rosenzweig, A. C. *J. Biol. Inorg. Chem.* **2017**, *22* (3), 307.
- (4) Pratt, C.; Tate, K. *Environ. Sci. Technol.* **2018**, *52* (11), 6084.
- (5) Da Silva, M. J. *Fuel Process. Technol.* **2016**, *145*, 42.
- (6) Olah, G. A. *Angew. Chemie - Int. Ed.* **2005**, *44* (18), 2636.
- (7) Sirajuddin, S.; Rosenzweig, A. C. *Biochemistry* **2015**, *54* (14), 2283.
- (8) Hedegård, E. D.; Ryde, U. *J. Biol. Inorg. Chem.* **2017**, *22* (7), 1029.
- (9) Vaaje-Kolstad, G.; Forsberg, Z.; Loose, J. S.; Bissaro, B.; Eijsink, V. G. *Curr. Opin. Struct. Biol.* **2017**, *44*, 67.
- (10) Beeson, W. T.; Phillips, C. M.; Cate, J. H. D.; Marletta, M. A. *J. Am. Chem. Soc.* **2012**, *134* (2), 890.
- (11) Hemsworth, G. R.; Davies, G. J.; Walton, P. H. *Curr. Opin. Struct. Biol.* **2013**, *23* (5), 660.
- (12) Quinlan, R. J.; Sweeney, M. D.; Lo Leggio, L.; Otten, H.; Poulsen, J.-C. N.; Johansen, K. S.; Krogh, K. B. R. M.; Jorgensen, C. I.; Tovborg, M.; Anthonsen, A.; Tryfona, T.; Walter, C. P.; Dupree, P.; Xu, F.; Davies, G. J.; Walton, P. H. *Proc. Natl. Acad. Sci.* **2011**, *108* (37), 15079.
- (13) Hemsworth, G. R.; Henrissat, B.; Davies, G. J.; Walton, P. H. *Nat. Chem. Biol.* **2014**, *10* (2), 122.
- (14) Harris, P. V.; Welner, D.; McFarland, K. C.; Re, E.; Navarro Poulsen, J. C.; Brown, K.; Salbo, R.; Ding, H.; Vlasenko, E.; Merino, S.; Xu, F.; Cherry, J.; Larsen, S.; Lo Leggio, L. *Biochemistry* **2010**, *49* (15), 3305.
- (15) O'Dell, W. B.; Agarwal, P. K.; Meilleur, F. *Angew. Chemie - Int. Ed.* **2017**, *56* (3), 767.
- (16) Frandsen, K. E. H.; Simmons, T. J.; Dupree, P.; Poulsen, J.-C. N.; Hemsworth, G. R.; Ciano, L.; Johnston, E. M.; Tovborg, M.; Johansen, K. S.; von Freiesleben, P.; Marmuse, L.; Fort, S.; Cottaz, S.; Driguez, H.; Henrissat, B.; Lenfant, N.; Tuna, F.; Baldansuren, A.; Davies, G. J.; Lo Leggio, L.; Walton, P. H. *Nat. Chem. Biol.* **2016**, *12*, 298.
- (17) Kim, S.; Stahlberg, J.; Sandgren, M.; Paton, R. S.; Beckham, G. T. *Proc. Natl. Acad. Sci.* **2014**, *111* (1), 149.
- (18) Wang, B.; Johnston, E. M.; Li, P.; Shaik, S.; Davies, G. J.; Walton, P. H.; Rovira, C. *ACS Catal.* **2018**, *8* (2), 1346.
- (19) Klinman, J. P. *J. Biol. Chem.* **2006**, *281* (6), 3013.
- (20) Yoshizawa, K.; Kihara, N.; Kamachi, T.; Shiota, Y. *Inorg. Chem.* **2006**, *45* (7), 3034.
- (21) Crespo, A.; Martí, M. A.; Roitberg, A. E.; Amzel, L. M.; Estrin, D. A. *J. Am. Chem. Soc.* **2006**, *128*

- (39), 12817.
- (22) Klinman, J. P.; Krueger, M.; Brenner, M.; Edmondson, D. E. *J. Biol. Chem.* **1984**, *259* (6), 3399.
- (23) Brenner, M. C.; Klinman, J. P. *Biochemistry* **1989**, *28* (11), 4664.
- (24) Vendelboe, T. V.; Harris, P.; Zhao, Y.; Walter, T. S.; Harlos, K.; El Omari, K.; Christensen, H. E. *M. Sci. Adv.* **2016**, *2* (4), e1500980.
- (25) Prigge, S. T.; Kolhekar, A. S.; Eipper, B. A.; Mains, R. E.; Amzel, L. M. *Science* **1997**, *278* (5341), 1300.
- (26) Prigge, S. T.; Eipper, B. A.; Mains, R. E.; Amzel, L. M. *Science* **2004**, *304* (5672), 864.
- (27) Meury, M.; Knop, M.; Seebeck, F. P. *Angew. Chemie - Int. Ed.* **2017**, *56* (28), 8115.
- (28) Fujisawa, K.; Tanaka, M.; Moro-oka, Y.; Kitajima, N. *J. Am. Chem. Soc.* **1994**, *22* (116), 12079.
- (29) Reynolds, A. M.; Gherman, B. F.; Cramer, C. J.; Tolman, W. B. *Inorg. Chem.* **2005**, *44* (20), 6989.
- (30) Würtele, C.; Gaoutchenova, E.; Harms, K.; Holthausen, M. C.; Sundermeyer, J.; Schindler, S. *Angew. Chemie - Int. Ed.* **2006**, *45* (23), 3867.
- (31) Cramer, C. J.; Tolman, W. B. *Acc. Chem. Res.* **2007**, *40* (7), 601.
- (32) Donoghue, P. J.; Gupta, A. K.; Boyce, D. W.; Cramer, C. J.; Tolman, W. B. *J. Am. Chem. Soc.* **2010**, *132* (45), 15869.
- (33) Kunishita, A.; Kubo, M.; Sugimoto, H.; Ogura, T.; Sato, K.; Takui, T.; Itoh, S. *J. Am. Chem. Soc.* **2009**, *131* (8), 2788.
- (34) Kunishita, A.; Ertem, M. Z.; Okubo, Y.; Tano, T.; Sugimoto, H.; Ohkubo, K.; Fujieda, N.; Fukuzumi, S.; Cramer, C. J.; Itoh, S. *Inorg. Chem.* **2012**, *51* (17), 9465.
- (35) Peterson, R. L.; Himes, R. A.; Kotani, H.; Suenobu, T.; Tian, L.; Siegler, M. A.; Solomon, E. I.; Fukuzumi, S.; Karlin, K. D. *J. Am. Chem. Soc.* **2011**, *133* (6), 1702.
- (36) Zhu, X. Q.; Zhang, M. T.; Yu, A.; Wang, C. H.; Cheng, J. P. *J. Am. Chem. Soc.* **2008**, *130* (8), 2501.
- (37) Maiti, D.; Fry, H. C.; Woertink, J. S.; Vance, M. A.; Solomon, E. I.; Karlin, K. D. *J. Am. Chem. Soc.* **2007**, *129* (2), 264.
- (38) Maiti, D.; Lee, D. H.; Gaoutchenova, K.; Würtele, C.; Holthausen, M. C.; Narducci Sarjeant, A. A.; Sundermeyer, J.; Schindler, S.; Karlin, K. D. *Angew. Chemie - Int. Ed.* **2008**, *47* (1), 82.
- (39) Elwell, C. E.; Gagnon, N. L.; Neisen, B. D.; Dhar, D.; Spaeth, A. D.; Yee, G. M.; Tolman, W. B. *Chem. Rev.* **2017**, *117* (3), 2059.
- (40) Neisen, B. D.; Gagnon, N. L.; Dhar, D.; Spaeth, A. D.; Tolman, W. B. *J. Am. Chem. Soc.* **2017**, *139* (30), 10220.
- (41) Abad, E.; Rommel, J. B.; Kästner, J. *J. Biol. Chem.* **2014**, *289* (20), 13726.
- (42) Donoghue, P. J.; Tehranchi, J.; Cramer, C. J.; Sarangi, R.; Solomon, E. I.; Tolman, W. B. *J. Am. Chem. Soc.* **2011**, *133* (44), 17602.
- (43) Dhar, D.; Yee, G. M.; Markle, T. F.; Mayer, J. M.; Tolman, W. B. *Chem. Sci.* **2017**, *8* (2), 1075.

- (44) Dhar, D.; Tolman, W. B. *J. Am. Chem. Soc.* **2015**, *137* (3), 1322.
- (45) Dhar, D.; Yee, G. M.; Spaeth, A. D.; Boyce, D. W.; Zhang, H.; Dereli, B.; Cramer, C. J.; Tolman, W. B. *J. Am. Chem. Soc.* **2016**, *138* (1), 356.
- (46) Decker, H.; Schweikardt, T.; Tuczek, F. *Angew. Chemie - Int. Ed.* **2006**, *45* (28), 4546.
- (47) Nillius, D.; Jaenicke, E.; Decker, H. *FEBS Lett.* **2008**, *582* (5), 749.
- (48) Pretzler, M.; Rompel, A. *Inorganica Chim. Acta* **2018**, *481*, 25.
- (49) Matoba, Y.; Kumagai, T.; Yamamoto, A.; Yoshitsu, H.; Sugiyama, M. *J. Biol. Chem.* **2006**, *281* (13), 8981.
- (50) Deeth, R. J.; Diedrich, C. *J. Biol. Inorg. Chem.* **2010**, *15* (2), 117.
- (51) Inoue, T.; Shiota, Y.; Yoshizawa, K. *J. Am. Chem. Soc.* **2008**, *130* (11), 16890.
- (52) Wang, V. C. C.; Maji, S.; Chen, P. P. Y.; Lee, H. K.; Yu, S. S. F.; Chan, S. I. *Chem. Rev.* **2017**, *117* (13), 8574.
- (53) Balasubramanian, R.; Smith, S. M.; Rawat, S.; Yatsunyk, L. A.; Stemmler, T. L.; Rosenzweig, A. C. *Nature* **2010**, *465* (7294), 115.
- (54) Wang, Y.; Tseng, C.; Chen, Y.; Huang, D.; Chan, S. I. *J. Bacteriol.* **2003**, *185* (20), 5915.
- (55) Martinho, M.; Choi, D. W.; DiSpirito, A. A.; Antholine, W. E.; Semrau, J. D.; Münck, E. *J. Am. Chem. Soc.* **2007**, *129* (51), 15783.
- (56) Lieberman, R. L.; Rosenzweig, A. C. *Nature* **2005**, *434* (7030), 177.
- (57) Chan, S. I.; Yu, S. S. F. *Acc. Chem. Res.* **2008**, *41* (8), 969.
- (58) Hakemian, A. S.; Kondapalli, K. C.; Telsler, J.; Hoffman, B. M.; Stemmler, T. L.; Rosenzweig, A. C. *Biochemistry* **2008**, *47* (26), 6793.
- (59) Smith, S. M.; Rawat, S.; Telsler, J.; Hoffman, B. M.; Stemmler, T. L.; Rosenzweig, A. C. *Biochemistry* **2011**, *50* (47), 10231.
- (60) Lieberman, R. L.; Kondapalli, K. C.; Shrestha, D. B.; Hakemian, A. S.; Smith, S. M.; Telsler, J.; Kuzelka, J.; Gupta, R.; Borovik, A. S.; Lippard, S. J.; Hoffman, B. M.; Rosenzweig, A. C.; Stemmler, T. L. *Inorg. Chem.* **2006**, *45* (20), 8372.
- (61) Ro, S. Y.; Ross, M. O.; Deng, Y. W.; Batelu, S.; Lawton, T. J.; Hurley, J. D.; Stemmler, T. L.; Hoffman, B. M.; Rosenzweig, A. C. *J. Biol. Chem.* **2018**, *293*, 10457.
- (62) Culpepper, M. A.; Cutsail, G. E.; Gunderson, W. A.; Hoffman, B. M.; Rosenzweig, A. C. *J. Am. Chem. Soc.* **2014**, *136* (33), 11767.
- (63) Cao, L.; Caldararu, O.; Rosenzweig, A. C.; Ryde, U. *Angew. Chemie - Int. Ed.* **2018**, *57* (1), 162.
- (64) Hung, S. C.; Chen, C. L.; Chen, K. H. C.; Yu, S. S. F.; Chan, S. I. *J. Chinese Chem. Soc.* **2004**, *51* (5), 1229.
- (65) Chan, S. I.; Wang, V. C. C.; Lai, J. C. H.; Yu, S. S. F.; Chen, P. P. Y.; Chen, K. H. C.; Chen, C. L.; Chan, M. K. *Angew. Chemie - Int. Ed.* **2007**, *46* (12), 1992.

- (66) Culpepper, M. A.; Cutsail, G. E.; Ho, B. M.; Rosenzweig, A. C. *J. Am. Chem. Soc.* **2012**, *134*, (18), 7640.
- (67) Wilkinson, B.; Zhu, M.; Priestley, N. D.; Nguyen, H.-H. T.; Morimoto, H.; Williams, P. G.; Chan, S. I.; Floss, H. G. *J. Am. Chem. Soc.* **1996**, *118* (4), 921.
- (68) Yu, S. S. F.; Wu, L. Y.; Chen, K. H. C.; Luo, W. I.; Huang, D. S.; Chan, S. I. *J. Biol. Chem.* **2003**, *278* (42), 40658.
- (69) Chan, S. I.; Chen, K. H. C.; Yu, S. S. F.; Chen, C. L.; Kuo, S. S. J. *Biochemistry* **2004**, *43* (15), 4421.
- (70) Chen, P. P. Y.; Chan, S. I. *J. Inorg. Biochem.* **2006**, *100* (4), 801.
- (71) Yoshizawa, K.; Shiota, Y. *J. Am. Chem. Soc.* **2006**, *128* (30), 9873.
- (72) Shiota, Y.; Yoshizawa, K. *Inorg. Chem.* **2009**, *48* (3), 838.
- (73) Itoyama, S.; Doitomi, K.; Kamachi, T.; Shiota, Y.; Yoshizawa, K. *Inorg. Chem.* **2016**, *55* (6), 2771.
- (74) Shiota, Y.; Juhász, G.; Yoshizawa, K. *Inorg. Chem.* **2013**, *52* (14), 7907.
- (75) Da Silva, J. C. S.; Pennifold, R. C. R.; Harvey, J. N.; Rocha, W. R. *Dalton Trans.* **2016**, *45* (6), 2492.
- (76) Mahyuddin, M. H.; Staykov, A.; Shiota, Y.; Miyanishi, M.; Yoshizawa, K. *ACS Catal.* **2017**, *7* (6), 3741.
- (77) Woertink, J. S.; Smeets, P. J.; Groothaert, M. H.; Vance, M. A.; Sels, B. F.; Schoonheydt, R. A.; Solomon, E. I. *Proc. Natl. Acad. Sci.* **2009**, *106* (45), 18908.
- (78) Yumura, T.; Hirose, Y.; Wakasugi, T.; Kuroda, Y.; Kobayashi, H. *ACS Catal.* **2016**, *6* (4), 2487.
- (79) Grundner, S.; Markovits, M. A. C.; Li, G.; Tromp, M.; Pidko, E. A.; Hensen, E. J. M.; Jentys, A.; Sanchez-Sanchez, M.; Lercher, J. A. *Nat. Commun.* **2015**, *6*, 7546.
- (80) Mirica, L. M.; Stack, T. D. P. *Inorg. Chem.* **2005**, *44* (7), 2131.
- (81) Lionetti, D.; Day, M. W.; Agapie, T. *Chem. Sci.* **2013**, *4* (2), 785.
- (82) Chen, P. P.-Y.; Yang, R. B.-G.; Lee, J. C.-M.; Chan, S. I. *Proc. Natl. Acad. Sci. U. S. A.* **2007**, *104* (37), 14570.
- (83) Nagababu, P.; Maji, S.; Kumar, M. P.; Chen, P. P. Y.; Yu, S. S. F.; Chan, S. I. *Adv. Synth. Catal.* **2012**, *354* (17), 3275.
- (84) Chan, S. I.; Chien, C. Y. C.; Yu, C. S. C.; Nagababu, P.; Maji, S.; Chen, P. P. Y. *J. Catal.* **2012**, *293*, 186.
- (85) Chan, S. I.; Lu, Y. J.; Nagababu, P.; Maji, S.; Hung, M. C.; Lee, M. M.; Hsu, I. J.; Minh, P. D.; Lai, J. C. H.; Ng, K. Y.; Ramalingam, S.; Yu, S. S. F.; Chan, M. K. *Angew. Chemie - Int. Ed.* **2013**, *52* (13), 3731.
- (86) Chen, P. P. Y.; Nagababu, P.; Yu, S. S. F.; Chan, S. I. *ChemCatChem* **2014**, *6* (2), 429.
- (87) Liu, C.-C.; Mou, C.-Y.; Yu, S. S.-F.; Chan, S. I. *Energy Environ. Sci.* **2016**, *9* (4), 1361.
- (88) Liu, Y. F.; Du, L. *Inorg. Chem.* **2018**, *57* (6), 3261.

- (89) Dean, J. A. *Lange's Handbook of Chemistry*; 1990.
- (90) Nagababu, P.; Yu, S. S. F.; Maji, S.; Ramu, R.; Chan, S. I. *Catal. Sci. Technol.* **2014**, *4* (4), 930.
- (91) Halfen, J. A.; Mahapatra, S.; Wilkinson, E. C.; Kaderli, S.; Young, V. G.; Que, L.; Zuberbühler, A. D.; Tolman, W. B. *Science* **1996**, *271* (5254), 1397.
- (92) Hatcher, L. Q.; Vance, M. A.; Sarjeant, A. A. N.; Solomon, E. I.; Karlin, K. D. *Inorg. Chem.* **2006**, *45* (7), 3004.
- (93) Goswami, V. E.; Walli, A.; Förster, M.; Dechert, S.; Demeshko, S.; Holthausen, M. C.; Meyer, F. *Chem. Sci.* **2017**, *8* (4), 3031.
- (94) Osako, T.; Ueno, Y.; Tachi, Y.; Itoh, S. *Inorg. Chem.* **2003**, *42* (24), 8087.
- (95) Osako, T.; Terada, S.; Tosha, T.; Nagatomo, S.; Furutachi, H.; Fujinami, S.; Kitagawa, T.; Suzuki, M.; Itoh, S. *Dalton Trans.* **2005**, *21* (7), 3514.
- (96) Karahalıs, G. J.; Thangavel, A.; Chica, B.; Bacsa, J.; Dyer, R. B.; Scarborough, C. C. *Inorg. Chem.* **2016**, *55* (3), 1102.
- (97) Cahoy, J.; Holland, P. L.; Tolman, W. B. *Inorg. Chem.* **1999**, *38*, 2161.
- (98) Ottenwaelder, X.; Rudd, D. J.; Corbett, M. C.; Hodgson, K. O.; Hedman, B.; Stack, T. D. P. *J. Am. Chem. Soc.* **2006**, *128* (29), 9268.
- (99) Garcia-Bosch, I.; Cowley, R. E.; Díaz, D. E.; Peterson, R. L.; Solomon, E. I.; Karlin, K. D. *J. Am. Chem. Soc.* **2017**, *139* (8), 3186.
- (100) Park, G. Y.; Qayyum, M. F.; Woertink, J.; Hodgson, K. O.; Hedman, B.; Narducci Sarjeant, A. A.; Solomon, E. I.; Karlin, K. D. *J. Am. Chem. Soc.* **2012**, *134* (20), 8513.
- (101) Keown, W.; Gary, J. B.; Stack, T. D. P. *J. Biol. Inorg. Chem.* **2017**, *22* (3), 289.
- (102) Citek, C.; Lin, B. L.; Phelps, T. E.; Wasinger, E. C.; Stack, T. D. P. *J. Am. Chem. Soc.* **2014**, *136* (41), 14405.
- (103) Citek, C.; Gary, J. B.; Wasinger, E. C.; Stack, T. D. P. *J. Am. Chem. Soc.* **2015**, *137* (22), 6991.
- (104) Chiang, L.; Keown, W.; Citek, C.; Wasinger, E. C.; Stack, T. D. P. *Angew. Chemie - Int. Ed.* **2016**, *128* (35), 10609.
- (105) Lewis, E. A.; Tolman, W. B. *Chem. Rev.* **2004**, *104* (2), 1047.
- (106) Mirica, L. M.; Ottenwaelder, X.; Stack, T. D. P. *Chem. Rev.* **2004**, *104* (2), 1013.
- (107) Karlin, K. D.; Hayes, J. C.; Gultneh, Y.; Cruse, R. W.; McKown, J. W.; Hutchinson, J. P.; Zubieta, J. *J. Am. Chem. Soc.* **1984**, *106* (7), 2121.
- (108) Réglıer, M.; Jorand, C.; Waegell, B. *J. Chem. Soc. Chem. Commun.* **1990**, *24*, 1752.
- (109) Hamann, J. N.; Herzigkeit, B.; Jurgeleit, R.; Tuczek, F. *Coord. Chem. Rev.* **2017**, *334*, 54.
- (110) Schottenheim, J.; Fateeva, N.; Thimm, W.; Krahmer, J.; Tuczek, F. *Zeitschrift für Anorg. und Allg. Chemie* **2013**, *639* (8–9), 1491.
- (111) Itoh, S.; Kumei, H.; Taki, M.; Nagatomo, S.; Kitagawa, T.; Fukuzumi, S. *J. Am. Chem. Soc.* **2001**,

- 123 (27), 6708.
- (112) Osako, T.; Ohkubo, K.; Taki, M.; Tachi, Y.; Fukuzumi, S.; Itoh, S. *J. Am. Chem. Soc.* **2003**, *125* (8), 11027.
- (113) Itoh, S.; Fukuzumi, S. *Acc. Chem. Res.* **2007**, *40* (7), 592.
- (114) Sanyal, I.; Mahroof, M. T.; Nasir, M. S.; Ghosh, P.; Cohen, B. I.; Gultneh, Y.; Cruse, R. W.; Farooq, A.; Karlin, K. D.; Liu, S.; Zubieta, J. *Inorg. Chem.* **1992**, *31* (21), 4322.
- (115) Mirica, L. M.; Vance, M.; Rudd, D. J.; Hedman, B.; Hodgson, K. O.; Solomon, E. I.; Stack, T. D. P. *Science* **2005**, *308* (5730), 1890.
- (116) Company, A.; Palavicini, S.; Garcia-Bosch, I.; Mas-Balleste, R.; Que, L. J.; Rybak-Akimova, E. V.; Casella, L.; Ribas, X.; Costas, M. *Chem. Eur. J.* **2008**, *14* (12), 3535.
- (117) Lucas, H. R.; Li, L.; Sarjeant, A. A. N.; Vance, M. A.; Solomon, E. I.; Karlin, K. D. *J. Am. Chem. Soc.* **2009**, *131* (9), 3230.
- (118) Dalle, K. E.; Gruene, T.; Dechert, S.; Demeshko, S.; Meyer, F. *J. Am. Chem. Soc.* **2014**, *136* (20), 7428.
- (119) Kindermann, N.; Bill, E.; Dechert, S.; Demeshko, S.; Reijerse, E. J.; Meyer, F. *Angew. Chemie - Int. Ed.* **2015**, *54* (6), 1738.
- (120) Kindermann, N.; Günes, C. J.; Dechert, S.; Meyer, F. *J. Am. Chem. Soc.* **2017**, *139* (29), 9831.
- (121) Kindermann, N.; Dechert, S.; Demeshko, S.; Meyer, F. *J. Am. Chem. Soc.* **2015**, *137* (25), 8002.
- (122) Warren, J. J.; Tronic, T. A.; Mayer, J. M. *Chem. Rev.* **2010**, *110* (12), 6961.
- (123) Haack, P.; Limberg, C.; Ray, K.; Braun, B.; Kuhlmann, U.; Hildebrandt, P.; Herwig, C. *Inorg. Chem.* **2011**, *50* (6), 2133.
- (124) Haack, P.; Kärgel, A.; Greco, C.; Dokic, J.; Braun, B.; Pfaff, F. F.; Mebs, S.; Ray, K.; Limberg, C. *J. Am. Chem. Soc.* **2013**, *135* (43), 16148.
- (125) Haack, P.; Limberg, C. *Angew. Chemie - Int. Ed.* **2014**, *53* (17), 4282.
- (126) Halvagar, M. R.; Solntsev, P. V.; Lim, H.; Hedman, B.; Hodgson, K. O.; Solomon, E. I.; Cramer, C. J.; Tolman, W. B. *J. Am. Chem. Soc.* **2014**, *136* (20), 7269.
- (127) Kochem, A.; Gennarini, F.; Yemloul, M.; Orio, M.; Le Poul, N.; Rivière, E.; Giorgi, M.; Faure, B.; Le Mest, Y.; Réglie, M.; Simaan, A. J. *Chempluschem* **2017**, *82* (4), 615.
- (128) Gennarini, F.; Kochem, A.; Isaac, J.; Mansour, A. T.; López, I.; Le Mest, Y.; Thibon-Pourret, A.; Faure, B.; Jamet, H.; Le Poul, N.; Belle, C.; Simaan, A. J.; Réglie, M. *Inorganica Chim. Acta* **2017**, *481*, 113.
- (129) Gennarini, F.; David, R.; López, I.; Le Mest, Y.; Réglie, M.; Belle, C.; Thibon-Pourret, A.; Jamet, H.; Le Poul, N. *Inorg. Chem.* **2017**, *56* (14), 7707.
- (130) Thomas, F.; Gellon, G.; Gautier-Luneau, I.; Saint-Aman, E.; Pierre, J. L. *Angew. Chemie - Int. Ed.* **2002**, *41* (16), 3047.
- (131) Isaac, J. A.; Mansour, A.-T.; David, R.; Kochem, A.; Philouze, C.; Demeshko, S.; Meyer, F.; Réglie, M.; Simaan, A. J.; Caldarelli, S.; Yemloul, M.; Jamet, H.; Thibon-Pourret, A.; Belle, C.

- Dalton Trans.* **2018**, 47 (29), 9665.
- (132) Quist, D. A.; Diaz, D. E.; Liu, J. J.; Karlin, K. D. *J. Biol. Inorg. Chem.* **2017**, 22 (2–3), 253.
- (133) Davenport, T. C.; Tilley, T. D. *Angew. Chemie - Int. Ed.* **2011**, 50 (51), 12205.
- (134) Brodsky, C. N.; Passard, G.; Ullman, A. M.; Jaramillo, D. E.; Bloch, E. D.; Huynh, M.; Gygi, D.; Nocera, D. G. *Dalton Trans.* **2018**, 48, 11903.
- (135) Passard, G.; Ullman, A. M.; Brodsky, C. N.; Nocera, D. G. *J. Am. Chem. Soc.* **2016**, 138 (9), 2925.
- (136) Davenport, T. C.; Tilley, T. D. *Dalton Trans.* **2015**, 44 (27), 12244.
- (137) Ziegler, M. S.; Levine, D. S.; Lakshmi, K. V.; Tilley, T. D. *J. Am. Chem. Soc.* **2016**, 138 (20), 6484.
- (138) Gomez, M.; Muller, G.; Rocamora, M. *Coord. Chem. Rev.* **1999**, 193–195, 769.
- (139) Dagonne, S.; Bellemin-Laponnaz, S.; Maise-François, A. *Eur. J. Inorg. Chem.* **2007**, 2007 (7), 913.
- (140) Walli, A.; Dechert, S.; Bauer, M.; Demeshko, S.; Meyer, F. *Eur. J. Inorg. Chem.* **2014**, 2014 (27), 4660.
- (141) Li, S. T.; Braun-Cula, B.; Hoof, S.; Dürr, M.; Ivanović-Burmazović, I.; Limberg, C. *Eur. J. Inorg. Chem.* **2016**, 25, 4017.
- (142) Li, S. T.; Braun-Cula, B.; Hoof, S.; Limberg, C. *Dalton Trans.* **2018**, 47 (2), 544.
- (143) Serrano-Plana, J.; Garcia-Bosch, I.; Company, A.; Costas, M. *Acc. Chem. Res.* **2015**, 48 (8), 2397.
- (144) Serrano-Plana, J.; Costas, M.; Company, A. *Inorg. Chem.* **2014**, 53 (24), 12929.
- (145) Dagonne, S.; Bellemin-Laponnaz, S.; Welter, R. *Organometallics* **2004**, 23 (12), 3053.
- (146) Newkome, G. R.; Garbis, S. J.; Majestic, V. K.; Fronczek, F. R.; Chiarilc, G. *J. Org. Chem.* **1981**, 46 (5), 833.
- (147) Pellizzaro, M. L.; Barrett, S. A.; Fisher, J.; Wilson, A. *J. Org. Biomol. Chem.* **2012**, 10 (25), 4899.
- (148) Boelrijk, A. E. M.; Neenan, T. X.; Reedijk, J. *Dalton Trans.* **1997**, 23, 4561.
- (149) Bechlars, B.; D'Alessandro, D. M.; Jenkins, D. M.; Iavarone, A. T.; Glover, S. D.; Kubiak, C. P.; Long, J. R. *Nat. Chem.* **2010**, 2 (5), 362.
- (150) Shimanouchi, T. *Tables of Molecular Vibrational Frequencies Consolidated Volume I*; 1972.
- (151) Evans, J. C.; Lo, G. Y.-S. *Spectrochim. Acta* **1965**, 21 (6), 1033.
- (152) Tyeklár, Z.; Jacobson, R. R.; Wei, N.; Murthy, N. N.; Zubieta, J.; Karlin, K. D. *J. Am. Chem. Soc.* **1993**, 115 (7), 2677.
- (153) Addison, A. W.; Rao, T. N. *J. Chem. Soc., Dalton Tans.* **1984**, 1, 1349.
- (154) West, D. X.; Liberta, A. E.; Padhye, S. B.; Chikate, R. C.; Sonawane, P. B.; Kumbhar, A. S.; Yerande, R. G. *Coord. Chem. Rev.* **1993**, 123, 49.
- (155) Belle, C.; Beguin, C.; Gautier-Luneau, I.; Hamman, S.; Philouze, C.; Pierre, J. L.; Thomas, F.; Torelli, S.; Saint-Aman, E.; Bonin, M. *Inorg. Chem.* **2002**, 41 (3), 479.

- (156) Torelli, S.; Belle, C.; Gautier-Luneau, I.; Pierre, J. L.; Saint-Aman, E.; Latour, J. M.; Le Pape, L.; Luneau, D. *Inorg. Chem.* **2000**, *39* (16), 3526.
- (157) Brown, E. V. *J. Org. Chem.* **1965**, *30* (5), 1607.
- (158) Huang, C. Y.; Kuan, K. Y.; Liu, Y. H.; Peng, S. M.; Liu, S. T. *Organometallics* **2014**, *33* (11), 2831.
- (159) Thibon-Pourret, A.; Gennarini, F.; David, R.; Isaac, J. A.; Lopez, I.; Gellon, G.; Molton, F.; Wojcik, L.; Philouze, C.; Flot, D.; Le Mest, Y.; Réglier, M.; Le Poul, N.; Jamet, H.; Belle, C. *Inorg. Chem.* **2018**, *57* (19), 12364.
- (160) Comba, P.; Morgen, M.; Wadepohl, H. *Polyhedron* **2013**, *52*, 1239.
- (161) Farrugia, L. J.; Lovatt, P. A.; Peacock, R. D. *J. Chem. Soc., Dalton Tans.* **1997**, *6*, 911.
- (162) Kodera, M.; Shimakoshi, H.; Tachi, Y.; Katayama, K.; Kano, K. *Chem. Lett.* **1998**, *27* (5), 441.
- (163) Monzani, E.; Battaini, G.; Perotti, A.; Casella, L.; Gullotti, M.; Santagostini, L.; Nardin, G.; Randaccio, L.; Geremia, S.; Zanello, P.; Opromolla, G. *Inorg. Chem.* **1999**, *38* (23), 5359.
- (164) Connelly, N. G.; Geiger, W. E. *Chem. Rev.* **1996**, *96* (2), 877.
- (165) Mabbott, G. A. *J. Chem. Educ.* **1983**, *60* (9), 697.
- (166) Brunschwig, B. S.; Creutz, C.; Sutin, N. *Chem. Soc. Rev.* **2002**, *31* (3), 168.
- (167) Robinson, M. B.; Day, P. *Adv. Inorg. Chem. Radiochem.* **1968**, *10*, 247.
- (168) Konezny, S. J.; Doherty, M. D.; Luca, O. R.; Crabtree, R. H.; Soloveichik, G. L.; Batista, V. S. **2012**.
- (169) Demadis, K. D.; Hartshorn, C. M.; Meyer, T. J. *Chem. Rev.* **2001**, *101* (9), 2655.
- (170) Eisenhart, T. T.; McCarthy, B. D.; Rountree, E. S.; Dempsey, J. L. *Inorg. Chem.* **2014**, *53* (19), 9983.
- (171) Lee, K. J.; Elgrishi, N.; Kandemir, B.; Dempsey, J. L. *Nat. Rev. Chem.* **2017**, *1* (5), 0039.
- (172) Costentin, C.; Drouet, S.; Robert, M.; Savéant, J. M. *J. Am. Chem. Soc.* **2012**, *134* (27), 11235.
- (173) Savéant, J.-M. *Elements of Molecular and Biomolecular Electrochemistry*; 2006.
- (174) Elgrishi, N.; McCarthy, B. D.; Rountree, E. S.; Dempsey, J. L. *ACS Catal.* **2016**, *6* (6), 3644.
- (175) Li, J.-H.; Liu, W.-J.; Yin, D.-L. *Synth. Commun.* **2004**, *34* (17), 3161.
- (176) Williams, D. B. G.; Lawton, M. *J. Org. Chem.* **2010**, *75* (24), 8351.
- (177) Rossini, E.; Bochevarov, A. D.; Knapp, E. W. *ACS Omega* **2018**, *3* (2), 1653.
- (178) Mayer, J. M. *Acc. Chem. Res.* **2011**, *44* (1), 36.
- (179) Mader, E. A.; Davidson, E. R.; Mayer, J. M. *J. Am. Chem. Soc.* **2007**, *129* (16), 5153.
- (180) Sastri, C. V.; Lee, J.; Oh, K.; Lee, Y. J.; Lee, J.; Jackson, T. A.; Ray, K.; Hirao, H.; Shin, W.; Halfen, J. A.; Kim, J.; Que, L.; Shaik, S.; Nam, W. *Proc. Natl. Acad. Sci. U. S. A.* **2007**, *104* (49), 19181.
- (181) Rountree, E. S.; Martin, D. J.; McCarthy, B. D.; Dempsey, J. L. *ACS Catal.* **2016**, *6* (5), 3326.

- (182) Costentin, C.; Nocera, D. G.; Brodsky, C. N. *Proc. Natl. Acad. Sci.* **2017**, *114* (43), 11303.
- (183) Dolomanov, O. V.; Bourhis, L. J.; Gildea, R. J.; Howard, J. A. K.; Puschmann, H. *J. Appl. Crystallogr.* **2009**, *42* (2), 339.
- (184) Frisch, M. J.; Trucks, G. W.; Schlegel, H. B.; Scuseria, G. E.; Robb, M. A.; Cheeseman, J. R.; Scalmani, G.; Barone, V.; Mennucci, B.; Petersson, G. A.; Nakatsuji, H.; Caricato, M.; Li, X.; Hratchian, H. P.; Izmaylov, A. F.; Bloino, J.; Zheng, G.; Sonnenberg, J. L.; Hada, M.; Ehara, M.; Toyota, K.; Fukuda, R.; Hasegawa, J.; Ishida, M.; Nakajima, T.; Honda, Y.; Kitao, O.; Nakai, H.; Vreven, T.; Montgomery, J. A.; Peralta, J. E.; Ogliaro, F.; Bearpark, M.; Heyd, J. J.; Brothers, E.; Kudin, K. N.; Staroverov, V. N.; Kobayashi, R.; Normand, J.; Raghavachari, K.; Rendell, A.; Burant, J. C.; Iyengar, S. S.; Tomasi, J.; Cossi, M.; Rega, N.; Millam, J. M.; Klene, M.; Knox, J. E.; Cross, J. B.; Bakken, V.; Adamo, C.; Jaramillo, J.; Gomperts, R.; Stratmann, R. E.; Yazyev, O.; Austin, A. J.; Cammi, R.; Pomelli, C.; Ochterski, J. W.; Martin, R. L.; Morokuma, K.; Zakrzewski, V. G.; Voth, G. A.; Salvador, P.; Dannenberg, J. J.; Dapprich, S.; Daniels, A. D.; Farkas, A.; Foresman, J. B.; Ortiz, J. V.; Cioslowski, J.; Fox, D. J. 2009,.
- (185) Cramer, C. J.; Włoch, M.; Piecuch, P.; Puzzarini, C.; Gagliardi, L. *J. Phys. Chem. A* **2006**, *110* (5), 1991.
- (186) Li, Z.; Liu, W. *J. Chem. Theory Comput.* **2016**, *12* (1), 238.

Abstract

Copper-oxygen adducts in enzymes have been proposed to be responsible for the activation of C-H bonds, a process that has industrial applications. The first part of this thesis is therefore dedicated to a discussion on various copper oxygenases and their model complexes. Recently, key reactive intermediates have emerged and among them mixed valent $\text{Cu}^{\text{II}}\text{Cu}^{\text{III}}$ species have been proposed to be responsible for strong C-H bond activation.

In this work the stabilisation and spectroscopic characterisation of high valent intermediates using dinucleating ligands based on a 1,8-naphthyridine spacer are explored. The generation of Cu_2O_2 species from the activation of O_2 by Cu^{II}_2 complexes is discussed. Two $\mu\text{-}\eta^2\text{:}\eta^2\text{-peroxo-Cu}^{\text{II}}_2$ complexes have been prepared at -80°C and characterised by spectroscopy and density functional theory (DFT). Our attempts at generating dinuclear systems using new dissymmetric ligands with an amide function are also discussed. Finally the successful characterisation of mixed valent $\text{Cu}^{\text{II}}\text{Cu}^{\text{III}}$ species by mono-electronic oxidation of Cu^{II}_2 complexes is described (cyclic voltammetry, electron paramagnetic resonance, UV-visible, near infrared and DFT).

The last part focusses on probing the reactivity of $\text{Cu}^{\text{II}}\text{Cu}^{\text{III}}$ species, for which the literature is almost inexistent. When sterically congested ligands are used to support the mixed valent system, intramolecular aliphatic C-H oxidation was observed, whether as the $\text{Cu}^{\text{II}}\text{Cu}^{\text{III}}$ species supported by a less bulky ligand was able to oxidise toluene. Interestingly the addition of a base made the system catalytic.

Key words: bio-inorganic chemistry, ligand design, copper, dioxygen activation, mixed valent species, catalysis.

Résumé

Les adduits cuivre-oxygène dans les métallo-enzymes ont été proposés comme étant responsables de l'activation de liaisons C-H, processus qui ont un intérêt pour des applications industrielles potentielles. La première partie de ce travail est consacrée à une présentation de différentes mono-oxygénases à cuivre et de leurs complexes modèles. Récemment, des intermédiaires réactionnels ont émergé et parmi ceux-ci, des espèces de valence mixte $\text{Cu}^{\text{II}}\text{Cu}^{\text{III}}$ ont été proposées comme étant des espèces réactives clés pour l'activation de liaisons C-H fortes.

Dans ce travail, à partir de ligands binucléants basés sur un espaceur 1,8-naphthyridine, la stabilisation et les caractérisations spectroscopiques de ce type d'intermédiaires à haut degré d'oxydation sont explorées. La préparation d'espèces Cu_2O_2 à partir de l'activation du dioxygène par les complexes Cu^{II}_2 est discutée. Deux complexes $\mu\text{-}\eta^2\text{:}\eta^2\text{-peroxo-Cu}^{\text{II}}_2$ ont été préparés à -80°C et caractérisés par différentes méthodes spectroscopiques associées à des calculs par la théorie de la fonctionnelle de la densité (DFT). A partir de nouveaux ligands dissymétriques possédant une fonction amide, nos tentatives pour contrôler la préparation des complexes binucléaires associés sont également présentées. Puis, les caractérisations des espèces à valence mixte $\text{Cu}^{\text{II}}\text{Cu}^{\text{III}}$ obtenues par mono-oxydation électronique des complexes Cu^{II}_2 sont décrites (voltammétrie cyclique, résonance paramagnétique électronique, UV-visible, proche infrarouge et DFT).

Enfin, ce travail est complété par l'étude de la réactivité des espèces $\text{Cu}^{\text{II}}\text{Cu}^{\text{III}}$, pour lesquelles la littérature est presque inexistante. Lorsque des ligands stériquement encombrés sont utilisés dans les espèces à valence mixte, des oxydations intramoléculaires sont observées, alors que l'espèce $\text{Cu}^{\text{II}}\text{Cu}^{\text{III}}$ possédant un ligand moins encombré oxyde le toluène. Il est à noter que l'ajout d'une base rend le système catalytique.

Mots clés: Chimie bio-inorganique, conception de ligands, cuivre, activation du dioxygène, espèces à valence mixte, catalyse.